Mass spectrometry investigations on biomolecular macrocomplexes in native solutions: New insights with LILBID-MS

Dissertation
zur Erlangung des Doktorgrades der Naturwissenschaften

vorgelegt beim Fachbereich Biochemie, Chemie und Pharmazie (FB 14)
der Goethe-Universität
in Frankfurt am Main

von
Jan Hoffmann
aus Hannover

Frankfurt 2010
(D30)

vom Fachbereich Biochemie, Chemie und Pharmazie (FB 14)
der Goethe-Universität als Dissertation angenommen.

Dekan: Herr Prof. Dr. D. Steinhilber

1. Gutachter: Herr Prof. Dr. B. Brutschy

2. Gutachter: Herr Prof. Dr. M. Karas

Datum der Disputation: 06.06.2011

Contents

List of Figures

List of acronyms

bR	bacteriorhodopsin
DDM	*N*-Dodecyl-β-D-maltoside
DLS	Dynamic light scattering
dsRNA	double stranded RNA
ESI	Electro Spray Ionization
HPLC	High pressure liquid chromatography
ICP-MS	Inductively Coupled Plasma - Mass Spectrometry
IR	infrared
LILBID	Laser induced liquid bead ion desorption
MALDI	Matrix Assisted Laser Desorption / Ionization
MS	Mass Spectrometry
PR	proteorhodopsin
Q-TOF	Quadrupole-TOF
TOF	Time of flight
UV	ultraviolett

1 Introduction

During recent decades mass spectrometry (MS) evolved into a very valuable tool for studying proteins and macromolecular complexes. Besides the great success of mass spectrometry in determining the primary structure of proteins, which brought proteomics significantly forward, the investigation of non-covalent complexes and their higher-order structures gets increasingly into the focus of mass spectrometry. For carrying out their biological function, proteins frequently interact with each other forming occasionally large complexes or even supercomplexes. Mass spectrometry allows to obtain informations such as the global architecture of proteins, the connectivity of subunits and the resulting relationship to biological function. Furthermore, with MS it is possible to gain access to the kinetics of assembly formation, quaternary structures and dissociation constants. Only small amounts of substance required for measuring the mass-to-charge ratio (m/z) and the high speed of analysis make MS a dedicated method to study protein complexes. Mass spectrometric investigation on non-covalent complexes evolved only recently as special preconditions must be fulfilled to preserve the weak interactions during the transfer from solution to the gas phase. Especially membrane proteins present a considerable challenge for the transfer into the gas phase as they have to be solubilised by detergents. To maintain a native quaternary structure an environment which is as native as possible is required.

Depending on the substances to be analysed, appropriate ionization techniques are applied to transfer the analyte into the gas phase. The investigation of biomolecules with MS is especially demanding in the ionization step. In particular it should be as soft as possible to avoid fragmentation or conformational changes during ionization. Today two widely adopted ionization methods suitable for the analysis of biomolecules are MALDI (Matrix-assisted laser desorption/ionisation) [1, 2] and ESI (Electrospray ionisation) [3, 4]. In MALDI the analyte molecules are embedded into an organic matrix. Upon irradiation with a UV or IR laser pulse the matrix absorbs the energy and releases the analyte by desorption/ablation. The exact mechanism of desorption and ion formation is still not completely understood. The strengths of MALDI-MS lie in

its simplicity of use and in its extremely high sensitivity. Furthermore the low charge states observed with MALDI-MS simplify the interpretation of the results, especially in case of complex sample mixtures, as the most abundant signal typically corresponds to singly charged species. A particular interesting field is the direct MALDI-MS analysis of tissues by means of laser ablation especially in combination with molecular imaging techniques termed MALDI-mass spectrometry imaging (MALDI-MSI) [5]. The localisation of proteins within tissues helps to identify and to understand a wide range of diseases by comparing healthy with morbid tissues. However, apart from the lack of a native environment MALDI suffers from a decreasing detection/desorption efficiency for very large complexes. In addition fragmentation occasionally occurs with less stable biomolecules. The detection of specific non-covalent complexes with MALDI-MS often is difficult, or hardly possible for membrane proteins, and requires careful tuning of instrumentation and sample preparation [6] because MALDI-MS is known to be less soft as compared to ESI-MS [7].

In ESI-MS on the other hand the analyte molecules are solubilised in aqueous solutions containing volatile organic solvents such as acetonitrile or methanol. This solution is pressed through a thin needle on which a high voltage is applied. At the tip of the needle a Taylor cone forms and eventually disperses into a plume, a spray consisting of highly charged droplets. Two theories describe the ionisation process: Either as a Coulomb explosion/fission of the highly charged droplets or as field emission of the analyte out of the droplets surface. However high concentrations of salt or detergent have a negative impact on the ionisation process resulting in a strongly decreased detection efficiency [8, 9]. The low salt tolerance of ESI-MS gives MALDI-MS some advantage regarding difficult to ionize biomolecules that require laborious purification steps [7]. As ESI is less tolerant to such crucial solvent additives it is less applicable to demanding biomolecular samples such as membrane proteins. On the other hand the high charge states of the ions extend the analytical possibilities due to charge state dependent fragmentation patterns and pathways in collision cells. However high charge states may result in a variety of conformations, non-native folding of proteins [10, 11, 12] and congestion of mass peaks by many different charge states. As ESI-MS is working with liquids it is easily possible to connect on-line separation techniques like liquid chromatography or capillary electrophoresis directly to the source which greatly enhances the analyzing possibilities of ESI-MS. This way complex sample mixtures can be untangled based on a variety of other characteristics than mass. In addition the rapid and high resolution separation allow even very small sample volumes of mixtures to be interfaced with ESI-

MS in particular with nanoESI (nESI).

Besides the requirement of mild and native conditions to transfer biomolecules from liquid into the gas phase, a high tolerance for salts is important as this often stabilises the structure of the complexes. As salts are usually considered "MS-unfriendly" components, the development of salt-tolerant techniques recently evolved. In particular, nanoESI has been shown to be significantly less susceptible for salts compared to conventional ESI-MS. The smaller size of the initial droplets and the resulting higher surface charge density most likely are responsible for this effect [13]. In general the solvent in nESI consists of an aqueous solution containing a volatile buffer such as ammonium acetate instead of the volatile organic compounds delivering an environment as native as possible. A further advantage over conventional ESI is the strongly reduced sample consumption which allows to study samples of low availability.

Another ESI modification is fused-droplet electrospray (FD-ESI) [14]. Here the sample solution is ultrasonically nebulised forming a fine aerosol. In addition charged droplets of methanol are generated by electrospraying from a capillary. The aerosol and the methanol droplets are brought together inside a reaction chamber. Inside the chamber the sample aerosol fuses with the charged methanol droplets from which the electrospray process continuously proceeds. The result is a very high salt-tolerance which allows to mass analyse proteins from solutions containing as much as 10% (w/w) of NaCl corresponding to a salt concentration of 1.7 mol/l.

Both ionisation methods are often extended with tandem mass spectrometry (MS/MS) techniques. Here a precursor ion is selected in a quadrupole, fragmented for example in a collision cell by collision induced dissociation (CID), by photodissociation or by electron capture dissociation (ECD) and the resulting fragments are then analysed by a detector. In this way a protein sequence can be obtained as well as subcomplex or subunit compositions. To further extend tandem mass spectrometry, several stages are applied in series leading to MS^n instruments. A further enhancement is the addition of ion mobility spectrometry (IMS) [15] to a mass spectrometer. In IMS ions drift by an uniform electric field through a tube filled with buffer gas. With the measured drift time and simulated collision cross-sections the ion shape can be derived in addition to the mass and subunit relations. Thus with IMS-MS it is sometimes possible to separate isomers.

Recently an alternative ion source, termed LILBID (Laser induced liquid bead ion desorption), was introduced by the group of Prof. Brutschy. In LILBID aqueous solutions (either a beam [16, 17, 18] or micro-droplets [19]) are transferred into vacuum and

subsequently irradiated by an mid-IR laser which leads to ablation of ions from the liquid target. The ions produced this way occur with low charge states, but normally higher charged than those observed with MALDI-MS. LILBID-MS is highly tolerant to salts, a wide range of buffering agents and detergents. Currently the salt-tolerance is higher than that of MALDI-MS and nESI but not as high as that of FD-ESI. The use of solutions providing an adjustable ionic strength and a defined pH result in an environment which is as native as possible for biomolecular complexes. If desired other chemicals like reducing agents or divalent salt ions can also be added. Thus this method is specifically designed for the analysis of non-covalent macromolecular complexes and in particular membrane proteins as already has been shown several times in previous works [20, 21]. Furthermore by elevating the laser energy intact complexes can be fragmented by thermolysis and reveal their subunit composition. Other important LILBID application are complexation studies of protein-protein interactions as well as protein-DNA/RNA and DNA-DNA binding. Previous works also include sequence specific binding of a synthetic ligand to DNA, the determination of a dissociation constant (K_D) of a protein-RNA complex and the detection of large macromolecular assemblies like the respiratoral complex I with a mass of 900 kDa and a 50S ribosome with a mass of 1.4 MDa [22, 23, 24].

The softness of LILBID usually results in ions, which are still protected by a shell of solvent and, in case of membrane proteins, detergent molecules. This leads to a unresolved broadening of the signals towards higher masses and thus hampers the accurate determination of masses compared to the high resolution spectra of MALDI- and ESI-MS. Another significant difference between LILBID and the other ionisation methods lies in the different fragmentation pathways. In MALDI and ESI fragmentation is commonly performed by means of post-source CID. While CID usually leads to dissociation of subunits in peripheral positions, the harsh laser conditions in LILBID result in a complete disassembly mirroring the thermal stability of the complex. Under moderate laser intensities only the weakly interacting subcomplexes are fragmented and hence the strongly interacting ones survive the desorption process. So truly complementary results are delivered by these different fragmentation pathways. In addition, CID allows for a finer controlled tuning of dissociation energy and also higher energies are possible so that covalent peptides can be fragmented.

Meanwhile several groups started using LILBID-MS for analysing biomolecular complexes [25, 26, 27, 28]. Furthermore, the application of LILBID-MS is not limited to biomolecules but was extended to study solvated electrons [29] and to mimic the *in situ* analysis of emitted plumes of water vapour and ice particles of the saturn moon

Enceladus [30].

The present work emphasises the advantages of using native solutions in LILBID-MS. The stability and complexation behaviours of biomolecules in solution phase change with varying buffer conditions. This is monitored by the salt-dependent stability of a 16-mer DNA double helix and the sequence-dependent hybridisation of a 60-mer DNA. Moreover, the oligomerisation of proteins using different buffers is exemplarily characterised for the lsm protein HvoLsm and the transcription factor TAp63α. The effect of varying detergents on the quaternary structure of membrane proteins is demonstrated for the retinal protein proteorhodopsin. Specific complexation will be shown for several protein-DNA and protein-RNA complexes. In general the relation of biological function and the complex structure will be discussed as well as possible biological applications of synthetic dendrimer molecules. Quaternary structures observed from solution phase will be compared with crystal structures where available. Furthermore several instrumental developments improve the sensitivity and signal-to-noise ratio of the method.

The outline of this thesis is as follows:

In chapter 2 the LILBID ion source and the experimental setup are described. Chapter 3 presents the results and is divided into three groups corresponding to different classes of complexes each with its own characteristics and requirements regarding its mass spectrometric analysis. Section 3.1 is attributed to solvable proteins and synthetic molecules, section 3.2 to nucleic acids and section 3.3 to membrane protein complexes.

2 Methods and Instruments

2.1 The LILBID source

The droplet source in LILBID-MS is a commercial piezo-driven droplet dispenser (Microdrop$^{(Tm)}$). The dispenser ejects tiny microdroplets of aqueous solutions at adjustable frequencies. They have a diameter of about 50 μm resulting in a volume of about 65pL, depending on the viscosity and surface tension of the liquid chosen. Starting at roughly 0.3 bar the droplets are transferred into high vacuum (10^{-5} mbar) via pressure-reduction apertures. There the droplets are irradiated one-by-one by mid-IR laser pulses with pulse intensities up to 100 MW/cm^2. As the droplets are very small only a short time is allowed to pass between injection of the droplets into high vacuum and mid-IR irradiation to avoid freezing of the droplets due to evaporative cooling. The laser pulses are generated by a home-build Nd:Yag pumped $LiNbO_3$ optical parametric oscillator (OPO) [31, 32], which is tuned to the very strong and broad absorption band of liquid water at around 3500 cm^{-1}. Thus the laser light directly excites the asymmetric OH stretch vibration ν_3 of water as well as the symmetric stretch vibration ν_1 (Fig.2.1 shows the absorption of water in the mid-IR range). At this frequency the penetration depth of the light in water is only about one micrometer. The excited stretch vibrations were shown to relax in bulk water within a few hundreds of femtoseconds [33] eventually resulting in heat. Thus the pulsewidth of the laser of about 6 ns most likely leads to an absorption of multiple photons, generating a high temperature. Due to the sudden and strong temperature gradient an increase in pressure is induced so that the supercritical state is reached.

Currently the desorption is best described as a laser-induced rapid phase transition into the supercritical state. There the dielectric constant ϵ is fastly decreased and the shielding of ions and counter-ions is significantly reduced. The supercritical phase rapidly expands into high vacuum comparable to the expansion of highly compressed gases. The rapid expansion leads to the disruption (explosion) of the droplets into smaller microdroplets which is demonstrated by a series of photographs in Fig.2.2 [19]. During

this ablation process part of the pre-formed analyte ions are set free and can be analysed by the mass spectrometer. By the reduction of density ϵ almost drops to zero and ion recombination is strongly increased. Only those ions with kinetic energies high enough to overcome the coulomb attraction of their counter ions escape into vacuum. They are termed "lucky survivors".

The rapid expansion of the supercritical water eventually leads to a shockwave disrupting the droplets. Investigations in our group on water droplets have shown that this shockwave propagates with a velocity of about 1000 m/s. Similar results were obtained by other groups for ethanol droplets where the shockwave was found to propagate with a velocity of about 1300 m/s [34]. Interestingly the observed velocities of analyte molecules evaporating from liquid water by laser ablation show a wider range. Reported values range from 300 m/s [35] to around 1000 m/s [36, 25] and even more than 2000 m/s [37]. All of these results have in common that the reported velocities strongly depend not only on the laser intensity but also on the laser wavelength. In addition these experiments were performed for small molecules with molecular masses of a few hundred Dalton. Furthermore these velocities arise as broad Maxwell-Boltzmann distributions. Finally it was shown by Maselli et al. that spontaneous evaporation leads to moderate cooling by means of molecular energy transfer involving many collisions [38]. This cooling effect is even more pronounced when using laser ablation.

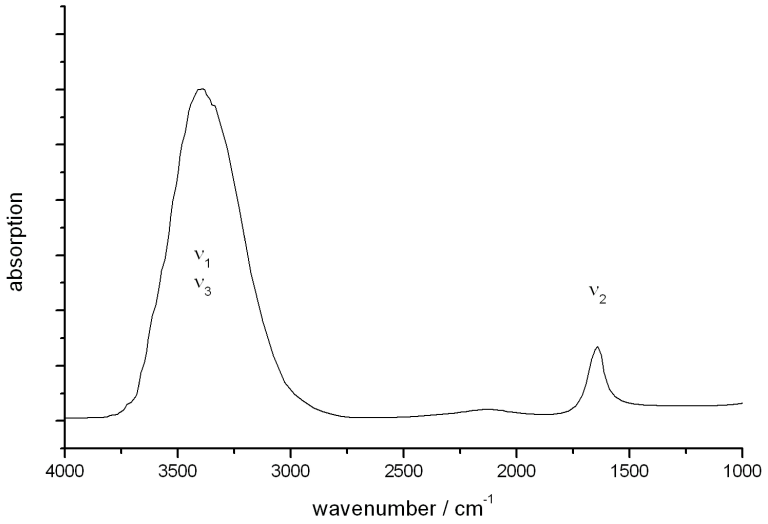

Figure 2.1: *Absorption of water in the mid-infrared. The following vibrational modes contribute to the absorption: the bending mode (ν_2) as well as the symmetric (ν_1) and asymmetric (ν_3) stretching. (Based on data from D.J. Segelstein [39])*

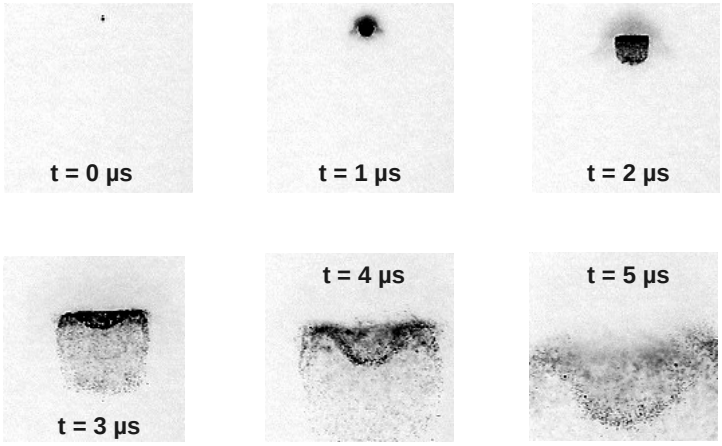

Figure 2.2: *Series of photographs illustrating the disruption of the microdroplet. Δt is one microsecond.*

Given an operating frequency of 10 Hz the sample-consumption lies in the range of 0.65 nL/s or 39 nL/min respectively. A typical LILBID mass spectrum averaged over 200 droplets results in an analyte consumption of only 13 nL. A total sample volume of a few microlitres at typically micromolar concentrations is sufficient for a mass analysis. This is a major advantage over the previously used ablation from a continuous liquid beam. In addition, by varying the laser energy LILBID operates in different modes of desorption: At low laser energy LILBID operates in an "ultra-soft" mode where intact complexes are observed. At elevated intensities more fragmentation occurs. First the complexes decay into their subcomplexes and at very high laser intensities the complexes dissociate into their covalent subunits. The effect of increasing fragmentation with increasing laser energy most likely is a thermolysis process. This laser-induced in-source fragmentation is an equivalent to dissociation in collision cells. However, the fragmentation pathways clearly are different.

The resolution of the mass spectra and the general signal quality can be improved in several ways. First, at elevated laser energies a higher amount of ions is desorbed resulting in an improved signal-to-noise ratio. Another implication is that the degree of desolvation increases at higher laser intensities which results in narrower peaks. Thus the choice of laser energy presents a balancing act between signal quality and avoidance of fragmentation, except for very stable complexes. Generally the achievable energy of the laser pulse is not sufficient to break covalent bonds or even to actively ionize molecules. Second, salt ions have a negative impact on the desorption process. In addition to the

recombination of ions and counter-ions in the supercritical phase, recombination also occurs in the gas phase after the disruption of the droplet. This is particular evident when working with high salt concentrations that strongly reduce the signal intensity. This can be partially compensated for by tuning the acceleration potentials accordingly.

In LILBID-MS fragile complexes, held together only by weak non-covalent interactions, can be readily observed. A prerequisite, though, is that the complexes are sufficiently stable so that they don't already dissociate at room temperature. An advantageous possibility to investigate complexes which dissociate at or below room temperature, is that the droplet dispenser and the water reservoir can be cooled down by a home-built peltier cooling device. In LILBID-MS ions are usually observed with low charge states. There is a propensity to observe in gas phase ions of the same polarity as in solution.

2.2 Time-of-flight mass spectrometry

The ablation process takes place inside the ion optics of a time-of-flight (TOF) spectrometer so that the droplet disruption is directly followed by the the mass analysis. Fig.2.3 shows a scheme of the mass spectrometer depicting the pressure ranges and the relative potentials. In general the resolution achievable with TOF instruments is not as good as the resolution observed with fourier-transform ion-cyclotron-resonance (FTICR) or orbitrap detectors. However, TOF spectrometers have the advantage of an unlimited m/z range which is important in the analysis of large and lowly charged complexes.

The TOF setup used throughout this work is a home-built Wiley-McLaren-type [40] time-of-flight mass spectrometer including an ion mirror (reflectron [41]) and a Daly-type [42] high-mass detector. Briefly in TOF spectrometers ions are accelerated to a given kinetic energy and separated by their time of flight according to their mass-to-charge ratio (m/z) where the flight time is proportional to the square root of m/z. Time-of-flight spectrometers allow to record complete spectra over the desired m/z range in a single scan. The electric pulses used for accelerating the ions are generated by home-built bipolar power supplies. The ion optics utilizes delayed extraction (time-lag focussing) [40] which is used to compensate for different kinetic energies of the ions. This includes the special case of ions with the same m/z and kinetic energy but flying in opposite directions with respect to the TOF axis. Here delayed extraction tries to compensate the so called "turn-around-time" which is the difference in the time of flight after the acceleration. The idea is to let the ions freely move for a variable time before they are accelerated. Thus they will reach different areas of the ion optics and hence will

gain different amount of kinetic energy according to the electric field gradient. Delayed extraction is especially advantageous in those cases where the distribution of kinetic energy of the ions is quite broad. A further advantage of this energy focussing technique is that the ions can freely expand before the acceleration. This way charge repulsion effects can be minimised.

In addition spatial focussing [40] is implemented which compensates for different initial positions of ions in the accelerating region, which would otherwise result in different flight times too. The Wiley-McLaren-type TOF implies a two-stage acceleration with which the space focus can be freely adjusted at a given geometry of the accelerating electrodes by tuning the applied voltages. Two inconvenient side-effects have to be noted: first, delayed extraction is mass-dependent [43] and second the two focussing techniques mentioned above are mutually exclusive [40] for this type of setup. Hence depending on the characteristics of the ion source a compromise between these two focussing techniques has to be found.

Furthermore an Einzel lens focusses the ion beam along the TOF axis while a newly introduced series of deflection plates is responsible for the beam-steering. Beam-steering is used to partially correct deviations from an isotropical distribution of the desorbed ions. The reflectron enhances the resolution by effectively extending the field-free drift range of the spectrometer. In addition, the reflectron also compensates for distributions of initial kinetic energies of the ions. Due to the two-stage implementation the reflectron generates a second space focus where the detector resides.

The detector consists of a multi-channel-plate (MCP) and incorporates a post-acceleration of the ions as well as a counterfield for rejection of metastable ions. These are ions that fragment inside the field-free drift region distributing the kinetic energy of the mother ion among the fragments. Due to the change of kinetic energy the fragments arrive at the detector at different flight times resulting in additional, artificial signals in the mass spectrum. The secondary electrons produced by the MCP from a colliding ion are converted into photons via a scintillator and eventually are detected by a photomultiplier.

Despite the beam-steering and variable focussing techniques implemented in the TOF setup the resolution currently is at best moderate. Mainly two reason are responsible for this behaviour. First of all, the desorbed ions have a distribution of high initial kinetic energies caused by the explosive expansion which is rather broad both in value and in direction which can not be compensated for in a TOF-only setup. One possible, in modern commercial instruments widely used, way to overcome this uncertainty in the flight

time is to apply an orthogonal TOF section. Second, due to an incomplete desolvation the ions have solvent molecules attached. The more additives are in the buffer, the more adducts are attached. One impressive example of solvent adducts can be found in the nESI spectrum of the small peptide gramidicin S where under mild ESI conditions up to 50 molecules of waters are attached [44]. Hence mixed distributions of solvent molecules and salt ions attached to large macromolecular complexes in combination with the broad distribution of initial kinetic energies lead to poorly resolved signals.

The recording of the mass spectra is performed with a 8-bit digitiser card (Aquiris). The hardware is controlled by a home-made software using LabView which allows for timing the measurement and data accumulation. LabView software is also used for calibrating and analysing the data. Especially the omnipresent background caused by evaporating water clusters [45], which appears at different flight times depending on experimental conditions, is subtracted this way.

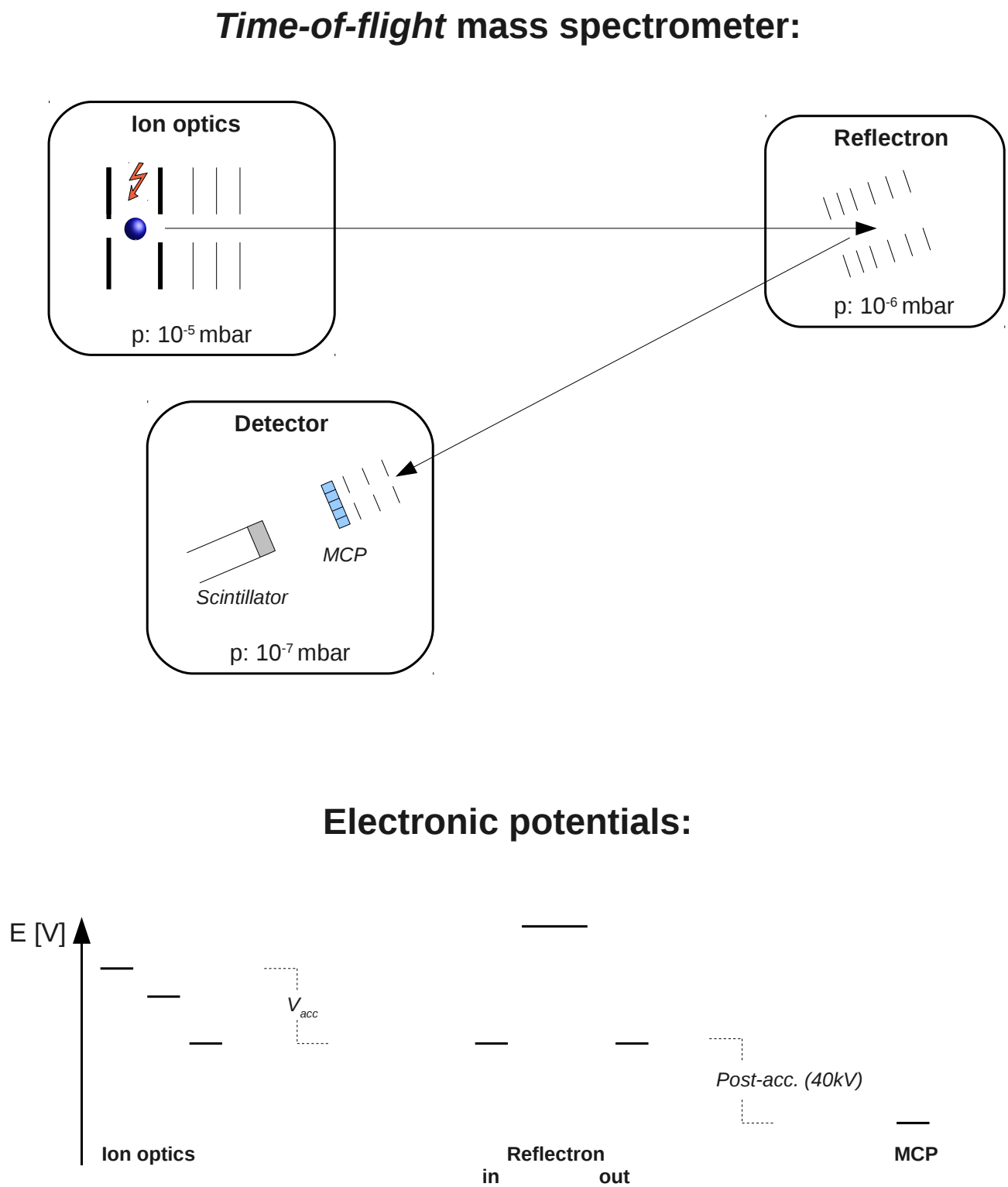

Figure 2.3: *Scheme of the time-of-flight mass spectrometer. Only essential parts are shown together with the respective pressure ranges. The lower panel illustrates a qualitative potential diagram.*

3 Results

In this chapter the most important results obtained during the course of my PhD work are presented. The chapter is divided into different classes of biomolecular complexes to highlight the achievements of LILBID in the particular fields and to group the corresponding mass spectrometric aspects of this method. As the results are either published or submitted for publication references for further reading are made where appropriate. A list of publications used for this thesis can be found on page 85 together with their abbreviations for identification.

3.1 Solvable proteins

This chapter is devoted to the analysis of solvable proteins with LILBID-MS and emphasises the implications of using different buffers and ionic strengths. Compared to nucleic acids (chapter 3.2) and membrane proteins (chapter 3.3) solvable proteins in general don't present substantial challenges for mass spectrometry. In fact the first mass spectra of proteins were recorded using solvable proteins. However the stability and structure of proteins is strongly influenced by the solution environment. As the native structure is required to establish specific non-covalent interactions such as forming homo- or heteromeric complexes or protein-ligand complexes, the ability to observe such structures may vary depending on the environment.

3.1.1 Characterising an archaeal Lsm protein

Sm proteins (antigens involved in Lupus erythematosu diseases and named after that patient where they were first discovered) and Sm-like (Lsm) proteins are a large family of proteins involved in RNA metabolism with representatives found in all three domains of life (bacteria, archaea and eukarya). With at least 18 different proteins the familiy of Sm/Lsm proteins in eukaryotes shows the the highest diversity. They all form heteroheptameric complexes and are involved in many RNA metabolisms like mRNA splicing,

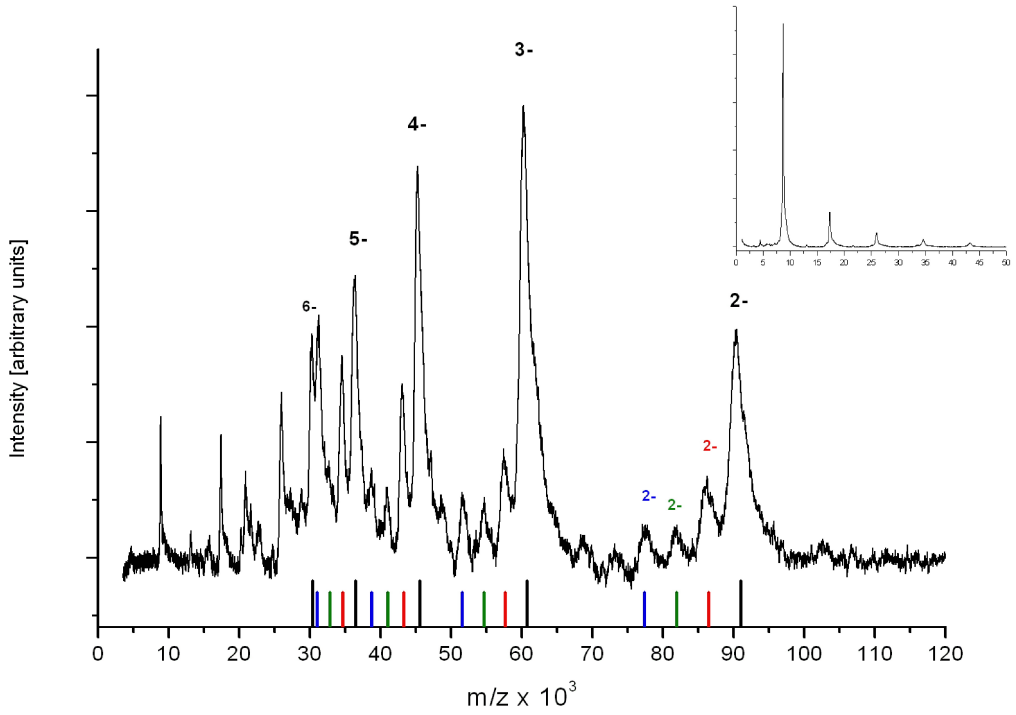

Figure 3.1: *Anion spectrum of HvoLsm in ammonium acetate buffer recorded under soft conditions. Labeled are the charge states of the 20-mer. In addition, charge distributions are marked with black bars (20-mer), red bars (19-mer), green bars (18-mer) and blue bars (17-mer). The inset depicts the spectrum recorded under high laser intensity.*

histone maturation, telomere maintenance and mRNA degradation[46]. The bacterial member of the Sm/Lsm family is the Hfq protein ((Sm-like protein found in *E. coli*) [47, 48] which forms homohexamers and also is involved in a plethora of functions [49] including the interaction with sRNAs and probably acting as an RNA chaperone. Little is known about the archaeal homologues of these proteins. It was shown that they form homoheptameric complexes [50, 51, 52, 53] and interact with RNA. Described in the following is the characterisation of the Lsm protein from the halophilic archeon *Haloferax volcanii* (HvoLsm) in collaboration with Prof. Soppa and Prof. Marchfelder which is published as ***paper 1***.

For this analysis the *lsm* gene was expressed in *E.coli* to produce a recombinant protein. LILBID-MS was applied to address the question of the quaternary structure. Therefore purified HvoLsm was dialysed in a 10mM NH_4OAc buffer adjusted to pH 7.5. The spectrum recorded under soft conditions (shown in Fig. 3.1) shows several charge distributions of several large complexes. The most abundant signal arises from a 20-mer

while signals from the 19-, 18- and 17-mers are also clearly visible. Under high laser intensity these complexes decompose mostly into monomers with a mass of about 8.5 kDa accompanied by other small fragments like dimers and trimers (inset of Fig. 3.1). Transferring an aliquot of this protein solution in a Tris buffer containing 50 mM of NaCl resulted in the spectra presented in Fig. 3.2. Now under soft conditions only a charge distribution of one complex corresponding to a mass of about 60 kDa is observed which clearly can be assigned to the homoheptamer. Under high laser energy the complex again decomposes into small fragments with the monomer showing the most intense signal. Moreover the high amount of salt in this buffer lead to a significant broadening of the individual peaks. Furthermore the Tris buffer in combination with the sodium chloride clearly stabilises the complex compared to the spectrum recorded under the same harsh conditions but using the NH_4OAc buffer (Fig 3.1) where the relative abundance of the monomer signal is significantly increased. These results demonstrate the advantage of using native solutions in LILBID-MS: choosing an inappropriate buffer often leads to unspecific oligomerisation resulting in a denaturated protein due to aggregation. In case of HvoLsm a simple buffer exchange reverted the oligomeric state to the native heptamer. As the native quaternary structure of this Lsm protein is preserved in LILBID-MS all requirements for characterising the RNA binding properties are met which is described in more detail in chapter 3.2.1.

3.1.2 The transcription factor TAp63α

The family of the p53 tumor suppressor in mammals contains two additional members, p63 and p73. Besides the fact that both p53 homologues serve important developmental functions [54, 55, 56], the possible role as tumor suppressors is also investigated [57, 58]. For both proteins many different isoforms exist, which is a result of combining several different C-terminal splice variants [59, 60, 61] with two different promoters producing either isoforms including (TA-isoforms) or lacking (ΔN-isoforms) the N-terminal transactivation domain [62]. In case of p63, the physiological functions of some of the isoforms have been revealed. By maintaining a stem cell population in the basal layer, ΔNp63α plays an important role in the development of stratified epithelial tissues [63]. The full-length isoform TAp63α however acts as a quality control factor in the female germ line [64] by inducing cell death upon lethal DNA damage. In contrast to p53, where activity is controlled by means of concentration [65, 66], TAp63α is already expressed at high levels in non-stressed oocytes [64] suggesting that its activity is under tight control of an inhibitory mechanism. It was shown previously that the last 70 amino acids of

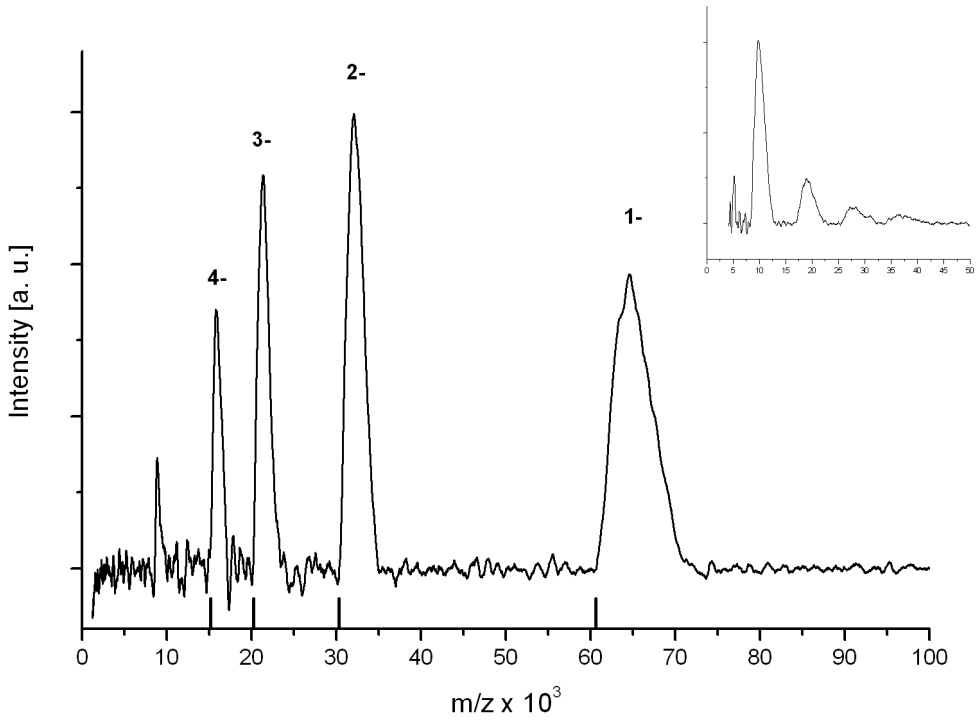

Figure 3.2: *Anion spectrum of HvoLsm in Tris/HCl buffer containing 50 mM NaCl recorded under soft conditions. Labeled are the charge states of the heptamer. Black bars indicate expected positions based on the theoretical mass. The inset depicts the spectrum recorded under high laser intensity.*

TAp63α act as a transactivation inhibitory domain (TID). By deleting this domain the transcriptional activity is increased several fold [67, 68, 62], however the exact inhibitory mechanism remained elusive.

To investigate, together with the group of Prof. Dötsch, the inhibitory mechanism of the TID, p63 was expressed in *E. coli*. All isoforms studied by LILBID-MS were expressed as an N-terminal maltose-binding-protein (MBP) fusion protein. In the LILBID anion spectrum of MBP-TAp63α (Fig. 3.3), using a 10mM NH_4OAc buffer, mostly dimers and tetramers were observed. In addition charge distributions of the hexamer and the octamer were detected. To exclude the possibility of aggregation, MBP-TAp63α was dialysed using a 10mM potassium phosphate buffer including either no salt or 50mM of NaCl. The corresponding mass spectra reveal either only dimers (50mM NaCl) or mainly dimers together with minor signals arising from the tetramer (no salt) (Fig. 3.4). These results suggest that MBP-TAp63α forms a dimer with a molecular weight of 232 kDa and that the lack of ionic strength in the buffer leads to unspecific aggregation. It

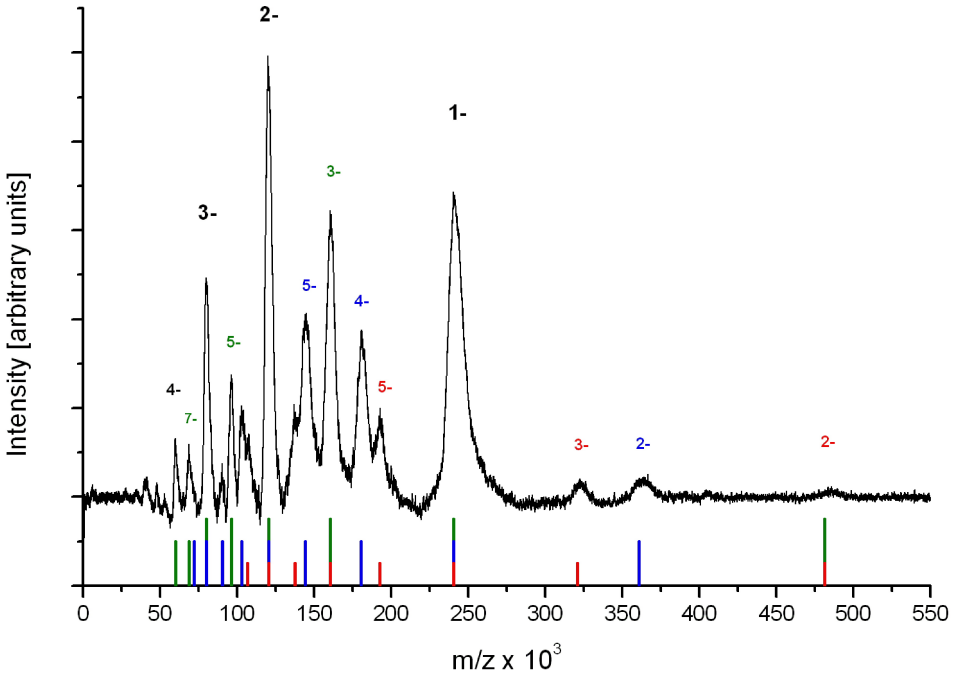

Figure 3.3: *LILBID anion spectrum of TAp63α after buffer exchange in ammonium acetate. Charge states of the oligomers are labeled. Colored bars additionally indicate charge distributions of the tetramer (green), hexamer (blue) and octamer(red).*

was not possible in LILBID-MS to further fragment the dimer into monomers indicating a high stability of this complex. As a consequence the higher oligomeric states occur only as multiples of the dimer. All members of the mammalian p53 family use a highly conserved oligomerisation domain (OD) to form tetramers that were shown to be the active state [69, 70, 71, 72]. The absence of tetramers in case of TAp63α implies that the dimeric conformation is the inactive state and further suggests that activation of this protein might involve the formation of tetramers. In size exclusion chromatography (SEC) analysis the active MBP-TAp63γ isoform (lacking the C-terminal TID) behaves as a significantly larger protein than MBP-TAp63α although it contains 193 amino acids less per monomer. It was previously shown in an alanine scanning experiment of the TID that the triple mutant MBP-TAp63αFTL shows a high activity [68] suggesting that the inhibitory function of the TID is destroyed by this mutation. MBP-TAp63αFTL also behaves in SEC analysis as a larger protein than MBP-TAp63α with a retention volume similar to that of MBP-TAp63γ. After calibration of the SEC column with compact globular proteins, the estimated mass of MBP-TAp63α (266 kDa) closely resembles the

theoretical value for a dimer (232 kDa). The predicted masses for MBP-TAp63γ and MBP-TAp63αFTL however exceeded the theoretical values of the assumed tetramers by far. This can be explained either by higher oligomeric states or by a conformation that deviates from a globular fold. As shape-independend methods multi angle light scattering (MALS) and LILBID-MS could prove the tetrameric state of both MBP-TAp63γ and MBP-TAp63αFTL in addition to the dimeric state of MBP-TAp63α. These findings nicely demonstrate that activation of p63 leads to tetramerisation and to an open, non-globular structure.

The formation of tetramers upon activation does not occur only *in vitro* but also *in vivo*. In non-stressed oocytes from mice embryos, TAp63α exclusively adopts a dimeric state. Substantial DNA damage, induced by γ-irradiation with 0.52 Gy, triggers the activation of TAp63α by phosphorylation, resulting in a significant increase of tetrameric species. It could be shown that this phosphorylation is not required to maintain an active, tetrameric state but rather serves as an initial trigger. Further details about the activation of TAp63α, inhibitory mechanisms, increased DNA binding affinity and the surprising stability of the active tetramer can be found in ***paper 2***.

3.1.3 Glycodendrimers

Another example of analysing solvable molecules by LILBID-MS, together with the group of Dr. Appelhans, is the investigation on poly(propyleneimine) and poly(propyleneamine) dendrimers. Dendrimers are large molecules with an enormous variety of precise, highly-branched (macro)molecular structures. By functionalysing the outer shell the vast amount of inner properties can be supplemented by additional functionalities resulting in a promising potential for material science, biological and medical applications. It was shown that dendritic structures could be used as drug carriers with the ability of a controlled release to specifically targeted organs and tissues [73, 74], as in virus-mimetic nanogel vehicles [75]. Furthermore, research on dendrimers and metal complexation significantly contributes to a broad range of fields including recycling/separation [76], magnetic resonance imaging [77], catalysis [78], sensing [79], and organic light emitting diodes [80]. Recent studies revealed that dendrimers as metal carrier systems could serve therapeutic and diagnostic uses in medical applications [73, 74].

The poly(propyleneimine) (PPI) dendrimers studied in the context of this work were third- to fifth-generation glycodendrimers with a dense maltotriose shell. The synthesis of these dendrimers is aimed at the development of dendritic carrier systems to be used as metal ion carriers in biological environments without the disadvantage of a

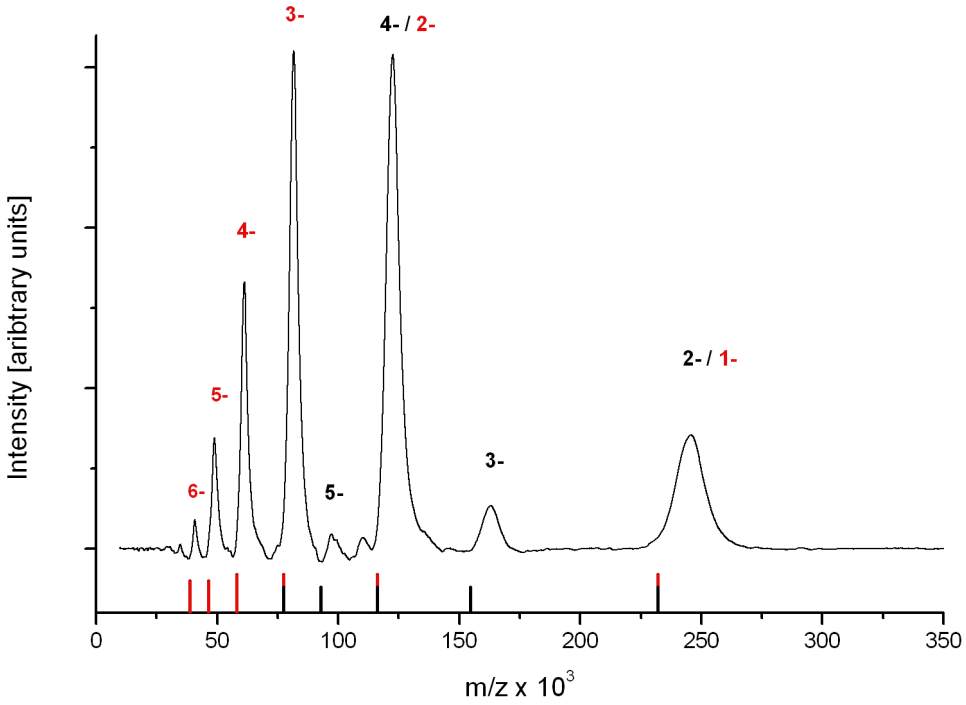

Figure 3.4: *LILBID anion spectrum of TAp63α after dialysis in KPO_4 buffer. Charge states of the dimer and tetramer are labeled. Charge distributions of the dimer and the tetramer, based on theoretical masses, are indicated by red and black bars respectively.*

coupled metal ligand. To introduce the saccharide shells onto the parent dendrimers, reductive amination was used. The yield of maltotriose coverage on the surface was determined by ^{1}H-NMR, LILBID-MS and MALDI-MS for third- to fith-generation glycodendrimers. A 100% yield corresponds to 32, 64 and 128 saccharide units for third-, fourth- and fifth-generation respectively. For the third- and fourth-generation all three methods mentioned above basically show the same results regarding the surface coverage (93% and 86% respectively), deviating only by one or two maltotriose units. In case of the fifth-generation, LILBID-MS and ^{1}H-NMR again agree on the yield (80%) however MALDI-MS shows a slightly higher surface coverage. In addition the yield decreases with increasing generation of the parent poly(propyleneimine) dendrimers. The corresponding LILBID anion spectra using aqueous solutions and concentrations of 5 μM, depicted in Fig. 3.5, reveals unusual broad peaks. The MALDI-MS spectra (see supplementary material of ***paper 3***) also show significantly broadened signals, albeit at lower signal-to-noise ratio especially for the smaller PPIs. The mass spectrometric

results suggest that these saccharide-decorated dendrimers exhibit a polydisperse distribution of the respective molecular weights, which can not be resolved for low charged ions. Furthermore in the LILBID spectrum of the smallest PPI (third-generation) it is clearly visible that the peak of the single charged ions is composed of a series of distinct signals. These signals differ in mass of about 500 Da which corresponds to individual maltotriose units, nicely demonstrating the polydisperse nature. As a consequence the above determined yields represent only the most prevalent molecular weights inside each distribution.

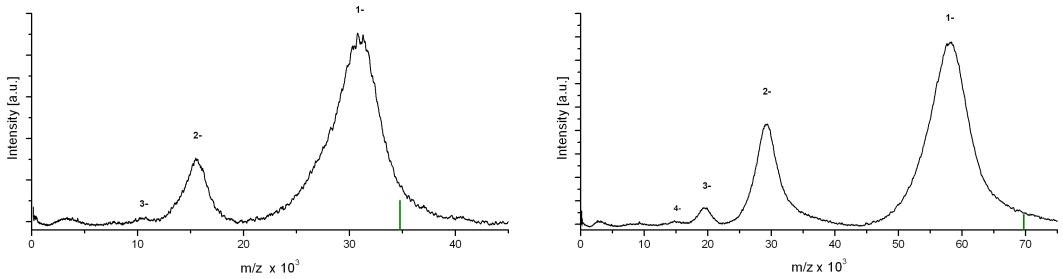

Figure 3.5: *LILBID anion spectra of maltotriose modified 4. generation (a) and 5. generation (b) dendrimers. The green bar represents a 100% surface coverage.*

The complexation capacity of these glycodendrimers for several metal ions was studied on the basis of the third-generation PPI with a dense maltose shell. UV/VIS spectroscopy revealed a very high binding capacity for UO_2(VI) ions with up to 34 ions per dendrimer and a very low one for Ag(I) and Eu(III) ions with 5 and 2 ions bound to one dendrimer respectively. The complexation capacity especially for Cu(II) ions was studied in more detail to investigate the dependence on dendrimer-generation and on the oligosaccharide shell. It could be shown that the capacity increases with increasing generation of the dendrimers and that the oligosaccharide modified dendrimers show similar capacities like the parent structures. Cu(II) complexation of the maltotriose modified dendrimers decreased only marginally compared to the maltose modified ones suggesting that the complexation mainly takes places inside the dendritic scaffold. Further details about coordination and symmetry of the complexes can be found in ***paper 3***. These oligosaccharide modified dendrimers are promising macromolecular systems and may be used for example in metal-based imaging techniques to aid medical diagnostics.

The other dendritic systems studied in the context of this work are fourth- and fifth-generation maltose modified poly(propyleneamine) (POPAM) dendrimers with empha-

sis on the encapsulation and release of the octahedral rhenium complex $[Re_6S_8(OH)_6]^{4-}$. Polyoxometalates including octahedral rhenium cluster complexes with terminal hydroxo and carboxylate ligands were recently recognised as a new class of potent enzyme inhibitors [81, 82, 83, 84]. Many of these cluster compounds, however, show poor hydrolytic stability together with an insufficient *in vivo* selectivity [81]. Such disadvantages may be overcome by encapsulation of these nanosized clusters in surface-modified dendritic systems. It is known that the anionic cluster $[Re_6S_8(OH)_6]^{4-}$ is slowly converted into an insoluble neutral species $[Re_6S_8(H_2O)_4(OH)_2]$ in aqueous solutions [85]. The long-time stability of the anionic complex in aqueous solution was followed over two weeks by UV/VIS spectroscopy. As expected the concentration steadily decreased during the whole time. However, when adding low amounts of maltose modified dendrimers the concentration did not change at all for at least one week. To analyse the uptake of anionic clusters ultrafiltration was performed to determine the final cluster concentration in the filtrate by ICP-MS. It turned out that almost all guest molecules are strongly bound by the dendrimers within 10 hours using a ten-fold excess of clusters.

LILBID-MS was performed to determine the loading capacity and long-time stability of either dendrimer generation. Therefore the dendrimers were incubated for 24 hours in aqueous solution with a ten-fold excess of rhenium clusters and ultrafiltrated afterwards. The respective retentates were analysed both after one week and after five weeks of the preparation. The LILBID anion spectra (Fig. 3.6) show a cluster uptake of four to five for the fourth-generation POPAM and an uptake of five to six for the fifth-generation POPAM one week after preparation. Interestingly the LILBID spectra of the same preparations after five weeks instead of one show similar uptakes of rhenium clusters. Again due to the polydisperse nature of these complexes, the uptake values represent the most prevalent yields as was observed for the oligosaccharide coverage in case of the PPI dendrimers (Fig. 3.5). However, the peak widths in the former case are a combination of two overlapping distributions: one arises from the surface coverage of maltose units and the second from the varying uptake of rhenium clusters. The LILBID spectra of the parent dendrimers reveal an almost 100% maltose coverage (Fig. 1-SI, supplementary material of ***paper 4***), a yield which is significant higher compared to the respective maltose modified PPI dendrimers. Furthermore, comparing the mass spectra of the POPAM dendrimers with and without rhenium clusters clearly demonstrate that the additional negative charges of the anionic clusters lead to a strongly increased signal intensity. Increasing the cluster concentration to a 20-fold excess during incubation leads to increased most prevalent uptakes of 12 and 14 clusters respectively. Here

dynamic light scattering (DLS) gave strong evidence of rhenium-cluster/POPAM aggregates with dimensions about 20 nm compared to about 6nm for both isolated rhenium-cluster/POPAM complexes at a ten-fold excess of clusters and the parent dendrimers. In contrast, in-situ preparation of rhenium-cluster/POPAM complexes in borate buffer using a ten-fold excess of clusters resulted in a lower uptake of one to three rhenium clusters for the fourth-generation POPAM. This can be explained by the large excess of borate ions competing the encapsulation of rhenium clusters.

It could be shown that the encapsulation of rhenium clusters within fourth- and fifth-generation POPAM dendrimers is maintained for at least one week in aqueous solution, clearly enhancing the hydrolytic stability of the clusters. After adding sodium chloride at an isotonic concentration, however, an asymptotic release of the encapsulated clusters could be seen and again explained by the large excess of competing anions. While the main part of the clusters are released within one day, the residual is delivered rather slowly. After four days 93% of the clusters were released from the fourth-generation and 86% from the fifth-generation dendrimers. In summary maltose modified POPAM dendrimers are promising systems to encapsulate and slowly release nanosized guest molecules and hence may be utilised for developing novel drug delivery systems. This includes the possibility of *in vivo* targeting after additional surface modifications.

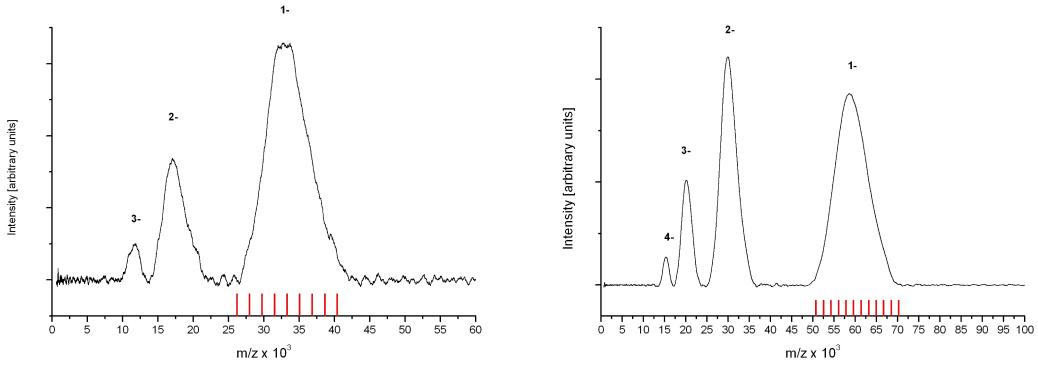

(a) (b)

Figure 3.6: *LILBID anion spectra of dendrimers after incubation with rhenium clusters. Red bars indicate mass shifts due to the uptake of one to nine clusters (4. generation PPI, (a)) respectively of one to twelve clusters (5. generation PPI, (b)).*

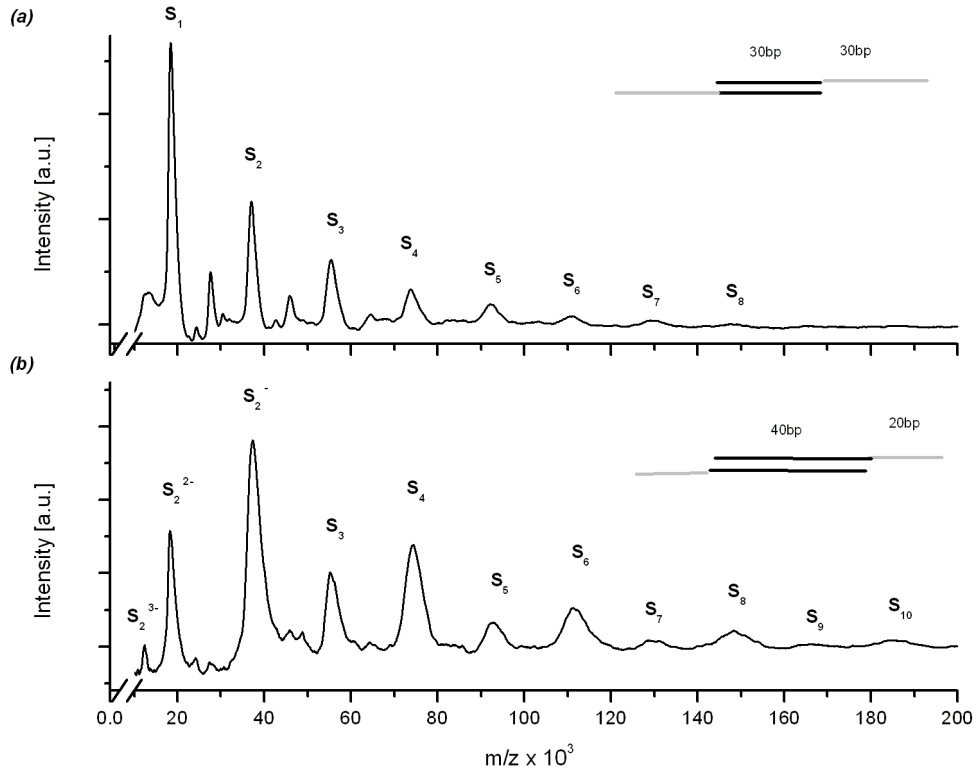

Figure 3.7: *LILBID anion spectra of two sets of DNA ladders. (a): symmetric pair and (b): asymmetric pair. The Sn represent the number of single strands for each oligomer.*

3.2 Nucleic acids

This chapter deals with the results of LILBID-MS achieved in the field of nucleic acids and the analysis of non-covalent interactions between them as well as binding studies with proteins such as a transcription factor. Due to their polarity and thermal lability nucleic acids have long presented a considerable challenge for mass spectrometry [86]. Modern mass spectrometry still encounters problems in the analysis of nucleic acids as in ESI-MS the ionization yield is very sensitive to salt contaminations and in MALDI-MS the sensitivity decreases with increasing size of the oligomers. Furthermore the detection of specific intermolecular complexes is often problematic with both methods [87].

As LILBID-MS works with native solutions and is highly salt tolerant, all requirements for the detection of large and specific intermolecular complexes are met. A model system to demonstrate the detection capabilities of LILBID-MS for unfragmented and large oligomers is the formation of DNA double strands. Fig. 3.7 shows the LILBID anion spectra of mixtures of different single strands. Here the sequence of the two com-

plementary single strands (60-mers) is chosen in a way that the resulting double strands have sticky ends of different length. One of the mixtures formes a duplex with symmetric sticky ends (30 bp / 30 bp) while the other forms an asymmetric duplex (40 bp / 20 bp). During self-assembly DNA ladders of different length and thermodynamic stability are formed which is illustrated in Fig. 3.7. In case of symmetric sticky ends the LILBID spectrum (Fig. 3.7(a)) shows a distribution of peaks corresponding to ladders of varying length while the intensity decreases exponentially with increasing size. The ladders formed by asymmetric sticky ends (Fig. 3.7(b)) show up as a distribution with an alternating intensity pattern with the even-numbered polymers being more intense than the odd-numbered ones. For the symmetric pairing an equal probability in the occurrence of even and odd numbered fragments can be expected. However for the asymmetric pairing the probability of even numbered oligomers is higher due to the higher binding enthalpy of 40 bp as compared to 20 bp found in the odd-numbered fragments. For comparison, the melting temperatures for the 20 bp, 30 bp and 40 bp regions predicted by the Zuker-algorithm [88] are 60°C, 73°C and 79°C respectively. The LILBID spectra correctly project these thermodynamic properties. The largest DNA ladder observed with this experiment has a mass of about 185 kDa corresponding to a duplex with 300 bp.

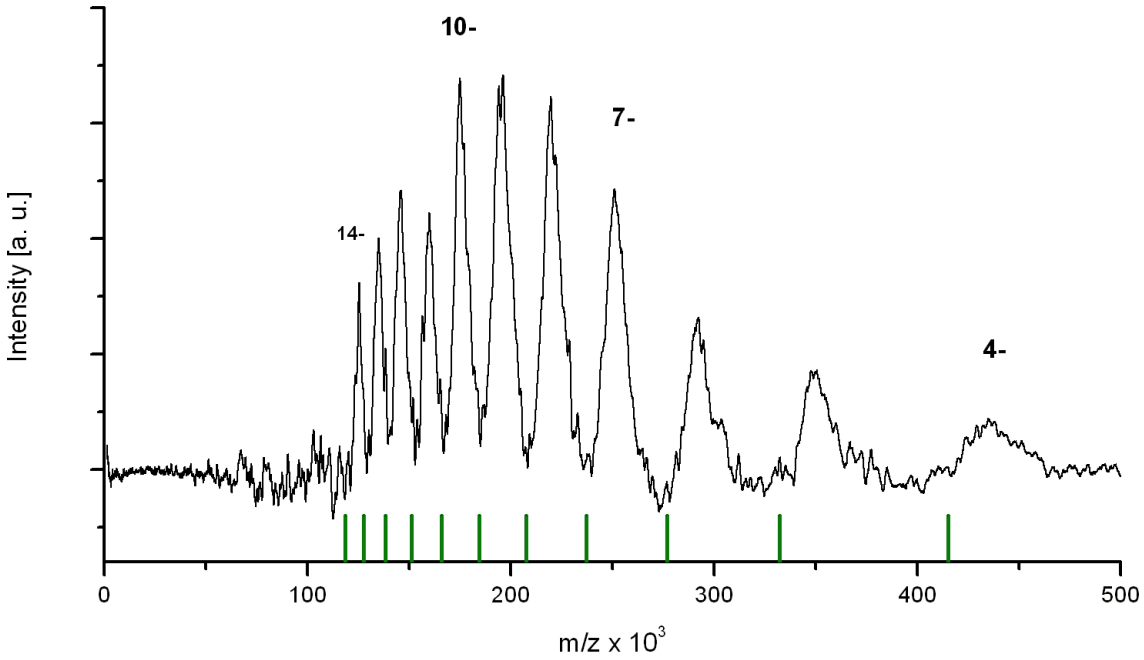

Figure 3.8: *LILBID anion spectrum of pUC19 at 80nM. The charge distribution of the theoretical mass is shown by the green bars.*

Although a 300 bp DNA can be considered a large oligomer for mass spectrometry LILBID-MS is readily able to detect even larger DNA. The anion spectrum of the 2686 bp plasmid pUC19 with a calculated molecular weight of 1.66 MDa (with protons as counter ions) is depicted in Fig. 3.8. The charge distribution ranges from four up to 14 negative charges all corresponding to the same mass. Due to the relative high amount of different charge states the mass can be quite accurately determined to 1.66 ± 0.01 MDa resulting in an error range of about 1%. The decreased signal-to-noise ratio in this spectrum is caused by a plasmid concentration of only 80 nM. Only few examples exist in literature describing the analysis of nucleic acids with a mass in the MDa range by mass spectrometry [89, 90, 91]. In addition these results were possible only after elaborate sample preparation techniques. Another benchmark regarding the sensitivity is shown in Fig. 3.9. Here one of the single strands of the DNA ladder experiment (Fig. 3.7) is diluted to a concentration of 9 nM in aqueous buffer. Fig. 3.9(a) depicts the anion spectrum averaged over 200 droplets while Fig. 3.9(b) shows a spectrum using only three droplets corresponding to an amount of substance of 117 amol and 1.8 amol respectively. As can be seen three droplets with a volume of 65 pL of a solution containing just 9 nM of an 60-mer oligomer still produces a reasonable signal-to-noise ratio.

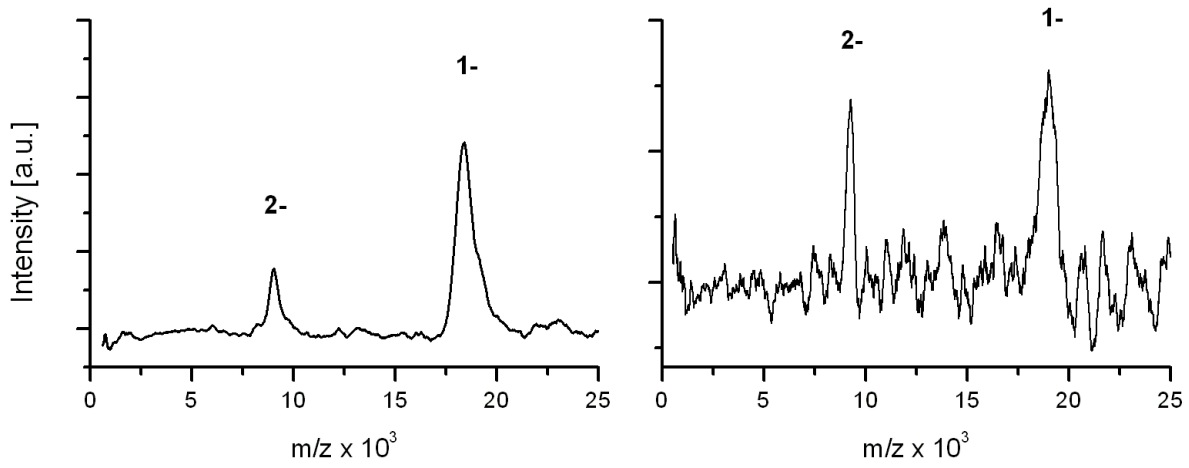

Figure 3.9: *LILBID anion spectra of a single stranded DNA (60-mer) at a concentration of 9 nM. (a): recorded using 200 droplets. (b) recorded using three droplets.*

It is commonly known that an increase of ionic strength leads to an increased stability of DNA double-helices. A measure for this is the melting temperature (T_m) which is the ambient temperature where half of the double strands break apart into their single strands. Especially Mg^{2+} ions have a strong influence on the stability as was observed in early investigations [92, 93]. Mg^{2+} ions interact with the negatively charged phosphate

groups of the backbone and thus neutralize the negative charges. The series of mass spectra of a 16 bp double strand (poly-A and poly-T respectively) shown in Fig. 3.10 illustrate the effect of cations. All spectra are recorded using the same experimental conditions except for buffer additives. In a solution consisting of only the buffering agent the double helix is totally dissociated (Fig. 3.10(a). As can be seen using a buffer containing 10mM of NaCl the melting temperature slightly increases. However as it's still below room temperature the DNA mainly exists in the melted state (Fig. 3.10(b). The addition of NaCl at a concentration of 10mM already leads to a significant broadening of the peaks and also is responsible for the slight shift towards higher masses of the observed m/z values of the ions. The use of 1 Mm $MgCl_2$ instead of the NaCl as salt additive leads to a strongly increased thermal stability of the double stranded DNA with a calculated melting temperature of 45.6°C (Fig. 3.10(c)). Here the mass spectrum shows an almost even distribution of melted and unmelted DNA. The clear fragmentation of the oligomer in spite of its high melting temperature (relative to room temperature) is accounted for by the additional energy from the desorption laser. In fact this fragmentation studies might be used to determine the binding energy in different fragmentation pathways due to different laser energies. In all three spectra the relative stabilities of the double strands are in good agreement with the calculated melting temperatures. Furthermore the specific effect of Mg^{2+} ions is clearly visible as the ionic strength alone cannot explain the observed stability compared to the spectra obtained with no salt or with 10mM of NaCl respectively.

3.2.1 DNA-protein and RNA-protein complexes

Despite the fact that nucleic acids themselves present a considerable challenge for mass spectrometry, the detection of sequence specific complexes of proteins with DNA or RNA is "still in its infancy" according to Carol Robinson [94]. The sequence specific binding of the NF-κB transcription factor p50 as dimer to a dsDNA containing the binding site is well characterized [95] and thus serves as a model system. In a competitive experiment two oligomers are mixed together with the protein p50. One of the oligomers is a control DNA of 48 bp (29.9 kDa) with a random sequence, while a match DNA of 15 bp (9.9 kDa) contains the binding site. The mass spectrum of p50 alone (Fig. 3.11(a)) reveals two overlapping charge distributions corresponding to the dimer of the protein and the monomer respectively. Upon adding the two oligomers p50 binds as a dimer only to the match DNA but does not bind the control DNA (Fig. 3.11(B)). The stoichiometry of this specific complex in the LILBID mass spectrum reflects the crystal structure

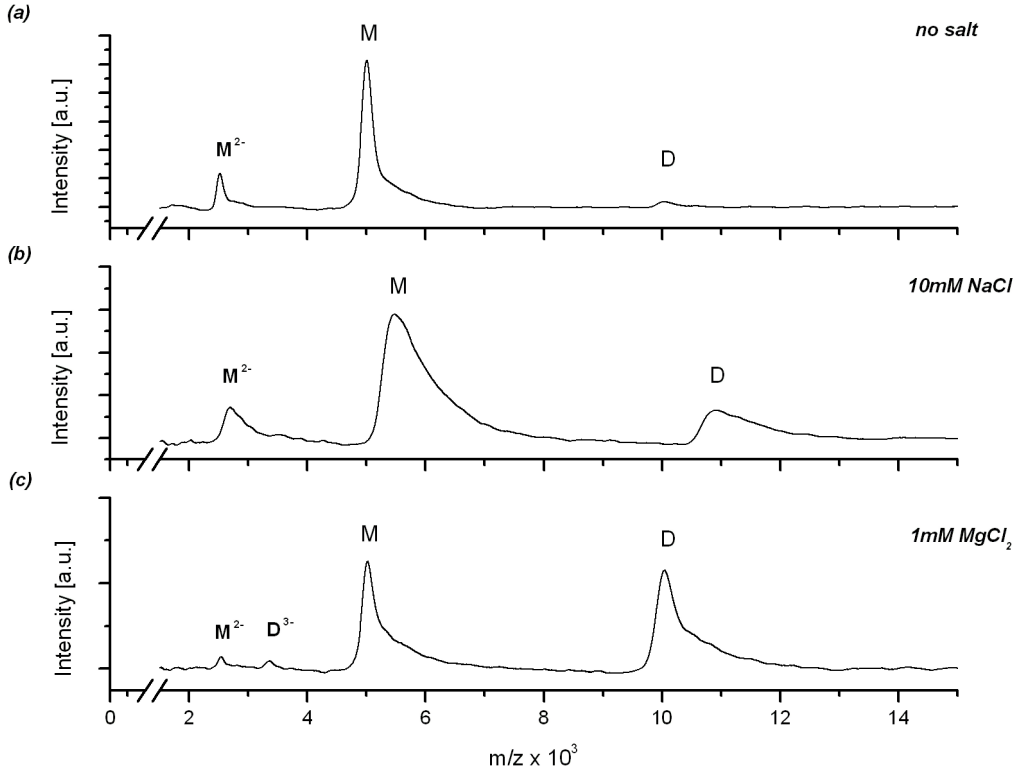

Figure 3.10: *LILBID anion spectra of a 16bp dsDNA recorded in different buffer compositions. (a): in 5 mM NH_4OAc. (b): plus 10 mM NaCl and (c): plus 1 mM $MgCl_2$*

[96] suggesting that this structure also exists in solution. The results presented in this chapter so far are discussed in detail in ***paper 5***.

One of the additional applications of LILBID-MS is the analysis of non-covalent RNA-protein complexes. The investigation of such complexes (compared to the DNA analogues) is further complicated by the fact that recognition of binding sites often is not given by the mere sequence alone but also by the correct structure. Due to the use of native solutions in LILBID-MS, proper folding of the RNA may be maintained and hence all requirements necessary to study specific interactions between proteins and RNA are given. These capabilities are exemplarily illustrated in the mechanism of how a virus suppresses RNA interference (RNAi) and by the characterisation of an archaeal Lsm protein.

RNAi suppression Triggered by recognition of dsRNA RNAi is a gene silencing mechanism to protect the genome against mobile genetic elements and the infection by viruses. However viruses developed different strategies to bypass the host's RNAi response by

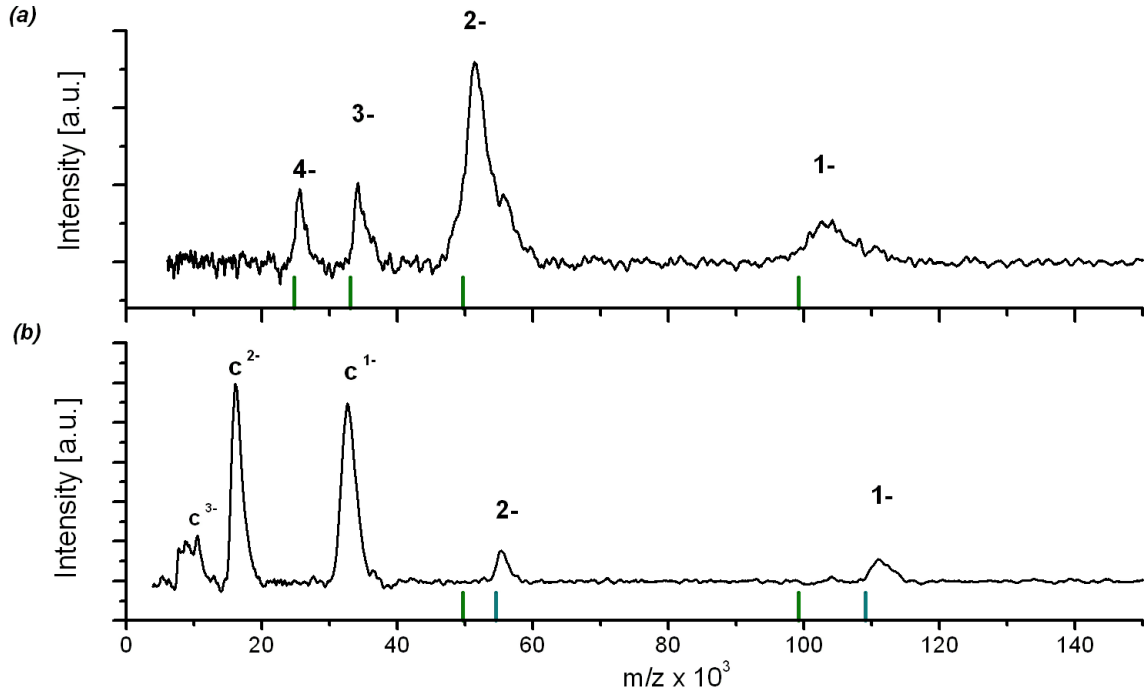

Figure 3.11: *LILBID anion spectra of NF-κB and its complex. (a): isolated p50. Indicated are the charge states and the charge distribution (green bars) based on the theoretical mass of the dimer. (b): after incubation with match and mismatch DNA. Additional charge distribution of the $p50_2$:DNA complex is shown in blue bars. Signals of the control DNA are labeled with* ***C****.*

viral suppressor proteins. Published in ***paper 6***, together with the group of Prof. J. Chen, are the oligonucleotide binding properties of the *Tomato aspermy virus* protein 2B (TAV_2B). There are several possible modes of suppression and it is not well understood how the TAV_2B protein suppresses RNAi. In plants a distribution of different siRNAs with different lengths is present. Shorter siRNAs (21-23 nucleotides) are involved in the RNAi response while longer species (25-27 nucleotides) are associated with transcriptional silencing. As suppression of RNAi may occur through a direct interaction with siRNA the binding property of TAV_2B to several siRNAs with lengths of 21, 25 and 27 nucleotides was investigated by total internal reflection fluorescence spectroscopy(TIRFS). The results showed that TAV_2B binds all three siRNAs but with a clear length preference for the 21-mer which is also found with another RNAi suppressor, P19 [97]. Furthermore the binding to single stranded RNAs with a length of 21 and 30 nucleotides as a possible mimic for mRNA was also investigated. Here TIRFS revealed that TAV_2B binds to single stranded RNAs too, but with a clear length preference for the longer species over the 21-mer. Finally TAV_2B is also able to bind miRNA.

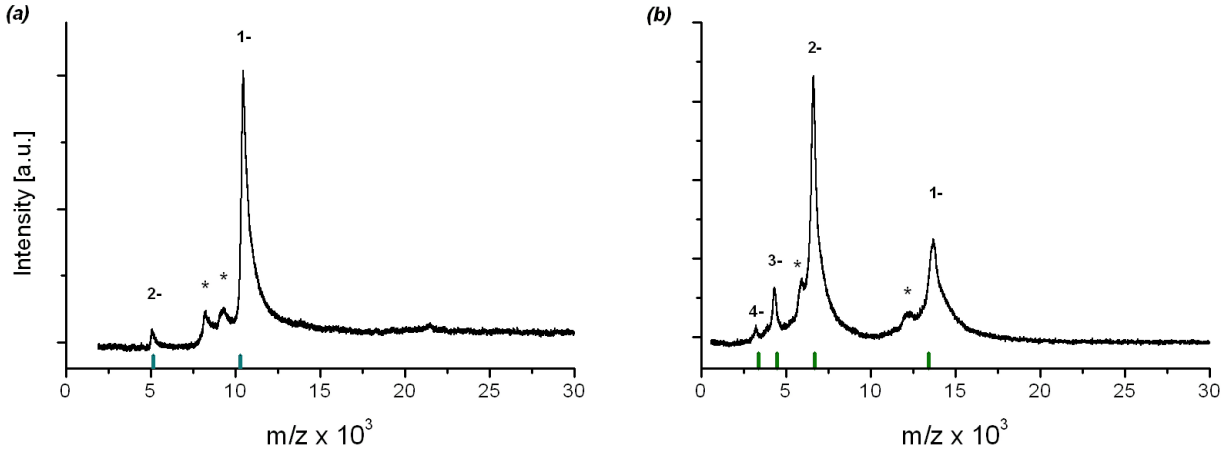

Figure 3.12: *LILBID anion spectra of the TAV_2B protein (a) and the siRNA (b). In both cases the charge states are labeled. Asterisks mark fragments introduced during preparation.*

All TIRFS experiments had in common that a certain critical protein concentration was needed to obtain any RNA binding to TAV_2B at all. Thus an oligomerisation of the protein might be required to bind the oligonucleotides. To further address the question of the oligomeric state, analytical gel filtration was applied to a mixture of unlabeled 21-mer siRNA (mass: 13.4 kDa) and TAV_2B protein (mass: 10.5 kDa). Here a new peak appears at a mass of about 67 kDa clearly suggesting the formation of a complex with higher degree of oligomerisation. When applying analytical gel filtration with UV/VIS detection to the same mixture but this time with fluorescently labeled siRNA, a molar ratio of 2:1 for the protein:siRNA complex could be deduced. Furthermore CD spectroscopy showed that in addition to the oligomerisation a conformational change also occurs. Upon binding of the siRNA the protein changes its conformation from a high percentage of random coil structure to a structure with 60% α-helix. The exact stoichiometry of this complex in solution still remains unknown, however the previously published crystal structure by Chen et al. revealed a 4:2 ratio of the protein:RNA complex [98]. Based on mutation studies and cross-linking experiments Chen et al. suggested that the tetramer of the protein is also a valid structure in solution in the absence of any RNA. Nevertheless affinity-purified TAV_2B migrates at physiological salt concentration as a monomeric species on an analytical gel filtration column.

LILBID-MS also showed only monomers in solution albeit at low salt concentration (Fig. 3.12(a)). Before applying LILBID-MS to a mixture of protein and RNA to find out the stoichiometry of the complex, as a prerequisite the 21-mer siRNA alone was measured and revealed a double stranded siRNA with a mass of about 13.4 kDa (Fig. 3.12(b)).

Incubating a mixture of 10 μM TAV_2B and 5 μm siRNA resulted in protein:RNA complexes with a mass of about 68.9 kDa (Fig. 3.13) corresponding to a 4:2 stoichiometry which is similar to that found in crystal structure.

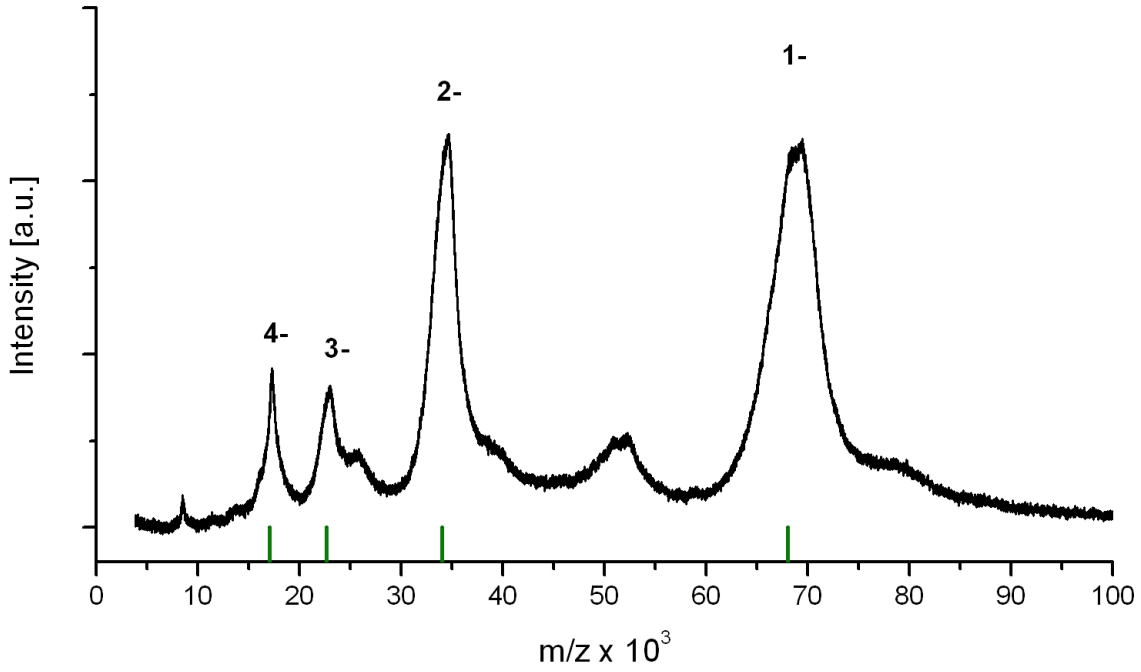

Figure 3.13: *LILBID anion spectrum of 4 μM TAV_2B and 2 μM of siRNA. Labeled are the charge states of the 4:2 complex. The green bars indicate the expected charge distribution of this complex based on the experimental masses of the protein and siRNA.*

In summary TAV_2B binds to several RNAs and hence may have multiple targets to suppress RNAi. Like the RNAi suppressor P21 [99] TAV_2B thus belongs to the class of more general suppressors as compared to P19 [97]. The latter is a specific suppressor with respect to the associated RNAi pathway. In addition the direct interaction with RNA implies both an oligomerisation and a conformational change.

Characterising the RNA binding properties of HvoLsm Here together with the groups of Prof. Marchfelder and Prof. Soppa the binding of the HvoLsm protein to RNA is described. The protein itself was already characterised by means of mass spectrometry in chapter 3.1.1. To study the interactions of HvoLsm with RNA an electrophoretic mobility shift assay (EMSA) was used. Therefore the protein was incubated together with two different poly-U RNAs with lengths of 15 nucleotides (U_{15}-RNA) and 30 nucleotides (U_{30}-RNA) respectively. The results showed that HvoLsm binds to both poly-U RNAs.

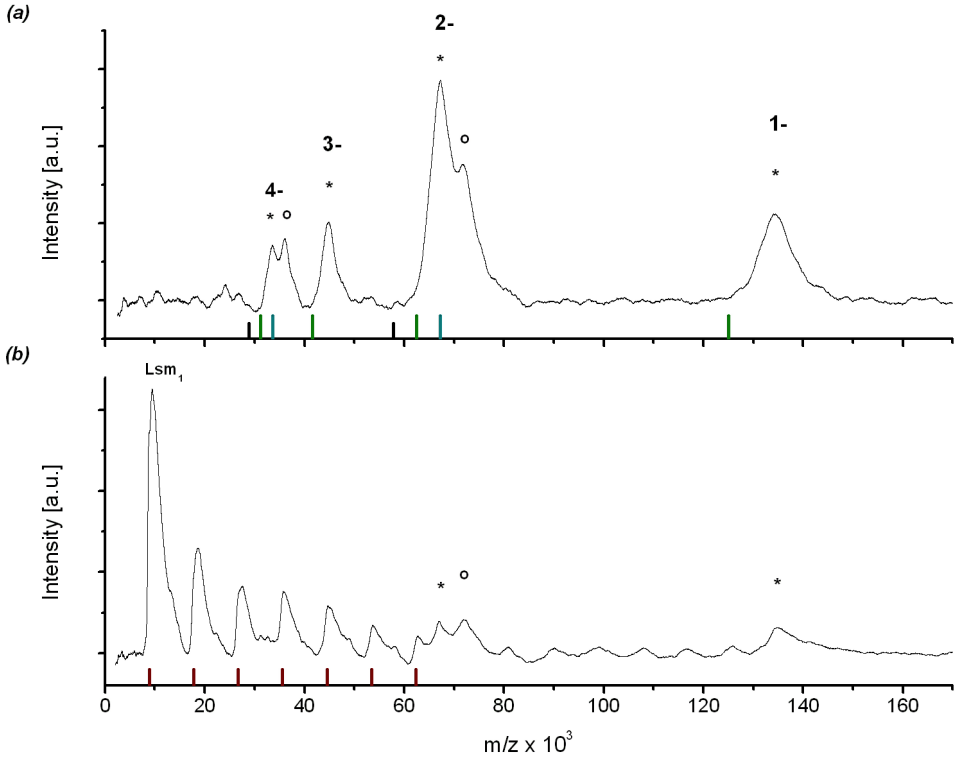

Figure 3.14: *LILBID anion spectra of HvoLsm after incubation with U_{30}-RNA recorded under soft (a) and harsh (b) conditions. Labeled are the charge distributions of the binary (blue) and ternary (green) complex. Labeled are the charge states of the binary (o) and ternary complex (*).*

By using an increasing protein concentration it was possible to determine a K_D of 72 nM for the HvoLsm:U_{30}-RNA interaction as seen by EMSA. Though the binding of poly-U RNA has been shown for several other archaeal Lsm proteins[51], eukaryotic ones[51, 100] and also for the bacterial Hfq[101] the relevance is unclear as poly-U stretches were not identified in *Haloferax* so far. The exact stoichiometric composition of the HvoLsm:RNA complexes was analysed by LILBID-MS. To avoid such broad peaks as seen in Fig. 3.2 the Tris buffer was modified to a reduced salt content of only 10mM NaCl but with an additional 1 Mm of $MgCl_2$ to stabilise the oligonucleotides (as was discussed in chapter 3.2; see Fig. 3.10). An aliquot of the RNA solution consisting of the afore mentioned buffer was heated to 80°C for a few minutes before protein was added. A mixture of 4 μM HvoLsm heptamer and 8 μM U_{30}-RNA was incubated for 30 minutes at room temperature. The mass spectrum recorded under soft conditions shows two overlapping charge distributions (Fig. 3.14(a)) corresponding to a heptamer:U_{30} complex with a mass of about 70 kDa (o) and a ternary complex assembled of two protein heptamers

and one U_{30}-RNA with a mass of about 130 kDa (*). Fig. 3.14(b) depicts the mass spectrum of the same mixture recorded under harsh conditions. Here fragments of the protein ranging from the monomer up to the intact heptamer are clearly visible. In addition signals from both HvoLsm:U_{30} complexes could be still detected demonstrating the high stability of these complexes compared to the isolated protein heptamer (Fig. 3.2). Most interestingly the ternary complex did not fragment stoichiometrically but instead single protein subunits are lost suggesting that the intra-heptamer interactions are weaker than the protein-RNA interactions. Alternatively, as the broadness of the peaks is not sufficient to distinguish between the initial loss of a HvoLsm monomer and the loss of the U_{30}-RNA, it could mean that first the RNA is lost and afterwards the protein subunits. Furthermore the formation of the observed ternary complex at excess of RNA indicates a specific interaction.

In addition the binding of HvoLsm to sRNA was exemplarily studied by LILBID-MS for the $sRNA_{30}$ (see publication for further details about this sRNA). Sample preparation protocols, incubation times and substrate concentrations were the same as for the HvoLsm:U_{30}-RNA complexation. The spectrum recorded under soft conditions (Fig. 3.15) revealed a charge distribution corresponding to a HvoLsm:$sRNA_{30}$ complex with a mass of about 102 kDa. Currently not assigned is an unexpected peak with a slightly lower mass of approximately 90 kDa. However as in the mass spectrum of $sRNA_{30}$ alone an unexpected peak also occurs it is accounted for an additional HvoLsm:RNA complex with an unknown RNA most likely a contamination. In contrast to the U_{30}-RNA no ternary complexes of HvoLsm with $sRNA_{30}$ have been detected.

In addition to poly-U RNA the Lsm protein from *Haloferax* interacts with sRNA, snoRNA and tRNA suggesting an involvement in many different pathways of RNA metabolism. Co-immunoprecipitation revealed about 30 different protein interaction partners which were identified by means of MS/MS analysis. Furthermore around 20 sRNAs could be identified that co-purified with HvoLsm. All these findings support the participation in many different pathways and hence further investigations on the particular interactions are necessary to characterise this archaeal Lsm protein.

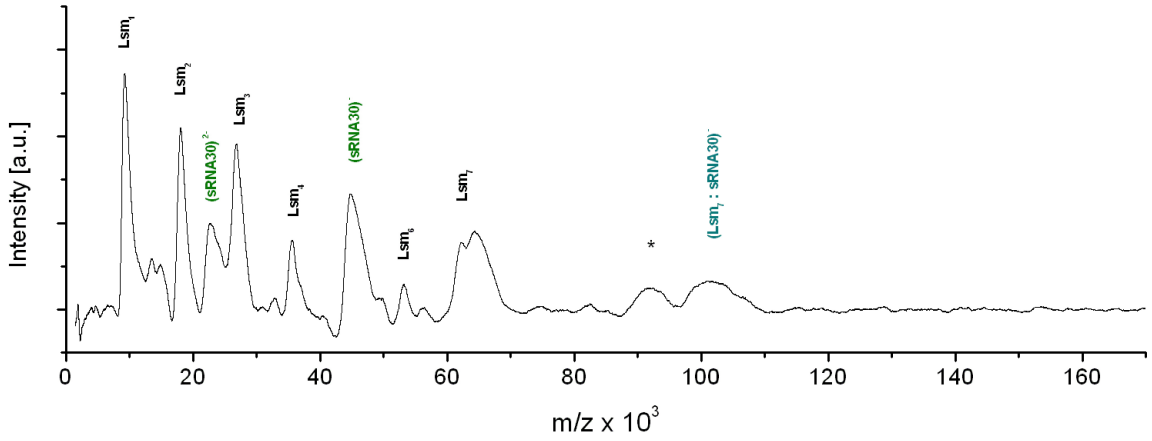

Figure 3.15: *LILBID anion spectrum of HvoLsm after incubation with $sRNA_{30}$-RNA recorded under soft conditions*

3.3 Membrane proteins

This chapter is focussed on new results of LILBID-MS recently achieved in the field of membrane proteins and the mass analysis of their subunit composition as well as in the determination of their quaternary structures. Due to their hydrophobicity membrane proteins present a considerable challenge for mass spectrometric analysis. The requirement of detergents to solubilise these proteins vastly limits the operation of ionisation techniques commonly used in modern mass spectrometry. In ESI the use of detergents often has an negative impact on the spraying process and thus sample preparation protocols need to be carefully adjusted to accommodate this constraint as was described only recently [102]. This means that the detergent concentration of the solution has to be kept just above the respective critical micelle concentration (CMC). During measurement attached detergent molecules are stripped off the protein ion by means of multiple collisions with inert gas. Due to the fragile nature of membrane protein complexes these steps can be difficult to attain. In MALDI-MS on the other hand new matrix cocktails containing detergents were recently introduced [103]. A detergent/matrix combination with functional cleavable detergents has also been successfully applied to MALDI-MS with hydrophobic proteins [104]. Upon cleavage, two inert compounds and the matrix are formed, essentially eliminating disturbing sources of surface active substances. In MALDI-MSI, an on-tissue tryptic digest incorporating the use of detergent was also described increasing the yield of tryptic peptides [105]. Furthermore, replacing the matrix with a polyvinylidene difluoride (PVDF) membrane which particularly adsorbs membrane proteins was recently investigated [106]. Using on-PVDF washing to remove salts

and detergents resulted in high quality MALDI spectra of membrane proteins.

The fact that LILBID-MS correctly transfers the effect of different buffers and buffer compositions on the complexation and oligomerisation of molecules in solution into gas phase still holds true for membrane proteins as is demonstrated further down in chapter 3.3.4. In addition it will be shown that both the type and the amount of detergent also may effect the structure and stability of membrane proteins.

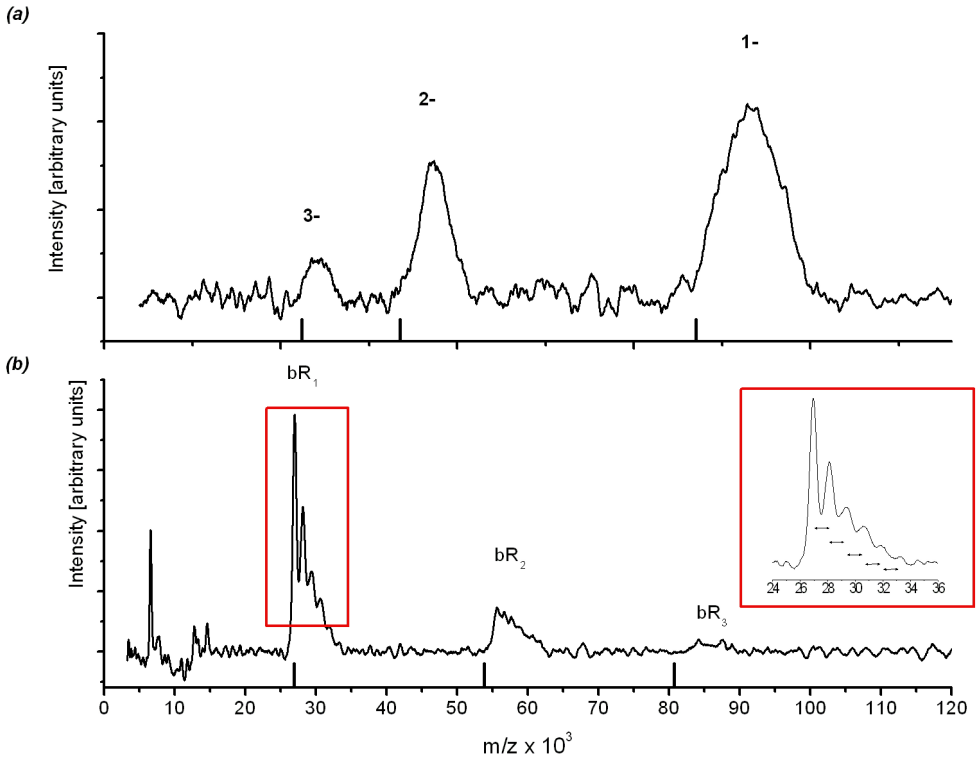

Figure 3.16: *LILBID anion spectra of bacteriorhodopsin. (a):recorded under soft conditions. Labeled are the charge states of the trimer. (b): recorded under harsh conditions. The oligomeric distribution is indicated by black bars. The inset shows a magnification of the monomer signal.*

3.3.1 Validating the potential of LILBID-MS to study quaternary structures of biomolecules by means of membrane proteins of known structure

A well characterised and well understood membrane protein, the haloarchaeal light-driven proton pump bacteriorhodopsin (bR), serves as a model system to test the abilities of LILBID-MS. As it is known from 2D and 3D crystals bR adopts a trimeric state [107,

108] and is the main constituent of a two-dimensional hexagonal crystal lattice, called the purple membrane. The LILBID mass spectrum recorded under soft conditions is depicted in 3.16(a). It shows only a single charge distribution of a trimer with unusually broad peaks. When recorded under harsh conditions the bR trimer dissociates almost completely into the monomer (3.16(b)) with a mass of 26.9 kDa which is very close to the calculated mass of 27,050 Da [109]. Given that result the mass of the trimer calculates to about 81 kDa, however the intensity maximum of the signals shown in Fig. 3.16(a) correspond to a mass of about 90 kDa for the trimer. This shift can be partially attributed to solvent attachments especially detergent molecules which are bound to the protein by hydrophobic interaction. The magnification of the monomer peak (inset in 3.16(b)) reveals the reason for the low resolution of the trimer signal: a series of small adducts with an incremental mass of 1.2 kDa appear with steadily decreasing intensity towards higher mass. These adducts may be assigned to lipid attachments. The most likely candidate is the sulfated triglycoside lipid S-TGA-1 which was also identified in lipid extracts from the purple membrane by ESI-MS [107] showing a mass of 1217.9 Da. This lipid and several other ones reside inside the central compartment of the bR trimer as seen by X-ray structure [107] and neutron diffraction [107]. Especially S-TGA-1 is crucial for the structure of bR by means of lipid-mediated stabilisation [107]. Thus LILBID-MS correctly depicts the native quaternary structure of bR including the crucial role of lipids. Furthermore it also shows that this structure is conserved in solution phase upon solubilisation with detergent. This is of particular relevance because even though the monomer is the active unit [110] the trimeric state is crucial for *in vivo* physiology [107].

Another example of comparing results obtained by LILBID-MS with known condensed phase structures is the potassium channel KcsA for which the 3D crystal structure is solved [111]. In the mass spectrum of KcsA recorded under soft conditions (Fig. 3.17(a)) a charge distribution of the tetramer with a mass of about 54 kDa is observed together with a monomer peak of low intensity. The spectrum recorded under high laser intensity (3.17(b)) reveals mostly monomers, with higher oligomeric states appearing only at low signal intensity. The magnification of the monomer peak (inset in Fig.3.17(b)) shows a splitting with a mass difference of about 400 Da. This shift was already observed by ESI-MS [112] and interpreted as a possible post-translational modification. In addition two distinct stoichiometric distributions are observed which differ in mass by about 4 kDa. This is accounted for by an incomplete cleavage since the preparation of the protein involved a chymotryptic cleavage of the C-terminal sequence of 33 amino acids and the

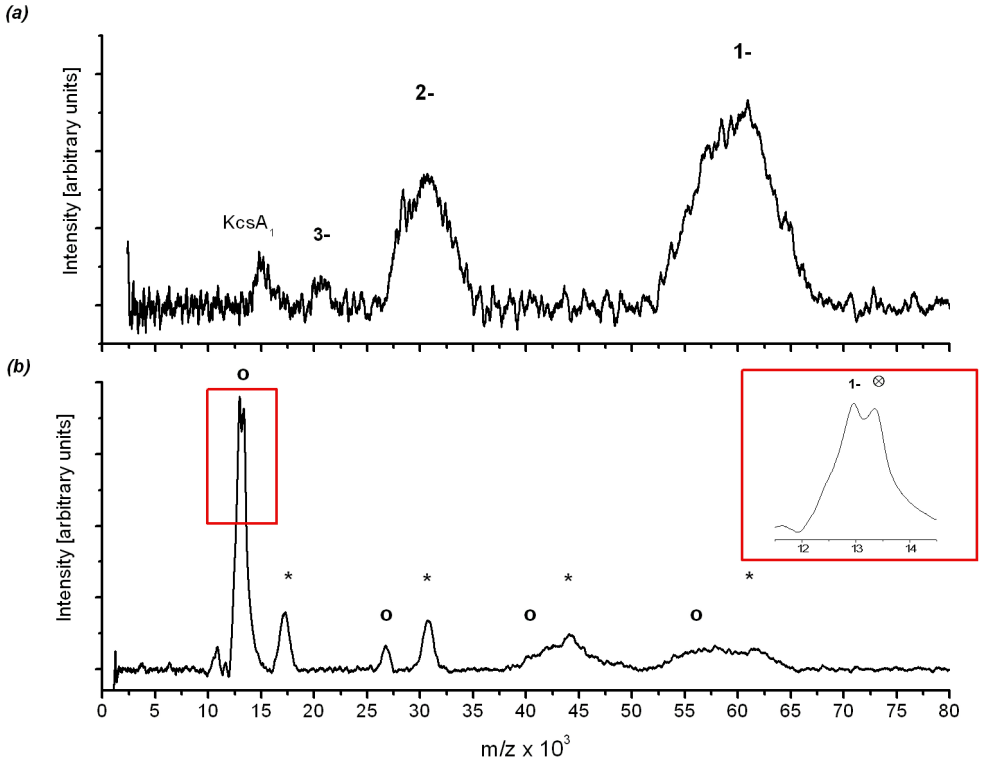

Figure 3.17: *LILBID anion spectra of KcsA recorded under soft (a) and harsh (b) conditions. The inset in (b) shows a magnification of the monomer signal.*

His-tag [113]. The spectrum recorded under soft conditions resulted in unusually broad peaks similar to those for bacteriorhodopsin (Fig. 3.16(a)). However the reason here are not lipid attachments in addition to solvent adducts but rather the two distributions which could not be resolved except for harsh conditions. The LILBID spectra revealed a quaternary structure of KcsA in solution which reflects the findings from crystal structure and hence suggest that this structure may be valid also *in vivo*.

3.3.2 Proteorhodopsin and the effect of different detergents

The investigation of proteorhodopsin (PR), a light-driven proton pump found in marine bacterioplanktons, is of particular interest as bR and PR share a high sequence- and structure-homology [114] and the 3D crystal structure is not yet available. However it was already shown that in 2D crystals PR forms mostly donut-shaped hexamers, whereas in the densely-packed non-crystalline lattice it is a mixture of hexamers and pentamers [108]. To address the question of the quaternary structure LILBID-MS was applied on a protein solution purified using 0.2% Triton-X 100 as detergent. Fig. 3.18(a)

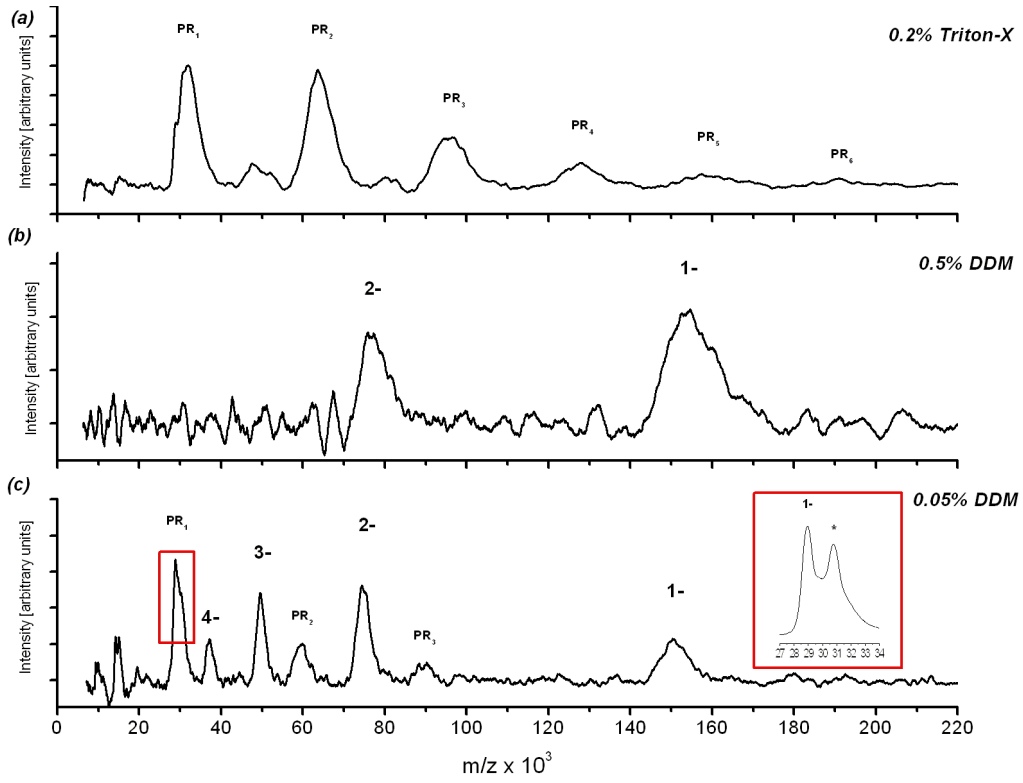

Figure 3.18: *LILBID anion spectra of proteorhodopsin in 0.2% Triton-X 100(a), 0.5% DDM (b) and 0.05% DDM (c). The inset in (c) is a magnification of the monomer signal.*

depicts the corresponding anion spectrum. Independent of the laser energy, the most dominant signals are those from the monomer and the dimer respectively. The overall oligomeric distribution ranges from the monomer up to the hexamer. Solubilising PR in DDM instead of Triton-X 100 surprisingly revealed a different stoichiometry: depending on the DDM concentration either only the pentamer in low charge states is observed (Fig. 3.18(b)) or the charge distribution of the pentamer is the most dominant signal among smaller oligomers (Fig. 3.18) whereas the fraction of the pentamer scales with laser intensity. In buffer conditions like those used for recording the spectrum shown in Fig. 3.18(c) it was not possible to obtain by 100% pentameric signals. The unusual broad peaks seen in Fig. 3.18(b) clearly result from the high detergent concentration compared to the signals of the same charge states of the pentamer in Fig. 3.18(c). The mass peak of the monomer is split into a signal of about 28.7 kDa (theoretical mass of the monomer: 28,823 Da [115]) and of about 30.7 kDa. At the N-terminal of PR a cleavable signal sequence is located which is required for correct insertion into the membrane. It is known that when PR is expressed with the signal sequence in *E.coli*, it is not

completely cleaved off [116]. Thus the double peak is consistent with the assumption of two different monomers [115]. The monomer still including the signal sequence has a calculated mass of 30,662 Da [115] and can be clearly assigned to the second mass of the monomer peak. The effect of the signal peptide on the quaternary structure is not known. However the LILBID spectra of PR cloned without the signal peptide suggests that there is no influence on the oligomeric state (Fig. 3.19). Furthermore the preferred stoichiometry of the pentamer found using DDM as detergent is partially consistent with the structure of PR reconstituted in lipids and disagrees with findings from size exclusion chromatography [117]. Since the initial solubilisation was done in DDM the quaternary structure of PR apparently is disrupted by Triton-X 100.

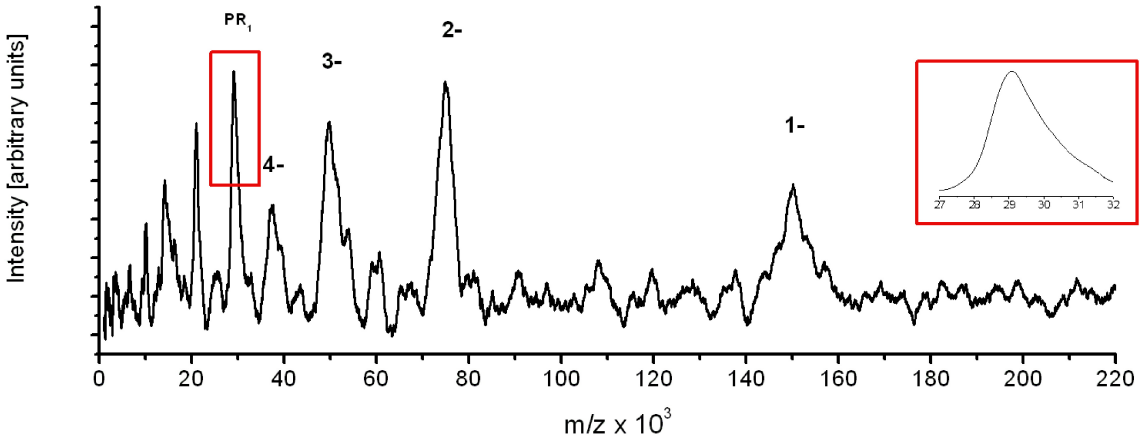

Figure 3.19: *LILBID anion spectrum of proteorhodopsin cloned without the N-terminal signal peptide. A magnification of the monomer signal is depicted in the inset.*

A further point of interest is the investigation of a possible dependence of the photocycle on the quaternary structure. It was already shown that the photocycles of PR purified with Triton-X 100 and of 2D crystals are almost identical [118]. As the findings of LILBID-MS clearly revealed mainly a monomeric state of PR when solubilised in Triton-X it suggests that the photocycles are independent on the oligomeric state and that the monomer might be the active unit. That would be an analogy to bR and further stimulate a discussion about the reason of the high stoichiometry found by independent methods. Further insight regarding the solution phase may come from comparing the photocycles of PR purified in different detergents.

3.3.3 Channelrhodopsin-2: one possible approach on the way to the native structure

An only recently detected retinal protein is Channelrhodopsin-2 (ChR2) which is found in green algae. It is widely used in bioengineering and neurosciences such as for photostimulation of neurons in neural circuits or for studying brain information processing in real-time. Furthermore, it was shown that visual function could be partially restored in blind mice by expressing this protein in inner retinal cells [119, 120]. Up to now not much is known about the quaternary structure and its functional relations. Therefore ChR2 was expressed in yeast and characterised by LILBID using different combinations of buffers and detergents. In all cases the only structure observed was that of the dimeric species under soft conditions (Fig. 3.20(a)). Even when the sample buffer contained 100mM sodium chloride only dimers could be detected, albeit at an immense peak broadening and a slight shift in the observed mass (Fig. 3.20(b)). The presence of an usual high amount of polar residues [121] most likely is responsible for detectable signals under these conditions. The dimeric structure could not be further fragmented by the desorption laser indicating a high stability of this complex. Too little is known to draw any final conclusions about the stoichiometry of the native structure. However, one possible approach was shown with the dimer but it is also possible that the real structure consists of multiples of the dimer. The results presented in this chapter so far are consolidated in ***paper 7***.

3.3.4 F_1F_o-ATP synthase: Membrane proteins and the role of buffers

As was already discussed the choice of buffer and buffer additives may have significant effects on the stability of the quaternary structures of biomolecules in solution (see chapter 3.2 for implications on nucleic acids and chapter 3.1.1 for the solvable protein HvoLsm). Naturally membrane proteins also are exposed to the influence of buffers as will be demonstrated now for the bacterial ATP synthase from *Bacillus pseudofirmus* as published in ***paper 6***. Furthermore the investigation of ATP synthases is of particular interest due to the high biological importance of this enzyme. ATP synthase (complex V) is ubiquitously found in bacteria, mitochondria and chloroplasts where it constitutes the final step in the respiratory chain by using energy to catalyse the production of adenosine triphosphate (ATP) - the "energy currency" of cells. The energy needed for this process is stored in the ion gradient across the membrane, established for example by

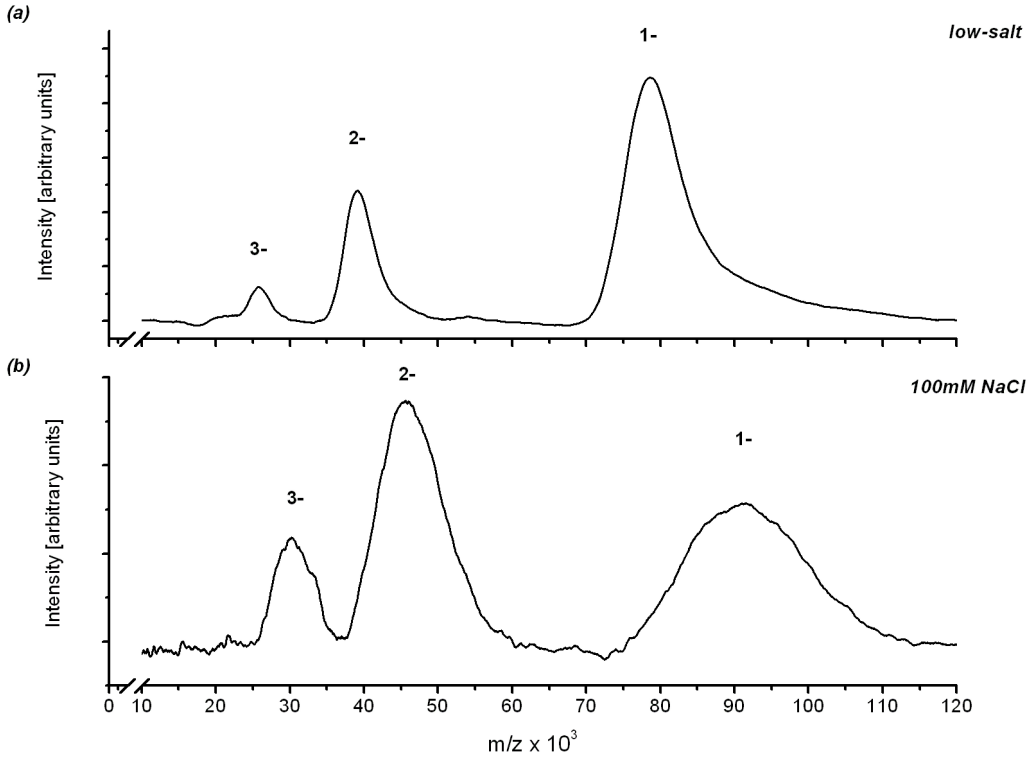

Figure 3.20: *LILBID anion spectra of Channelrhodopsin-2 recorded using a desalted buffer (a) and the standard sample buffer (b).*

the respiratory chain or by light-driven proton pumps. The simplest form of F_1F_o-ATP synthases can be found in bacteria. It consists of two domains: the water soluble F_1 subcomplex which contains the catalytic center which is connected to the hydrophobic F_o subcomplex by peripheral and central stalks. The main constituent of the membrane embedded F_o subcomplex is the ring, the "turbine-motor", which is responsible for ion translocation across the membrane. Since the detailed mechanism of the ATP synthesis has been discovered [122, 123, 124, 125] it is clear that for one complete turn of the membrane embedded ring three molecules of ATP are produced. As the ions are transported between two adjacent subunits of the ring, the size of the ring determines the amount of ions needed for a complete turn. Hence the analysis of the ring stoichiometry presents a measure for the efficiency of ATP production, which was already performed in previous LILBID works[20]. Furthermore macromolecular complexes which consist of both a water soluble and a hydrophobic domain often show a decreased stability which further complicates the analysis by mass spectrometry.

The LILBID anion spectra of the *B. pseudofirmus* OF4 ATP synthase recorded using different buffers is depicted in Fig. 3.21. In the first example purification involved dialysis

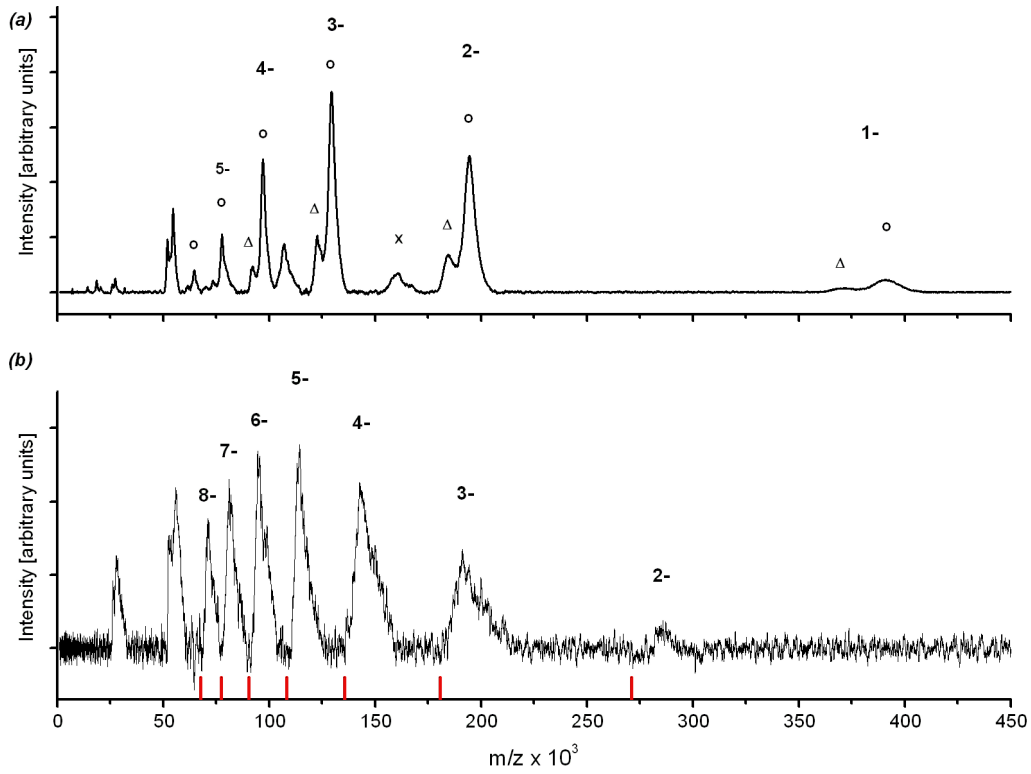

Figure 3.21: *LILBID anion spectra of the OF4 ATP synthase recorded after dialysis in ammonium acetate (a) and after buffer exchange in Tris/HCl containing 1 Mm of $MgCl_2$ (b).*

in a NH_4OAc buffer. The main contributions in the mass spectrum recorded under soft conditions are charge distributions of the F_1 subcomplex and of the F_1 subcomplex most likely lacking the δ subunit with masses of about 384 kDa and 363 kDa respectively. In addition signals of the hydrophobic F_o subcomplex with a mass of about 154 kDa occur at low peak intensity as well as contributions of the α and β subunits. Hence these results suggest that the holo-complex is already dissociated in solution. As the intact holo-complex surprisingly was not observed this protein was measured in a different buffer consisting of Tris/HCl, DDM and 1 mM of $MgCl_2$. As is illustrated in Fig. 3.21(b) this time the intact complex could be detected under soft conditions with a mass of about 542 kDa. To investigate whether the Tris buffer or the Mg^{2+} ions are responsible for the increased stability of the whole complex the sample was transferred into both a NH_4OAc buffer with and without 1 mM $MgCl_2$. The corresponding spectrum of the NH_4OAc solution containing $MgCl_2$ and recorded under soft conditions is shown in Fig. 3.22. The signal-to-noise ratio considerably increased compared to the results in Tris buffer (Fig. 3.21(b)) whereas the resolution hardly changed under mild desorption conditions.

The charge distribution of the ions measured in NH_4OAc buffer clearly shifted to lower charge states which is accounted for by the protonating effect of the NH_4^+ ions. Finally it was not possible to obtain signals of the intact enzyme using an NH_4OAc buffer without $MgCl_2$. This further demonstrates that Mg^{2+} ions are crucial for complex stability and function, a fact which was investigated very early in ATP synthase research [126] and confirmed many times since. When recorded under harsh conditions fragmentation of the subcomplexes into the individual subunits takes place as shown in Fig. 3.23. All eight expected subunits could be assigned and the masses seen by LILBID-MS closely agree with the calculated ones.

An additional point of interest regarding native mass spectrometry is the question of the absolute charge states of the subunits in solution. An appropriate model to study this are the anion signals of the highly charged [123] α and β subunits. For bacterial F_1F_o-ATP synthases the signal intensities of these two subunits are approximately equal as observed in Fig. 3.23 and also for the *Bacillus* sp. strain TA2.A1 [127]. This is not surprising when comparing the theoretical isoelectric points (pIs): in OF4 the pI of the α unit is 5.11 and that for the β subunit is 5.01. Hence the signal intensities are expected to be approximately the same when measured at pH 7.5. In mammalian F_1F_o-ATP synthases, as seen for mitochondrial bovine and human heart ATP synthases (***paper 8***), the β subunits occur with a relative high signal intensity whereas the α subunits are hardly visible. The pIs for the α subunits are 8.28 for the human complex and 8.27 for the bovine one. The β subunits both have an pI of 5.0. Thus the α subunits carry less negative charges than the β subunits and are only weakly detected in the anion mode. Finally in F_1F_o-ATP synthases from *Yarrowia lipolytica* the α subunit (pI 6.6) occurs at approximately half the intensity of the β subunit (pI 4.81) [128]. Though calculated isoelectric points may not reflect the accurate charge states of the functioning proteins, LILBID-MS correctly reflects the relative charge states in solution.

Furthermore, when comparing the masses of those subunits which are part of both, eukaryotic and bacterial F_1F_o-ATP synthases, a peculiar pattern can be observed. Selected subunits are conserved among all F_1F_o-ATP synthases [129] including the α, β and γ subunits as well as the c subunit which forms the rotor ring. Also the δ and ϵ subunits are conserved, but differences are observed between the bacterial and mammalian complexes.

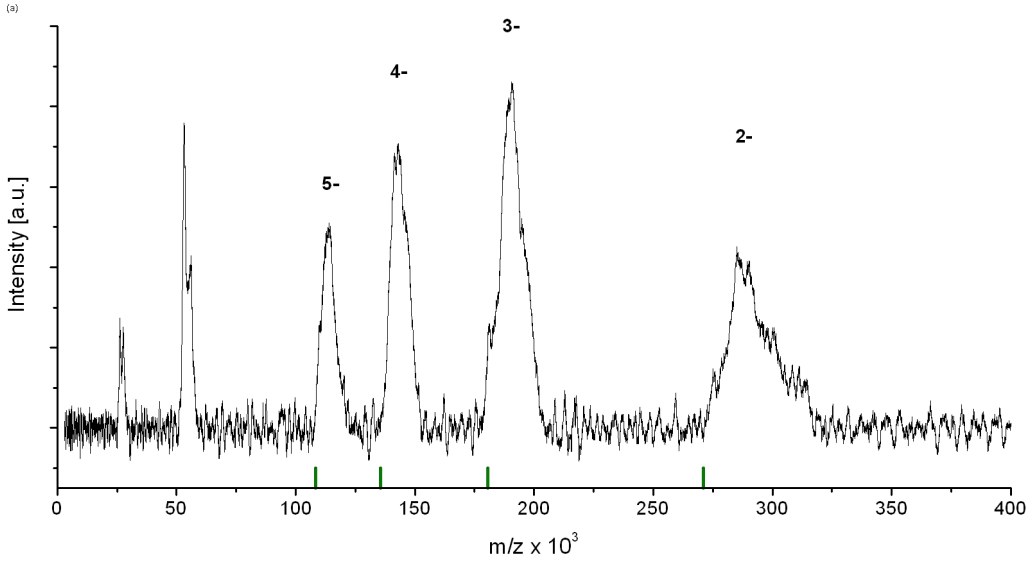

Figure 3.22: *LILBID anion spectrum of OF4 ATP synthase in ammonium acetate buffer containing 1mM $MgCl_2$. The charge states of complex V are labeled.*

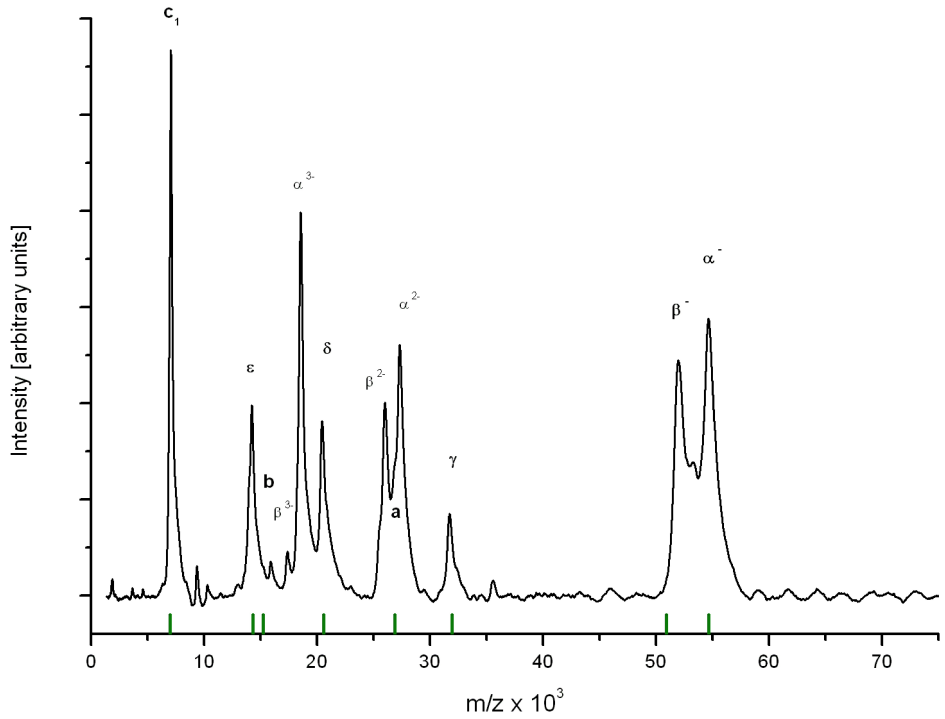

Figure 3.23: *LILBID anion spectrum of the OF4 ATP synthase recorded under harsh conditions. The subunits are labeled and the corresponding theoretical masses are indicated by bars.*

4 Bibliography

[1] M. Karas and F. Hillenkamp. Laser desorption ionization of proteins with molecular masses exceeding 10000 daltons. *Analytical Chemistry*, 60(20):2299–2301, 1988.

[2] K. Tanaka, H. Waki, Y. Ido, S. Akita, Y. Yoshida, and Y. Yoshida. Protein and polymer analysis up to m/z 100 000 by laser ionization time-of-flight mass spectrometry. *Rapid Communications In Mass Spectrometry*, 2:151–153, 1988.

[3] C. M. Whitehouse, R. N. Dreyer, M. Yamashita, and J. B. Fenn. Electrospray interface for liquid chromatographs and mass spectrometers. *Analytical Chemistry*, 57(3):675–679, 1985.

[4] J. B. Fenn, M. Mann, C. K. Meng, S. F. Wong, and C. M. Whitehouse. Electrospray ionization for mass-spectrometry of large biomolecules. *Science*, 246(4926):64–71, 1989.

[5] R. M. Caprioli, T. B. Farmer, and J. Gile. Molecular imaging of biological samples: Localization of peptides and proteins using maldi-tof ms. *Analytical Chemistry*, 69(23):4751–4760, 1997.

[6] G. Bolbach. Matrix-assisted laser desorption/ionization analysis of non-covalent complexes: Fundamentals and applications. *Current Pharmaceutical Design*, 11(20):2535–2557, 2005.

[7] C. Bich and R. Zenobi. Mass spectrometry of large complexes. *Current Opinion In Structural Biology*, 19(5):632–639, 2009.

[8] R. R. O. Loo, N. Dales, and P. C. Andrews. Surfactant effects on protein-structure examined by electrospray-ionization mass-spectrometry. *Protein Science*, 3(11):1975–1983, 1994.

[9] K. L. Rundlett and D. W. Armstrong. Mechanism of signal suppression by an ionic surfactants in capillary electrophoresis electrospray ionization mass spectrometry. *Analytical Chemistry*, 68(19):3493–3497, 1996.

[10] C. T. Reimann, I. Velazquez, and O. Tapia. Proteins in vacuo. denaturation of highly-charged lysozyme studied by molecular dynamics simulations. *Journal of Physical Chemistry B*, 102(46):9344–9352, 1998.

[11] I. A. Kaltashov and R. R. Abzalimov. Do ionic charges in esi ms provide useful information on macromolecular structure? *Journal of the American Society For Mass Spectrometry*, 19(9):1239–1246, 2008.

[12] A. A. Shvartsburg, F. M. Li, K. Q. Tang, and R. D. Smith. Characterizing the structures and folding of free proteins using 2-d gas-phase separations: Observation of multiple unfolded conformers. *Analytical Chemistry*, 78(10):3304–3315, 2006.

[13] R. Juraschek, T. Dulcks, and M. Karas. Nanoelectrospray - more than just a minimized-flow electrospray ionization source. *Journal of the American Society For Mass Spectrometry*, 10(4):300–308, 1999.

[14] D. Y. Chang, C. C. Lee, and J. Shiea. Detecting large biomolecules from high-salt solutions by fused-droplet electrospray ionization mass spectrometry. *Analytical Chemistry*, 74(11):2465–2469, 2002.

[15] B. T. Ruotolo, J. L. P. Benesch, A. M. Sandercock, S. J. Hyung, and C. V. Robinson. Ion mobility-mass spectrometry analysis of large protein complexes. *Nature Protocols*, 3(7):1139–1152, 2008.

[16] W. Kleinekofort, J. Avdiev, and B. Brutschy. A new method of laser desorption mass spectrometry for the study of biological macromolecules. *International Journal of Mass Spectrometry and Ion Processes*, 152(2-3):135–142, 1996.

[17] F. Sobott, W. Kleinekofort, and B. Brutschy. Cation selectivity of natural and synthetic ionophores probed with laser-induced liquid beam mass spectrometry. *Analytical Chemistry*, 69(17):3587–3594, 1997.

[18] A. Wattenberg, R. D. Barth, and B. Brutschy. Copper-binding abilities of the tripeptide diglycylhistidine studied by laser-induced liquid beam ionization/desorption mass spectrometry in aqueous solution. *Journal of Mass Spectrometry*, 32(12):1350–1355, 1997.

[19] N. Morgner, H. D. Barth, and B. Brutschy. A new way to detect noncovalently bonded complexes of biomolecules from liquid micro-droplets by laser mass spectrometry. *Australian Journal Of Chemistry*, 59(2):109–114, 2006.

[20] T. Meier, N. Morgner, D. Matthies, D. Pogoryelov, S. Keis, G. M. Cook, P. Dimroth, and B. Brutschy. A tridecameric c ring of the adenosine triphosphate (atp) synthase from the thermoalkaliphilic bacillus sp strain ta2.a1 facilitates atp synthesis at low electrochemical proton potential. *Molecular Microbiology*, 65(5):1181–1192, 2007.

[21] T. Meier, N. Morgner, D. Matthies, D. Pogoryelov, and B. Brutschy. Mass determination of membrane protein complexes in detergent solution: The c rings from f-atp synthases. *Biochimica Et Biophysica Acta-bioenergetics*, 1777:S19–S20, 2008.

[22] N. Morgner, H. D. Barth, T. L. Schmidt, A. Heckel, U. Scheffer, M. Gobel, P. Fucini, and B. Brutschy. Detecting specific ligand binding to nucleic acids: A test for ultrasoft laser mass spectrometry. *Zeitschrift Fur Physikalische Chemie-international Journal of Research In Physical Chemistry & Chemical Physics*, 221(5):689–704, 2007.

[23] N. Morgner, H. D. Barth, B. Brutschy, U. Scheffer, S. Breitung, and M. Gobel. Binding sites of the viral rna element tar and of tar mutants for various peptide ligands, probed with lilbid: A new laser mass spectrometry. *Journal of the American Society For Mass Spectrometry*, 19(11):1600–1611, 2008.

[24] N. Morgner, V. Zickermann, S. Kerscher, I. Wittig, A. Abdrakhmanova, H. D. Barth, B. Brutschy, and U. Brandt. Subunit mass fingerprinting of mitochondrial complex i. *Biochimica Et Biophysica Acta-Bioenergetics*, 1777(10):1384–1391, 2008.

[25] A. Charvat and B. Abel. How to make big molecules fly out of liquid water: applications, features and physics of laser assisted liquid phase dispersion mass spectrometry. *Physical Chemistry Chemical Physics*, 9(26):3335–3360, July 2007.

[26] E. Rapp, A. Charvat, A. Beinsen, U. Plessmann, U. Reichl, A. Seidel-Morgenstern, H. Urlaub, and B. Abel. Atmospheric pressure free liquid infrared maldi mass spectrometry: Toward a combined esi/maldi-liquid chromatography interface. *Analytical Chemistry*, 81(1):443–452, January 2009.

[27] T. Kondow, F. Mafune, and J. Y. Kohno. What is a liquid beam? *Australian Journal of Chemistry*, 59(2):79–80, 2006.

[28] J. Kohno and T. Kondow. Uv laser induced proton-transfer of protein molecule in the gas phase produced by droplet-beam laser ablation. *Chemical Physics Letters*, 463(1-3):206–210, September 2008.

[29] K. R. Siefermann, Y. X. Liu, E. Lugovoy, O. Link, M. Faubel, U. Buck, B. Winter, and B. Abel. Binding energies, lifetimes and implications of bulk and interface solvated electrons in water. *Nature Chemistry*, 2(4):274–279, 2010.

[30] F. Postberg, S. Kempf, J. Schmidt, N. Brilliantov, A. Beinsen, B. Abel, U. Buck, and R. Srama. Sodium salts in e-ring ice grains from an ocean below the surface of enceladus. *Nature*, 459(7250):1098–1101, 2009.

[31] J.A. Giordmaine and R. C. Miller. Tunable coherent parametric oscillation in linbo3 at optical frequencies. *Physical Review Letters*, 14(24):973–&, 1965.

[32] F. Huisken, A. Kulcke, D. Voelkel, C. Laush, and J. M. Lisy. New infrared injection-seeded optical parametric oscillator with high-energy and narrow bandwidth output. *Applied Physics Letters*, 62(8):805–807, February 1993.

[33] M. F. Kropman, H. K. Nienhuys, S. Woutersen, and H. J. Bakker. Vibrational relaxation and hydrogen-bond dynamics of hdo : H2o. *Journal of Physical Chemistry A*, 105(19):4622–4626, 2001.

[34] A. Terasaki. Dynamics of clusters initiated by photon and surface impact. *Journal of Physical Chemistry A*, 111(32):7671–7689, August 2007.

[35] D. E. Otten, A. J. Trevitt, B. D. Nichols, G. F. Metha, and M. A. Buntine. Infrared laser desorption of hydroquinone from a water-ethanol liquid beam. *Journal of Physical Chemistry A*, 107(32):6130–6135, 2003.

[36] Frank Sobott. *Charakterisierung und Anwendung der LILBI Laserdesorptions-Massenspektrometrie*. PhD thesis, Goethe Universität Frankfurt am Main, 2000.

[37] B. Abel, A. Charvat, U. Diederichsen, M. Faubel, B. Girmannc, J. Niemeyer, and A. Zeeck. Applications, features, and mechanistic aspects of liquid water beam desorption mass spectrometry. *International Journal of Mass Spectrometry*, 243(2):177–188, 2005.

[38] O. J. Maselli, J. R. Gascooke, W. D. Lawrance, and M. A. Buntine. Benzene internal energy distributions following spontaneous evaporation from a water-ethanol solution. *Journal of Physical Chemistry C*, 113(2):637–643, 2009.

[39] D.J. Segelstein. The complex refractive index of water. Master's thesis, University of Missouri-Kansas City, 1981.

[40] W. C. Wiley and I. H. McLaren. Time-of-flight mass spectrometer with improved resolution. *Review of Scientific Instruments*, 26(12):1150–1157, 1955.

[41] B. A. Mamyrin, V. I. Karataev, D. V. Shmikk, and V. A. Zagulin. Mass-reflectron a new nonmagnetic time-of-flight high-resolution mass-spectrometer. *Zhurnal Eksperimentalnoi I Teoreticheskoi Fiziki*, 64(1):82–89, 1973.

[42] W. A. P. Young, R. G. Ridley, and N. R. Daly. Fast counting in mass spectrometry with scintillation detector. *Nuclear Instruments & Methods*, 51(2):257–&, 1967.

[43] E. D. Erickson, G. E. Yefchak, C. G. Enke, and J. F. Holland. Mass dependence of time-lag focusing in time-of-flight mass-spectrometry - an analysis. *International Journal of Mass Spectrometry and Ion Processes*, 97(1):87–106, 1990.

[44] S. E. Rodriguez-Cruz, J. S. Klassen, and E. R. Williams. Hydration of gas-phase ions formed by electrospray ionization. *Journal of the American Society For Mass Spectrometry*, 10(10):958–968, 1999.

[45] M. Faubel, S. Schlemmer, and J. P. Toennies. A molecular-beam study of the evaporation of water from a liquid jet. *Zeitschrift Fur Physik D-atoms Molecules and Clusters*, 10(2-3):269–277, 1988.

[46] S. Thore, C. Mayer, C. Sauter, S. Weeks, and D. Suck. Crystal structures of the pyrococcus abyssi sm core and its complex with rna - common features of rna binding in archaea and eukarya. *Journal of Biological Chemistry*, 278(2):1239–1247, 2003.

[47] T. Moller, T. Franch, P. Hojrup, D. R. Keene, H. P. Bachinger, R. G. Brennan, and P. Valentin-Hansen. Hfq: a bacterial sm-like protein that mediates rna-rna interaction. *Molecular Cell*, 9(1):23–30, 2002.

[48] A. X. Zhang, K. M. Wassarman, J. Ortega, A. C. Steven, and G. Storz. The sm-like hfq protein increases oxys rna interaction with target mrnas. *Molecular Cell*, 9(1):11–22, 2002.

[49] P. Valentin-Hansen, M. Eriksen, and C. Udesen. The bacterial sm-like protein hfq: a key player in rna transactions. *Molecular Microbiology*, 51(6):1525–1533, 2004.

[50] I. Toro, S. Thore, C. Mayer, J. Basquin, B. Seraphin, and D. Suck. Rna binding in an sm core domain: X-ray structure and functional analysis of an archaeal sm protein complex. *Embo Journal*, 20(9):2293–2303, 2001.

[51] T. Achsel, H. Stark, and R. Luhrmann. The sm domain is an ancient rna-binding motif with oligo(u) specificity. *Proceedings of the National Academy of Sciences of the United States of America*, 98(7):3685–3689, 2001.

[52] B. M. Collins, S. J. Harrop, G. D. Kornfeld, I. W. Dawes, P. M. G. Curmi, and B. C. Mabbutt. Crystal structure of a heptameric sm-like protein complex from archaea: Implications for the structure and evolution of snrnps. *Journal of Molecular Biology*, 309(4):915–923, 2001.

[53] C. Mura, D. Cascio, M. R. Sawaya, and D. S. Eisenberg. The crystal structure of a heptameric archaeal sm protein: Implications for the eukaryotic snrnp core. *Proceedings of the National Academy of Sciences of the United States of America*, 98(10):5532–5537, 2001.

[54] A. A. Mills, B. H. Zheng, X. J. Wang, H. Vogel, D. R. Roop, and A. Bradley. p63 is a p53 homologue required for limb and epidermal morphogenesis. *Nature*, 398(6729):708–713, 1999.

[55] A. Yang, R. Schweitzer, D. Q. Sun, M. Kaghad, N. Walker, R. T. Bronson, C. Tabin, A. Sharpe, D. Caput, C. Crum, and F. McKeon. p63 is essential for regenerative proliferation in limb, craniofacial and epithelial development. *Nature*, 398(6729):714–718, 1999.

[56] A. Yang, N. Walker, R. Bronson, M. Kaghad, M. Oosterwegel, J. Bonnin, C. Vagner, H. Bonnet, P. Dikkes, A. Sharpe, F. McKeon, and D. Caput. p73-deficient mice have neurological, pheromonal and inflammatory defects but lack spontaneous tumours. *Nature*, 404(6773):99–103, 2000.

[57] E. R. Flores, S. Sengupta, J. B. Miller, J. J. Newman, R. Bronson, D. Crowley, A. Yang, F. McKeon, and T. Jacks. Tumor predisposition in mice mutant for p63 and p73: Evidence for broader tumor suppressor functions for the p53 family. *Cancer Cell*, 7(4):363–373, 2005.

[58] R. Tomasini, K. Tsuchihara, M. Wilhelm, M. Fujitani, A. Rufini, C. C. Cheung, F. Khan, A. Itie-Youten, A. Wakeham, M. S. Tsao, J. L. Iovanna, J. Squire, I. Jurisica, D. Kaplan, G. Melino, A. Jurisicova, and T. W. Mak. Tap73 knockout shows genomic instability with infertility and tumor suppressor functions. *Genes & Development*, 22(19):2677–2691, 2008.

[59] V. De Laurenzi, A. Costanzo, D. Barcaroli, A. Terrinoni, M. Falco, M. Annicchiarico-Petruzzeli, M. Levrero, and G. Melino. Two new p73 splice variants, gamma and delta, with different transcriptional activity. *Journal of Experimental Medicine*, 188(9):1763–1768, 1998.

[60] V. De Laurenzi, M. V. Catani, A. Terrinoni, M. Corazzari, G. Melino, A. Costanzo, M. Levrero, and R. A. Knight. Additional complexity in p73: induction by mitogens in lymphoid cells and identification of two new splicing variants epsilon and zeta. *Cell Death and Differentiation*, 6(5):389–390, 1999.

[61] M. Kaghad, H. Bonnet, A. Yang, L. Creancier, J. C. Biscan, A. Valent, A. Minty, P. Chalon, J. M. Lelias, X. Dumont, P. Ferrara, F. McKeon, and D. Caput. Monoallelically expressed gene related to p53 at 1p36, a region frequently deleted in neuroblastoma and other human cancers. *Cell*, 90(4):809–819, 1997.

[62] A. N. Yang, M. Kaghad, Y. M. Wang, E. Gillett, M. D. Fleming, V. Dotsch, N. C. Andrews, D. Caput, and F. McKeon. p63, a p53 homolog at 3q27-29, encodes multiple products with transactivating, death-inducing, and dominant-negative activities. *Molecular Cell*, 2(3):305–316, 1998.

[63] M. Senoo, F. Pinto, C. P. Crum, and F. McKeon. p63 is essential for the proliferative potential of stem cells in stratified epithelia. *Cell*, 129(3):523–536, 2007.

[64] E. K. Suh, A. Yang, A. Kettenbach, C. Bamberger, A. H. Michaelis, Z. Zhu, J. A. Elvin, R. T. Bronson, C. P. Crum, and F. McKeon. p63 protects the female germ line during meiotic arrest. *Nature*, 444(7119):624–628, 2006.

[65] C. L. Brooks and W. Gu. p53 ubiquitination: Mdm2 and beyond. *Molecular Cell*, 21(3):307–315, 2006.

[66] M. Wade, Y. V. Wang, and G. M. Wahl. The p53 orchestra: Mdm2 and mdmx set the tone. *Trends In Cell Biology*, 20(5):299–309, 2010.

[67] Z. Serber, H. C. Lai, A. Yang, H. D. Ou, M. S. Sigal, A. E. Kelly, B. D. Darimont, P. H. G. Duijf, H. van Bokhoven, F. McKeon, and V. Dotsch. A c-terminal inhibitory domain controls the activity of p63 by an intramolecular mechanism. *Molecular and Cellular Biology*, 22(24):8601–8611, 2002.

[68] W. E. Straub, T. A. Weber, B. Schafer, E. Candi, F. Durst, H. D. Ou, K. Rajalingam, G. Melino, and V. Dotsch. The c-terminus of p63 contains multiple regulatory elements with different functions. *Cell Death & Disease*, 1, 2010.

[69] W. M. Chan, W. Y. Siu, A. Lau, and R. Y. C. Poon. How many mutant p53 molecules are needed to inactivate a tetramer? *Molecular and Cellular Biology*, 24(8):3536–3551, 2004.

[70] P. Chene. The role of tetramerization in p53 function. *Oncogene*, 20(21):2611–2617, 2001.

[71] P. D. Jeffrey, S. Gorina, and N. P. Pavletich. Crystal-structure of the tetramerization domain of the p53 tumor-suppressor at 1.7 angstroms. *Science*, 267(5203):1498–1502, 1995.

[72] W. T. Lee, T. S. Harvey, Y. Yin, P. Yau, D. Litchfield, and C. H. Arrowsmith. Solution structure of the tetrameric minimum transforming domain of p53. *Nature Structural Biology*, 1(12):877–890, 1994.

[73] W. Lesniak, A. U. Bielinska, K. Sun, K. W. Janczak, X. Y. Shi, J. R. Baker, and L. P. Balogh. Silver/dendrimer nanocomposites as biomarkers: Fabrication, characterization, in vitro toxicity, and intracellular detection. *Nano Letters*, 5(11):2123–2130, 2005.

[74] X. G. Shi, S. H. Wang, S. Meshinchi, M. E. Van Antwerp, X. D. Bi, I. H. Lee, and J. R. Baker. Dendrimer-entrapped gold nanoparticles as a platform for cancer-cell targeting and imaging. *Small*, 3:1245–1252, 2007.

[75] E. S. Lee, D. Kim, Y. S. Youn, K. T. Oh, and Y. H. Bae. A virus-mimetic nanogel vehicle. *Angewandte Chemie-international Edition*, 47(13):2418–2421, 2008.

[76] E. de Jesus and J. C. Flores. Dendrimers: Solutions for catalyst separation and recycling-a review. *Industrial & Engineering Chemistry Research*, 47(21):7968–7981, 2008.

[77] V. J. Venditto, C. A. S. Regino, and M. W. Brechbiel. Pamam dendrimer based macromolecules as improved contrast agents. *Molecular Pharmaceutics*, 2(4):302–311, 2005.

[78] J. N. H. Reek, S. Arevalo, R. Van Heerbeek, P. C. J. Kamer, and P. W. N. M. Van Leeuwen. Dendrimers in catalysis. *Advances In Catalysis, Vol 49*, 49:71–151, 2006.

[79] D. Astruc, C. Ornelas, and J. Ruiz. Metallocenyl dendrimers and their applications in molecular electronics, sensing, and catalysis. *Accounts of Chemical Research*, 41(7):841–856, 2008.

[80] S. H. Hwang, C. N. Moorefield, and G. R. Newkome. Dendritic macromolecules for organic light-emitting diodes. *Chemical Society Reviews*, 37(11):2543–2557, 2008.

[81] J. T. Rhule, C. L. Hill, and D. A. Judd. Polyoxometalates in medicine. *Chemical Reviews*, 98(1):327–357, 1998.

[82] C. E. Muller, J. Iqbal, Y. Baqi, H. Zimmermann, A. Rollich, and H. Stephan. Polyoxometalates - a new class of potent ecto-nucleoside triphosphate diphosphohydrolase (ntpdase) inhibitors. *Bioorganic & Medicinal Chemistry Letters*, 16(23):5943–5947, 2006.

[83] E. Coppi, A. M. Pugliese, H. Stephan, C. E. Muller, and F. Pedata. Role of p2 purinergic receptors in synaptic transmission under normoxic and ischaemic conditions in the ca1 region of rat hippocampal slices. *Purinergic Signalling*, 3(3):203–219, 2007.

[84] F. M. Sansom, P. Riedmaier, H. J. Newton, M. A. Dunstone, C. E. Muller, H. Stephan, E. Byres, T. Beddoe, J. Rossjohn, P. J. Cowan, A. J. F. d'Apice, S. C. Robson, and E. L. Hartland. Enzymatic properties of an ecto-nucleoside triphosphate diphosphohydrolase from legionella pneumophila - substrate specificity and requirement for virulence. *Journal of Biological Chemistry*, 283(19):12909–12918, 2008.

[85] K. A. Brylev, Y. V. Mironov, S. S. Yarovoi, N. G. Naumov, V. E. Fedorov, S. J. Kim, N. Kitamura, Y. Kuwahara, K. Yamada, S. Ishizaka, and Y. Sasaki. A family of octahedral rhenium cluster complexes [re(6)q(8)(h2o)(n)(oh)(6-n)](n-4)

(q = s, se; n=0-6): Structural and ph-dependent spectroscopic studies. *Inorganic Chemistry*, 46(18):7414–7422, 2007.

[86] R.B. Cole. *Electrospray Ionization Mass Spectrometry. Fundamentals, Instrumentations and Applications.* John Wiley: New York, 1997.

[87] I.A. Kaltashov and S.J. Eyles. *Mass Spectrometry in Biophysics. Conformation and Dynamics of Biomolecules.* Wiley Interscience: Hoboken, 2005.

[88] N. R. Markham and M. Zuker. Dinamelt web server for nucleic acid melting prediction. *Nucleic Acids Research*, 33:W577–W581, 2005.

[89] T. Nohmi and J. B. Fenn. Electrospray mass-spectrometry of poly(ethylene glycols) with molecular-weights up to 5 million. *Journal Of The American Chemical Society*, 114(9):3241–3246, 1992.

[90] R. D. Chen, X. H. Cheng, D. W. Mitchell, S. A. Hofstadler, Q. Y. Wu, A. L. Rockwood, M. G. Sherman, and R. D. Smith. Trapping, detection, and mass determination of coliphage t4 dna ions of 10(8) da by electrospray-ionization fourier-transform ion-cyclotron resonance mass-spectrometry. *Analytical Chemistry*, 67(7):1159–1163, 1995.

[91] X. H. Cheng, D. G. Camp, Q. Y. Wu, R. Bakhtiar, D. L. Springer, B. J. Morris, J. E. Bruce, G. A. Anderson, C. G. Edmonds, and R. D. Smith. Molecular weight determination of plasmid dna using electrospray ionization mass spectrometry. *Nucleic Acids Research*, 24(11):2183–2189, 1996.

[92] G. S. Manning. Molecular theory of polyelectrolyte solutions with applications to electrostatic properties of polynucleotides. *Quarterly Reviews of Biophysics*, 11(2):179–246, 1978.

[93] A. E. Every and I. M. Russu. Influence of magnesium ions on spontaneous opening of dna base pairs. *Journal of Physical Chemistry B*, 112(25):7689–7695, 2008.

[94] M. G. McCammon and C. V. Robinson. Structural change in response to ligand binding. *Current Opinion In Chemical Biology*, 8(1):60–65, 2004.

[95] C. Kunsch, S. M. Ruben, and C. A. Rosen. Selection of optimal kappa-b/rel dna-binding motifs - interaction of both subunits of nf-kappa-b with dna is required for transcriptional activation. *Molecular And Cellular Biology*, 12(10):4412–4421, 1992.

[96] C. W. Muller, F. A. Rey, M. Sodeoka, G. L. Verdine, and S. C. Harrison. Structure of the nf-kappa-b p50 homodimer bound to dna. *Nature*, 373(6512):311–317, 1995.

[97] K. Q. Ye, L. Malinina, and D. J. Patel. Recognition of small interfering rna by a viral suppressor of rna silencing. *Nature*, 426(6968):874–878, 2003.

[98] H. Y. Chen, J. Yang, C. Q. Lin, and Y. AdamYuan. Structural basis for rna-silencing suppression by tomato aspermy virus protein 2b. *Embo Reports*, 9(8):754–760, 2008.

[99] K. Q. Ye and D. J. Patel. Rna silencing suppressor p21 of beet yellows virus forms an rna binding octameric ring structure. *Structure*, 13(9):1375–1384, 2005.

[100] T. Achsel, H. Brahms, B. Kastner, A. Bachi, M. Wilm, and R. Luhrmann. A doughnut-shaped heteromer of human sm-like proteins binds to the 3 '-end of u6 snrna, thereby facilitating u4/u6 duplex formation in vitro. *Embo Journal*, 18(20):5789–5802, 1999.

[101] M. A. Schumacher, R. F. Pearson, T. Moller, P. Valentin-Hansen, and R. G. Brennan. Structures of the pleiotropic translational regulator hfq and an hfq-rna complex: a bacterial sm-like protein. *Embo Journal*, 21(13):3546–3556, 2002.

[102] N. P. Barrera, S. C. Isaacson, M. Zhou, V. N. Bavro, A. Welch, T. A. Schaedler, M. A. Seeger, R. N. Miguel, V. M. Korkhov, H. W. van Veen, H. Venter, A. R. Walmsley, C. G. Tate, and C. V. Robinson. Mass spectrometry of membrane transporters reveals subunit stoichiometry and interactions. *Nature Methods*, 6(8):585–U49, 2009.

[103] R. R. O. Loo and J. A. Loo. Matrix-assisted laser desorption/ionization-mass spectrometry of hydrophobic proteins in mixtures using formic acid, perfluorooctanoic acid, and sorbitol. *Analytical Chemistry*, 79(3):1115–1125, 2007.

[104] J. L. Norris, N. A. Porter, and R. M. Caprioli. Combination detergent/maldi matrix: Functional cleavable detergents for mass spectrometry. *Analytical Chemistry*, 77(15):5036–5040, 2005.

[105] M. C. Djidja, S. Francese, P. M. Loadman, C. W. Sutton, P. Scriven, E. Claude, M. F. Snel, J. Franck, M. Salzet, and M. R. Clench. Detergent addition to tryptic digests and ion mobility separation prior to ms/ms improves peptide yield and

protein identification for in situ proteomic investigation of frozen and formalin-fixed paraffin-embedded adenocarcinoma tissue sections. *Proteomics*, 9(10):2750–2763, 2009.

[106] C. Y. Chang, H. K. Liao, C. G. Juo, S. H. Chen, and Y. J. Chen. Improved analysis of membrane protein by pvdf-aided, matrix-assisted laser desorption/ionization mass spectrometry. *Analytica Chimica Acta*, 556(1):237–246, 2006.

[107] L. O. Essen, R. Siegert, W. D. Lehmann, and D. Oesterhelt. Lipid patches in membrane protein oligomers: Crystal structure of the bacteriorhodopsin-lipid complex. *Proceedings of the National Academy of Sciences of the United States of America*, 95(20):11673–11678, 1998.

[108] A. L. Klyszejko, S. Shastri, S. A. Mari, H. Grubmuller, D. J. Muller, and C. Glaubitz. Folding and assembly of proteorhodopsin. *Journal of Molecular Biology*, 376(1):35–41, 2008.

[109] D. R. Barnidge, E. A. Dratz, A. J. Jesaitis, and J. Sunner. Extraction method for analysis of detergent-solubilized bacteriorhodopsin and hydrophobic peptides by electrospray ionization mass spectrometry. *Analytical Biochemistry*, 269(1):1–9, 1999.

[110] N. A. Dencher, K. D. Kohl, and M. P. Heyn. Photochemical cycle and light dark-adaptation of monomeric and aggregated bacteriorhodopsin in various lipid environments. *Biochemistry*, 22(6):1323–1334, 1983.

[111] D. A. Doyle, J. M. Cabral, R. A. Pfuetzner, A. L. Kuo, J. M. Gulbis, S. L. Cohen, B. T. Chait, and R. MacKinnon. The structure of the potassium channel: Molecular basis of k+ conduction and selectivity. *Science*, 280(5360):69–77, 1998.

[112] J. A. A. Demmers, A. van Dalen, B. de Kruijff, A. J. R. Heck, and J. A. Killian. Interaction of the k+ channel kcsa with membrane phospholipids as studied by esi mass spectrometry. *Febs Letters*, 541(1-3):28–32, 2003.

[113] B. Endeward, J. A. Butterwick, R. MacKinnon, and T. F. Prisner. Pulsed electron-electron double-resonance determination of spin-label distances and orientations on the tetrameric potassium ion channel kcsa. *Journal of the American Chemical Society*, 131(42):15246–15250, 2009.

[114] R. Rangarajan, J. F. Galan, G. Whited, and R. R. Birge. Mechanism of spectral tuning in green-absorbing proteorhodopsin. *Biochemistry*, 46:12679–12686, 2007.

[115] T. Friedrich, S. Geibel, R. Kalmbach, I. Chizhov, K. Ataka, J. Heberle, M. Engelhard, and E. Bamberg. Proteorhodopsin is a light-driven proton pump with variable vectoriality. *Journal of Molecular Biology*, 321(5):821–838, 2002.

[116] N. Pfleger, A. C. Worner, J. Yang, S. Shastri, U. A. Hellmich, L. Aslimovska, M. S. M. Maier, and C. Glaubitz. Solid-state nmr and functional studies on proteorhodopsin. *Biochimica Et Biophysica Acta-bioenergetics*, 1787(6):697–705, 2009.

[117] H. J. Liang, G. Whited, C. Nguyen, and G. D. Stucky. The directed cooperative assembly of proteorhodopsin into 2d and 3d polarized arrays. *Proceedings of the National Academy of Sciences of the United States of America*, 104(20):8212–8217, 2007.

[118] G. Schafer, S. Shastri, M. K. Verhoefen, V. Vogel, C. Glaubitz, J. Wachtveitl, and W. Mantele. Characterizing the structure and photocycle of pr 2d crystals with cd and ftir spectroscopy. *Photochemistry and Photobiology*, 85(2):529–534, 2009.

[119] A. D. Bi, J. J. Cui, Y. P. Ma, E. Olshevskaya, M. L. Pu, A. M. Dizhoor, and Z. H. Pan. Ectopic expression of a microbial-type rhodopsin restores visual responses in mice with photoreceptor degeneration. *Neuron*, 50(1):23–33, 2006.

[120] P. S. Lagali, D. Balya, G. B. Awatramani, T. A. Munch, D. S. Kim, V. Busskamp, C. L. Cepko, and B. Roska. Light-activated channels targeted to on bipolar cells restore visual function in retinal degeneration. *Nature Neuroscience*, 11(6):667–675, 2008.

[121] P. Hegemann. Algal sensory photoreceptors. *Annual Review of Plant Biology*, 59:167–189, 2008.

[122] P. D. Boyer. The atp synthase - a splendid molecular machine. *Annual Review of Biochemistry*, 66:717–749, 1997.

[123] J. P. Abrahams, A. G. W. Leslie, R. Lutter, and J. E. Walker. Structure at 2.8-angstrom resolution of f1-atpase from bovine heart-mitochondria. *Nature*, 370(6491):621–628, 1994.

[124] R. K. Nakamoto, J. A. B. Scanlon, and M. K. Al-Shawi. The rotary mechanism of the atp synthase. *Archives of Biochemistry and Biophysics*, 476(1):43–50, 2008.

[125] H. Noji, R. Yasuda, M. Yoshida, and K. Kinosita. Direct observation of the rotation of f-1-atpase. *Nature*, 386(6622):299–302, 1997.

[126] M. E. Pullman, H. S. Penefsky, A. Datta, and E. Racker. Partial resolution of the enzymes catalyzing oxidative phosphorylation .1. purification and properties of soluble, dinitrophenol-stimulated adenosine triphosphatase. *Journal of Biological Chemistry*, 235(11):3322–3329, 1960.

[127] N. Morgner, J. Hoffmann, H. D. Barth, T. Meier, and B. Brutschy. Lilbid-mass spectrometry applied to the mass analysis of rna polymerase ii and an f1fo-atp synthase. *International Journal of Mass Spectrometry*, 277(1-3):309–313, 2008.

[128] L. Sokolova, I. Wittig, H. D. Barth, H. Schagger, B. Brutschy, and U. Brandt. Laser-induced liquid bead ion desorption-ms of protein complexes from blue-native gels, a sensitive top-down proteomic approach. *Proteomics*, 10(7):1401–1407, 2010.

[129] P. D. Boyer. The binding change mechanism for atp synthase - some probabilities and possibilities. *Biochimica Et Biophysica Acta*, 1140(3):215–250, 1993.

5 Summary

The analysis of biomolecular macrocomplexes requires certain preconditions to be fulfilled. The preparation of biomolecular samples usually results in low yields. Due to this constraint of low availability any method should provide a sufficient sensitivity to cope with typical sample amounts. Biomolecules also often show a reduced stability, i.e. a propensity for fragmentation upon ionisation, which requires reasonable soft methods for the investigation. Furthermore macromolecular complexes usually are composed by means of non-covalent interactions presenting additional demands on the softness. This holds true for specific complexes like protein-ligand or DNA double strand binding. For the formation of non-covalent, specific complexes the biomolecules' native structure and environment are a basic prerequisite and hence crucial. Therefore it is desirable during analysis to keep the biomolecules in a native environment to preserve their structure and weak interactions. A native environment preferably consists of an aqueous solution containing a buffering agent and salts to define a pH and ionic strength.

One suitable method for analysing biomolecules is mass spectrometry. Mass spectrometry is capable of high throughput screening as well as determining masses with high accuracy and high sensitivity. Especially since the availability of MALDI-MS and ESI-MS mass spectrometry evolved to a versatile tool to investigate biomolecular complexes. Both, MALDI- and ESI-MS are sufficiently soft methods to observe fragile biomolecules. Yet both methods have their advantages and disadvantages.

During the recent years an alternative mass spectrometric approach has been developed in our group, termed LILBID-MS. In LILBID microdroplets of aqueous solution containing buffer, salt and further additives among the analyte molecules are injected into vacuum and irradiated one-by-one by mid-IR laser pulses. The absorption of the energy by the water leads to a rapid ablation of the preformed analyte ions. LILBID is highly tolerant for the addition of salts and detergents allowing to study biomolecular complexes in a native environment. As LILBID-MS is soft enough to avoid fragmentation, specific non-covalent complexes can be analysed directly from their native environment by this method. In addition fragmentation can be induced on demand by

increasing the laser intensity which allows for the study of subunit compositions. A further prominent property of LILBID is the possibility to study hydrophobic membrane proteins due to the tolerated use of detergents. A high sensitivity is responsible for a very low sample consumption: typically a sample volume of a few microlitres with an analyte concentration in the micromolar range is sufficient for a mass spectrometric analysis.

During the course of this work, several instrumental improvements mostly concerning ion focussing and beam steering were introduced. Together with refinements of different modes of measurement the result is a significantly improved signal-to-noise ratio as well as a further improvement in sensitivity. In addition the accessible m/z range for a given flight time has been vastly increased. The new possibilities that LILBID now offers for the study of biomolecular complexes were investigated.

Due to the low availability of biomolecular samples the methods sensitivity is of crucial importance. The sensitivity of LILBID-MS was shown on the basis of an aqueous solution of a 16-mer DNA single strand at a concentration of 9nM. A series of decreasing numbers of droplets used for a single mass spectrum was recorded. A reasonable signal-to-noise ratio could be still obtained when using three droplets for averaging corresponding to an amount of substance of about $1.8 \cdot 10^{-18}$mole corresponding to about 10^6 molecules. Apart from low concentrations large excess of salt or detergent too reduce the desorption efficiency and hence the signal intensity. The effect of high amounts of salt was investigated for the solvable protein HvoLsm using an aqueous, non-volatile Tris/HCl buffer containing 50mM of NaCl as well as for the transcription factor TAp63α using a non-volatile potassiumphosphate buffer containing 100mM of NaCl. Except for the decreased signal intensity and resolution, reasonable mass spectra could be recorded in both cases whereas for TAp63α the high excess of salt made it necessary to use more droplets. For investigating the effect of detergent on the signal intensity a concentration series of DDM, ranging from 0.05% to 0.5% DDM, was recorded for the membrane protein proteorhodopsin. The signal intensity steadily decreased with increasing concentration of DDM whereas the highest concentration for which reasonable signals could be recorded was 0.5% DDM, again due to the use of a large number of droplets. For even higher concentrations of DDM hardly any signals could be obtained. Thus it has been shown that LILBID-MS offers a sufficient sensitivity to cope with challenging conditions such as low analyte concentrations as well as a high amount of salt or detergent.

To maintain a native structure of biomolecules and hence the ability to form specific complexes a native, aqueous environment is required. This was tested for the solvable

proteins HvoLsm and TAp63α. Both proteins, when measured in non-volatile buffers containing high concentrations of salt, resulted in mass spectra showing native quaternary structures of a heptamer and dimer for HvoLsm and TAp63α respectively. However, upon transferring the analyte into a salt-free ammonium acetate buffer, HvoLsm revealed strong unspecific aggregation with oligomers up to the 20-mer whereas for TAp63α oligomers up to the octamer were detected. As a result it was shown that buffered, aqueous solutions sometimes do not provide a sufficient native environment but that the corresponding buffers play an important role.

Utilisation a native environment it was shown that the transcription factor TAp63α, a potential tumor suppressor, exists as a dimer. This finding is totally unexpected with respect to textbook knowledge since the homologue p53 exclusively forms tetramers. Further experiments using different methods verified the dimeric state of the inactive molecule. Upon activation a tetrameric state is adopted vastly increasing its DNA binding affinity. The mechanisms of inhibition and activation of TAp63α clearly are different than those of its well-known homologue, p53. Thus these results gave deeper insights in the promising field of tumor suppression.

An especially promising class of molecules with prospective application in medical diagnostics and therapy are dendrimers. These highly branched, symmetric polymers can be modified and functionalised in manifold ways to obtain a wide range of defined properties. Potential applications include the use as carrier systems, controlled drug release and tissue specific targeting. Here a series of polypropyleneimine dendrimers with different sugar modified surfaces were characterised. It was shown that the surface coverage results in a polydisperse mass distribution with almost 100% yields except for the higher generations. To investigate the potential use in radioisotope imaging techniques the complexation with Cu(II) ions was studied. As a result the complexation was found to increase with increasing dendrimer generation and is also slightly dependent on the respective sugar coating. In case of maltose modified polypropyleneamine dendrimers a similar polydisperse distribution of the maltose coverage was found. In addition the inclusion and release of the octahedral rhenium cluster $[Re_6S_8(OH)_6]^{4-}$ was studied. LILBID-MS could show that the loading capacity is generation dependent with highest uptakes of four to five cluster and five to six cluster for the fourth and fifth generation respectively. Furthermore it turned out that the *in-situ* preparation resulted in significant lower uptakes compared to post-synthesis incubation. Finally, incapsulation was sustained for at least one week, demonstrating the long-time stability of these complexes. So dendrimers present exciting molecules to be used as carrier systems, es-

pecially as polyoxometalates such as the studied rhenium cluster are known to show antiviral and antitumoral properties in cancer cells.

The ability to detect specific binding in LILBID-MS was investigated by means of nucleic acids, as they still present a considerable challenge for mass spectrometric analysis. Therefore two different sets of double stranded DNA with complementary sticky ends were studied. Each set forms long ladders of DNA connected by their sticky ends. In case where these ends were each 30 bases long, a pattern of oligomers with steadily decreasing signal intensity was observed. However, for the DNA where one sticky end was 20 bases long and the other one 40 bases, an alternating intensity pattern favouring even numbered fragments and even larger oligomers was detected. The increased stability in the latter case, especially for the even numbered species, is in perfect agreement with theoretical predicted melting temperatures of the complementary regions. To further study the stability, a 16-mer dsDNA was recorded using a series of buffers, differing only in the type and amount of salt. Here, the DNA showed the lowest stability when using a salt-free buffer, a slightly increased stability in the buffer with 10^{-5}M NaCl and the highest one when using the buffer with 10^{-6}M $MgCl_2$. Again, the relative stabilities are in good agreement with the calculated melting temperatures. The by far highest stability in this series for $MgCl_2$ can not be explained by the ionic strength alone and hence is an specific effect of magnesium. In addition, a competitive experiment with the well-known transcription factor p50, a match DNA containing the corresponding binding site and a mismatch DNA revealed only complexes of the p50 dimer bound to the double strand of the match DNA. Thus sequence specific binding both within dsDNA and for DNA-protein complexes can be detected with LILBID-MS. Furthermore, relative thermodynamics in solution phase are correctly transferred into the gas phase mass spectra. Finally, very large DNA such as the 2686 bp plasmid pUC19 can be easily detected by LILBID-MS with high sensitivity using a concentration of only 80nM.

An important and effective example of genomic defense is RNA interference (RNAi) which protects organisms against infection of viruses. However, some viruses developed strategies to bypass this defense mechanism by suppressing RNAi. The effect of RNAi suppression was studied for the *Tomato aspermy virus* which expresses the protein 2B (TAV_2B). After incubation with siRNA LILBID-MS revealed the stoichiometry of the TAV_2B:siRNA complex as a 4:2 stoichiometry. The stoichiometry in solution phase as seen by LILBID was later also found in the crystal structure. In addition LILBID data and gel filtration experiments agree on the fact that the isolated protein exists as a monomeric species in absence of RNA. As a result binding to siRNA oligomerises

and induces a conformational change in TAV_2B. Another example of studying specific complexes in native environment is the Lsm protein of the archeon *Haloferax volcanii*. Lsm proteins are involved in a plethora of RNA processing pathways and hence play a major role in RNA metabolism. Little is known so far about the archaeal members of this protein family. Here LILBID has shown that the recombinant protein binds to poly(U)-RNA and to a sRNA. For poly(U)-RNA a 1:1 complex was found with respect to the Lsm heptamer as well as a ternary complex consisting of two protein heptamers and the RNA. The physiological role of Lsm binding to poly(U)-RNA is unclear though, as poly(U) stretches have not been identified yet in the RNA population of *Haloferax volcanii*. In case of the sRNA only a complex with 1:1 stoichiometry could be detected. Due to the large amount of possible target RNAs as well as protein interaction partners, the characterisation of HvoLsm has just begun.

As was already shown in previous works, one particular strength of LILBID-MS is the ability to detect hydrophobic membrane proteins by using aqueous buffers and solubilisation of the membrane proteins in detergents. To compare the quaternary structure of membrane proteins as measured with LILBID with crystal structures where available, the light-driven proton pump bacteriorhodopsin and the potassium channel KcsA were studied. In case of bacteriorhodopsin the well-known trimeric state was observed. Though the trimer is not required for the function of this protein it is crucial for the *in vivo* physiology. At high laser power the trimer almost completely fragments into monomers revealing at least one type of lipids attached. For KcsA the tetramer is the functioning unit and was also detected by LILBID. However, the results show two distinct distributions of tetrameric species which is accounted for an incomplete cleavage during protein preparation. In addition LILBID observed a split monomer signal with a mass difference of about 400Da which was already seen in ESI-MS and interpreted as possible post-translational modification. For both membrane proteins the quaternary structure in solution phase resembles the respective crystal structure.

Another light-driven proton pump, for which the crystal structure is not yet available, is proteorhodopsin. For proteorhodopsin 2D crystals show either ring-shaped hexameric species or a mixture of penta- and hexamers depending on the topology of the used lipids. In LILBID no distinct complexes could be detected using Triton-X 100 as detergent. Instead, a steadily decreasing intensity pattern of oligomers ranging from the monomer up to the hexamer was observed. However, when using DDM as detergent, the pentameric species was the dominant signal. Furthermore, the fraction of the pentameric signals increased with increasing DDM concentration. In addition the same detergent-

dependent structures were recorded when cloning proteorhodopsin without the signal peptide proving that the signal peptide has no influence on the stoichiometry. Thus by comparing the photocycles of this protein solubilised in different detergents one could potentially gain access to the question about the active unit.

A new exciting light-driven ion channel is Channelrhodopsin-2 due to its relevance in bioengineering and neurosciences. The exact stoichiometry of a functioning, complete channel is not known so far. Therefore the protein was expressed in yeast and analysed by LILBID using different combinations of detergents and buffers. In all cases Channelrhodopsin-2 exists as a dimeric species which could not further be fragmented by the desorption laser. Too little is known to draw any definite conclusion at this time yet one possible approach is now available.

F_1F_o-ATP synthases are ion-driven nanomotors producing or hydrolising adenosine triphosphate (ATP), the "energy currency" of all life forms. ATP synthases present a precarious type of molecules as they are composed of a membrane-embedded part (F_o) and a soluble part (F_1), both loosely connected via non-covalent interactions of a few subunits. The main constituent of the hydrophobic part is the c-ring, whose size determines the ion/ATP ratio as three ATP molecules are produced per complete turn of the ring. Hence the exact knowledge of the complex stoichiometry is of great importance. Characterisation of ATP synthases by LILBID was already demonstrated in previous works for several F-type and A-type ATP synthases. However, the study of F_1F_o-ATP synthase from *Bacillus pseudofirmus* OF4 revealed new aspects concerning the mass spectrometric analysis. After dialysis in ammonium acetate buffer it was not possible to detect signals of the intact holo-complex under soft conditions. Instead, charge distributions of separated F_1 and F_o subcomplexes were observed as well as further fragments of the F_1. Under harsh conditions signals of all subunits were obtained. Thus the complex already dissociated mostly into the membrane-embedded and the soluble parts. However, when using a Tris/HCl buffer containing $MgCl_2$ the charge distribution of the intact complex was detected. Additionally, when using an ammonium acetate buffer with added magnesium chloride the whole complex could also be detected in contrast to the dialysed sample. These results verify that magnesium is needed to stabilise the coupling between F_1 and F_o. Furthermore, the relative signal intensities were exemplarily compared for the highly charged α and β subunits of different F-type ATP synthases. As a result the intensities reflect the respective charge state in solution at a given pH as expressed by the isoelectric point.

All in all LILBID-MS is a promising alternative mass spectrometric method and offers

new applications. Due to the use of native environments the structures observed present the native ones and solution phase dynamics is reflected by this method. The main emphasis is placed on the investigation of large macrocomplexes, non-covalent interactions and especially membrane proteins.

Planned improvements for the future include the adoption of LILBID to a Q-TOF instrument, a work which already started. Preliminary experiments show promising results at high resolution. Furthermore, making use of the MS/MS facility will enhance the possibilities of LILBID. To complement structural information, gas-phase spectroscopy will be potentially included.

6 Zusammenfassung

Massenspektrometrische Untersuchungen an Biomolekülen benötigen Methoden, die spezielle Voraussetzungen erfüllen. Da Biomolekülkomplexe oft nicht in großen Mengen vorliegen, muss eine solche Methode empfindlich genug sein, um mit niedrigem Probenverbrauch Analysen durchführen zu können. Darüber hinaus sollten die Methoden sanft genug sein, um auch nicht-kovalent gebundene Komplexe unfragmentiert nachweisen zu können. Nichtkovalente Wechselwirkungen spielen eine wichtige Rolle in spezifischen Komplexierungen wie Protein-Ligand oder DNA Doppelstrang Bindungen. Die Grundvoraussetzung für das Ausbilden spezifischer, nichtkovalenter Komplexe ist die native dreidimensionale Struktur der beteiligten Moleküle. Daher ist es unbedingt nötig, makromolekulare Komplexe in einer Umgebung zu analysieren, die der natürlichen sehr ähnlich ist, um die Struktur und schwach gebundene Wechselwirkungen zu erhalten. Solch eine native Umgebung besteht vorzugsweise aus einer wässrigen Lösung, welche Puffer und Salze enthält, um Ionenstärke und pH festlegen zu können.

Eine geeignete Methode um Biomoleküle zu charakterisieren ist die Massenspektrometrie. Mit Massenspektrometrie können Untersuchungen mit hohem Durchsatz durchgeführt und Massen mit hoher Genauigkeit und Empfindlichkeit nachgewiesen werden. Besonders mit der Einführung von MALDI-MS und ESI-MS hat sich Massenspektrometrie zu einem nützlichen und wichtigen Werkzeug entwickelt, um Biomoleküle zu erforschen. Beide Methoden sind ausreichend sanft um fragile Komplexe nachweisen zu können. Dennoch besitzen diese Methoden ihre Stärken und Schwächen.

Während der letzten Jahre wird in der Gruppe von Prof. Brutschy ein alternativer massenspektrometrischer Ansatz, LILBID-MS genannt, entwickelt. In LILBID werden Mikrotröpfchen wässriger Pufferlösungen in Hochvakuum eingebracht und einzeln mit IR Laserpulsen bestrahlt. Die resonante Absorption der Energie in Wasser führt zu einer rasanten Verdampfung der Lösungsmittelmoleküle und zum Freisetzen der gelösten Analytionen. LILBID ist sehr tolerant gegenüber der Zugabe von Salzen und Detergentien und bietet daher ein natives Umfeld für Untersuchungen an biomolekularen Komplexen. Da die LILBID-MS sanft genug ist, um Fragmentation zu vermeiden, können spezifische

nichtkovalente Komplexe mit dieser Methode direkt aus nativer Umgebung analysiert werden. Bei Bedarf kann eine Fragmentation der zu untersuchenden Moleküle durch Erhöhung der Laserleistung induziert werden. Dadurch wird es möglich die Zusammensetzung durch Untereinheiten zu studieren. Eine weitere bedeutende Eigenschaft von LILBID-MS, bedingt durch die Toleranz von Detergens, ist die Möglichkeit, hydrophobe Membranproteine zu untersuchen. Die hohe Empfindlichkeit ist für einen niedrigen Probenverbrauch verantwortlich: typischerweise ist ein Probenvolumen von einigen Mikrolitern mit einer Probenkonzentration im mikromolaren Bereich für eine massenspektrometrische Analyse ausreichend.

Im Verlauf dieser Arbeit wurden mehrere Verbesserungen, größtenteils im Bereich der Ionenoptik und Strahlkontrolle, eingeführt. Zusammen mit Verfeinerungen der unterschiedlichen Messmodi ist das Ergebnis ein maßgeblich verbessertes Signal/Rausch-Verhältnis und eine verbesserte Empfindlichkeit. Zusätzlich wurde dadurch der zugängliche m/z Bereich bei gegebener Flugzeit enorm erweitert. Die neuen Möglichkeiten, die LILBID nun für die Analyse biomolekularer Komplexe bietet, wurden untersucht.

Aufgrund der oftmals niedrigen Verfügbarkeit biomolekularer Proben ist die Empfindlichkeit der eingesetzten Untersuchungsmethode von großer Bedeutung. Die Empfindlichkeit von LILBID-MS wurde anhand einer wässrigen Pufferlösung eines 60-mer DNA Einzelstranges mit einer Konzentration von 9 nM gezeigt. Eine Serie abnehmender Tröpfchenzahl je Spektrum wurde aufgezeichnet. Dabei zeigte sich, dass bei Benutzung von nur drei Tröpfchen für ein Spektrum immer noch ein vernünftiges Signal/Rausch-Verhältnis erreicht werden konnte, was einer verbrauchten Stoffmenge von etwa $1,8{\cdot}10^{-18}$ Mol entspricht. Neben einer niedrigen Konzentration führen große Überschüsse an Salz oder Detergens in der Lösung ebenfalls zu einer verringerten Desorptionswahrscheinlichkeit und damit zu einer verschlechterten Signalintensität. Der Einfluss hoher Salzkonzentrationen wurde sowohl für das lösliche Protein HvoLsm anhand des nicht-flüchtigen Puffers Tris/HCl mit einer Salzkonzentration von 50 mM NaCl und für den Transkriptionsfaktor TAp63α anhand eines Kaliumphosphatpuffers mit 100 mM NaCl untersucht. Abgesehen von einer verringerten Signalintensität und Auflösung konnten in beiden Fällen vernünftige Massenspektren aufgenommen werden, wobei der hohe Salzüberschuss bei TAp63α eine höhere Tröpfchenzahl erforderte. Um den Einfluss von Detergentien auf die Signalintensität zu untersuchen, wurde mit dem Membranprotein Proteorhodopsin eine Konzentrationsreihe des Detergens DDM, von 0,05% bis 0,5%, aufgenommen. Die Signalintensität nahm mit zunehmender DDM-Konzentration ab, wobei die höchste Detergenskonzentration, mit der vernünftige Signale nachgewiesen werden konnten, bei

0,5% lag. Somit konnte gezeigt werden, dass LILBID-MS eine hinreichende Empfindlichkeit besitzt, um den Anforderungen anspruchsvoller Proben gerecht zu werden.

Die Proteine HvoLsm und TAp63α wurden ebenfalls dazu benutzt, um den Einfluss verschiedener Puffersysteme auf die quartäre Struktur zu untersuchen. Wenn nichtflüchtige Puffer mit hohen Salzkonzentrationen eingesetzt wurden, zeigten die Massenspektren die native Struktur des Heptamers für HvoLsm und des Dimers für TAp63α. Wenn die Proben jedoch in einen salzfreien Ammoniumazetat Puffer überführt wurden, zeigten die Massenspektren eine zum Teil erhebliche Aggregation der Proteine, die im Fall von HvoLsm zur Ausbildung von 20-meren und im Fall von TAp63α zur Ausbildung von Octameren führte. Es konnte also gezeigt werden, dass gepufferte, wässrige Lösungen nicht in jedem Fall eine ausreichend native Umgebung darstellen, und dass die entsprechende Puffersubstanz großen Einfluss auf die Struktur nehmen kann.

Mittels einer nativen Umgebung konnte gezeigt werden, dass der Transkriptionsfaktor TAp63α in seiner inaktiven Form als Dimer vorliegt, was mit weiteren Methoden überprüft wurde. Weiterhin konnte gezeigt werden, dass die Aktivierung von TAp63α zur Bildung von Tetrameren führt. Die Mechanismen der Inhibition und Aktivierung unterscheiden sich deutlich von denen des homologen p53. Somit trägt dieses Ergebnis dazu bei, das Verständnis dieses potentiellen Tumorsuppressors zu erweitern.

Eine besonders viel versprechende Klasse synthetischer Moleküle mit möglichen Anwendungen in der medizinischen Diagnose und Therapie sind Dendrimere. Diese hochgradig verzweigten, symmetrischen Polymere können in vielfältiger Weise modifiziert werden, um ihre Eigenschaften zu anzupassen. Eine Serie von Polypropylenimin-Dendrimeren mit unterschiedlichen Zuckersubstituenten wurde mit LILBID-MS charakterisiert. Dabei konnte gezeigt werden, dass die Oberflächenbedeckung eine polydisperse Massenverteilung aufweist, wobei der Bedeckungsgrad, mit Ausnahme der höheren Dendrimergenerationen, nahezu 100% beträgt. Um den potentiellen Einsatz in radioisotopischen Bildgebungsverfahren zu erkunden, wurde das Komplexierungsverhalten mit Cu(II) Ionen studiert. Hierbei ergab sich, dass die Cu(II)-Komplexierung mit zunehmender Dendrimergeneration zunahm und dass es zusätzlich eine geringfügige Abhängigkeit von der Art des Zuckersubstituenten gibt. Im Fall von Maltose-modifizierten Polypropylenamin-Dendrimeren zeigte sich eine ähnlich polydisperse Massenverteilung der Oberflächenbedeckung. Hier wurde zusätzlich der Einschluss des octahedralen Rheniumcluster $[Re_6S_8(OH)_6]^{4-}$ in das Dendrimergerüst und die Abgabe untersucht. LILBID-MS konnte zeigen, dass die Ladekapazität generationsabhängig ist mit vier bis fünf beziehungsweise fünf bis sechs Clustern für die vierte beziehungsweise fünfte Dendrimergeneration.

Darüber hinaus resultierte die Inkubation während der *in situ* Präparation in einer deutlich schlechteren Aufnahme. Der Einschluss der Rheniumcluster in den unterschiedlichen Dendrimeren war für mindestens eine Woche aufrechterhalten, was eindrucksvoll die Langzeitstabilität veranschaulicht. Dendrimere stellen einen interessanten Ansatz dar, Trägersysteme für die medizinische Anwendung zu entwickeln. Insbesondere von den hier vorgestellten Rheniumclustern ist bekannt, dass sie antivirale und antitumorale Eigenschaften besitzen.

Die Möglichkeit, spezifische Bindungen mit LILBID nachzuweisen, wurde im Speziellen an Wechselwirkungen zwischen DNA Einzelsträngen nachgewiesen, da diese immer noch eine bedeutende Herausforderung für die Massenspektrometrie darstellen. Für diesen Zweck wurden DNA Doppelstränge entworfen, die unterschiedlich lange, komplementäre Überhänge ("sticky ends") besitzen, an denen sich unterschiedliche DNA Leitern ausbilden können. In Abhängigkeit der Länge der "sticky ends" konnten verschiedene Leiter-Verteilungen beobachtet werden, deren Muster die unterschiedlichen Stabilitäten widerspiegeln. Die relativen Stabilitäten stimmen sehr gut mit theoretisch vorhergesagten Schmelztemperaturen überein. Die relativen Stabilitäten eines 16-mer DNA Doppelstranges in einer Serie von Puffern, die sich nur in der Art und der Konzentration des Salzes unterscheiden, stimmen ebenfalls sehr gut mit vorhergesagten Schmelztemperaturen überein. Darüber hinaus lässt sich die höchste Stabilität in dem Puffer, der Magnesiumchlorid enthält, nicht durch die Ionenstärke allein erklären und muss demnach ein spezifischer Effekt des Magnesiums sein. Zusätzlich konnte anhand eines kompetitiven Experimentes mit dem gut untersuchten Transkriptionsfaktor p50, einer DNA mit Bindestelle sowie einer DNA ohne Bindestelle, nur der Komplex bestehend aus p50 Homodimer und der DNA mit Bindestelle beobachtet werden. Sequenz spezifische Bindungen können also verlässlich mit LILBID nachgewiesen werden, sowohl innerhalb doppelsträngiger DNA als auch innerhalb DNA-Protein Komplexe. Des weiteren werden thermodynamische Verhältnisse aus der wässrigen Phase in den Massenspektren abgebildet. Sogar sehr große DNA wie das 2686 bp Plasmid pUC19 kann mit hoher Empfindlichkeit bei einer Konzentration von nur 80 nM nachgewiesen werden.

Ein effektiver Weg, den genomischen Code zu schützen ist RNA Interferenz (RNAi), die den Organismus zum Beispiel vor Virusinfektionen bewahrt. Der *Tomato aspermy virus* hat jedoch eine Möglichkeit entwickelt, diesen Verteidigungsmechanismus zu umgehen, indem er ein Protein exprimiert, welches RNAi unterdrückt. Mittels LILBID-MS konnte gezeigt werden, dass das TAV_2B Protein zusammen mit siRNA Komplexe mit einer 4:2 Stöchiometrie bildet. Zusätzlich konnte nachgewiesen werden, dass das Protein

erst durch die Bindung an RNA oligomerisiert und darüber hinaus die Konformation ändert. Die Struktur des Komplexes wurde bereits mit Röntgenkristallstrukturanalyse gefunden und entspricht der quartären Struktur in Lösung. Ein weiteres Beispiel, mit LILBID-MS Protein-RNA Komplexe aus nativer Umgebung zu untersuchen ist das Lsm Protein aus *Haloferax volcanii* (HvoLsm). Lsm Proteine sind in eine Vielzahl von RNA Stoffwechseln involviert und spielen demnach eine wichtige Rolle im RNA Haushalt. Über die Lsm Proteine der Archaeen ist noch wenig bekannt. Hier konnte gezeigt werden, dass das rekombiante HvoLsm in nativer Umgebung als Heptamer sowohl an sRNA als auch an poly(U)-RNA bindet, wobei es mit poly(U)-RNA auch zur Ausbildung ternärer Komplexe kam. Die Bedeutung der Bindung an poly(U)-RNA ist unklar, da solch eine RNA in *Haloferax volcanii* noch nicht nachgewiesen werden konnte. Aufgrund der hohen Anzahl an bis jetzt identifizierten möglichen Ziel-RNAs und Protein-Interaktions-Partner, ist dies nur der erste Schritt in der Charakterisierung von HvoLsm.

Die wohl wichtigste Eigenschaft von LILBID-MS ist die Möglichkeit, Membranproteine zu analysieren. Anhand der lichtgetriebenen Protonenpumpe Bakteriorhodpsosin und des Kaliumkanals KcsA wurden Kristallstrukturen mit quartären Strukturen in Lösung verglichen. Für Bakteriorhodpsosin konnte der physiologisch relevante Trimer in Lösung nachgewiesen werden. Bei hoher Laserleistung fragmentiert der Komplex in Monomere, wobei hier mindestens eines der nativen Lipide detektiert wurde. Es ist bekannt, dass der Tetramer die funktionelle Einheit des Kaliumkanals KcsA darstellt. Unter sanften Bedingungen konnte mit LILBID-MS der Tetramer in Lösung nachgewiesen werden. Die Fragmentation unter hoher Laserleistung offenbarte zwei unterschiedliche Fragmentverteilungen, vermutlich das Resultat einer unvollständigen Spaltung während der Präparation. Zusätzlich konnten zwei unterschiedliche Massen des Monomers beobachtet werden, die sich um etwa 400 Da unterscheiden und als mögliche post-translationale Modifikation interpretiert wurden. Somit konnte gezeigt werden, dass die quartäre Struktur der Kristallstruktur dieser beiden Membranproteine unter geeigneten Bedingungen auch in Lösung erhalten ist.

Für die lichtgetriebene Protonenpumpe Proteorhodopsin ist die Kristallstruktur noch nicht gelöst. 2D Kristalle jedoch zeigen in Abhängigkeit der Lipidstruktur ringförmige Hexamere oder eine Mischpopulation aus Penta- und Hexameren. Die mit LILBID-MS ermittelte Struktur zeigte in Lösung eine ausgeprägte Detergensabhängigkeit. In Triton-X 100 konnte keine ausgeprägte Struktur beobachtet werden. Stattdessen zeigte sich eine Verteilung von Mono- bis Hexameren mit stetig abnehmenden Signalintensitäten. In DDM hingegen bestand die bevorzugte Struktur aus Pentameren, deren

Anteil am Gesamtsignal mit zunehmender Detergenskonzentration zunahm. Dieselbe Detergensabhängigkeit konnte ebenfalls beobachtet werden, wenn das Protein ohne Signalpeptid kloniert wurde, was dessen Einfluss auf die Stöchiometrie ausschließt. Diese Ergebnisse zeigen, dass LILBID-MS eine geeignete Methode ist, den Zusammenhang zwischen Funktion und Struktur zu untersuchen.

Durch die Möglichkeit, lichtinduziert Zellen zu polarisieren, findet Channelrhodopsin-2, ein lichtgetriebener Ionenkanal selektiv für Kationen, eine breite Anwendung in Biotechnologien und Neurowissenschaften. Dessen ungeachtet ist die Stöchiometrie des funktionellen Kanals und des nativen, physiologisch relevanten Komplexes zur Zeit unbekannt. Mit LILBID-MS konnten Lösung ausschließlich dimere Komplexe in verschiedenen Puffer/Detergens Kombinationen nachgewiesen werden. Darüber hinaus zeigte der Dimer eine erhöhte Stabilität, da er nicht durch den Desorptionslaser fragmentiert werden konnte. Der Mangel an weiteren Erkenntnissen lässt keine eindeutigen Schlüsse zu. Dennoch konnte mit LILBID-MS ein möglicher Ansatz aufgezeigt werden.

Adenosin Triphosphat (ATP), die "Energiewährung" jeglicher Lebensform, wird von F_1F_o-ATP Synthase produziert. Dieser Nanomotor ist aus einem membranständigen (F_o) und einem löslichen Teil (F_1) aufgebaut, was die massenspektrometrische Analyse besonders erschwert, da diese großen Komplexe sehr instabil sind. Anhand der F_1F_o-ATP Synthase aus *Bacillus pseudofirmus* OF4 wurden neue Aspekte in der Charakterisierung dieser Komplexe mittels MS gefunden. So war es nach Dialyse in Ammoniumazetat Puffer nicht möglich, Signale des intakten Komplexes zu detektieren. Stattdessen wurden Ladungsverteilungen der isolierten Subkomplexe F_1 und F_o beobachtet. Unter hoher Laserleistung fragmentierten die Subkomplexe und sämtliche Untereinheiten des Gesamtkomplexes konnten beobachtet werden. Wenn jedoch der nichtflüchtige Puffer Tris/HCl mit MgCl_2 benutzt wurde, konnte die intakte ATP-Synthase nachgewiesen werden. Zusätzlich wurde gezeigt, dass Magnesium die Kopplung zwischen den Subkomplexen stabilisiert. Darüber hinaus wurde anhand der α und β Untereinheiten nachgewiesen, dass die relativen Signalintensitäten die Ladungszustände in Lösung bei einem gegeben pH gemäß dem isoelektrischen Punkt widerspiegeln.

Zusammengefasst stellt LILBID-MS eine viel versprechende, alternative Methode in der Massenspektrometrie dar, die neue Möglichkeiten bietet. Aufgrund des Einsatzes nativer Umgebungen bleiben natürliche Strukturen erhalten und werden als solche nachgewiesen. Thermodynamische Verhältnisse in der flüssigen Phase werden zumindest qualitativ im Massenspektrum abgebildet. Haupteinsatzgebiet dieser Methode sind Untersuchungen an großen Makrokomplexen, nichtkovalenten Wechselwirkungen und vor allem

an Membranproteinen.

Für die Zukunft geplant ist der Einsatz der LILBID Quelle an einem Q-TOF Instrument, um die Auflösung deutlich zu steigern. Diese Arbeit hat bereits begonnen und erste viel versprechende Ergebnisse geliefert. Des weiteren wird Tandem-MS zum Einsatz kommen, um Zugang zu verschiedenen Fragmentationswegen und Verteilungen zu bekommen. Um die strukturellen Informationen zu ergänzen, ist die Implementierung einer Gasphasen-Spektroskopie angedacht.

7 Contribution to the papers

Probing the limits of liquid droplet laser desorption mass spectrometry in the analysis of oligonucleotides and nucleic acids. LILBID measurements and analysis of the data were performed by me. The experiments were partly conceptualised by me and partly by the collaboration partners. I did the development of sample preparation protocols where necessary. The improvements of the setup to increase sensitivity were introduced by me.

ATP synthases: cellular nanomotors characerized by LILBID mass spectrometry. LILBID measurements and analysis of the data were performed by me. The experiments were designed by me as well as sample preparation with regard to the LILBID measurements.

Multiple Targets for Suppression of RNA Interference by Tomato Aspermy Virus Protein 2B. LILBID measurements and analysis of the data were performed by me. The experiments were designed by me as well as sample preparation with regard to the LILBID measurements.

The Archaeal Lsm Protein Binds To Small RNAs. LILBID measurements and analysis of the data were performed by me. The experiments were partly designed by me and partly by the collaboration partners. I did the development of sample preparation protocols with regard to the LILBID measurements.

Studying the stoichiometries of membrane proteins by mass spectrometry: microbial rhodopsins and a potassium ion channel. LILBID measurements and analysis of the data were performed by me. The experiments were conceptualised by me. I did the development of sample preparation protocols with regard to the LILBID measurements. I introduced more improvements to the spectrometer to further increase the sensitivity.

DNA damage in oocytes induces an irreversible switch of the quality control factor TAp63α from dimer to tetramer. LILBID measurements, analysis of the data and compassing the experiments were performed by me. Sample preparation with regard to the LILBID measurements was partly performed by me and partly by the collaboration partners.

Dense-shell glycodendrimers: UV/Vis and electron paramagnetic resonance study of metal ion complexation. LILBID measurements, analysis of the data and planing the experiments were performed by me. I did the development of sample preparation protocols with regard to the LILBID measurements where necessary.

Sugar-decorated dendritic nanocarriers: Encapsulation and release of the octahedral rhenium cluster complex $[Re_6S_8(OH)_6]^{4-}$. LILBID measurements, analysis of the data and compassing the experiments were performed by me. I did the development of sample preparation protocols with regard to the LILBID measurements where necessary.

Acknowledgements

Here I would like to thank those people without this thesis would not had been possible.

First of all I am highly indebted to **Prof. Bernd Brutschy** for giving me the opportunity to work on the exciting topic of LILBID-MS. The discerning supervision he provided was (and still is) a great pleasure as was the guidance and his advices.

I appreciate the help of **Dr. Hans-Dieter Barth** in countless technical and non-technical discussions and I am also grateful for the outstanding collaboration in method development.

In particular I am glad to thank the members of the mass spectrometry laboratory **Dr. Nina Morgner, Lucie Sokolova** and **Mihaela Cernescu** for fruitful discussions and in general for having a nice time.

I am obliged to **Mr. Martin Engels** for his exceeding support on the many electronic devices he made and to the workshop team under the administration of **Mr. Helmut Jäger** for their remarkable expertise and help in developing the experimental setup.

I like to thank all the collaboration partners for beeing longanimous with me and answering all my questions.

I am also thankful to **Mrs. Renate Gregori** for maintaining a red-tape operation and for her endless patience.

Many thanks to the present and former members of the group for their help, advices and an amicable working atmosphere (**Dr. Maksim Kunitski, Dr. Yevgeniy Nosenko, Dr. Fuat Altunsu, Michael Barashkov, Dr. Chayan Nandi** and **Peter Richter**).

Finally I acknowledge my wife **Olga** and my daughter **Lena** for their love, encouragement and support during these years.

Curriculum Vitae

Personal

Name:	Jan Hoffmann
Address:	Schwarzerlenweg 90 65933 Frankfurt am Main Germany
Telephone:	+49(0)69-798-29434
Email:	Hoffmann@chemie.uni-frankfurt.de
Date of Birth:	1st March 1976
Place of Birth:	Hannover, Germany

Education

Dec. 2006 – Dec. 2010	PhD at Institute of Physical and Theoretical Chemistry; Goethe University Frankfurt Title: *Mass spectrometry investigations on biomolecular macrocomplexes in native solutions: New insights with LILBID-MS* Scientific Supervisor: Prof. B. Brutschy
Oct. 2006	Dipl. Thesis at Institute of Biophysics; Goethe University Frankfurt Title: *Lichtinduzierte FTIR differenzspektroskopische Untersuchungen an der NADH:Ubichinon-Oxidoreduktase aus E.coli: Kopplung zwischen Elektronen- und Protonentransfer* Scientific Supervisor: Prof. P. Hellwig
Apr. 2001 – Oct. 2006	Department of Physics

Publications

"*DNA damage in oocytes induces an irreversible switch of the quality control factor TAp63α from dimer to tetramer* "
G.B. Deutsch, E.M. Zielonka, D. Coutandin, T.A. Weber, B. Schäfer, J. Hannewald, L.M. Luh, F.G. Durst, M. Ibrahim, J. Hoffmann, F.H. Niesen, A. Sentürk, H. Kunkel, B. Brutschy, E. Schleiff, S. Knapp, A. Acker-Palmer, M. Grez, F. McKeon and V. Dötsch
Cell, currently in revision.

"*ATP synthases: cellular nanomotors characterized by LILBID mass spectrometry*"
J. Hoffmann, L. Sokolova, L. Preiss, D.B. Hicks, T.A. Krulwich, N. Morgner, I. Wittig, H. Schägger, T. Meier and B. Brutschy
Physical Chemistry Chemical Physics, 2010, 12(41): p. 13375-82.

"*The archaeal Lsm protein binds to small RNAs*"
S. Fischer, J. Benz, B. Spath, LK. Maier, J. Straub, M. Granzow, M. Raabe, H. Urlaub, J. Hoffmann, B. Brutschy , T. Allers, J. Soppa and A. Marchfelder
Journal of Biological Chemistry, 2010, 285(45): p. 34429-38.

"*Studying the stoichiometries of membrane proteins by mass spectrometry: microbial rhodopsins and a potassium ion channel*"
J. Hoffmann, L. Aslimovska, C. Bamann, C. Glaubitz, E. Bamberg and B. Brutschy
Physical Chemistry Chemical Physics, 2010, 12(14): p. 3480-85.

"*Sugar-Decorated Dendritic Nanocarriers: Encapsulation and Release of the Octahedral Rhenium Cluster Complex* $[Re_6S_8(OH)_6]^{4-}$"
M. Kubeil, H. Stephan, HJ. Pietzsch, G. Geipel, D. Appelhans, B. Voit, J. Hoffmann, B. Brutschy, Y.V. Mironov, K.A. Brylev, V.E. Fedorov
Chemistry – An Asian Journal, 2010, DOI:10.1002/asia.201000284

"*Dense-shell glycodendrimers: UV/Vis and electron paramagnetic resonance study of metal ion complexation*"
D. Appelhans, U. Oertel, R. Mazzeo, H. Komber, J. Hoffmann, S. Weidner, B. Brutschy , B. Voit and M.F. Ottaviani
Proceedings of the Royal Society A – Mathematical, Physical and Engineering Sciences, 2010, 466(2117): p. 1489 -1513.

"*Probing the limits of liquid droplet laser desorption mass spectrometry in the analysis of oligonucleotides and nucleic acids*"
J. Hoffmann, T.L. Schmidt, A. Heckel and B. Brutschy
Rapid Communications in Mass Spectrometry, 2009, 23(14): p. 2176-2180.

"*Multiple Targets for Suppression of RNA Interference by Tomato Aspermy Virus Protein 2B*"
U.J. Rashid, J. Hoffmann, B. Brutschy, J. Piehler and J.C. Chen
Biochemistry, 2008, 47(48): p. 12655-12657.

"*LILBID-mass spectrometry applied to the mass analysis of RNA polymerase II and an F1Fo-ATP synthase*"
N. Morgner, J. Hoffmann, HD. Barth, T. Meier and B. Brutschy
International Journal of Mass Spectrometry, 2008, 277(1-3): p. 309-313.

Talks

PTC seminar
Frankfurt am Main, 21 June 2010

109. Bunsentagung
Bielefeld, 13-15 May 2010

107. Bunsentagung
Saarbrücken, 1-3 May 2008

Posters

42. DGMS-Tagung
Konstanz, 8-11 March 2009

International Bunsen Discussion Meeting
Leipzig, 27-30 September 2009

Publications on which this thesis is based

paper 1 *The Archaeal Lsm Protein Binds To Small RNAs*

paper 2 *DNA damage in oocytes induces an irreversible switch of the quality control factor TAp63α from dimer to tetramer*

paper 3 *Dense-shell glycodendrimers: UV/Vis and electron paramagnetic resonance study of metal ion complexation*

paper 4 *Sugar-decorated dendritic nanocarriers: Encapsulation and release of the octahedral rhenium cluster complex* $[Re_6S_8(OH)_6]^{4-}$

paper 5 *Probing the limits of liquid droplet laser desorption mass spectrometry in the analysis of oligonucleotides and nucleic acids*

paper 6 *Multiple Targets for Suppression of RNA Interference by Tomato Aspermy Virus Protein 2B*

paper 7 *Studying the stoichiometries of membrane proteins by mass spectrometry: microbial rhodopsins and a potassium ion channel*

paper 8 *ATP synthases: cellular nanomotors characerized by LILBID mass spectrometry*

THE JOURNAL OF BIOLOGICAL CHEMISTRY VOL. 285, NO. 45, pp. 34429–34438, November 5, 2010

The Archaeal Lsm Protein Binds to Small RNAs*[S]

Received for publication, March 1, 2010, and in revised form, July 18, 2010 Published, JBC Papers in Press, September 7, 2010, DOI 10.1074/jbc.M110.118950

Susan Fischer[‡], Juliane Benz[‡], Bettina Späth[‡], Lisa-Katharina Maier[‡], Julia Straub[§], Michaela Granzow[§], Monika Raabe[¶], Henning Urlaub[¶], Jan Hoffmann[‖], Bernd Brutschy[‖], Thorsten Allers[**], Jörg Soppa[§], and Anita Marchfelder[‡1]

*From [‡]Biology II, Ulm University, 89069 Ulm, Germany, the [§]Institute of Molecular Biosciences, Goethe-University, 60438 Frankfurt, Germany, the [¶]Max-Planck-Institute for Biophysical Chemistry, Bioanalytical Mass Spectrometry Group, 37077 Göttingen, Germany, the [‖]Institute of Physical and Theoretical Chemistry, Goethe-University, 60438 Frankfurt, Germany, and the **Institute of Genetics, University of Nottingham, Queen's Medical Centre, Nottingham NG7 2UH, United Kingdom*

Proteins of the Lsm family, including eukaryotic Sm proteins and bacterial Hfq, are key players in RNA metabolism. Little is known about the archaeal homologues of these proteins. Therefore, we characterized the Lsm protein from the haloarchaeon *Haloferax volcanii* using *in vitro* and *in vivo* approaches. *H. volcanii* encodes a single Lsm protein, which belongs to the Lsm1 subfamily. The *lsm* gene is co-transcribed and overlaps with the gene for the ribosomal protein L37e. Northern blot analysis shows that the *lsm* gene is differentially transcribed. The Lsm protein forms homoheptameric complexes and has a copy number of 4000 molecules/cell. *In vitro* analyses using electrophoretic mobility shift assays and ultrasoft mass spectrometry (laser-induced liquid bead ion desorption) showed a complex formation of the recombinant Lsm protein with oligo(U)-RNA, tRNAs, and an small RNA. Co-immunoprecipitation with a FLAG-tagged Lsm protein produced *in vivo* confirmed that the protein binds to small RNAs. Furthermore, the co-immunoprecipitation revealed several protein interaction partners, suggesting its involvement in different cellular pathways. The deletion of the *lsm* gene is viable, resulting in a pleiotropic phenotype, indicating that the haloarchaeal Lsm is involved in many cellular processes, which is in congruence with the number of protein interaction partners.

Sm and Sm-like (Lsm) proteins constitute a large family of proteins known to be involved in RNA metabolism. Representatives of this family are found in all three domains: bacteria, archaea, and eukarya. All of them share a common bipartite sequence motif, known as the Sm domain, consisting of two conserved segments separated by a region of variable length and sequence. The bacterial family member is the Hfq protein (1, 2), which has a plethora of functions (3). Hfq is a highly conserved protein encoded within many bacterial genomes (4). Although the protein does not show a high similarity to the Lsm proteins on the primary structure level, it possesses striking similarities in both function and tertiary and quaternary structure to the eukaryotic Lsm proteins (3, 5). Hfq monomers assemble to form highly stable hexamers (6), which bind preferentially to A/U-rich sequences (7, 8) but have a relaxed RNA binding specificity and participate in many stages of RNA metabolism. It was therefore proposed that Hfq is an ancient, less specialized form of the Lsm proteins (9). One of the identified functions of Hfq is its interaction with sRNAs (10). It has been proposed that the protein acts as an RNA chaperone that might simultaneously recognize the sRNA and its target and facilitate its interaction. An *Escherichia coli hfq* insertion mutant showed pleiotropic phenotypes including decreased growth rates and yields, increased cell sizes, and an increased sensitivity to stress conditions (11–13). These defects are at least in part a reflection of the fact that Hfq is required for the function of several sRNAs including DsrA, RprA, Spot42, OxyS, and RhyB (14–17).

Eukaryotes have the most diverse members of the Sm/Lsm protein family. They contain at least 18 different Sm and Lsm proteins involved in mRNA splicing, histone maturation, telomere maintenance, and mRNA degradation that form at least six different heteroheptameric complexes (18). The Lsm proteins alone form at least two heteroheptameric complexes: the nuclear Lsm2-8, a large fraction of which associates with U6 snRNA,[2] and the cytoplasmic Lsm1-7, which functions in mRNA degradation (19, 20). The Lsm proteins that associate with U6 snRNA are necessary for its stability (21–23), binding to the U-rich region at the 3′ end of the U6 snRNA. Additional functions of the nuclear Lsm proteins are the involvement in processing pre-snoRNA, pre-rRNA, pre-tRNA precursor, and nuclear pre-mRNA decay (5).

The fact that Lsm proteins have been found in archaea (22–25) suggests that they were present in a common ancestor shared by archaea and eukarya. This correlates with the observation that several eukaryotic proteins clearly evolved from archaea-related precursors (26) and that snoRNAs have also been found in archaea (27). Some archaea, such as the *Pyrococcus* species and halophilic archaea, encode only one Lsm protein (Lsm1), whereas others encode two (Lsm1 and Lsm2) (23). The Lsm1 and Lsm2 proteins have been shown to be associated *in vivo* (28), so they might also form heteromeric complexes. Crenarchaeota have an additional Lsm protein, Lsm3, which

* This work was supported by the Deutsche Forschungsgemeinschaft through SPP 1258 Priority Program "Sensory and Regulatory RNAs in Prokaryotes" Grants DFG Ma1538/11-1 and So264/14-1.

[S] The on-line version of this article (available at http://www.jbc.org) contains supplemental Tables S1–S3 and Figs. S1–S6.

[1] To whom correspondence should be addressed. E-mail: anita.marchfelder@uni-ulm.de.

[2] The abbreviations used are: snRNA, small nuclear RNA; snoRNA, small nucleolar RNA; LILBID, laser-induced liquid bead ion desorption; sRNA, small RNA.

contains a traditional Sm domain fused to a second domain by a flexible linker (29, 30).

The archaeal Lsm1 proteins have been shown to form heptamers (28, 31–33) and bind RNA (18, 28, 31). The Lsm2 protein from *Archaeoglobus fulgidus* has been reported to form a hexameric (34) or a heptameric (31) complex. The Lsm3 protein has also been shown to form 14-mer complexes (30), a process of which some of the Lsm1 proteins are also capable (35).

Interestingly, *Methanocaldococcus jannaschii* lacks a classical Lsm gene (9, 36) but contains an Hfq-like protein. Although some data have been acquired on the structure and RNA binding characteristics of the archaeal Lsm protein, so far the function and interaction partners of the Lsm protein in archaea have not been revealed.

Here, we analyze the Lsm protein from the halophilic archaeon *Haloferax volcanii*. *H. volcanii* encodes only one Lsm protein, which makes it easier to employ genetic methods for analyzing the biological function of the archaeal Lsm proteins. Recently, it has been shown that *H. volcanii* also has an sRNA population potentially involved in gene expression regulation (37, 38). To investigate whether the *Haloferax* Lsm is involved in sRNA regulation and to clarify its biological function, we generated a deletion strain for Lsm and analyzed the *in vivo* and *in vitro* function of this protein.

EXPERIMENTAL PROCEDURES

Strains and Culture Conditions—*H. volcanii* strains H119 (Δ*pyrE2*, Δ*trpA*, Δ*leuB*) (39) and Δ*lsm* (Δ*pyrE2*, Δ*trpA*, Δ*leuB*, Δ*lsm*) were grown aerobically at 45 °C in Hv-YPC or Hv-Ca medium (39). The term "normal growth conditions" for *H. volcanii* used here stands for aerobic growth at 45 °C and 2.1 M NaCl.

Generation of the pTA927 Vector—To generate pTA927, a 131-bp KpnI fragment containing the terminator sequence of the *H. volcanii* L11e rRNA gene (40) was inserted at the KpnI site of pTA230 (39). Next, a 224-bp region of the *tnaA* promoter (41) was amplified by PCR and inserted at the ApaI and ClaI sites; the reverse primer incorporated a novel NdeI site (at the ATG start codon) for cloning the regulatable gene. Finally, a synthetic transcription terminator sequence (5′-GGCCGCACCTCTGGACCATCGCATTTTTCGGCGCG-3′) was inserted downstream between the NotI and BstXI sites. The sequence of pTA927 is available upon request.

Isolation and Analysis of RNA—Total RNA was isolated according to Chomczynski and Sacchi (42). For Northern blot analysis the aliquots were separated on formaldehyde-containing agarose gels, transferred to nylon membranes by downward capillary blotting, and UV cross-linked. Digoxigenin-labeled DNA probes were synthesized as described (43). Digoxigenin-dUTP was purchased from Roche Applied Science. After hybridization using standard stringency conditions (50% formamide, 50 °C), the membrane was washed successively in 2× SSC, 0.1% SDS at room temperature and 1× SSC, 0.1% SDS at 50 °C. Detection of digoxigenin-labeled probes was performed as described (44).

For the analysis of 5′ and 3′ ends of the *lsm* transcript, the circularized RNA RT-PCR approach was used (45). First, total RNA was circularized with RNA ligase. Then a gene-specific cDNA was generated using a primer specific for the *lsm* ORF. The DNA was amplified by a PCR and a subsequent nested PCR using four primers specific for the ORFs of the *lsm* and the *l37e* genes. The PCR product was purified and sequenced, and the comparison of the sequence with the *H. volcanii* genome allowed the identification of the 5′ and 3′ ends of the transcript.

Production of the Haloferax Lsm Protein in E. coli and Generation of Antibodies—The *lsm* gene sequence was taken from HaloLex (46). Chromosomal DNA from *H. volcanii* was isolated using the alternative rapid chromosomal isolation method as published in the Halohandbook (75). The reading frame of the Lsm protein was amplified from *Haloferax* genomic DNA using primers Sm1 (primer sequences are available upon request) and Sm2, which contained the restriction sites NcoI and NotI, respectively. The resulting PCR product was digested with NcoI and NotI and cloned into the vector pET29a (Novagen), which was previously digested with the same restriction enzymes, yielding the plasmid pET29a-Sm. pET29a-Sm was transformed into Bl21-AI (Novagen), and the Lsm protein was expressed and purified according to the manufacturer's protocol using S-protein-agarose (Novagen). For the production of antibodies, 0.5 mg of purified protein were sent to Davids Biotechnology (Regensburg, Germany).

Western Blot Analysis and Determination of Lsm Copy Number—For Western blot analysis cytoplasmic extracts of *H. volcanii* (20 μg) were separated by SDS-PAGE and transferred to a nylon membrane by semi-dry blotting (1.5 h with 2 mA/cm^2). The membrane was blocked using skimmed milk powder, incubated with the newly generated antiserum (see above) or the preimmune serum at dilutions of 1:500, washed, and incubated with the secondary, peroxidase-conjugated goat anti-rabbit antibody. Peroxidase activity was detected with the chemiluminescence substrates luminol and *para*-hydroxycoumaric acid. Light emission was detected with films. The generated antiserum reacted with several bands, all but one of which also reacted with the preimmune serum. The specific band had the expected size of ~9 kDa.

For the quantification of the Lsm copy number, cytoplasmic extracts were prepared of 2.3×10^8 *H. volcanii* cells. They were used for Western blot analysis alongside with 1–50-ng aliquots of purified Lsm protein. The film was scanned, and the signals were quantified using ImageJ. The aliquots of the purified Lsm protein were used to generate a standard curve, which was used to quantify the Lsm amount in cell extracts. The value was used to calculate the Lsm molecules/cell using a molecular mass of 8.25 kDa.

Substrate Preparation and Binding of the Recombinant Protein to RNA—Substrates for the electrophoretic mobility shift assays were prepared as follows. U_{15}- and U_{30}-RNA oligonucleotides were generated by Sigma. Wheat tRNA (tRNA isolated from wheat germ, type V; Sigma) and oligo(U)-RNA were labeled at the 3′ end using [α-^{32}P]pCp as described (47). EMSAs were carried out as described (48) with the following modifications: 100 ng of recombinant Lsm protein was used if not indicated otherwise. For the determination of the dissociation constant of Lsm/oligo(U)-RNA (K_D), 0.1 pmol (0.6 ng) of U_{15}-RNA were incubated with increasing amounts of Lsm protein

(0.012–24 pmol, equating 0.1–200 ng). If all of the proteins are present as homoheptameric complexes, 0.1–200 ng of protein would equate to 1.7 fmol–3.4 pmol of Lsm complexes.

Laser-induced Liquid Bead Ion Desorption-MS—LILBID is a novel mass spectrometry method that allows an exact mass determination of single macromolecules dissolved in droplets of solution containing an adequate buffer, pH, ion strength, etc., as described previously (49). Briefly, droplets of solution of analyte are ejected by a piezo-driven droplet generator and transferred into a high vacuum. There, they are irradiated droplet by droplet (d = 50 μm, V = 65 pl, 10 Hz) by a pulsed IR laser tuned to the stretching vibration of water at 2.9 μm. By laser ablation the droplets explode, ejecting preformed biomolecular ions into the vacuum. The total volume of solution required for the mass determination is only few microliters in typically micromolar concentration. The method is ideal for studying biomolecules of low availability (49). The amount of energy transferred into noncovalent complexes by the IR desorption/ablation process can be controlled in a wide range, starting from ultrasoft to harsh conditions, just by varying the laser intensity (50). At ultrasoft conditions large macromolecules can be detected in their native stoichiometry. The complexes are detected in different charged states, preferentially as anions. The number of charge states observed increases with the size of the molecules but is less than those observed in electro spray ionization and considerably more than in MALDI. To investigate the quaternary structure of the Lsm protein, we dialyzed the recombinant protein against a buffer (50 mM NaCl, 10 mM of Tris/HCl, pH 7.5). Complexes were analyzed using LILBID-MS. To analyze the binding of Lsm proteins to oligo(U)-RNA, 8 μM oligo(U)-RNA (U_{30}) were incubated at room temperature for 30 min with 4 μM of heptameric Lsm complexes in a buffer containing 20 mM NaCl, 2 mM $MgCl_2$, and 10 mM Tris/HCl, pH 7.5. The resulting complexes were analyzed using LILBID-MS. To investigate the binding to sRNAs, 4 μM of Lsm heptamers were incubated with 8 μM of $sRNA_{30}$ at room temperature for 30 min. Again the resulting complexes were analyzed using LILBID-MS.

Generation of the lsm Deletion Strain—The *lsm* reading frame was completely removed in the *H. volcanii* strain H119 using the pop-in/pop-out method (39, 51). The upstream and downstream regions of the *lsm* gene were amplified by PCR using chromosomal DNA from *H. volcanii* and primers SmKO/FLAG1, SmKO3, SmKO/FLAG2, and SmKO4, respectively, yielding fragments Sm1 and Sm2, both ~1 kb long. PCR primers contained different restriction sites: ApaI (SmKO/FLAG1), EcoRV (SmKO3), EcoRV (SmKO/FLAG2), and XbaI (SmKO4). Both PCR fragments were first cloned into pBluescriptII (Stratagene), yielding plasmids pblue-Sm1 and pblue-Sm2 and subsequently subcloned into the integrative vector pTA131 containing the *pyrE2* marker (39), yielding pTA131-Sm1/2. This plasmid was integrated into the chromosomal DNA of *H. volcanii* (strain H119, pop-in). The plasmid containing the *pyrE2* marker was forced out by plating the cells on 5-fluoro-orotic acid (pop-out). Southern blot analysis was carried out as described in Ref. 52 with the following modifications. Chromosomal DNA was isolated from wild type and knock-out strains and digested using XhoI. 10 μg of digested DNA was separated on a 0.8% agarose gel and transferred to a nylon membrane (Hybond^{TM}-N; GE Healthcare). Hybridization probe Sm1 was generated by PCR using primers SmKO/FLAG1 and SmKO3 on template pblue-Sm1, yielding a 1-kb fragment, which was subsequently radioactively labeled using the random prime kit Readiprime^{TM} II (GE Healthcare).

Co-immunoprecipitation—To isolate an S100 extract, the cells were grown to stationary phase in Hv-Ca^+ broth including 0.25 mM tryptophane and harvested at OD_{650} = 2.8. The cells were pelleted, and the resulting pellets were washed with enriched PBS (2.5 M NaCl, 150 mM $MgCl_2$, 1× PBS (137 mM NaCl, 2.7 mM KCl, 10 mM Na_2PO_4, 2 mM $KHPO_4$, pH 7.4)). The cells were again pelleted, resuspended in enriched PBS containing 1% formaldehyde, and incubated for 20 min at 45 °C. To stop the cross-linking reaction, glycine was added to a final concentration of 0.25 M and incubated for 5 min at 45 °C. The cells were washed twice with enriched PBS at 4 °C, and then lysis buffer (50 mM Tris, pH 7.4, 1 mM EDTA, 10 mM $MgCl_2$, 1 mM $CaCl_2$) containing 150 μl of proteinase inhibitor (Sigma) was added. After ultracentrifugation (100,000 × g for 30 min) RNase A was added to a final concentration of 400 μg/ml extract, and the mixture was incubated for 30 min at 37 °C. Subsequently, NaCl was added to a final concentration of 150 mM, and the lysate was frozen at −80 °C. For affinity purification, 1.6 ml of anti-FLAG M2 affinity gel (Sigma) was washed 10 times with 10 ml of ice-cold washing buffer (50 mM Tris/HCl, pH 7.4, 150 mM NaCl) before the lysate was added. After incubation overnight (14–16 h) at 4 °C, anti-FLAG M2 affinity gel was washed eight times with 10 ml of ice-cold washing buffer. The elution of the FLAG fusion protein was performed by using 4 ml of washing buffer, to which 3× FLAG peptide was added (final concentration, 150 ng/μl). The samples were incubated at 4 °C with gentle shaking. In a final elution step the affinity gel was rinsed with 2 ml of washing buffer. For the isolation of co-precipitated RNA, the cross-link reaction was released by incubating the samples at 95 °C for 20 min. The fraction was treated with 20 μg of proteinase K for 30 min at 37 °C in 100 μl of buffer (100 mM Tris/HCl, pH 7.5, 12.5 mM EDTA, 150 mM NaCl, 0.2% SDS). The solution was extracted with phenol-chloroform-isoamylalcohol. The aqueous phase containing RNA was precipitated, and the resulting pellet was dissolved in water. An aliquot of the RNA fraction was 3′-labeled with [α-^{32}P]pCp as described (53).

Mass Spectrometry—For mass spectrometric analysis proteins associated with the FLAG only, the FLAG-Lsm (without cross-link), and the FLAG-Lsm (with cross-link) proteins were dissolved in 1× loading buffer, and cross-linked samples were incubated for 20 min at 95 °C. The samples were then loaded onto a 4–12% NuPAGE-Gel (Invitrogen). After Coomassie staining, the gel lanes were cut into 23 slices, and the proteins were in-gel digested with trypsin according to Ref. 54. Extracted peptides were analyzed by LC-MS/MS on a Q-ToF instrument (Waters) under standard conditions. Peptide fragment spectra were searched against a target decoy database for *H. volcanii* (46) using MASCOT as a search engine. Peptides with a peptide score lower than 25 were omitted from the results. Scaffold software (Proteome Software, Inc., Portland, OR) was used for

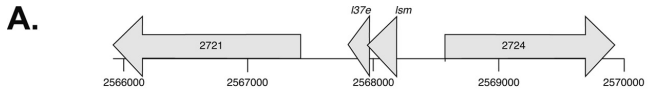

B.

```
ATGAGCGGCCGACCCCTCGACGTCCTCGAAGCGTCACTCGACGAGCCGGTGACGGTTCTCCTCAAGGACGGAAA   lsm
CGCGTACTTCGGCGTCCTCGCTGGTTACGACCAGCACATGAACGTCGTACTCGAAGAAGCGCTGGACGAAGACA
CCGTGCCCGGGGATATCGAACTCGAGCAAGTCCAAGACACAACCATTATACGCGGCGATAACGTCGTCACCATC
AAAGCATGACGGGTGCAGGAACCCCCAGCCAAGGAAAGAAGAACAAGACGACGCACGTCAAGTGCCGTCGCTGC   l37e
GGCGAGAAGTCCTACCACGTGAAGAAGAAGGTCTGCTCGTCTTGCGGCTTCGGTAAGTCGAAGAAGCGTCGGAG
CTACGCCTGGCAGTCGAAGTCCGGCGACAACTAA
```

FIGURE 1. **Genomic location of the Lsm protein gene.** *A*, the operon containing the genes for Lsm and L37e is bordered by the gene for a potential hydrolase (HVO_2724) and the gene for an amidophosphoribosyltransferase (HVO_2721). The genomic region is given below in nucleotides. *B*, the reading frames for the Lsm protein (shown in *light gray*) and the ribosomal protein L37e (shown in *dark gray*) overlap by 4 nt (shown in *bold type*).

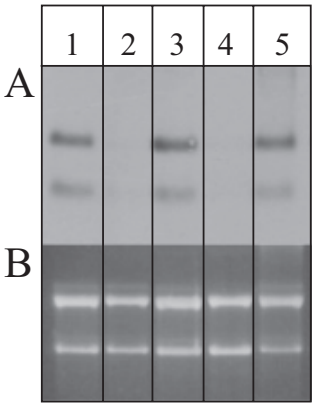

FIGURE 2. **Differential expression of the *lsm* gene.** *A*, the transcript levels of the *lsm* gene in cells grown under different conditions were determined by Northern blot analysis. *B*, the corresponding agarose gel shows that all of the lanes were loaded with the same amount of RNA. The following conditions were applied: aerobic growth in 2.1 M NaCl at 42 °C (*lane 1*), at 30 °C (*lane 2*), and at 48 °C (*lane 3*); anaerobic, nitrate-respirative growth (*lane 4*); and 1.5 M NaCl (*lane 5*).

data evaluation (see supplemental tables). The proteins that were co-purified with the FLAG peptide in the control reaction were subtracted from the proteins co-purified with the FLAG-Lsm protein. In Table 1 only proteins, which were present in all three FLAG-Lsm purifications with at least four MS/MS spectra in each of the three independent isolations are listed. The complete list of identified proteins is shown in supplemental Table S3.

DNA Microarray Analysis—The affinity-purified FLAG-tagged Lsm complexes and a negative control (FLAG peptide not tagged to Lsm) were used for RNA isolation as described (see "Co-immunoprecipitation" above). 1-μg aliquots of the two fractions were used for cDNA synthesis, labeling, and DNA microarray analysis as described, using a self-constructed DNA microarray for *H. volcanii* (55). sRNA-specific oligonucleotide probes were added to the DNA microarray to allow the analysis of sRNA gene expression.[3] Three independent experiments were performed, including a dye swap. The analysis of DNA microarray results was performed as described (55).

RESULTS AND DISCUSSION

Little is known about the archaeal Lsm proteins and therefore we were interested in unraveling the function of the archaeal Lsm protein using *in vitro* and *in vivo* approaches.

The Lsm Reading Frame Overlaps with the Reading Frame for a Ribosomal Protein—Using a BLAST search (56) with previously described archaeal Lsm proteins (23), we identified the Lsm protein gene in the genome of *H. volcanii* (46). *H. volcanii* contains a single *lsm* gene (HVO_2723), which encodes a protein of 76 amino acids with a molecular mass of 8.25 kDa and an pI of 3.9. The *Haloferax* Lsm protein was found to belong to the Lsm1 subfamily of Lsm proteins. The *lsm* gene overlaps by four nucleotides with a gene annotated to encode the L37e ribosomal protein (HVO_2722; Fig. 1). To analyze the conservation of gene order and Lsm protein sequence in the domain archaea, a BLAST search was used to identify similar proteins and their genes. The gene order is highly conserved in archaea. In more than 40 archaeal genomes, the gene for the L37e proteins follows the *lsm* gene. In more than 30 genomes, the two genes are very closely spaced or overlap, so that co-transcription can be assumed. The multiple sequence alignment of the *H. volcanii* Lsm1 and 31 other archaeal Lsm1 proteins (supplemental Fig. S1*A*) shows that the protein is highly conserved in archaea with the exception of the regions corresponding to β-sheets 2 and 3 in the structure of the *P. abyssi* Lsm (18), which is variable in the whole family and especially in the six haloarchaeal Lsm proteins. It should be noted that the three residues that form a highly specific binding pocket for uridine in the *P. abyssi* Lsm are universally conserved, indicating specific uridine binding in all of the archaeal Lsm1 proteins.

Expression of the lsm Gene and Determination of Lsm Copy Number—Northern blot analyses were used as a first approach to analyze the expression of the *lsm* gene. Using a probe against the two overlapping genes, two transcripts of ~430 and ~210 nt, respectively, could be detected (Fig. 2). Gene-specific probes revealed that the smaller transcript was derived from the gene for the L37e protein, which can either be a primary transcript initiated from a promoter localized within the open reading frame of the upstream located *lsm* gene or originate from the processing of the bicistronic transcript. According to the genome sequence, a bicistronic transcript should be 404 nt, and a transcript encoding only L37e should be 177 nt. Using circularized RNA RT-PCR (45, 57), we determined that the bicistronic transcript is leaderless and contains a 3′-UTR of 41 nt, in excellent agreement with the Northern blot results (data not shown).

To observe a potential differential regulation of transcription, Northern blot analyses were performed using RNA from cells cultivated under different conditions. During aerobic growth, the transcript levels did not change throughout the

[3] J. Straub, C. Lange, and J. Soppa, unpublished data.

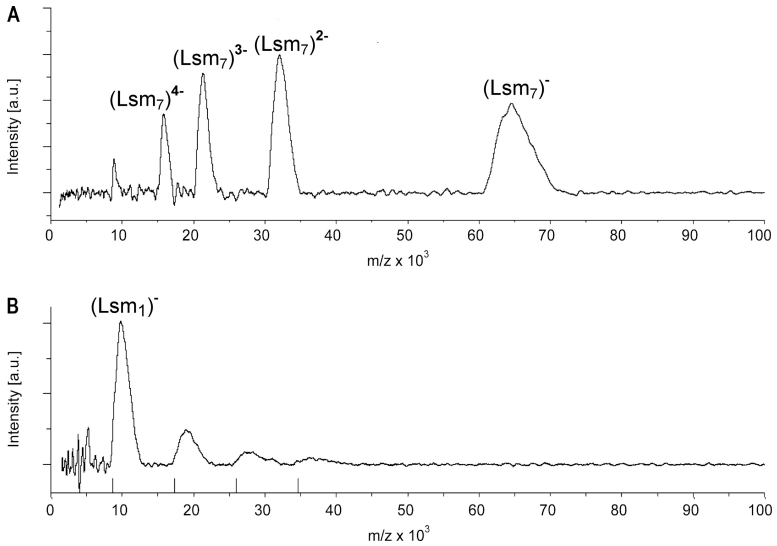

FIGURE 3. **The Lsm protein forms homoheptameric complexes.** *A*, in soft mode native mass spectrometry clearly shows that the *Haloferax* Lsm protein forms heptameric complexes. Depicted are the charge states of the heptamer. *B*, under harsh conditions the heptamer completely dissociates into fragments mostly into the monomer. Markers on the *x* axis indicate the masses of Lsm monomers, dimers, trimers, and tetramers (for $z = 1$).

growth curve, from early exponential to stationary phase (data not shown). It was also identical during growth at low salt (1.5 M NaCl; Fig. 2), high salt (3 M NaCl, data not shown), and high temperature (48 °C; Fig. 2). By contrast, both the bicistronic and the monocistronic transcript were undetectable in the cultures grown at a low temperature (30 °C; Fig. 2) or via nitrate-respirative growth (Fig. 2). Taken together, both transcripts were apparently co-regulated and are present in *H. volcanii* under most but not all conditions.

For the analysis of the Lsm protein, we expressed the *lsm* gene in *E. coli* to produce a recombinant protein. The gene was efficiently expressed to yield a pure fraction of recombinant Lsm protein (supplemental Fig. S3), against which an antiserum was generated. Western blot analysis was used for the relative quantification of the protein levels in cytoplasmic extracts from cells grown at different salt concentrations (1.2, 2.5, and 3 M) either to the exponential or stationary phase. In each case, the Lsm protein levels were identical; thus, we found no indication for translational regulation (data not shown). For the absolute quantification of the intracellular protein level, a standard curve was generated using heterologously produced and purified Lsm protein (see below), revealing that *H. volcanii* contains ~4,000 Lsm molecules/cell (supplemental Fig. S2). By contrast, 50,000–60,000 copies of Hfq are present in rapidly growing *E. coli* cells in the exponential phase, but the level is rapidly down-regulated to ~20,000 copies/cell at the onset of the stationary phase (3, 58). We found no reports about intracellular copy numbers of additional Lsm proteins, neither in prokaryotes nor in eukaryotes.

The Recombinant Lsm Protein Forms Homoheptamers—To investigate whether the *Haloferax* Lsm protein forms homomeric complexes, we employed ultrasoft mass spectrometry (LILBID-MS) (see "Experimental Procedures" for details) (49). This approach revealed that the protein forms homoheptamers *in vitro* (Fig. 3*A* and data not shown). Under harsh conditions (high laser intensity), the complex could be fragmented and masses corresponding to Lsm monomers, dimers, trimers, and tetramers were observed (Fig. 3*B*). Other archaeal Lsm1-type proteins also form homoheptamers (28, 31–33), in contrast to proteins of the Hfq and Lsm2 subfamilies, which form exclusively homohexamers (Hfq) or have the potential to form homohexamers (Lsm2) (6, 36). The eukaryotic Lsm proteins have been shown to form heteroheptamers (28, 31–33). Therefore, as for other archaeal proteins involved in transcription, replication, or translation, the archaeal Lsm proteins can be regarded as a closer mimic and simpler model for the eukaryotic proteins, which have added further complexity during evolution. Thus, the archaeal Lsm proteins are much better models for the eukaryotic proteins than the bacterial Hfq protein (5).

Characterization of Lsm-RNA Interactions in Vitro—To analyze whether the recombinant Lsm protein binds RNA, we incubated it with oligo(U)-RNA (U_{15}- and U_{30}-RNA) and investigated the interaction using EMSA. The gel shift analysis showed that the recombinant Lsm indeed binds U_{30}-RNA. Using U_{30}-RNA and increasing Lsm protein concentrations, we determined the dissociation constant K_D to be 72 nM (Fig. 4*A* and supplemental Fig. S4). Binding to oligo(U)-RNA has been shown for eukaryotic Lsm proteins (31, 59), for other archaeal ones (31), and also for Hfq (6). The physiological significance of the archaeal Lsm binding to oligo(U)-RNA is unclear because oligo(U) stretches have not been identified in the RNA population from *Haloferax* so far.

Because the *E. coli* Hfq and the yeast Lsm protein were suggested to be involved in tRNA processing and modification (60–62), we incubated the archaeal Lsm protein with tRNAs. EMSA revealed that the *Haloferax* Lsm protein also binds to tRNAs (Fig. 4*B*).

Native Mass Spectrometry Confirms Lsm-RNA Interactions—An additional approach to study RNA binding by Lsm and to unravel the stoichiometry of complex formation LILBID-MS was used. Purified Lsm protein was incubated with U_{30}-RNA, and mass spectrometry analysis under ultrasoft conditions (low laser intensity) confirmed that one Lsm heptamer bound to U_{30}-RNA and revealed in addition that another complex forms consisting of two Lsm heptamers bound to U_{30}-RNA (Fig. 5*A*). Analysis under harsh conditions (high laser intensity) revealed that the ternary complex was very

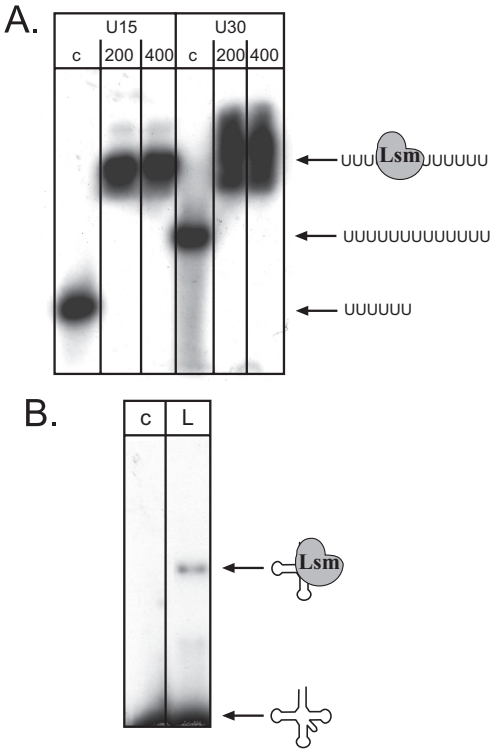

FIGURE 4. **Haloferax Lsm binds to RNA.** *A*, the recombinant Lsm protein was incubated with oligo(U)-RNA and subsequently loaded onto nondenaturing PAGE. *Lanes c*, control reaction without proteins; *lanes 200* and *400*, incubation with 200 and 400 ng of recombinant Lsm protein, respectively. *U15* and *U30*, incubation with U_{15}-RNA and U_{30}-RNA, respectively. RNA and complex are shown schematically at the *right*. *B*, tRNA is also bound by the Lsm protein. Incubation of Lsm with a wheat tRNA fraction shows that Lsm also binds to tRNAs. *Lane c*, control reaction without protein. *Lane L*, incubation with 100 ng of Lsm protein. RNA and complex are shown schematically on the *right*.

stable, and Lsm subunits were lost, whereas the complex remains otherwise intact (Fig. 5*B*).

LILBID-MS was also used to clarify whether sRNAs bind to Lsm. Incubation of Lsm with $sRNA_{30}$ and subsequent analysis with LILBID-MS revealed that an Lsm-$sRNA_{30}$ complex forms but, in contrast to U_{30}-RNA ternary complexes (Lsm-$sRNA_{30}$-Lsm), were not detected (Fig. 6).

Deletion of the Lsm Frame Is Viable—To pinpoint the biological function of the archaeal Lsm protein, we generated an *lsm* deletion mutant using the pop-in/pop-out method (39, 51, 63). Because the overlap of the *lsm* and *l37e* genes indicated translational coupling, care was taken to generate an in-frame deletion mutant that left translational coupling intact and avoided putative polar effects. After pop-out selection, small and large colonies were observed. Southern blot analysis revealed that only the small colonies contained the *lsm* deletion (termed Δ*lsm*), and the large colonies still contained the wild type *lsm* gene (supplemental Fig. S5). Comparison of the Δ*lsm* deletion mutant and the wild type under standard growth conditions (see "Experimental Procedures") revealed that the mutant exhibited an extensive lag phase before the onset of growth and had a reduced growth rate (Fig. 7). Comparison of the growth capabilities of mutant and wild type under various conditions revealed that the phenotypic difference between the two strains was variable, *e.g.* the mutant grew nearly as well as the wild type on casamino acids, pyruvate, xylose, and arabinose (lower growth yield on arabinose) but was severely compromised on glycerine and sucrose (data not shown). Therefore, it seems that the importance of the Lsm protein for cellular physiology is different for various metabolic pathways. To gain further insight into the function of Lsm, we decided to identify its interaction partners.

Co-immunoprecipitation Reveals Several Interaction Partners—To identify the interaction partners of the Lsm protein, we constructed a FLAG-Lsm fusion protein. For that purpose we first generated the expression vector pTA927, which is based on pTA230 (39) and features the tryptophan-inducible *tnaA* promoter for regulatable gene expression in *Haloferax* (41). Subsequently, the FLAG peptide cDNA was cloned in-frame downstream and upstream, respectively, of the Lsm reading frame into the pTA927 vector. In addition, a plasmid was constructed encoding only the FLAG peptide as a negative control. *Haloferax* was transformed with the plasmids, and expression was analyzed using Western blots (supplemental Fig. S6*A*), showing that both fusion proteins were efficiently expressed in *Haloferax*. The *lsm* deletion strain Δ*lsm* was likewise transformed with the plasmids, resulting in *Haloferax* strains expressing only the plasmid-encoded FLAG-Lsm fusion proteins. *H. volcanii* has an intracellular salt concentration of 2.5–4 M KCl, and it is currently not known whether any protein and ribonucleoprotein complexes require high salt concentrations for stability *in vitro*. Therefore, interacting RNA and protein molecules were cross-linked to the Lsm protein by incubating the *Haloferax* cells with formaldehyde before cell lysis to prevent disintegration of complexes during dialysis against low salt buffer. Cross-linking offers the additional advantage that transient interactions and low affinity partners are captured. As control, additional preparations were performed without the addition of formaldehyde to compare formaldehyde-treated and untreated samples. After the formaldehyde treatment, the cells were lysed, and an S100 protein extract was isolated. To remove proteins attached to the Lsm protein via RNA molecules, the S100 was digested with RNase A. Subsequently, the fusion protein and its interaction partners were isolated from the S100 extract using anti-FLAG affinity agarose.

To identify which proteins bind to the FLAG peptide, a control was prepared in parallel with only the FLAG peptide (without the Lsm protein). All of the precipitations were done in triplicate.

Identification of Protein Interaction Partners—For the analysis of protein interaction partners, the cross-link was reversed, and the proteins were separated with 3–12% SDS-PAGE (supplemental Fig. S6*B*). The proteins were subsequently analyzed by LC-MS/MS. The control preparation containing only the FLAG peptide revealed very few protein molecules, and in the three independent preparations only six proteins

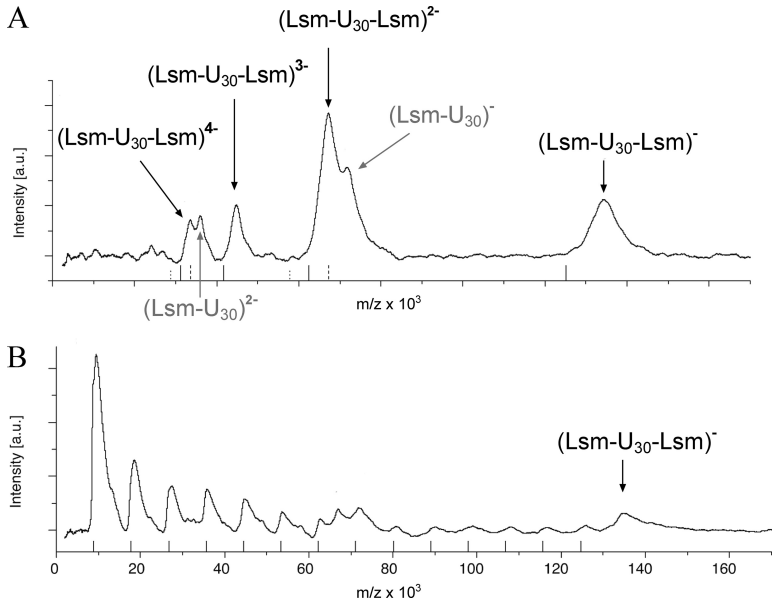

FIGURE 5. **Two Lsm complexes bind to oligo(U)-RNA.** *A*, in soft mode native mass spectrometry shows mostly a ternary complex consisting of two Lsm heptamers bound to one U_{30}-RNA molecule. The charge states of the ternary complex are indicated. In addition, a binary complex could also be detected with a lower signal intensity (shown in *gray*). *B*, under harsh conditions the complexes partially dissociate into smaller fragments. As can be clearly seen, the ternary complex does not dissociate stoichiometrically but rather loses a varying number of monomers.

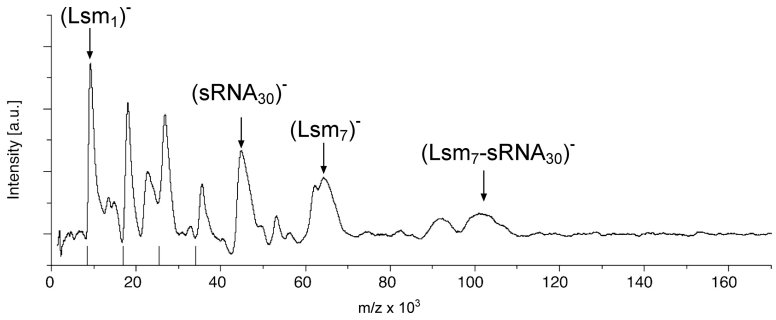

FIGURE 6. **The Lsm complex binds to $sRNA_{30}$.** LILBID-MS shows a significant amount of unbound heptamer as well as unbound $sRNA_{30}$. In addition, a binary complex could be detected preceded by a complex of unexpected size. A second complex of unexpected size was also found, which cannot be explained. However, analysis of the RNA alone also revealed a peak of the expected mass of 42 kDa and a second, unexpected peak. Although further experiments are needed to explain the unexpected peaks, the results clearly show the absence of the ternary complex (two Lsm heptamers: one RNA) with $sRNA_{30}$, which was the major complex with U_{30}-RNA. In addition, the results confirmed the higher affinity of the Lsm protein to U_{30}-RNA compared with $sRNA_{30}$, because in the former case the total protein amount was bound in a complex with RNA, whereas in the latter case a considerable fraction of the protein remained unbound.

were present in all three samples (supplemental Table S1), showing that few proteins bind to the FLAG tag. The precipitation of proteins from the FLAG-Lsm sample, which was not treated with formaldehyde before cell lysis, also revealed only very few proteins. In this case, only a single protein was identified that was present in all three independent samples, indicating that without cross-linking no specific interaction partner can be isolated (supplemental Table S2) and thus that the cross-linking step is required to identify interaction partners. The comparison of FLAG-Lsm co-immunoprecipitation with and without cross-link clearly showed that the purification procedure interrupts existing complexes and that cross-linking is required to keep the complexes intact upon lowering the salt concentration from the intracellular 2.1 M KCl to 150 mM NaCl.

To identify proteins specific for Lsm co-immunoprecipitation, the proteins identified by mass spectrometry in the control (FLAG only) (supplemental Table S1) were subtracted from those identified in the FLAG-Lsm co-immunoprecipitation, resulting in proteins specific for the Lsm co-immunoprecipitation (Table 1). Therefore, the proteins listed in Table 1 are true interaction partners, because proteins from the control co-purification (FLAG only) were subtracted, and in addition an RNase digest was performed. Altogether 33 proteins were identified; a similar high number of interaction partners has been found for the bacterial Hfq (57 proteins (64)) and the eukaryotic Sm and Lsm proteins (5). Furthermore, the proteins identified here as interaction partners belong to similar functional classes as the partners identified for the bacterial Hfq and eukaryotic Lsm proteins (5): *e.g.* ribosomal proteins, elongation factors, tRNA synthetases, chaperones, and ribonucleases. Details such as the regions of the Lsm protein involved in the interactions remain to be analyzed, but the apparent functional conservation of the protein is striking, and the number of interaction partners confirms the versatility of these proteins.

The Archaeal Lsm Protein Interacts with sRNAs and snoRNAs—To identify the RNA interaction partners, the cross-link was reversed, and the RNA was isolated from this fraction. An aliquot was labeled with [α-^{32}P]pCp, revealing several RNA molecules binding to Lsm (supplemental Fig. S6*C*). To further identify the RNA molecules, we employed DNA microarray analysis. Labeled cDNA was generated from the RNA, which co-purified with the FLAG-Lsm protein and with the FLAG only peptide, respectively. Competitive hybridization with a self-constructed DNA microarray led to

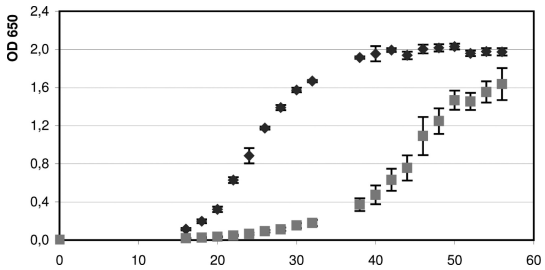

FIGURE 7. **Comparison of wild type and *lsm* deletion strain.** Comparison of the growth curves of wild type (*dark gray diamonds*) and deletion strain (*light gray squares*) shows that the *lsm* deletion results in slower growth. The *x* axis indicates the time of growth in hours.

TABLE 1

Proteins interacting with the Lsm protein

Co-immunoprecipitation with the FLAG-Lsm fusion protein revealed several proteins associated specifically with the Lsm protein (proteins co-purified with the control were subtracted). Proteins are grouped into functional classes. The number of obtained MS/MS spectra is shown. Only proteins that were present in all three FLAG-Lsm purifications with at least four MS/MS spectra in each of the three independent isolations are listed. The complete list of identified proteins is shown in supplemental Table 3. In addition, supplemental Table 3 lists the accession numbers and the number of MS/MS spectra for all three replicas.

	Protein	Number of MS/MS spectra
Translation		
1	Translation elongation factor aEF-2	47
2	Translation elongation factor aEF-1 α subunit	29
3	Ribosomal protein S3	10
4	Threonyl-tRNA synthetase	9
5	Ribosomal protein S3a.eR	8
6	Valyl-tRNA synthetase	7
Stress-related		
7	Heat shock protein Cct2	32
8	Heat shock protein Cct1	30
9	CBS domain pair, putative	16
10	Thermosome subunit 3	10
11	UspA domain protein	7
Nucleic acid metabolism		
12	DNA-directed RNA polymerase subunit A	15
13	mRNA 3-end processing factor homolog	13
14	Sugar-specific transcriptional regulator TrmB	6
15	Putative nuclease	6
16	DNA-directed RNA polymerase subunit B	5
17	Replication factor C small subunit	4
Cell cycle		
18	Cell division control protein 48	15
19	Cell division control protein 48	12
20	SMC-like protein Sph2	10
Diverse functions		
21	Betaine aldehyde dehydrogenase	16
22	Chlorite dismutase family protein	12
23	Pyruvate-ferredoxin oxidoreductase α subunit	10
24	Predicted hydrolase	10
25	Aconitate hydratase, putative	10
26	Coiled-coil protein	9
27	Fumarate hydratase class II	9
28	Proteasome subunit α1	8
29	Putative orotatephosphoribosyl transferase	8
30	Phosphopyruvate hydratase	7
31	Aspartate carbamoyltransferase	7
32	Short chain family oxidoreductase	7
33	Inosine-5-monophosphate dehydrogenase	6

the identification of 20 sRNAs that co-purified with the Lsm protein (Table 2). Several of these RNAs have recently been identified as candidate sRNAs (Ref. 38 and Table 1 therein): intergenic sRNAs 30, 34, 132, 304, and 308; antisense sRNAs 25 and 144; and sense sRNAs 15 and 93. Seven of the Lsm-

TABLE 2

RNAs interacting with the Lsm protein

RNA isolated from the co-immunoprecipitation with the FLAG-Lsm fusion protein was used to hybridize DNA microarrays. Several RNAs associated with the Lsm protein could be identified. The red/green ratio denotes the average signal strengths of cDNAs generated from RNA co-purified with the FLAG-Lsm protein divided by the average signal strengths of a negative control cDNA generated from RNA purified from cultures only expressing the FLAG peptide. RNAs termed "sRNA" were previously identified as sRNAs in *Haloferax* (37,38). RNAs termed "H" and "p" had been predicted as sRNAs using bioinformatic approaches.[4]

RNA	Ratio of red/green
H225.1	194,02
sRNA25	29,71
sRNA30	22,76
sRNA144	17,76
sRNA34	16,44
p12	15,15
sRNA15	14,15
sRNA93	12,77
sRNA308	9,83
sRNA132	9,62
p5	9,10
sRNA45	8,91
H225.2r	7,30
H230	6,95
H11.1	5,45
H62r	2,30
sRNA140	2,16

binding RNAs (H225.1, p12, p5, H225.2r, H230, H11.1, and H62r) had been predicted as sRNAs using bioinformatic approaches.[4] The DNA microarray results show for the first time that these predicted sRNAs are indeed expressed. A snoRNA (sRNA45) that had been predicted as C/D box snoRNA[4] was also identified. Interestingly, the 7 S RNA also co-purified with the Lsm protein. The binding of Lsm to sRNAs suggests a similar function of the archaeal protein in the regulatory network of sRNAs as for the bacterial Hfq protein. Unfortunately, so far no targets have been identified for an archaeal sRNA; thus, the influence of Lsm on sRNA/target RNA interaction remains to be determined.

The binding of the Lsm protein to a potential C/D box snoRNA is interesting because the attachment of an Lsm protein to a snoRNA has not yet been found in archaea. The archaeal C/D box snoRNAs and their function have been studied in detail in *Sulfolobus solfataricus* (65). Three proteins have been identified that associate with the snoRNA to form the methylation guide complex: L7Ae, aFib, and aNop56/58. Homologues for all three proteins are also present in *H. volcanii*. Interestingly, the aNop56/58 homologue is also found as a protein interaction partner in the co-immunoprecipitation but not L7Ae and aFib (Table 1). Because the eukaryotic counterparts of the archaeal Lsm protein bind to snoRNAs, it is likely that the archaeal Lsm protein binds to archaeal snoRNAs. The specific role of that interaction remains to be determined.

The lsm Deletion Mutant Exhibits a Pleiotropic Phenotype—Although the Lsm protein is involved in many processes, it is not essential. The mutant has severe growth defects compared with the wild type under a variety of conditions, supporting the suggestion that Lsm is involved in many different pathways. Similar observations have been made in bacteria, where Hfq is involved in several processes. Deletions of the *E. coli hfq* gene

[4] J. Straub, B. Stoll, B. Tjaden, B. Voss, W. R. Hess, A. Marchfelder, and J. Soppa, in preparation.

resulted in pleiotropic physiological effects, and the lack of phenotype under specific conditions was also observed (11, 13, 66, 67). The construction of *hfq* deletion mutants in other bacterial species revealed a fundamental role of Hfq in the virulence of pathogenic bacteria (67–73). No apparent phenotype emerged from an *hfq* knock-out in *Staphylococcus aureus* (74). In summary, deletion mutants of prokaryotic *lsm* genes revealed that Lsm proteins are involved in many processes, and their absence results in pleiotropic phenotypes.

Acknowledgments—We thank Elli Bruckbauer for expert technical assistance and Katharina Jantzer for growth experiments with the lsm mutant. Furthermore, we thank members of the SPP 1258 Priority Program for helpful discussions.

REFERENCES

1. Møller, T., Franch, T., Højrup, P., Keene, D. R., Bächinger, H. P., Brennan, R. G., and Valentin-Hansen, P. (2002) *Mol. Cell* **9,** 23–30
2. Zhang, A., Wassarman, K. M., Ortega, J., Steven, A. C., and Storz, G. (2002) *Mol. Cell* **9,** 11–22
3. Valentin-Hansen, P., Eriksen, M., and Udesen, C. (2004) *Mol. Microbiol.* **51,** 1525–1533
4. Sun, X., Zhulin, I., and Wartell, R. M. (2002) *Nucleic. Acids Res.* **30,** 3662–3671
5. Wilusz, C. J., and Wilusz, J. (2005) *Nat. Struct. Mol. Biol.* **12,** 1031–1036
6. Schumacher, M. A., Pearson, R. F., Møller, T., Valentin-Hansen, P., and Brennan, R. G. (2002) *EMBO J.* **21,** 3546–3556
7. Senear, A. W., and Steitz, J. A. (1976) *J. Biol. Chem.* **251,** 1902–1912
8. de Haseth, P. L., and Uhlenbeck, O. C. (1980) *Biochemistry.* **19,** 6146–6151
9. Nielsen, J. S., Bøggild, A., Andersen, C. B., Nielsen, G., Boysen, A., Brodersen, D. E., and Valentin-Hansen, P. (2007) *RNA* **13,** 2213–2223
10. Wassarman, K. M., Repoila, F., Rosenow, C., Storz, G., and Gottesman, S. (2001) *Genes Dev.* **15,** 1637–1651
11. Tsui, H. C., Leung, H. C., and Winkler, M. E. (1994) *Mol. Microbiol.* **13,** 35–49
12. Brown, L., and Elliott, T. (1996) *J. Bacteriol.* **178,** 3763–3770
13. Muffler, A., Fischer, D., and Hengge-Aronis, R. (1996) *Genes Dev.* **10,** 1143–1151
14. Massé, E., and Gottesman, S. (2002) *Proc. Natl. Acad. Sci. U.S.A.* **99,** 4620–4625
15. Møller, T., Franch, T., Udesen, C., Gerdes, K., and Valentin-Hansen, P. (2002) *Genes Dev.* **16,** 1696–1706
16. Sledjeski, D. D., Whitman, C., and Zhang, A. (2001) *J. Bacteriol.* **183,** 1997–2005
17. Zhang, A., Altuvia, S., Tiwari, A., Argaman, L., Hengge-Aronis, R., and Storz, G. (1998) *EMBO J.* **17,** 6061–6068
18. Thore, S., Mayer, C., Sauter, C., Weeks, S., and Suck, D. (2003) *J. Biol. Chem.* **278,** 1239–1247
19. Tharun, S., He, W., Mayes, A. E., Lennertz, P., Beggs, J. D., and Parker, R. (2000) *Nature* **404,** 515–518
20. Bouveret, E., Rigaut, G., Shevchenko, A., Wilm, M., and Séraphin, B. (2000) *EMBO J.* **19,** 1661–1671
21. Pannone, B. K., Xue, D., and Wolin, S. L. (1998) *EMBO J.* **17,** 7442–7453
22. Mayes, A. E., Verdone, L., Legrain, P., and Beggs, J. D. (1999) *EMBO J.* **18,** 4321–4331
23. Salgado-Garrido, J., Bragado-Nilsson, E., Kandels-Lewis, S., and Séraphin, B. (1999) *EMBO J.* **18,** 3451–3462
24. Klenk, H. P., Clayton, R. A., Tomb, J. F., White, O., Nelson, K. E., Ketchum, K. A., Dodson, R. J., Gwinn, M., Hickey, E. K., Peterson, J. D., Richardson, D. L., Kerlavage, A. R., Graham, D. E., Kyrpides, N. C., Fleischmann, R. D., Quackenbush, J., Lee, N. H., Sutton, G. G., Gill, S., Kirkness, E. F., Dougherty, B. A., McKenney, K., Adams, M. D., Loftus, B., Peterson, S., Reich, C. I., McNeil, L. K., Badger, J. H., Glodek, A., Zhou, L., Overbeek, R., Gocayne, J. D., Weidman, J. F., McDonald, L., Utterback, T., Cotton, M. D., Spriggs, T., Artiach, P., Kaine, B. P., Sykes, S. M., Sadow, P. W., D'Andrea, K. P., Bowman, C., Fujii, C., Garland, S. A., Mason, T. M., Olsen, G. J., Fraser, C. M., Smith, H. O., Woese, C. R., and Venter, J. C. (1997) *Nature* **390,** 364–370
25. Smith, D. R., Doucette-Stamm, L. A., Deloughery, C., Lee, H., Dubois, J., Aldredge, T., Bashirzadeh, R., Blakely, D., Cook, R., Gilbert, K., Harrison, D., Hoang, L., Keagle, P., Lumm, W., Pothier, B., Qiu, D., Spadafora, R., Vicaire, R., Wang, Y., Wierzbowski, J., Gibson, R., Jiwani, N., Caruso, A., Bush, D., Safer, H., Patwell, D., Prabhakar, S., McDougall, S., Shimer, G., Goyal, A., Pietrokovski, S., Church, G. M., Daniels, C. J., Mao, J. I., Rice, P., Nölling, J., and Reeve, J. N. (1997) *J. Bacteriol* **179,** 7135–7155
26. Pühler, G., Leffers, H., Gropp, F., Palm, P., Klenk, H. P., Lottspeich, F., Garrett, R. A., and Zillig, W. (1989) *Proc. Natl. Acad. Sci. U.S.A.* **86,** 4569–4573
27. Omer, A. D., Lowe, T. M., Russell, A. G., Ebhardt, H., Eddy, S. R., and Dennis, P. P. (2000) *Science.* **288,** 517–522
28. Törö, I., Thore, S., Mayer, C., Basquin, J., Séraphin, B., and Suck, D. (2001) *EMBO J.* **20,** 2293–2303
29. Khusial, P., Plaag, R., and Zieve, G. W. (2005) *Trends Biochem. Sci.* **30,** 522–528
30. Mura, C., Phillips, M., Kozhukhovsky, A., and Eisenberg, D. (2003) *Proc. Natl. Acad. Sci. U.S.A.* **100,** 4539–4544
31. Achsel, T., Stark, H., and Lührmann, R. (2001) *Proc. Natl. Acad. Sci. U.S.A.* **98,** 3685–3689
32. Collins, B. M., Harrop, S. J., Kornfeld, G. D., Dawes, I. W., Curmi, P. M., and Mabbutt, B. C. (2001) *J. Mol. Biol.* **309,** 915–923
33. Mura, C., Cascio, D., Sawaya, M. R., and Eisenberg, D. S. (2001) *Proc. Natl. Acad. Sci. U.S.A.* **98,** 5532–5537
34. Törö, I., Basquin, J., Teo-Dreher, H., and Suck, D. (2002) *J. Mol. Biol.* **320,** 129–142
35. Mura, C., Kozhukhovsky, A., Gingery, M., Phillips, M., and Eisenberg, D. (2003) *Protein Sci.* **12,** 832–847
36. Sauter, C., Basquin, J., and Suck, D. (2003) *Nucleic Acids Res.* **31,** 4091–4098
37. Soppa, J., Straub, J., Brenneis, M., Jellen-Ritter, A., Heyer, R., Fischer, S., Granzow, M., Voss, B., Hess, W. R., Tjaden, B., and Marchfelder, A. (2009) *Biochem. Soc Trans.* **37,** 133–136
38. Straub, J., Brenneis, M., Jellen-Ritter, A., Heyer, R., Soppa, J., and Marchfelder, A. (2009) *RNA Biol* **6,** 281–292
39. Allers, T., Ngo, H. P., Mevarech, M., and Lloyd, R. G. (2004) *Appl. Environ. Microbiol.* **70,** 943–953
40. Shimmin, L. C., and Dennis, P. P. (1996) *J. Bacteriol.* **178,** 4737–4741
41. Large, A., Stamme, C., Lange, C., Duan, Z., Allers, T., Soppa, J., and Lund, P. A. (2007) *Mol. Microbiol.* **66,** 1092–1106
42. Chomczynski, P., and Sacchi, N. (1987) *Anal. Biochem.* **162,** 156–159
43. Herrmann, U., and Soppa, J. (2002) *Mol. Microbiol.* **46,** 395–409
44. Baumann, A., Lange, C., and Soppa, J. (2007) *BMC Cell Biol.* **8,** 21
45. Yokobori, S., and Pääbo, S. (1995) *Proc. Natl. Acad. Sci. U.S.A.* **92,** 10432–10435
46. Pfeiffer, F., Broicher, A., Gillich, T., Klee, K., Mejía, J., Rampp, M., and Oesterhelt, D. (2008) *Arch. Microbiol.* **190,** 281–299
47. Hölzle, A., Fischer, S., Heyer, R., Schütz, S., Zacharias, M., Walther, P., Allers, T., and Marchfelder, A. (2008) *RNA* **14,** 928–937
48. Späth, B., Kirchner, S., Vogel, A., Schubert, S., Meinlschmidt, P., Aymanns, S., Nezzar, J., and Marchfelder, A. (2005) *J. Biol. Chem.* **280,** 35440–35447
49. Morgner, N., Barth, H., and Brutschy, B. (2006) *Aust. J. Chem.* **59,** 109–114
50. Morgner, N., Kleinschroth, T., Barth, H. D., Ludwig, B., and Brutschy, B. (2007) *J. Am. Soc. Mass Spectrom.* **18,** 1429–1438
51. Bitan-Banin, G., Ortenberg, R., and Mevarech, M. (2003) *J. Bacteriol.* **185,** 772–778
52. Sambrook, J., and Russell, D. (2001) *Molecular Cloning: A Laboratory Manual*, pp. 6.47–6.58, Cold Spring Harbor Press, New York
53. Kunzmann, A., Brennicke, A., and Marchfelder, A. (1998) *Proc. Natl. Acad. Sci. U.S.A.* **95,** 108–113
54. Shevchenko, A., Wilm, M., Vorm, O., and Mann, M. (1996) *Anal Chem.* **68,** 850–858

55. Zaigler, A., Schuster, S. C., and Soppa, J. (2003) *Mol. Microbiol* **48,** 1089–1105
56. Altschul, S. F., Madden, T. L., Schäffer, A. A., Zhang, J., Zhang, Z., Miller, W., and Lipman, D. J. (1997) *Nucleic Acids Res.* **25,** 3389–3402
57. Brenneis, M., Hering, O., Lange, C., and Soppa, J. (2007) *PLoS Genet* **3,** e229
58. Azam, T. A., and Ishihama, A. (1999) *J. Biol. Chem.* **274,** 33105–33113
59. Achsel, T., Brahms, H., Kastner, B., Bachi, A., Wilm, M., and Lührmann, R. (1999) *EMBO J.* **18,** 5789–5802
60. Kufel, J., Allmang, C., Verdone, L., Beggs, J. D., and Tollervey, D. (2002) *Mol. Cell Biol.* **22,** 5248–5256
61. Lee, T., and Feig, A. L. (2008) *RNA* **14,** 514–523
62. Zhang, A., Wassarman, K. M., Rosenow, C., Tjaden, B. C., Storz, G., and Gottesman, S. (2003) *Mol. Microbiol.* **50,** 1111–1124
63. Allers, T., and Mevarech, M. (2005) *Nat. Rev. Genet.* **6,** 58–73
64. Butland, G., Peregrín-Alvarez, J. M., Li, J., Yang, W., Yang, X., Canadien, V., Starostine, A., Richards, D., Beattie, B., Krogan, N., Davey, M., Parkinson, J., Greenblatt, J., and Emili, A. (2005) *Nature* **433,** 531–537
65. Omer, A. D., Ziesche, S., Ebhardt, H., and Dennis, P. P. (2002) *Proc. Natl. Acad. Sci. U.S.A.* **99,** 5289–5294
66. Muffler, A., Traulsen, D. D., Fischer, D., Lange, R., and Hengge-Aronis, R. (1997) *J. Bacteriol.* **179,** 297–300
67. Sittka, A., Pfeiffer, V., Tedin, K., and Vogel, J. (2007) *Mol. Microbiol.* **63,** 193–217
68. Christiansen, J. K., Larsen, M. H., Ingmer, H., Søgaard-Andersen, L., and Kallipolitis, B. H. (2004) *J. Bacteriol.* **186,** 3355–3362
69. Ding, Y., Davis, B. M., and Waldor, M. K. (2004) *Mol. Microbiol.* **53,** 345–354
70. Lucchetti-Miganeh, C., Burrowes, E., Baysse, C., and Ermel, G. (2008) *Microbiology* **154,** 16–29
71. Robertson, G. T., and Roop, R. M., Jr. (1999) *Mol. Microbiol.* **34,** 690–700
72. Sharma, A. K., and Payne, S. M. (2006) *Mol. Microbiol.* **62,** 469–479
73. Sonnleitner, E., Hagens, S., Rosenau, F., Wilhelm, S., Habel, A., Jäger, K. E., and Bläsi, U. (2003) *Microb. Pathog.* **35,** 217–228
74. Bohn, C., Rigoulay, C., and Bouloc, P. (2007) *BMC Microbiol.* **7,** 10
75. Dyall-Smith, M. L. (2001) *The Halohandbook: Protocols for Haloarchael Genetics*, http://www.haloarchaea.com/resources/halohandbook/Halohandbook_2008_v7.pdf

DNA damage in oocytes induces an irreversible switch of the quality control factor TAp63α from dimer to tetramer

Gregor B. Deutsch[1*], Elisabeth M. Zielonka[2,3*], Daniel Coutandin[1*], Tobias A. Weber[1], Birgit Schäfer[1], Jens Hannewald[4], Laura M. Luh[1], Florian G. Durst[1], Mohamed Ibrahim[5], Jan Hoffmann[6], Frank H. Niesen[7], Aycan Sentürk[8], Hana Kunkel[9], Bernd Brutschy[6], Enrico Schleiff[5], Stefan Knapp[7,10], Amparo Acker-Palmer[8], Manuel Grez[9], Frank McKeon[2,3,11], Volker Dötsch[1#]

[1]*Institute of Biophysical Chemistry and Center for Biomolecular Magnetic Resonance; Goethe University; Frankfurt, 60438; Germany.*

[2]*ISIS; University of Strasbour; Strasbourg, 67000; France.*

[3]*the Genome Institute of Singapore; A-STAR; Singapore, 138672; Singapore.*

[4] *MS-DTB-C Protein Purification; Merck KGaA; Darmstadt, 64293; Germany.*

[5]*Institute of Molecular and Cell Biology of Plants; Goethe University;Frankfurt, 60438; Germany.*

[6]*Institute of Physical and Theoretical Chemistry; Goethe University; Frankfurt, 60438; Germany.*

[7]*Nuffield Department of Medicine, Structural Genomics Consortium, Old Road Campus Research Building; Oxford University; Oxford, OX3 7DQ; UK.*

[8] *Frankfurt Institute for Molecular Life Sciences (FMLS) and Institute of Cell Biology and Neuroscience; Goethe University; Frankfurt, 60438; Germany.*

[9]*Georg-Speyer Haus; Frankfurt 60596; Germany.*

[10]*Department of Clinical Pharmacology, Structural Genomics Consortium, Old Road Campus Research Building; Oxford University; Oxford, OX3 7DQ; UK.*

[11]*Department of Cell Biology; Harvard Medical School; Boston, MA 02115; USA.*

[#]Correspondence: *vdoetsch@em.uni-frankfurt.de*

[*] *These authors contributed equally to this work.*

SUMMARY

TAp63α, a homologue of the p53 tumor suppressor, is a quality control factor in the female germ line. Remarkably, already undamaged oocytes express high levels of the protein, suggesting that TAp63α's activity is under tight control of an inhibitory mechanism. Biochemical studies have proposed that inhibition requires the C-terminal transactivation inhibitory domain. However, the exact mechanism by which TAp63α is inhibited remained unknown. Here we show that TAp63α is kept in an inactive dimeric state. We reveal that relief of inhibition leads to tetramer formation with ~20-fold higher DNA affinity. *In vivo*, phosphorylation triggered tetramerization of TAp63α is not reversible by dephosphorylation. Furthermore, we show that a helix

in the oligomerization domain of p63 is crucial for tetramer stabilization and competes with the transactivation domain for the same binding site. Our results demonstrate how TAp63α is inhibited by complex domain-domain-interactions that provide the basis for regulating quality control in oocytes.

HIGHLIGHTS

TAp63α is inhibited in a dimeric state by complex domain-domain-interactions.

Phosphorylation triggered TAp63α activation upon DNA damage requires tetramerization.

Tetramer stabilization requires the second helix H2 of the tetramerization domain.

Tetramerization domain binding by the transactivation domain is competed by helix H2.

INTRODUCTION

In mammals the family of the p53 tumor suppressor contains two additional members, p73 and p63 (Kaghad et al., 1997; Schmale and Bamberger, 1997; Senoo et al., 1998; Trink et al., 1998; Yang et al., 1998). Originally, their discovery had sparked the speculation that tumor suppression might be achieved by an entire network of p53-like factors. However, detailed studies including gene inactivation experiments in mice, have revealed that both p53 homologues serve important developmental functions (Mills et al., 1999; Yang et al., 1999; Yang et al., 2000). p73 knock-out mice suffer from hippocampal

dysgenesis, hydrocephalus, chronic infections and inflammation, as well as abnormalities in pheromone sensory pathways. Loss of p63 results in even more severe defects, including limb truncations, lack of a multi-layered skin and other epithelial structures. These phenotypes led to the identification of six p63 related developmental syndromes in humans that are characterized by deformation of the limbs and/or skin abnormalities (Celli et al., 1999; McGrath et al., 2001). In contrast to these clear developmental functions the question if both proteins also act as tumor suppressors is still debated. Recent investigations of heterozygous and TAp73 specific knock-out mice, however, have suggested that at least this protein can act as a real tumor suppressor (Flores et al., 2005; Tomasini et al., 2008).

The investigation of the physiological role of both proteins is further complicated by the existence of many different isoforms of p63 and p73 and potentially by the formation of mixed oligomers between both proteins (Coutandin et al., 2009; Joerger et al., 2009) (Figure 1A). Isoforms are created by combining several different C-terminal splice variants (De Laurenzi et al., 1999; De Laurenzi et al., 1998; Kaghad et al., 1997; Yang et al., 1998) with two different promoters that produce isoforms either with (TA-isoforms) or without (ΔN-isoforms) the N-terminal transactivation domain (Yang et al., 1998).

In the case of p63, detailed analysis has started to reveal the physiological functions of some isoforms. ΔNp63α, the isoform produced by combination of the second promoter with the longest C-terminal splice variant, plays an important role in the development of stratified epithelial tissues including skin by maintaining a stem cell population in the basal layer (Senoo et al., 2007). Inactivation of this isoform seems to be responsible for the

severe developmental defects seen in the knock-out mice as well as in human patients with p63 mutations (Rinne et al., 2007). In contrast, TAp63α, the isoform containing the long α C-terminus and the full N-terminal transactivation domain, serves a quite different function. It is found in oocytes where it acts as a quality control factor that monitors the genetic stability of these cells (Suh et al., 2006). TAp63α expression in murine oocytes can be detected from day E18.5 on and at day P5, when murine oocytes are arrested in prophase of meiosis I, all oocytes show strong nuclear expression. After oocytes are recruited for ovulation, TAp63α expression is lost. Previous experiments have shown that γ-irradiation results in phosphorylation of TAp63α followed by the elimination of all premature oocytes while mature ones that do not express p63 are not affected (Suh et al., 2006).

Due to its ability to induce cell death the activity of TAp63α must be regulated very tightly. In contrast to p53 that is kept at very low concentrations in non-stressed cells and only increases when triggered by oncogenic signals (Brooks and Gu, 2006; Wade et al., 2010), TAp63α reaches high expression levels already in non-stressed oocytes (Suh et al., 2006). This observation has suggested that the activity of TAp63α must be regulated by keeping it in an inactive state. In cell culture based transactivation experiments TAp63α indeed showed only a very low transcriptional activity. By deletion mutagenesis we have revealed in previous experiments that the last 70 amino acids of TAp63α act as a transactivation inhibitory domain (TID). Deletion or mutation of this TI domain increases TAp63α's low transcriptional activity several fold (Serber et al., 2002; Straub et al., 2010;

Yang et al., 1998). The exact mechanism of how the TID inhibits the activity of TAp63α, however, remained unknown.

Here we show both *in vitro* and *in vivo* that TAp63α is kept in a closed dimeric conformation in non-stressed oocytes while γ-irradiation triggered phosphorylation promotes the formation of active tetramers. The active state of TAp63α is stabilized by a special structure of its tetramerization domain, making the activation process basically irreversible.

RESULTS

TAp63α forms a closed dimeric conformation

To characterize the inhibitory mechanism of the TID we expressed TAp63α in *E. coli*. Surprisingly, size exclusion chromatography (SEC) analysis of purified TAp63α suggested that it forms dimers instead of the expected tetramers (Figure 1B). All mammalian members of the p53 protein family use a highly conserved oligomerization domain (OD) to form tetramers that were shown to be the active state (Chan et al., 2004; Chene, 2001; Jeffrey et al., 1995; Lee et al., 1994). The concentration of TAp63α used in the SEC experiment was orders of magnitude higher (3-15 μM) than the K_D for tetramerization of p63 (12 nM) (Brandt et al., 2009), excluding the possibility that simple dilution can explain the absence of tetramers. This result implied that TAp63α adopts a

dimeric, inactive conformation and further suggested that activation of p63 might be linked to the formation of tetramers. To address this question we performed SEC analysis with the transcriptionally active TAp63γ isoform that lacks the TID. Obtaining soluble TAp63γ required its expression as an N-terminal maltose-binding-protein (MBP) fusion protein. For comparability we also expressed TAp63α fused to MBP. SEC analysis of MBP-TAp63γ showed that it behaves as a significantly larger protein than MBP-TAp63α despite the fact that it contains 193 amino acids less per monomer (Figure 1B).

In a previous alanine scanning experiment of the TID we have found that the triple mutant F605A T606A L607A (TAp63αFTL) shows high transcriptional activity suggesting that this mutation destroys the inhibitory function of the TID (Straub et al., 2010). SEC-analysis showed that MBP-TAp63αFTL also behaves as a much larger protein than MBP-TAp63α with a retention volume similar to MBP-TAp63γ (Figure 1B).

The classification of TAp63α as a dimer was based on a calibration of the SEC column with compact globular proteins. The predicted molecular weights of 160 kDa for TAp63α and 266 kDa for MBP-TAp63α closely resemble the theoretical values for the dimers of 150 kDa and 232 kDa, respectively. Estimation of the molecular weights of MBP-TAp63αFTL and MBP-TAp63γ, however, resulted in values exceeding the theoretical ones for the assumed tetramers by far. These findings could be explained either if the active forms adopt an oligomeric state higher than tetrameric or if the conformation of the tetramers deviates from a globular fold. To investigate the oligomeric state of all proteins by determining their mass independently of their shape, we used multi angle light

scattering (MALS) analysis. The results shown in Figures 1C-1F confirm that TAp63α and MBP-TAp63α form dimers while MBP-TAp63αFTL and MBP-TAp63γ exist as tetramers. In combination with these MALS analysis the SEC data demonstrate that activation not only leads to tetramerization but also to the formation of a non-globular and open structure. The same results were obtained with cross linking experiments (Figure S1A-S1D available online) and further supported by mass spectrometry (LILBID) analysis (Figure S1E) and analytical ultracentrifugation (Figure S1F and Table S1).

Phosphorylation triggers the formation of active TAp63α tetramers *in vivo*

In mice expression of TAp63α can be detected from embryonic day 18.5 on with all oocytes showing strong expression at day P5 when murine oocytes are arrested in prophase of meiosis I (dictyate arrest) (Suh et al., 2006). p63 expression is maintained at a high level until oocytes are recruited for ovulation. DNA damage during this time triggers activation of p63 and destruction of the oocytes. To investigate if our results obtained *in vitro* can explain the behavior of TAp63α in oocytes we analyzed the oligomeric state of TAp63α in five day old mice by SEC. Figure 2A shows that γ-irradiation of mice with 0.52 Gy triggers phosphorylation of TAp63α and leads to a reduction of its concentration relative to non-irradiated oocytes. Analysis of the SEC fractions of samples obtained from non-irradiated mice revealed a strong signal in the dimer fraction (1.55 mL) and no detectable signal in the tetramer fraction (1.3 mL, calibrated with bacterially expressed p63 isoforms, Figure S2A-

S2C) (Figure 2A-2C). In contrast, samples obtained from irradiated mice showed a significant signal in the tetramer fraction (Figure 2A, Figure 2D and 2E). The *in vivo* concentration of tetrameric TAp63α in irradiated oocytes is expected to be significantly higher than seen in the SEC experiments since oocyte lysis and SEC analysis lead to a minimum ten-fold dilution of the sample. We confirmed that dilution shifts the equilibrium towards dimers by reducing the concentration of bacterially expressed MBP-TAp63γ in SEC experiments (Figure S2D and S2E). While virtually exclusively tetrameric at a concentration of 3-15 µM, MBP-TAp63γ displays an almost equal distribution between dimers and tetramers at 30 nM (Figure S2). These results indicate that TAp63α in non stressed oocytes is kept in a dimeric and closed conformation and that DNA damage triggers the formation of tetramers *in vivo*. The significantly higher concentration of TAp63α in non-irradiated versus irradiated cells further suggests that the formation of tetramers is not suppressed by keeping the intracellular concentration low (as it is discussed for p53) but actively by domain-domain interactions involving the TID.

Tetramerization increases the DNA binding affinity

We next investigated the functional consequences of tetramer formation. Previous experiments in oocytes have demonstrated that phosphorylation increases TAp63α's DNA binding affinity ~20-fold (Suh et al., 2006). To investigate if this increase in DNA affinity can be explained by the formation of tetramers we measured K_D values for the binding of

MBP-TAp63α, MBP-TAp63αFTL and MBP-TAp63γ to the p21 promoter response element using fluorescence anisotropy. Figure 3A-3C (and Figure S3A and S3B) reveal that dimeric MBP-TAp63α binds the p21 promoter response element with a K_D of 7.51 ± 1.32 μM. For tetrameric MBP-TAp63αFTL and MBP-TAp63γ K_D values of 0.38 ± 0.04 μM and 0.34 ± 0.08 μM were measured, respectively. These measurements demonstrate that the change from a closed dimeric to an open tetrameric state increases the DNA binding affinity by ~20-fold, similar to the studies carried out in oocytes.

Phosphorylation is not required for maintaining the tetrameric state

Previous investigations have revealed that treatment of phosphorylated TAp63α with λ-phosphatase does not decrease the DNA binding affinity to its original value (Suh et al., 2006). This result suggests that phosphorylation serves as a trigger for the activation process but is not essential to maintain the active state. Since the active state is the tetramer, dephosphorylation should not affect the oligomerization equilibrium. To investigate the influence of the phosphorylation status on the oligomeric state we performed SEC analysis of λ-phosphatase treated TAp63α obtained from irradiated oocytes. The dephosphorylated sample indeed showed a high percentage of tetramers and only a relatively small increase in the dimer concentration compared to phosphorylated TAp63α (Figure 3D-3G). *In vitro* control experiments showed that λ-phosphatase treatment leads to complete dephosphorylation (Figure S3C and S3D). This result suggests that tetramer formation

constitutes an almost irreversible activation switch triggered by phosphorylation. Such an irreversible activation would require the formation of a state that is locked in the active conformation. In the case of TAp63α, such a mechanism would have to stabilize the tetrameric state by shifting the equilibrium towards this oligomeric form. Recently, we and others have discovered that p63 contains an additional helix within its oligomerization domain (OD) that is not present in the p53 OD (Coutandin et al., 2009; Joerger et al., 2009). This second helix stabilizes the tetramer by reaching across the tetrameric interface. The real physiological importance of this helix was so far not known. Since this helix must adopt a different conformation or orientation within the closed dimeric state, it might be the element that locks TAp63α in its tetrameric form after phosphorylation induced activation. This model is supported by the observation that deletion of this helix renders the active-state mimetic mutant TAp63αFTL dimeric while deletion had no effect on TAp63α (Figure 4). Furthermore, transactivation assays revealed that deletion of the second helix reduced the transcriptional activity by 50% (Figure S4), comparable to the activity of dimeric forms of TAp63γ (Straub et al., 2010) and p53(Davison et al., 2001).

The tetramerization domain is essential for forming the closed conformation

This model of regulating the activity of p63 by controlling the oligomerization state assigns a pivotal role to the tetramerization domain (as TD we define the OD with the second helix). The structure of the TD is a dimer of dimers (Jeffrey et al., 1995; Lee et al.,

1994). Two monomers each contribute one strand to the formation of an antiparallel β-sheet. This small β-sheet is stabilized by two α-helices, one from each monomer, that also arrange in an antiparallel orientation. Tetramers are formed by interaction of the helices of two dimers that form a four helix bundle. The most obvious model would explain the inhibition of TAp63α by selective blocking of the tetramerization interface without affecting the dimerization interface. To probe the importance of the tetramerization interface we mutated Met374 to Gln and Ile378 to Arg (TAp63αMI), known from p53 to create dimers (Davison et al., 2001) (Figure 5A and 5B). These mutations increased the transcriptional activity significantly, reaching 55% activity of wild type TAp63γ (Figure 5E), which is similar to the activity of dimeric p53 and TAp63γ mutants reported previously (Davison et al., 2001; Straub et al., 2010). In GST-pulldown assays with an external TI domain the TAp63αMI mutant was also effectively pulled down, in contrast to wild type TAp63α (Figure 5F and 5G). In these experiments only p63 isoforms with an open conformation can be pulled down (Serber et al., 2002). Both results demonstrate that this double mutation induces an open conformation by disrupting the inhibitory mechanism mediated by the TID. Met374 and Ile378 are located in the center of the tetramerization interface. We also mutated Leu384 and Met385, located at its edge, to Ala (Figure 5A and Figure 5C-5D). The L384A and L384A/M385A mutants (TAp63αL and TAp63αLM) showed very low activity in transactivation assays and no interaction in pulldown experiments (Figure 5E-5G). These results demonstrate that only mutations in the central region of the tetramerization domain disrupt the inhibitory mechanism, creating an open dimeric form (Figure S5).

An attractive model of the inhibitory mechanism would explain the formation of dimeric TAp63α by direct interaction of the TID with the tetramerization interface. In principle, NMR titration experiments would allow a direct mapping of the binding site. However, the p63 OD is tetrameric at concentrations typically used for NMR (even without the second helix) rendering the tetramerization interface inaccessible for a potential interaction with the TID. Consequently, NMR titrations of the p63 OD with a peptide derived from the TID (601-616) containing the FTL motif did not show any interaction. Interestingly, titration experiments of the p73 OD known to exist as a mixture of dimers and tetramers (Coutandin et al., 2009) with the p63 TID peptide resulted in the disappearance of all peaks by the formation of soluble aggregates. Repeating this titration with the p73 TD that forms stable tetramers that are stabilized by the second helix did not show any interaction (data not shown). Although these experiments are quite indirect and involve mixing of p63 and p73 domains they suggest that the p63 TID can interact with the p73 OD but not with the p73 TD, the difference between both being that the p73 OD exists in an equilibrium with dimeric forms with an accessible tetramerization interface.

The N-terminal transactivation domain binds to the OD of p63

Based on previous pulldown experiments we had suggested that formation of the closed state of TAp63α involves both the N-terminal transactivation domain (TA) and the C-terminal TID (Serber et al., 2002). To further investigate the importance of the TA

domain for the formation of the closed conformation we performed SEC analysis of ΔNp63α, a natural occurring isoform lacking the first 45 amino acids (Yang et al., 1998). Figure 6A shows that ΔNp63α is tetrameric demonstrating that the simultaneous presence of both the TA and the TI domains is necessary for the formation of a closed, dimeric conformation.

To test whether the OD can interact with the TA domain we titrated the p63 OD with peptides derived from the TA1 (9-32) and TA2 (49-78) regions of the transactivation domain (Burge et al., 2009). While the TA2 peptide did not interact, titrations with the TA1 peptide showed strong chemical shift perturbations (CSP) (Figure 6B, 6C and 6F). Mapping these CSPs onto the OD structure revealed that the binding site for this peptide overlaps with the location of the second helix within the TD (Figure 6E). This result predicts that the TA1 peptide should not interact with the TD of p63 which contains the second helix. Repeating the titration experiments with the p63 TD indeed showed only very small chemical shift changes, suggesting that both the second helix of the TD and the TA1 peptide compete for the same binding site.

The N-terminal transactivation domain of p53 contains three important residues, Phe19, Trp23 and Leu26, that are known to be involved in binding transcriptional co-activators (Kussie et al., 1996). In addition, Mdm2 uses the same region for binding p53 (Horikoshi et al., 1995; Kussie et al., 1996; Lu and Levine, 1995; Thut et al., 1995). In the crystal structure of a peptide derived from the p53 transactivation domain in complex with Mdm2, the same three amino acids form one face of a helix and are deeply buried in a

hydrophobic pocket of Mdm2. All three amino acids are conserved in p63. If binding of the N-terminal transactivation domain to the OD contributes to inhibition the most likely mechanism would involve burying these three amino acids to prevent them from interacting with the transcriptional machinery. Mutating these residues to alanine resulted in a complete loss of interaction with the OD, suggesting that these three amino acids are indeed important for binding, probably by forming one face of a helix (Figure 6D and 6F).

Model of the structural regulation of p63's activity

The data reported here suggest the following model for the regulation of the activity of TAp63α in oocytes. In non-stressed oocytes that are not recruited for ovulation yet, the protein is kept in a dimeric, closed and inactive conformation (Figure 7) Both the N-terminal transactivation domain and the C-terminal TI domain are required to form this closed state. The TD plays an essential role as a structural integration domain that interacts with the TA on one side and potentially with the TID on the tetramerization interface. Additional direct contacts between the TA and TI domains might be possible as suggested by pulldown experiments. The activity of this compact dimeric form is reduced by decreasing its DNA-binding affinity and probably further by burying important amino acids of the TA. Activation for example induced by γ-irradiation requires phosphorylation which triggers a conformational switch that releases the inhibitory interactions, allowing TAp63α to tetramerize and to interact with the transcriptional machinery through its TA. The active

tetrameric state is stabilized by the second helix of the TD that reaches across the interface and occupies the binding site of the TA. This model explains how TAp63α can reach high expression levels in oocytes without inducing apoptosis. Activation of TAp63α, however, is an "irreversible" process that once started leads to the destruction of the oocytes.

DISCUSSION

The model presented for the regulation of TAp63α's transcriptional activity differs significantly from the model proposed for p53, the most famous member of this protein family. The main regulatory mechanism that determines the activity of p53 seems to be its stability. In non-stressed cells p53 is kept at low concentrations through fast degradation by the E3 ubiquitin ligases Mdm2 and Mdmx (Wade et al., 2010). Oncogenic signals result in a stabilization of p53 that leads to an increased cellular concentration. TAp63α on the other hand, is already highly expressed in non-stressed oocytes. DNA damage triggers a conformational change that activates the protein. In contrast to p53, this active form seems to be more susceptible to degradation than the inactive one (Figure 2A). This interpretation is supported by cell culture based experiments showing that transcriptional inactive p63 forms accumulate to much higher intracellular concentrations than active ones (Straub et al., 2010). Furthermore, it has been demonstrated that efficient degradation requires an accessible TA domain (Ying et al., 2005). Our NMR data indicate that the three amino acids that are important for binding of p53 to Mdm2 and that are conserved in p63 are most

likely not accessible in the inhibited dimeric conformation. While the interaction of p63 with Mdm2 is still discussed controversially in the literature it is obvious that interaction and possible degradation could only occur after activation and the formation of an open state of TAp63α. Regulating the intracellular concentration of TAp63α most likely involves other mechanisms for example other E3 ligases. To this end the Hect-domain E3 ligase ITCH has been shown to ubiquitinate and promote the degradation of p63 (Rossi et al., 2006). Another mechanisms that might be specific for the closed dimeric conformation is sumoylation that occurs at the very end of the C-terminus of TAp63α where a classical sumoylation site exists. In cell culture experiments mutation of the sumoylation site increased TAp63α's intracellular concentration (Straub et al., 2010). It might therefore be possible that the inhibited dimeric form gets slowly degraded through sumoylation while the active form becomes ubiquitinated by E3 ligases such as ITCH or Mdm2. Degradation of activated TAp63α might occur in oocytes that show a sublethal amount of DNA damage. Measurements of dose-response curves have shown that γ-irradiation with 0.1 Gy results on average in 1 double strand break per cell. Most of the oocytes survive this condition with only a small fraction of TAp63α becoming phosphorylated. Irradiation with 0.45 Gy, however, produces on average 10 double strand breaks per cell and leads to the elimination of virtually all premature oocytes that show p63 expression (Suh et al., 2006). Degradation of activated TAp63α might therefore help to establish a certain threshold for the induction of cellular death in oocytes.

A further difference between TAp63α and p53 is that TAp63α is expressed in cells arrested in prophase of meiosis I. Consequently TAp63α induces only cellular death and not cell cycle arrest. From an evolutionary standpoint, quality control of the genetic integrity of oocytes seems to the original function of the p53 protein family and cell cycle arrest and tumor suppression evolutionary later developed abilities. This hypothesis is based on the identification of p53-like genes in invertebrate species, for example C. elegans. Without renewable tissue and with a relatively short life span, this worm does not require tumor suppression mechanisms. However, its germ cells express a p53-like protein, Cep-1. Both structurally and functionally Cep-1 resembles more closely p63 (Derry et al., 2001; Ou et al., 2007), suggesting that p63 and quality control in germ cells are the ancestral member and function of this protein family.

EXPERIMENTAL PROCEDURES

Protein expression and purification in *E. coli*. Genes for murine TAp63α, TAp63γ, TAp63αFTL(Straub et al., 2010) and TAp63αR (TAp63α carrying the mutation R279H in the DBD(Celli et al., 1999)) were cloned into the pMAL-c4X vector (New England Biolabs, NEB). All proteins had an additional C-terminal non cleavable His_6-tag. The gene for TAp63α was cloned in the pBH4 vector as well (gift from Wendell Lim laboratory, UCSF, CA, USA) for expression with an N-terminal His_6-tag, cleavable with TEV protease. The gene for murine ΔNp63α from amino acids 1-561 was cloned into a modified pMAL vector leading to a fusion protein having a N-terminal His_6-tag followed by MBP

and a TEV protease cleavage site (His-MBP-ΔNp63α^{PPR}). Proteins were expressed in T7 express competent *E. coli* cells (NEB) and purified using Ni-Sepharose Fast Flow (GE Healthcare) and Amylose resin (NEB) according to standard protocols. Proteins were further purified by size exclusion chromatography (SEC) using a preparative Superose 6 column (GE Healthcare) in 10 mM potassium phosphate buffer, pH = 7.6 with 200 mM NaCl. All following experiments were performed in this buffer if not denoted differently.

Protein expression in rabbit reticulocyte lysate. N-terminally myc-tagged murine TAp63α, TAp63αFTL and TAp63α and TAp63αFTL lacking helix H2 in the TD (TAp63αΔHelix, TAp63αFTLΔHelix), TAp63α bearing the L384A and M385A mutation (TAp63αLM), TAp63α harboring the L384A mutation (TAp63αL) and TAp63α harboring the TD mutations M374Q and I378R (TAp63αMI) were expressed from a pcDNA3.1 vector in rabbit reticulocyte lysate (TNT Quick Coupled Transcription/Translation Systems, Promega) using 1 µg plasmid DNA. Proteins were used for SEC analysis with a Superose 6 PC 3.2/30 column (GE Healthcare).

Size exclusion chromatography (SEC). SEC of recombinant proteins expressed in *E. coli* was performed at 16 °C using a Superose 6 10/300 GL column (GE Healthcare) The column was calibrated using Blue Dextran 2000 and the calibration standard proteins Thyroglobulin (669 kDa), Ferritin (440 kDa), Aldolase (158 kDa) and Ovalbumin (43 kDa) (HMW Calibration Kit, GE Healthcare). Analytical SEC of p63 was performed at 4 °C using a Superose 6 PC 3.2/30 column (GE Healthcare) at a flow rate of 0.05 mL/min with

collection of 50 µL elution fractions. Relevant SEC fractions were analyzed by Western blotting.

Fluorescence anisotropy. Fluorescence anisotropy experiments were performed at room temperature using a Jasco spectrofluorometer FP-6500 (Jasco Labortechnik). Purified MBP-TAp63α, MBP-TAp63αFTL and MBP-TAp63γ expressed in *E. coli* were added to 15 nM of 5'-Fluorescein tagged 30 bp dsDNA with the sequence of the p21 promoter response element (5'-GGCAGGAACATGTCCCAACATGTTGAGCCG-3') in final monomeric concentrations between 0.1-15 µM in a total volume of 500 µL. Protein and DNA were incubated for 30 min at room temperature before being measured. Fluorescence anisotropy was measured with excitation at 488 nM and emission at 516 nm. Each experimental series was repeated three times (MBP-TAp63α and MBP-TAp63αFTL) or twice (MBP-TAp63γ) and averaged. Data were analyzed using the software Origin (OriginLab Corporation). Fitting the data to an equation assuming one binding site or two binding sites showed a better agreement for the later model. The dissociation constants K_D were, therefore, calculated by fitting the data to

the equation shown below resembling a two-binding-site model:

$$Y = \frac{A^{C1}K_2[P] + A^{C2}[P]^2 + K_1K_2A^D}{K_1K_2 + K_2[P] + [P]^2}$$

with Y being the measured fluorescence anisotropy, A^{C1}, A^{C2} and A^D the fluorescence anisotropy values of a complex with one p63 oligomer bound to DNA, of a complex with

two p63 oligomers bound to DNA and of the free DNA, respectively, [P] the monomeric concentration of the protein and K_1 and K_2 the two binding constants. For MBP-TAp63αFTL and MBP-TAp63γ the K_D values for the second binding site were 47.1 ± 115.7 µM and 20.8 ± 18.0 µM, respectively, suggesting that they represent unspecific binding. For MBP-TAp63α a negative K_D value of -0.021 ± 0.02 µM was obtained which we cannot interpret at the moment. Control experiments were performed with MBP-TAp63α, MBP-TAp63αFTL, MBP-TAp63γ and MBP-TAp63αR as described. 300 nM of 5'-Fluorescein tagged 39 bp dsDNA with either a p63 binding sequence designed on the basis of a SELEX (Ortt and Sinha, 2006) screening (5'-CCTATTCTAGACATGTGAGGACATGTCGATACTTATTCC-3') or a random sequence (5'-CGAGTTGTAAGTCGAATTGATACCATAATGCACTACACG-3') were used.

Multiangle Light Scattering (MALS). SEC-MALS experiments were performed at room temperature using a Superdex 200 5/150 GL column (GE Healthcare) at a flow rate of 0.3 mL/min. Elution of 80 µL of purified proteins of ~ 1 mg/mL concentration was detected using an Optilab rEX Refractive Index Detector and a Dawn Heleos II at a Laser wavelength of 658 nm (Wyatt Technology) to measure the intensity of the Rayleigh scattering as a function of the angle to determine the weight average molar mass $\overline{M}_W$ of peak locations. Data were processed using ASTRA software package 5.3.4.11 (Wyatt Technology).

Mice and irradiation. The animal care and handling were performed according to the guidelines set by the World Health Organization (Geneva, Switzerland). Five day old (P5) female CD-1 mice were purchased from Charles River Laboratories. The animals were divided into two groups, NIRR (wild type non-irradiated) and IRR (irradiated wild type). The IRR mice were exposed to 0.52 Gy of whole-body gamma-irradiation on a rotating turntable in a ^{137}Cs irradiator, at a dose rate of 2,387 Gy/min. The ovaries of both groups were harvested after 6 h.

Analysis of murine ovary extracts. 16 Ovaries of NIRR and IRR mice were separately lysed by mechanical force in 50 mM sodium phosphate, pH = 7.2, 150 mM NaCl, 0.1 % Triton X-100, EDTA free protease inhibitor cocktail (Roche) and phosphatase inhibitor cocktail (Roche) in a total volume of 70 µL. After centrifugation at 20000 g for 15 min at 4 °C the supernatant was injected on a Superose 6 PC 3.2/30 column (GE Healthcare) equilibrated with 50 mM sodium phosphate, 100 mM NaCl, EDTA free protease inhibitor cocktail and phosphatase inhibitor cocktail at 4 °C and eluted at a flow rate of 0.05 mL/min. Elution fractions of 50 µL volume were collected and mixed with reducing loading buffer for western blot analysis. Samples were separated using 10 % Bis-Tris NuPAGE gels (Invitrogen) in MOPS buffer at 4 °C and subsequently transferred on a Hybond-P membrane (GE Healthcare) using a XCell II blot module (Invitrogen). After transfer the blots were blocked with 5 % skim milk in TBS buffer containing 0.1 % TWEEN-20 and probed over night at 4 °C with 4A4(Suh et al., 2006) antibody directed against p63. Detection was performed using goat anti-mouse IgG peroxide conjugate (Sigma Aldrich). The blots were quantified using Biometra BioDocAnalyze 2.0 software.

λ-Phosphatase treatment. 30 ovaries of IRR mice were lysed in 50 mM sodium phosphate, pH = 7.2, 150 mM NaCl, EDTA free protease inhibitor cocktail (Roche) and 1.25 mM $MnCl_2$ in a final volume of 120 µL as described above. Afterwards the lysate was split into two fractions of 60 µL each. To one fraction 15 µL of λ-Protein Phosphatase (NEB), to the other 15 µL of λ-Protein Phosphatase storage buffer were added. Both samples were incubated at 30 °C for 45 min. Samples were centrifuged and analyzed by SEC and Western blotting as described above.

NMR titrations. 100 µM human p63 OD (358-391) and human p63 TD (358-416) were cloned and expressed as described (Coutandin et al., 2009). Peptides (wt p63 TA1 (9-32) and p63 TA1FWL with the triple mutation F16A, W20A, L23A and mutation F10W) were ordered from Genscript (Piscataway, NJ, USA). NMR titration experiments (up to 15-fold excess of peptide) of 15N labeled protein samples in 25 mM HEPES, 50 mM Arg, 50 mM Glu, pH = 7.5 were performed at 303 K on Bruker Avance spectrometers equipped with ^{1}H triple resonance, z-gradient cryogenic probes operating at proton frequencies of 900 and 800 MHz. The resonances of human p63 OD were assigned with TROSY-based HNCACB and HNCACO experiments. The spectra were analyzed with UCSF SPARKY 3.114. Structural Models of human p63 OD based on the structure of human p73 TD (PDB ID 2KBY) are illustrated using Pymol 1.0.

Glutaraldehyde cross links. *E. coli* expressed and purified MBP-TAp63α, MBP-TAp63αFTL and MBP-TAp63γ at concentrations of 0.5, 2 and 10 µM and TAp63α at concentrations of 0.5, 2 and 4 µM were cross linked with glutaraldehyde (Merck) at a final

concentration of 0.125 % (*w*/*v*). Samples were incubated at 16 °C and the cross linking reaction stopped after 3, 20 and 68 min by the addition of reducing loading buffer. The samples were immediately analyzed by SDS-PAGE using 4-12 % Bis-Tris NuPAGE gels (Invitrogen) followed by Coomassie staining.

LILBID mass spectrometry. The mass spectra were recorded using the previously described LILBID-MS method(Hoffmann et al., 2009; Morgner et al., 2007). In brief, tiny droplets of native solution (V ~ 65pL) are injected into high vacuum where they are irradiated by mid-IR laser pulses. During the subsequent explosion of the droplets the molecules of interest are set free and analyzed by a time-of-flight mass spectrometer (TOF). For the spectrum shown in Fig. S2 MBP-TAp63α expressed in *E. coli* was dialyzed over night against 10 mM potassium phosphate, pH = 7.6 without NaCl. Approximately 5µL of solution were loaded into the mass spectrometer.

Analytical Ultracentrifugation. Samples were studied in a solution of 20 mM potassium phosphate pH 7.5, 200 mM NaCl, at a temperature of 4 °C. Sedimentation of particles was monitored using the absorbance optics in a Beckman XL-I Analytical Ultracentrifuge equipped with a Ti-50 rotor. Sedimentation equilibrium experiments were carried out on samples at monomer concentrations of 1-8 µM, in six-sector cells, employing rotor speeds of 7,000, 9,000 and 24,000 rpm. At each speed, radial scans were collected after 22 and 24 hours and compared to confirm that equilibrium conditions had been established. The later of these scans was used for global fitting (i.e., 6 scans per protein) to a monomer-dimer association model in HETEROANALYSIS(Cole, 2004) or in ULTRASPIN(www.ultraspin.mrc-cpe.cam.ac.uk), using the doubled monomolecular

weight as the molecular weight of the smallest species in the solution (i.e., the 'monomer') and a partial specific volume, V*, calculated using SEDNTERP(Laue et al., 1992). AUC sedimentation velocity experiments, performed prior to the equilibrium experiments, showed the absence of monomers under the experimental conditions.

***In vitro* phosphorylation.** Radiolablling of MBP-TAp63α was performed as described previously(Schleiff et al., 2003a; Schleiff et al., 2003b). The phosphorylation profile was visualised by colloidal coomassie staining and autoradiography.

Cell culture experiments. Transactivation assays of TAp63α, TAp63γ, TAp63αLM, TAp63αM, TAp63αMI as well as the corresponding western blot analyses were performed as described previously(Straub et al., 2010). Each measurement was carried out in triplicates.

Pulldown experiments. Pulldown experiments using TAp63αLM, TAp63αL, TAp63αMI, TAp63γ, TAp63α, TAp63αΔHelix, TAp63αFTL and TAp63αFTLΔHelix expressed in rabbit reticulocyte lysate as well as the corresponding western blot analyses were performed as described previously(Straub et al., 2010). Each experiment was performed three times and the results were averaged.

Western blotting. Western blot analysis was performed as described previously(Straub et al., 2010).

SUPPLEMENTAL INFORMATION

Supplemental Information includes 5 figures and one table an can be found online.

ACKNOWLEDGEMENTS

The research was funded by the DFG (DO 545/2-1), EU-Grant EPISTEM (LSHB-CT-019067), the Centre for Biomolecular Magnetic Resonance at the University of Frankfurt (BMRZ) and the Cluster of Excellence Frankfurt (Macromolecular Complexes). The Structural Genomics Consortium is a registered charity (number 1097737) that receives funds from the Canadian Institutes for Health Research, the Canadian Foundation for Innovation, Genome Canada through the Ontario Genomics Institute, GlaxoSmithKline, Karolinska Institutet, the Knut and Alice Wallenberg Foundation, the Ontario Innovation Trust, the Ontario Ministry for Research and Innovation, Merck & Co., Inc., the Novartis Research Foundation, the Swedish Agency for Innovation Systems, the Swedish Foundation for Strategic Research and the Wellcome Trust. The authors declare no competing financial interests.

REFERENCES

Brandt, T., Petrovich, M., Joerger, A.C., and Veprintsev, D.B. (2009). Conservation of DNA-binding specificity and oligomerisation properties within the p53 family. BMC Genomics *10*, 628.

Brooks, C.L., and Gu, W. (2006). p53 ubiquitination: Mdm2 and beyond. Mol Cell *21*, 307-315.

Burge, S., Teufel, D.P., Townsley, F.M., Freund, S.M., Bycroft, M., and Fersht, A.R. (2009). Molecular basis of the interactions between the p73 N terminus and p300: effects on transactivation and modulation by phosphorylation. Proc Natl Acad Sci U S A *106*, 3142-3147.

Celli, J., Duijf, P., Hamel, B.C., Bamshad, M., Kramer, B., Smits, A.P., Newbury-Ecob, R., Hennekam, R.C., Van Buggenhout, G., van Haeringen, A., *et al.* (1999). Heterozygous germline mutations in the p53 homolog p63 are the cause of EEC syndrome. Cell *99*, 143-153.

Chan, W.M., Siu, W.Y., Lau, A., and Poon, R.Y. (2004). How many mutant p53 molecules are needed to inactivate a tetramer? Mol Cell Biol *24*, 3536-3551.

Chene, P. (2001). The role of tetramerization in p53 function. Oncogene *20*, 2611-2617.

Cole, J.L. (2004). Analysis of heterogeneous interactions. Methods Enzymol *384*, 212-232.

Coutandin, D., Löhr, F., Niesen, F., Ikeya, T., Weber, T., Schäfer, B., Bullock, A., Yang, A., Güntert, P., Knapp, S., *et al.* (2009). Conformational stability and activity of p73 require a second helix in the tetramerization domain. Cell Death Differ *16*, 1582-1589.

Davison, T.S., Nie, X., Ma, W., Lin, Y., Kay, C., Benchimol, S., and Arrowsmith, C.H. (2001). Structure and functionality of a designed p53 dimer. J Mol Biol *307*, 605-617.

De Laurenzi, V., Catani, M., Terrinoni, A., M, C., G, M., A, C., M, L., and Knight, R. (1999). Additional complexity in p73: induction by mitogens in lymphoid cells and identification of two new splicing variants epsilon and zeta. Cell Death Differ *6*, 389-390.

De Laurenzi, V., Costanzo, A., Barcaroli, D., Terrinoni, A., Falco, M., Annicchiarico-Petruzzelli, M., Levrero, M., and Melino, G. (1998). Two new p73 splice variants, g and d, with different transcriptional activity. J Exp Med *188*, 1763-1768.

Derry, W.B., Putzke, A.P., and Rothman, J.H. (2001). Caenorhabditis elegans p53: role in apoptosis, meiosis, and stress resistance. Science *294*, 591-595.

Flores, E.R., Sengupta, S., Miller, J.B., Newman, J.J., Bronson, R., Crowley, D., Yang, A., McKeon, F., and Jacks, T. (2005). Tumor predisposition in mice mutant for p63 and p73: evidence for broader tumor suppressor functions for the p53 family. Cancer Cell *7*, 363-373.

Hoffmann, J., Schmidt, T.L., Heckel, A., and Brutschy, B. (2009). Probing the limits of liquid droplet laser desorption mass spectrometry in the analysis of oligonucleotides and nucleic acids. Rapid Commun Mass Spectrom *23*, 2176-2180.

Horikoshi, N., Usheva, A., Chen, J., Levine, A.J., Weinmann, R., and Shenk, T. (1995). Two domains of p53 interact with the TATA-binding protein, and the adenovirus 13S E1A protein disrupts the association, relieving p53-mediated transcriptional repression. Mol Cell Biol *15*, 227-234.

Jeffrey, P.D., Gorina, S., and Pavletich, N.P. (1995). Crystal structure of the tetramerization domain of the p53 tumor suppressor at 1.7 angstroms. Science *267*, 1498-1502.

Joerger, A.C., Rajagopalan, S., Natan, E., Veprintsev, D.B., Robinson, C.V., and Fersht, A.R. (2009). Structural evolution of p53, p63, and p73: implication for heterotetramer formation. Proc Natl Acad Sci U S A *106*, 17705-17710.

Kaghad, M., Bonnet, H., Yang, A., Creancier, L., Biscan, J.C., Valent, A., Minty, A., Chalon, P., Lelias, J.M., Dumont, X., *et al.* (1997). Monoallelically expressed gene related to p53 at 1p36, a region frequently deleted in neuroblastoma and other human cancers. Cell *90*, 809-819.

Kussie, P.H., Gorina, S., Marechal, V., Elenbaas, B., Moreau, J., Levine, A.J., and Pavletich, N.P. (1996). Structure of the MDM2 oncoprotein bound to the p53 tumor suppressor transactivation domain. Science *274*, 948-953.

Laue, T.M., Shah, B.D., Ridgeway, T.M., and Pelletier, S.L., eds. (1992). Analytical Ultracentrifugation in Biochemistry and Polymer Science (Royal Society of Chemistry).

Lee, W., Harvey, T.S., Yin, Y., Yau, P., Litchfield, D., and Arrowsmith, C.H. (1994). Solution structure of the tetrameric minimum transforming domain of p53. Nat Struct Biol *1*, 877-890.

Lu, H., and Levine, A.J. (1995). Human TAFII31 protein is a transcriptional coactivator of the p53 protein. Proc Natl Acad Sci U S A *92*, 5154-5158.

McGrath, J.A., Duijf, P.H., Doetsch, V., Irvine, A.D., de Waal, R., Vanmolkot, K.R., Wessagowit, V., Kelly, A., Atherton, D.J., Griffiths, W.A., *et al.* (2001). Hay-Wells syndrome is caused by heterozygous missense mutations in the SAM domain of p63. Hum Mol Genet *10*, 221-229.

Mills, A.A., Zheng, B., Wang, X.J., Vogel, H., Roop, D.R., and Bradley, A. (1999). p63 is a p53 homologue required for limb and epidermal morphogenesis. Nature *398*, 708-713.

Morgner, N., Kleinschroth, T., Barth, H.D., Ludwig, B., and Brutschy, B. (2007). A novel approach to analyze membrane proteins by laser mass spectrometry: from protein subunits to the integral complex. J Am Soc Mass Spectrom *18*, 1429-1438.

Ortt, K., and Sinha, S. (2006). Derivation of the consensus DNA-binding sequence for p63 reveals unique requirements that are distinct from p53. FEBS letters *580*, 4544-4550.

Ou, H.D., Löhr, F., Vogel, V., Mäntele, W., and Dötsch, V. (2007). Structural evolution of C-terminal domains in the p53 family. Embo J *26*, 3463-3473.

Rinne, T., Brunner, H.G., and van Bokhoven, H. (2007). p63-associated disorders. Cell Cycle *6*, 262-268.

Rossi, M., Aqeilan, R.I., Neale, M., Candi, E., Salomoni, P., Knight, R.A., Croce, C.M., and Melino, G. (2006). The E3 ubiquitin ligase Itch controls the protein stability of p63. Proc Natl Acad Sci U S A *103*, 12753-12758.

Schleiff, E., Jelic, M., and Soll, J. (2003a). A GTP-driven motor moves proteins across the outer envelope of chloroplasts. Proc Natl Acad Sci U S A *100*, 4604-4609.

Schleiff, E., Soll, J., Kuchler, M., Kuhlbrandt, W., and Harrer, R. (2003b). Characterization of the translocon of the outer envelope of chloroplasts. J Cell Biol *160*, 541-551.

Schmale, H., and Bamberger, C. (1997). A novel protein with strong homology to the tumor suppressor p53. Oncogene *15*, 1363-1367.

Senoo, M., Pinto, F., Crum, C.P., and McKeon, F. (2007). p63 Is essential for the proliferative potential of stem cells in stratified epithelia. Cell *129*, 523-536.

Senoo, M., Seki, N., Ohira, M., Sugano, S., Watanabe, M., Inuzuka, S., Okamoto, T., Tachibana, M., Tanaka, T., Shinkai, Y., *et al.* (1998). A second p53-related protein, p73L, with high homology to p73. Biochem Biophys Res Commun *248*, 603-607.

Serber, Z., Lai, H.C., Yang, A., Ou, H.D., Sigal, M.S., Kelly, A.E., Darimont, B.D., Duijf, P.H., Van Bokhoven, H., McKeon, F., *et al.* (2002). A C-terminal inhibitory domain controls the activity of p63 by an intramolecular mechanism. Mol Cell Biol *22*, 8601-8611.

Straub, W.E., Weber, T.A., Schäfer, B., Candi, E., Durst, F., Ou, H.D., Rajalingam, K., Melino, G., and Dötsch, V. (2010). The C-terminus of p63 contains multiple regulatory elements with different functions. Cell Death Dis *1*, e5.

Suh, E.K., Yang, A., Kettenbach, A., Bamberger, C., Michaelis, A.H., Zhu, Z., Elvin, J.A., Bronson, R.T., Crum, C.P., and McKeon, F. (2006). p63 protects the female germ line during meiotic arrest. Nature *444*, 624-628.

Thut, C.J., Chen, J.L., Klemm, R., and Tjian, R. (1995). p53 transcriptional activation mediated by coactivators TAFII40 and TAFII60. Science *267*, 100-104.

Tomasini, R., Tsuchihara, K., Wilhelm, M., Fujitani, M., Rufini, A., Cheung, C.C., Khan, F., Itie-Youten, A., Wakeham, A., Tsao, M.S., *et al.* (2008). TAp73 knockout shows genomic instability with infertility and tumor suppressor functions. Genes Dev *22*, 2677-2691.

Trink, B., Okami, K., Wu, L., Sriuranpong, V., Jen, J., and Sidransky, D. (1998). A new human p53 homologue. Nat Med *4*, 747-748.

Wade, M., Wang, Y.V., and Wahl, G.M. (2010). The p53 orchestra: Mdm2 and Mdmx set the tone. Trends Cell Biol *20*, 299-309.

www.ultraspin.mrc-cpe.cam.ac.uk, Center for Protein Engineering.

Yang, A., Kaghad, M., Wang, Y., Gillett, E., Fleming, M.D., Dotsch, V., Andrews, N.C., Caput, D., and McKeon, F. (1998). p63, a p53 homolog at 3q27-29, encodes multiple

products with transactivating, death-inducing, and dominant-negative activities. Mol Cell *2*, 305-316.

Yang, A., Schweitzer, R., Sun, D., Kaghad, M., Walker, N., Bronson, R.T., Tabin, C., Sharpe, A., Caput, D., Crum, C., *et al.* (1999). p63 is essential for regenerative proliferation in limb, craniofacial and epithelial development. Nature *398*, 714-718.

Yang, A., Walker, N., Bronson, R., Kaghad, M., Oosterwegel, M., Bonnin, J., Vagner, C., Bonnet, H., Dikkes, P., Sharpe, A., *et al.* (2000). p73-deficient mice have neurological, pheromonal and inflammatory defects but lack spontaneous tumours. Nature *404*, 99-103.

Ying, H., Chang, D.L., Zheng, H., McKeon, F., and Xiao, Z.X. (2005). DNA-binding and transactivation activities are essential for TAp63 protein degradation. Mol Cell Biol *25*, 6154-6164.

FIGURE LEGENDS

Figure 1. TAp63α is kept in an inactive dimeric state

(A) Comparison of the domain structure of p53, TAp63α, TAp63γ and ΔNp63α. (B) SEC chromatogram of TAp63α (green), MBP-TAp63α (black), MBP-TAp63αFTL (red) and MBP-TAp63γ (blue). Apparent molecular weights are indicated. Void volume and elution volumes of globular standard proteins with corresponding molecular weights are shown on the x-axis. (C-F) Change of differential refractive index (dRI, solid line) and of the molecular weight of the protein peak (MW, dotted line) in SEC-MALS analysis of MBP-TAp63α (C), TAp63α (D), MBP-TAp63αFTL (E) and MBP-TAp63γ (F). Calculated molecular weights are displayed. See also Figure S1 and Table S1.

Figure 2. Activation of TAp63α by phosphorylation in oocytes leads to tetramerization

(A) Western blot analysis of murine ooycte samples. p63 signals in the lysate of murine oocytes, SEC elution fractions at 1.3 mL (tetrameric protein) and 1.55 mL (dimeric protein) for both non-irradiated (NIRR) and γ-irradiated (IRR) oocytes are displayed. (B) Western blot of SEC elution fractions from 1.2 to 1.65 mL of NIRR ovary lysate. Bar diagram showing relative p63 signal intensities of the Western blot shown in (C). The sum of the intensities of all fractions was set to 100%. Corresponding data and analysis for IRR ovary lysate is shown in (D) and (E). See also Figure S2.

Figure 3. Functional consequences of tetramer formation

(A-C) DNA-binding of MBP-TAp63α (A), MBP-TAp63αFTL (B) and MBP-TAp63γ (C) to the p21 response element measured by fluorescence anisotropy. Solid lines show the fit to a two-binding-site model (see Supplemental Information). Error bars show standard deviation. (D) Western blot analysis of SEC elution fractions between 1.1 and 1.7 mL of IRR ovary lysate without λ-phosphatase treatment. (E) Bar diagram representing the relative p63 intensities of the Western blot shown in (D). Corresponding Western blot and bar diagram for IRR lysate with λ-phosphatase treatment are shown in (F) and (G), respectively. See also Figure S3.

Figure 4. The second Helix of the TD is essential for tetramer formation

(A) Western blot analysis of SEC elution fractions between 1.05 and 1.70 mL of TAp63α expressed in rabbit reticulocyte lysate using an anti-myc antibody. (B) Bar diagram showing the relative p63 intensities of the Western blot shown in (A). Corresponding data and analysis of TAp63αFTL, TAp63αΔHelix and TAp63αFTLΔHelix are shown in (C), (D), (E), (F) and (G), (H), respectively. See also Figure S4.

Figure 5. The TD of TAp63α plays an essential role in maintaining the inhibited dimeric state

(A) Sequence alignment of the TDs of human p73 and murine p63. Conserved regions are indicated by grey boxes. Amino acids that were mutated in p63 are shown in red, cyan and orange. (B-D) Structure of the human p73 TD (PDB access code: 2KBY). Side chains of residues that are homologous to the amino acids mutated in p63 are shown in the same colors as in (A). (B) shows mutations in TAp63αMI, (C) shows mutations in TAp63αL and (D) shows mutations in TAp63αLM. (E) Transcriptional activities on the p21 promoter in SAOS2 cells normalized to the protein concentration of TAp63αLM, TAp63αL, TAp63αMI, TAp63α and TAp63γ. Error bars show standard deviation. (F) Western blot analysis of pulldown experiments with TAp63αLM, TAp63αL, TAp63αMI, TAp63α and TAp63γ. The input and pulldown for each protein are shown. (G) Bar diagram showing the quantitative analysis of the pulldown experiments shown in (F). Error bars show standard deviation. See also Figure S5.

Figure 6. p63 TA1 binds to the oligomerization domain of p63

(A) SEC chromatogram of His-MBP-ΔNp63α^{PPR} lacking the last 25 unstructured residues. The apparent molecular weight is indicated. Void volume and elution volumes of globular standard proteins with corresponding molecular weights are shown on the x-axis. (B) Chemical shift pertubations (CSPs) on p63 OD (color coded) and p63 TD (gray) after addition of p63 TA1. OD residues showing CSPs are colored in blue, those with CSP > 0.1

ppm are shown in red and those with CSPs > 0.05 ppm are shown in yellow. (C and D) [^{15}N,^{1}H]-TROSY spectra of ^{15}N-labeled p63 OD in presence (red) and absence (blue) of p63 TA1 (C) and of p63 TA1FWL (D). (E) Model of p63 TD based on the structure of human p73 TD. Residues are colored according to the code in (B). Helix H2 of the TD (white) lies on top of the TA1-OD interaction interface. H2 is either shown as a ribbon or as a space-filling model. (F) Sequences of p63 TA1 and p63 TA1FWL with the additional F10W mutation for UV_{280nm}-based quantification.

Figure 7. Model of the inhibition of TAp63α

Activation requires interruption of the TA-TID-TD interactions resulting in an open conformation that enables tetramerization. Tetramers are then stabilized by helix H2 in the TD that reaches across the tetramerization interface.

Figure 1

Click here to download Figure: Deutsch et al. Figure 1.pdf

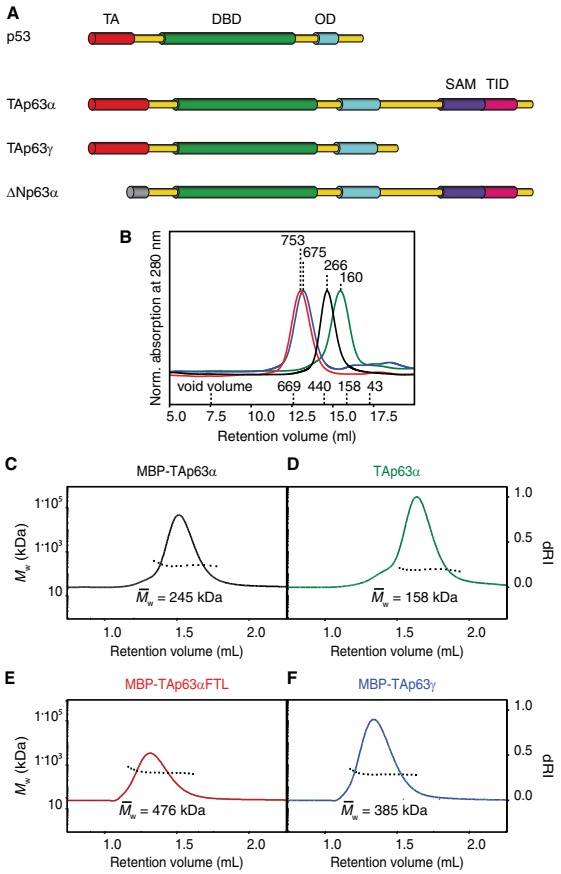

Figure 1

Figure 2

Click here to download Figure: Deutsch et al. Figure 2.pdf

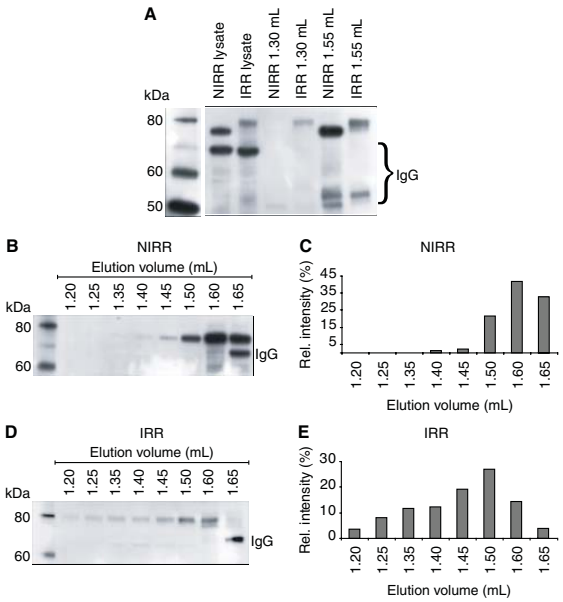

Figure 2

Figure 3

Click here to download Figure: Deutsch et al. Figure 3.pdf

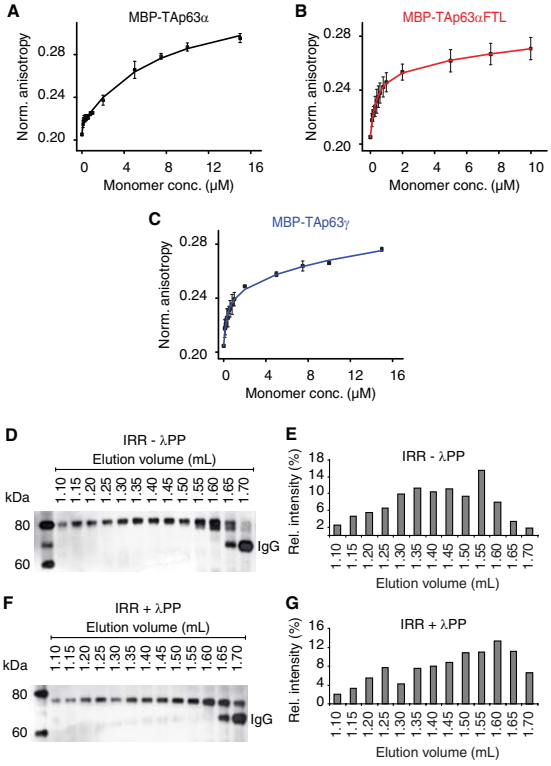

Figure 3

Figure 4

Click here to download Figure: Deutsch et al. Figure 4.pdf

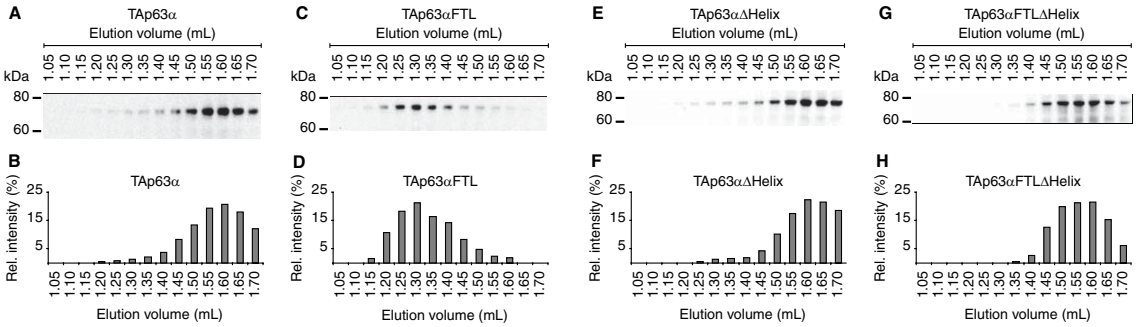

Figure 4

Figure 5

Click here to download Figure: Deutsch et al. Figure 5.pdf

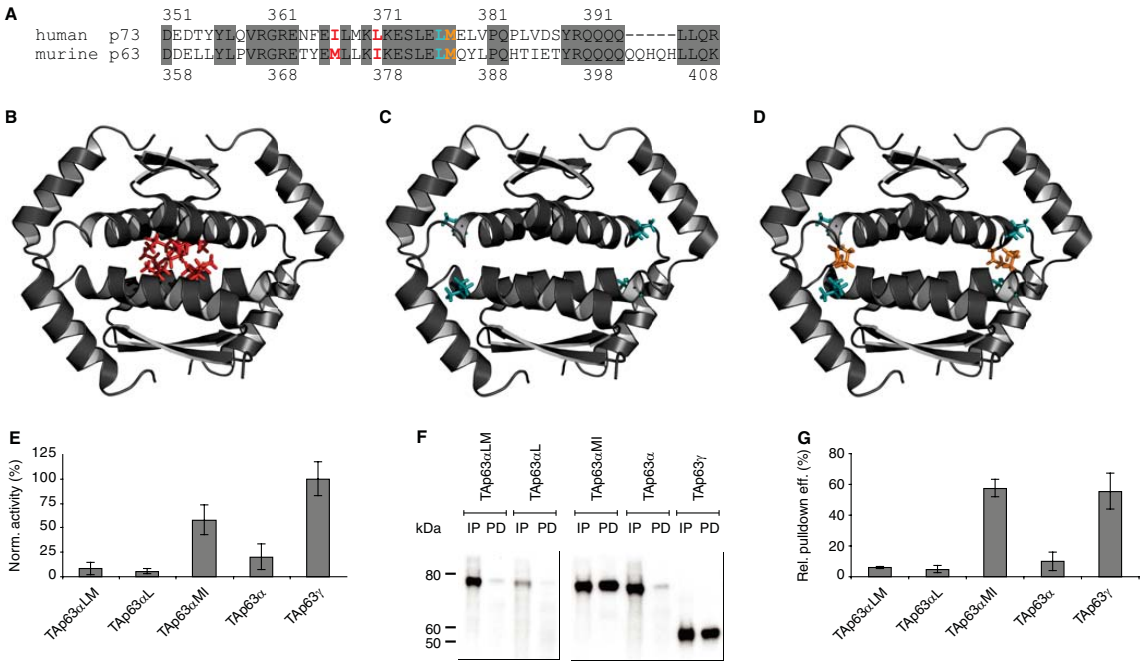

Figure 5

Figure 6

Click here to download Figure: Deutsch et al. Figure 6.pdf

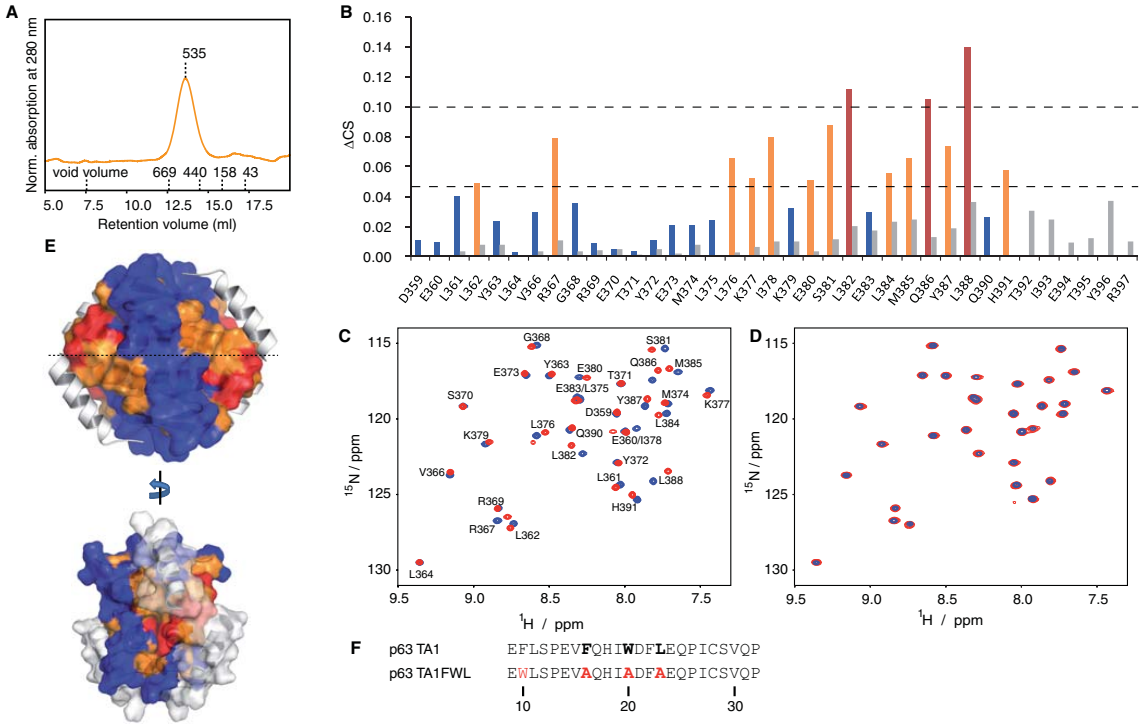

Figure 6

Figure 7
Click here to download Figure: Deutsch et al. Figure 7.pdf

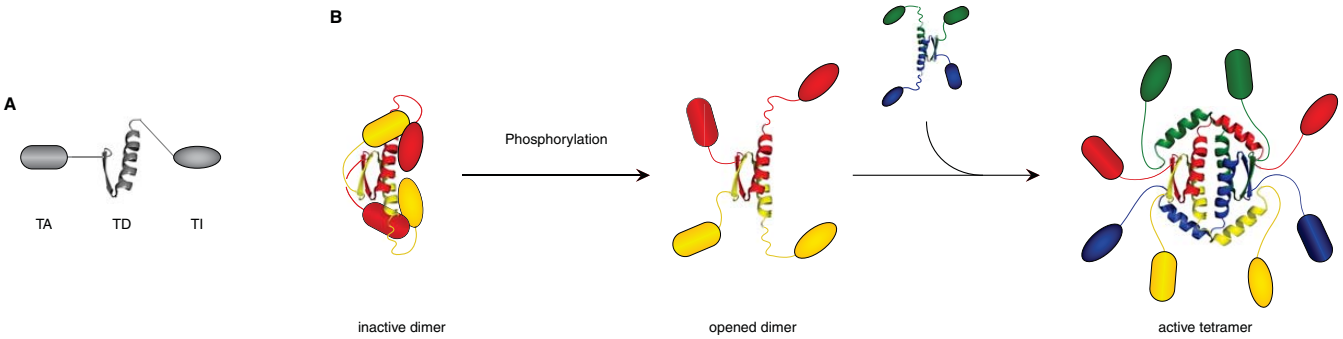

Figure 7

PROCEEDINGS OF THE ROYAL SOCIETY A

Proc. R. Soc. A (2010) **466**, 1489–1513
doi:10.1098/rspa.2009.0107
Published online 26 August 2009

Dense-shell glycodendrimers: UV/Vis and electron paramagnetic resonance study of metal ion complexation

By Dietmar Appelhans[1,*], Ulrich Oertel[1], Roberto Mazzeo[2], Hartmut Komber[1], Jan Hoffmann[3], Steffen Weidner[4], Bernhard Brutschy[3], Brigitte Voit[1] and Maria Francesca Ottaviani[2,*]

[1]*Leibniz Institute of Polymer Research Dresden, Hohe Str. 6, 01069 Dresden, Germany*
[2]*Department of Geological Sciences, Chemical and Environmental Technologies, University of Urbino, 61029 Urbino, Italy*
[3]*Institute for Physical and Theoretical Chemistry, Goethe Universität, Max-von-Laue-Str. 7, 60438 Frankfurt, Germany*
[4]*Division I.3 Structure Analysis: Polymer Analysis, BAM—Federal Institute for Materials Research and Testing, Richard-Willstätter-Strasse 11, 12489 Berlin, Germany*

The development of dendritic metal ion carrier systems for use in a biological environment is a challenging task as the carrier system must possess multiple features (e.g. a protective shell for metal decomplexation, targeting functions, metal–intradendrimer complexes, etc.) to substitute for the function of metal proteins in processes such as copper metabolism. Thus, Cu(II) complexation by a series of poly(propyleneimine) glycodendrimers ranging up to the fifth generation that have either a dense maltose or maltotriose shell was investigated by UV/Vis spectroscopy and electron paramagnetic resonance (EPR). As a necessary step towards potential biological application, we elucidated the complexation capacity, location of the Cu(II)–dendrimer complexes and the Cu(II) coordination sphere in the dendritic environment. A generation-dependent Cu(II) complexation was found. Furthermore, analysis of the EPR spectra revealed that internal and external Cu(II) coordination and the symmetry (axial and rhombic) of the generated complexes depend on the oligosaccharide shell, dendrimer generation and the relative concentrations of Cu(II) and the dendrimers. Both axial and rhombic symmetries are generation dependent, but also distort with increasing generation number. External coordination of Cu(II) is supported by sugar groups and water molecules. Finally, a third-generation dendrimer with a maltose shell was used to explore the general complexation behaviour of the dendritic poly(propyleneimine) scaffold towards different metal ions [Cu(II), Ag(I), VO(IV), Ni(II), Eu(III) and UO_2(VI)].

Keywords: glycodendrimers; metal ion complexation; metal ion–intradendrimer complexes; electron paramagnetic resonance study

*Authors for correspondence (applhans@ipfdd.de; maria.ottaviani@uniurb.it).

Electronic supplementary material is available at http://dx.doi.org/10.1098/rspa.2009.0107 or via http://rspa.royalsocietypublishing.org.

One contribution of 7 to a Special feature ‘Current research trends in dendritic materials’.

Received 26 February 2009
Accepted 17 April 2009

1. Introduction

The need to increase our fundamental understanding of highly branched architecture, as well as its promising potential for material and life science applications, motivates intensive research efforts in the expanding field of dendrimer chemistry (Bosman *et al.* 1999; Boas & Heegaard 2004; Lee *et al.* 2005; Agarwal *et al.* 2008; Hwang *et al.* 2008). This focus on dendrimers, large molecules with precise (macro)molecular structures, is due to their availability and outstanding/unusual properties that make them suitable for a broad range of applications. One challenging aspect of dendrimer chemistry is the complexation/coordination of metal ions by central core units (Saudan *et al.* 2004), interior and exterior branches (Bosman *et al.* 1997; Diallo *et al.* 2004) and complexing units in the outer shell (Wiener *et al.* 1996). Thus, work on dendrimers contributes significantly to the metal complexation field (Crooks *et al.* 2001*a*,*b*), which includes recycling and separation (de Jesus & Flores 2008), magnetic resonance imaging (Venditto *et al.* 2005), catalysis (Reek *et al.* 2006), sensing (Astruc *et al.* 2008) and organic light emitting diodes (Hwang *et al.* 2008).

Recent studies have focused on using dendrimers as metal carrier systems for therapeutic and diagnostic applications in biological environments. First, *in vitro* and *in vivo* trials have successfully demonstrated the transfection of dendrimer-stabilized metal nanoparticles that can serve as biomarkers of cellular trafficking, target cancer cells and aid imaging (Lesniak *et al.* 2005; Shi *et al.* 2007). Additionally, the accumulation of dendrimers without targeting properties in various organs has also been reported (Minchin 2008). Despite these findings, however, the use of dendrimers as metal ion carriers for such applications requires further structural improvements, allowing only metal ion–intradendrimer complexes to exist in order to avoid decomplexation processes easily initiated by, for example, enzymes and proteins *in vivo*. The well-established unmodified poly(amidoamine) (PAMAM) (Crooks *et al.* 2001*a*,*b*; Diallo *et al.* 2008) and poly(propyleneimine) (PPI) (Bosman *et al.* 1997) dendrimers are known to complex with a variety of metal ions in organic and aqueous solution, but these complexations preferably take place on the dendrimer surface. Such metal ion complexes will be destroyed by proteins and bio-active compounds that detoxify cells. Thus, these dendrimers are not suited for use as artificial proteins for metal ion transport in intracellular traffic. Thus, multifunctional dendrimers, capable of forming metal ion–intradendrimer complexes, performing targeting functions, possessing a protective shell for decomplexation and so on, are necessary to substitute for metal–protein functions in copper metabolism (e.g. Kodama & Fujisawa 2008). Owing to their well-defined oligosaccharide protection, dense-shell dendrimers may fulfil these criteria for use as metal ion carriers for biological applications (Appelhans *et al.* 2007). Here, we have undertaken further efforts to synthesize and characterize large glycodendrimers, ranging up to the fifth generation, with a dense maltose shell (Klajnert *et al.* 2008). We investigate their metal ion complexation capacity compared with first- and second-generation glycodendrimers with dense maltose shells (Appelhans *et al.* 2007). Based on our preliminary Cu(II) complexation study (Appelhans *et al.* 2007), we expected to find a preference for Cu(II)–intradendrimer complexes.

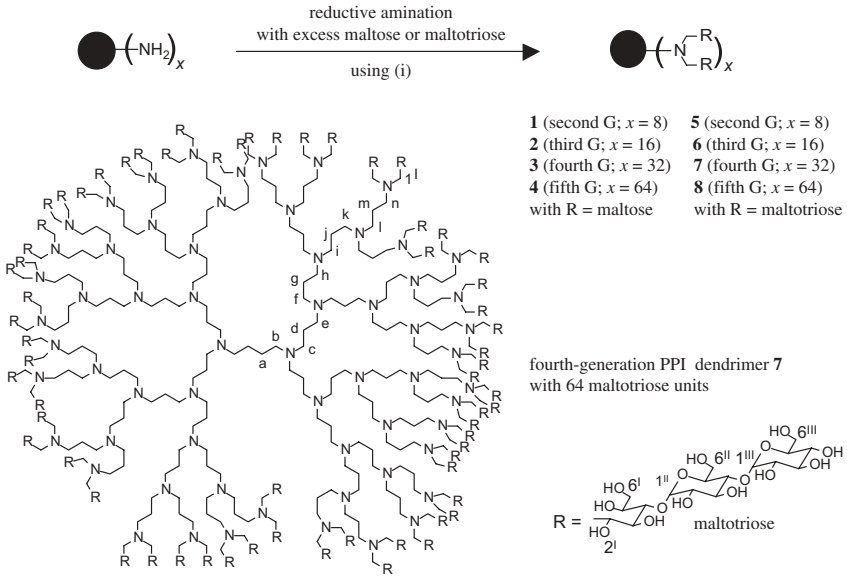

reaction condition (i): DAB-Am8, DAB-Am16, DAB-Am32 or DAB-Am64 with maltose monohydrate or maltotriose (ratio NH_2/oligosaccharide 1 : 5 –1 : 24)/BH_2*Py complex in Na borate solution at 50°C for 7 days followed by dialysis in distilled water and freeze drying

Scheme 1. Synthetic scheme of the preparation of second- to fifth-generation PPI dendrimers **1**–**4** with maltose and **5**–**8** with maltotriose shell and structure of fourth-generation PPI dendrimer **7**.

The aim of our work is to study the generation-dependent metal ion complexation capacity of higher generation PPI glycodendrimers with dense oligosaccharide shells. We therefore identify, quantify and characterize preferred metal ion–intradendrimer complexes. Furthermore, we determine whether an extended dendritic PPI scaffold surrounded by a dense oligosaccharide shell is able to undergo the desired metal ion complexation in aqueous solution preferably governed by tertiary amino groups and whether oligosaccharide shells affect internal or external metal ion complexation in the dendrimer sphere. To the best of our knowledge, glycodendrimers are mainly used as carrier systems for drugs, molecular recognition of surfaces of biologically active macromolecules and systems and the stabilization of Au and Ag nanoparticles, but not for the transport of metal ions in cellular uptake, including the targeting of specific cellular locations.

Here we report on the synthesis and characterization of maltotriose-modified third- to fifth-generation PPI dendrimers using a series of glycodendrimers ranging up to the fifth generation (scheme 1) that possess either a dense maltose or maltotriose shell. This should enable the development of dendritic carrier systems without a coupled metal ligand to be used as metal ion carriers in a biological environment. In this context, the Cu(II) complexation of the dense shell glycodendrimers was studied by UV/Vis spectroscopy, and

further details about the location and coordination of generation-dependent Cu(II)–dendrimer complexes were revealed by electron paramagnetic resonance (EPR). Computer-aided analysis of EPR spectra has already been demonstrated to be a very powerful tool to study dendrimer structure and the complexation ability of different external and internal dendrimer sites (Ottaviani *et al.* 1994, 1997, 2000, 2002). In particular, knowledge about the location of the Cu(II) complexes within the dendritic structure is important for use of glycodendrimers as metal ion carriers in a biological environment. Finally, a third-generation PPI dendrimer with a maltose shell was selected as a potential representative of large glycodendrimers to study complexation behaviour towards different metal ions [UO_2(VI), Eu(III), VO(IV), Cu(II), Ag(I), Ni(II)].

2. Experimental section

(*a*) *Materials*

Poly(propyleneimine) (PPI) dendrimers of second (DAB-Am8), third (DAB-Am16), fourth (DAB-Am32) and fifth generations (DAB-Am62) were supplied by SyMO-Chem (Eindhoven, The Netherlands). Maltose monohydrate (Mal), maltotriose (Mal-III), sodium borate (Na borate) and the borane pyridine complex (BH_3*Py, 8 M solution in THF) were used as purchased from Fluka. $EuCl_3$*$6H_2O$ (Eu(III), 99.9%, Janssen), $VOSO_4$*$3H_2O$ (VO(IV), Aldrich), $UO_2(CH_3COO)_2$*$2H_2O$ (UO_2(VI), 98%, Chemapol), $AgNO_3$ (Ag(I), purissimum, VEB Feinchemie Sebnitz), $CuSO_4$*$5H_2O$ (Cu(II), p.A., VEB Laborchemie Apolda) and $Ni(CH_3COO)_2$*$4H_2O$ (Ni(II), 99%, Fluka) were used as received. Water was purified after reverse osmosis (Milli RO 5, Millipore, USA) using a MilliQ+ system (Millipore) to give a conductivity of 18.2 MΩ cm^{-1}.

(*b*) *Characterization of dendrimers*

NMR measurements were carried out on a Bruker DRX 500 NMR spectrometer operating at 500.13 MHz for ^1H and at 125.75 MHz for ^{13}C using D_2O as a solvent. Sodium 3-(trimethylsilyl)-3,3,2,2-tetradeuteropropionate was added for internal calibration (δ (^{13}C) = 0 ppm and δ (^1H) = 0 ppm). Signal assignments were performed by a combination of 1D and 2D NMR experiments using the standard pulse sequences provided by Bruker. *IR investigations* were carried out on a Bruker IFS66 spectrometer equipped with a heatable Golden Gate Diamond ATR-Unit (Specac). One hundred scans for one spectrum were added at a spectral resolution of 4 cm^{-1}. *Laser-induced liquid bead ion/desorption mass spectrometry* (LILBID-MS) was used to determine the molar mass of **6**–**8**. The method is described elsewhere (Morgner *et al.* 2006). Dendrimer samples were prepared in aqueous solution with concentrations between 1×10^{-6} and 5×10^{-6} M for **6**–**8**. All measurements were performed in anionic or cationic mode. The instrument was calibrated with bovine serum albumin. *Matrix-assisted laser desorption/ionization time-of-flight mass spectrometry* (MALDI-TOF-MS): a Bruker Reflex III instrument (Bruker Daltonik GmbH, Bremen, Germany), equipped with a nitrogen laser (337 nm), working in a linear mode at an acceleration voltage of 20 kV was used. Approximately 10 mg of α-cyanocinnamic

acid dissolved in 1 ml methanol (MeOH) was used as a matrix. The sample concentration was 2 mg ml^{-1} (in MeOH). Both solutions were mixed in a ratio of 50/20 (v/v) prior to deposition (1 µl) on the MALDI target. Typically, 200 shots were accumulated for one spectrum. The instrument was calibrated with biopolymer standards.

(*c*) *Synthesis of maltose-modified poly(propyleneimine) dendrimers*

Maltose-modified second-generation PPI (**1**) was synthesized according to the literature (Appelhans *et al.* 2007). Maltose-modified third- to fifth-generation PPI dendrimers (**2**–**4**) were synthesized according to the literature (Klajnert *et al.* 2008).

(*d*) *Synthesis of maltotriose-modified poly(propyleneimine) dendrimers*

Maltotriose-modified second-generation PPI (**5**) was synthesized according to the literature (Appelhans *et al.* 2007).

(i) *Maltotriose-modified third-generation poly(propyleneimine)* (***6***)

Third-generation PPI dendrimer (DAB-Am16) (0.2 g, 1.186×10^{-4} mol), maltotriose (9.57 g, 19 mmol) and borane–pyridine complex (2.37 ml, 19 mmol, 8 M solution) were taken up in a sodium borate buffer (25 ml, 0.1 M). The reaction solution was stirred at 50°C for 7 days. Then, the crude product was purified by dialysis with deionized water for 3 days; **6** was obtained from freeze drying. The yield was 1.89 g (92%) as a solid. ^{1}H NMR (D_2O): $\delta = 1.3$–2.3 (a, d, g and j); 2.4–3.3 (1^{I}, b, c, e, f, h, i, k); 3.44 (4^{III}); 3.5–4.5 (2^{I}–6^{I}, 2^{II}–6^{II}, 2^{III}, 3^{III}, 5^{III}, 6^{III}); 4.95–5.6 ppm (1^{II}, 1^{III}) (figure S1, electronic supplementary material). ^{13}C NMR (D_2O): $\delta = 21.5$–26.5 (a, d, g, j); 51.5–57.5 (b, c, e, f, h, i, k); 58–62 (1^{I}); 63.3 (6^{II}, 6^{III}); 65–66.5 (6^{I}); 71.0 (2^{I}); 72.2 (4^{III}); 73.9, 74.3, 74.6, 75.6, 75.8 and 76.2 (2^{II}, 2^{III}, 3^{I}–3^{III}, 5^{I}–5^{III}); 79.9 (4^{II}); 83–86 (4^{I}); 99.0, 102.7 and 103.5 ppm (1^{II}, 1^{III}) (figure S4, electronic supplementary material). IR: $\nu = 3274.6$ (OH); 2920.3 (CH, CH_2); 1013.2 cm^{-1} (C−O). LILBID-MS: $C_{664}H_{1232}N_{30}O_{480}$ (17 316.8 g mol^{-1} relating to 32 maltotriose units connected to the surface of third-generation PPI dendrimer DAB-Am16); $m/z = 16\,400$ [$(M - 2 \times$ maltotriose units$)^{-}$].

(ii) *Maltotriose-modified fourth-generation poly(propyleneimine)* (***7***)

The same reaction conditions and working procedures as for the synthesis of **6** were used to isolate 1.26 g (82%) of **7** as a solid using fourth-generation PPI dendrimer (DAB-Am32) (0.2 g, 5.691×10^{-5} mol) and maltotriose (4.59 g; 9.1 mmol). ^{1}H NMR (D_2O): $\delta = 1.2$–2.2 (a, d, g, j, m); 2.3–3.35 (1^{I}, b, c, e, f, h, i, k, l, n); 3.44 (4^{III}); 3.5–4.5 (2^{I}–6^{I}, 2^{II}–6^{II}, 2^{III}, 3^{III}, 5^{III} 6^{III}); 4.95–5.6 ppm (1^{II}, 1^{III}). ^{13}C NMR (D_2O): $\delta = 21$–27 (a, d, g, j, m); 49.2 (n′, $-CH_2-NH-CH_2-R$, R = maltotriose); 51–58 (b, c, e, f, h, i, k, l, n); 58–62 (1^{I}); 63.4 (6^{II}, 6^{III}); 65–67 (6^{I}); 70.9 (2^{I}); 72.2 (4^{III}); 73.9, 74.3, 74.6, 75.5, 75.8 and 76.2 (2^{II}, 2^{III}, 3^{I}–3^{III}, 5^{I}–5^{III}); 80.0 (4^{II}); 82–86 (4^{I}); 99.1, 102.8 and 103.2 ppm (1^{II}, 1^{III}). IR: $\nu = 3278.0$ (OH); 2923.5 (CH, CH_2); 1014.4 cm^{-1} (C−O). LILBID-MS: $C_{1336}H_{2480}N_{62}O_{960}$ (34773.8 g mol^{-1} relating to 64 maltotriose units connected to the surface of fourth-generation PPI dendrimer DAB-Am32); $m/z = 31\,000$ [$(M - 8 \times$ maltotriose units$)^{-}$].

(iii) *Maltose-modified fifth-generation poly(propyleneimine)* (***8***)

The same reaction conditions and working procedures as for the synthesis of **6** were used to isolate 0.69 g (73%) of **8** as a solid using fifth-generation PPI dendrimer DAB-Am64 (0.1 g, 1.362×10^{-5} mol) and maltotriose (8.769 g; 17.4 mmol). ^{1}H NMR (D_2O): $\delta = 1.2$–2.2 (a, d, g, j, m and p); 2.2–3.3 (1^{I}, b, c, e, f, h, i, k, l, n, o, q); 3.43 (4^{III}); 3.5–4.55 (2^{I}–6^{I}, 2^{II}–6^{II}, 2^{III}, 3^{III}, 5^{III}, 6^{III}); 4.9–5.6 ppm (1^{II}, 1^{III}). ^{13}C NMR (D_2O): $\delta = 21$–27 (a, d, g, j, m, p); 50–57 (b, c, e, f, h, i, k, l, n, o, q); 58–62 (1^{I}); 63.3 (6^{II}, 6^{III}); 65–67 (6^{I}); 72 (4^{III}); 73.0–78.0 (2^{II}, 2^{III}, 3^{I}–3^{III}, 5^{I}–5^{III}); 80 (4^{II}); 83–86 (4^{I}); 102.8 ppm (1^{II}, 1^{III}) (figure S2, electronic supplementary material). IR: $\nu = 3278.0$ (OH); 2923.5 (CH, CH_2); 1014.4 cm^{-1} (C−O). LILBID-MS: $C_{2680}H_{4976}N_{126}O_{1920}$ (69687.88 g mol^{-1} relating to 128 maltotriose units connected to the surface of fifth-generation PPI dendrimer DAB-Am64); $m/z = 58\,000$ $[(M - 24 \times \text{maltotriose})^{-}]$.

(*e*) *Metal ion complexation by UV/Vis spectroscopy*

UV/Vis spectra were recorded at room temperature (22 ± 2°C) on a Lambda 800 spectrophotometer (Perkin–Elmer, Germany). Slit width was 1 nm. Titration experiments of dendrimer **2** with the different transition metal salts (starting volume 2.5 ml) were carried out at room temperature (22 ± 2°C) in a sealed cuvette (quartz glass suprasil, thickness d indicated at the legends, Hellma, Germany) by stepwise addition (gas-tight microlitre syringe, through the serum cap) of appropriate amounts of a concentrated metal salt solution in water. At the end of the titration, dendrimer **2** was diluted by approximately 30 per cent of the starting volume. For each metal salt concentration, the spectra were corrected for the dilution by applying the appropriate factor. Cu(II) titration experiments with higher glycodendrimer generations were carried out according to our previous report (Appelhans *et al.* 2007). Dendrimer concentrations are mentioned in the figures as M. The solid glycodendrimers were dried under a vacuum at 50°C overnight and stored at 4–8°C prior to use. The drying process for the glycodendrimers was also used before starting the EPR study.

(*f*) *Cu(II) complexation by electron paramagnetic resonance experiments*

(i) *Sample preparation*

Both dendrimers and copper nitrate hydrate ($Cu(NO_3)_2 * 2.5H_2O$, Sigma-Aldrich, ACS reagent 98%) were dissolved in deionized water. The concentration of dendrimers was 0.1 M in the external surface groups (each generation, the dendrimer concentration was multiplied by the number of surface groups), whereas the concentration of Cu(II) was varied from 0.01 to 0.1 M. The molecular weights of the glycodendrimers and the molar ratios between [Cu(II)] and [glycodendrimers] for the starting and final concentrations of Cu(II) are shown in the electronic supplementary material. After different equilibration times (freshly prepared to 24 h), 100 µl of the dendrimer–copper solution was inserted into an EPR tube (1 mm internal diameter). In all cases, reproducibility of the results was controlled by repeating the EPR analysis three times under identical experimental conditions for each sample.

(ii) *Method*

EPR spectra were recorded by means of an EMX-Bruker spectrometer operating at the X-band (9.5 GHz) and interfaced with a PC (software from Bruker for handling and analysis of the EPR spectra). The temperature was controlled with a Bruker ST3000 variable temperature assembly cooled with liquid nitrogen. EPR spectra were recorded for the different samples as a function of temperature (in the room temperature range, from 318 K down to 250 K; then, directly at 150 K).

(iii) *Computation of electron paramagnetic resonance spectra*

The low-temperature EPR spectra were computed by using Bruker's WIN-EPR SimFonia Software v. 1.25 and by the method reported in Bennett *et al.* (2002). The parameters used for computation were the g_{ii} components (accuracy in the third decimal, on the basis of the computation itself) for the coupling between the electron spin and the magnetic field; the A_{ii} components (accuracy of approx. 3%) for the coupling between the electron spin and the nuclear spin ($I_{Cu} = 3/2$) and the line widths of the x-, y- and z-lines. Transitions where $\Delta M_I \neq 0$ were not included in the simulations. **A** and **g** were assumed to have the same principal axes, and a Gaussian line shape was used. The values of the **g** and **A** parameters giving the best agreement with the experimental data were found by trial and error. In most cases, the spectra were constituted by several components owing to different coordination and complex geometries of Cu(II) in the dendrimer structure. In some cases, the subtraction between the spectra in different experimental conditions allowed the extraction of the signals constituting the overall spectra. In all cases, we tried to fit the experimental signal by adding a maximum of two computed components, reproducing the main spectral features. However, the different components either extracted by subtraction or computed were normalized and then integrated twice to calculate the integral area, which was used to calculate the relative intensities of the components. This means that both by the subtraction procedure for experimental spectra and by adding computed components to fit the experimental spectra relative percentages of the different components were obtained with an accuracy of 3 per cent. We noted that simulations of observed EPR signals provide a useful means of estimating the spectral parameters, but do not necessarily produce unique fits. However, we trusted the parameters that provided the best fit of a series of spectra under similar experimental conditions.

3. Results and discussion

(*a*) *Glycodendrimers*

To study glycodendrimer metal ion complexation by UV/Vis spectroscopy and EPR, second- to fifth-generation PPI dendrimers were selected for decoration with a dense maltose and maltotriose shell (scheme 1). Reductive amination, a well-established synthetic method, was used to introduce various (oligo-)saccharide units in order to obtain glycodendrimers **1**–**4** with a dense maltose shell and

Table 1. Yield of **6**–**8**, determination of attached maltotriose on PPI surface by ^{1}H NMR, theoretical molar mass (MM) of **6**–**8**, observed molar mass by LILBID-MS and MALDI-TOF-MS and calculated maltotriose units on PPI surface by LILBID-MS and MALDI-TOF-MS.

				LILBID-MS		MALDI-TOF-MS	
	yield (%)	maltotriose units by NMR[a]	$MM_{theoretical}$ ($g\,mol^{-1}$)	$MM_{observed}$ ($g\,mol^{-1}$)	maltotriose	$MM_{observed}$ ($g\,mol^{-1}$)	maltotriose
6	92	30 (32)	17 316.8	16 400	30	16 770	31
7	82	55 (64)	34 773.8	31 000	56	31 700	57
8	73	103 (128)	69 687.9	58 000	104	62 000	112

[a]Determined by ^{1}H NMR using the integral ratio of the anomeric CH group signal of maltotriose to that of the internal $-CH_2\mathbf{CH_2}CH_2$ groups of the dendritic PPI matrix taking into account the PPI generation (estimated error: ±2%); number in brackets represents the theoretical value for 100% conversion of amino functionalities.

5–**8** with a dense maltotriose shell (scheme 1). In addition to using previously described glycodendrimers **1**–**5** (Appelhans *et al.* 2007; Klajnert *et al.* 2008), the third- to fifth-generation PPI dendrimers **6**–**8** with a dense maltotriose shell had to be synthesized. Surprisingly, we were able to synthesize glycodendrimers **6**–**8** using the same reaction conditions and working procedures as reported for glycodendrimers **1**–**5** (scheme 1) (Appelhans *et al.* 2007; Klajnert *et al.* 2008). The results of the reductive amination of the dendrimers **6**–**8** (scheme 1) are summarized in table 1. Dendrimers **6**–**8** were characterized using NMR, IR, MALDI-TOF-MS and LILBID-MS.

Structural characterization of **6**–**8** was performed to determine the preferred conversion of the surface amino groups of the parent amino-terminated third- to fifth-generation PPI dendrimers with the bulky maltotriose units. The chemical structure of the maltotriose-modified PPI dendrimers **6**–**8** was determined by ^{13}C NMR investigation. As a representative example, the ^{13}C NMR spectrum of the fourth-generation PPI dendrimer **7** is presented in figure 1. Generally, the spectra are characterized by broadened signals for the PPI core, whereas the signals of the middle and terminal glucose units are narrow. The signals of the reacted α-glucose unit are broadened, and only the main signals are assignable. The ^{13}C NMR spectra also did not detect any unsubstituted PPI terminal amino groups, as indicated by the absence of signals in the 40–43 ppm region. On the other hand, the presence of monosubstituted terminal amino groups of the PPIs is indicated by signals with low intensity in the 48–50 ppm region (e.g. n′ in figure 1). A previously described method (Appelhans *et al.* 2007) was used to calculate the degree of PPI substitution by ^{1}H NMR. The signal intensity of the anomeric CH group of the maltotriose (4.9–5.6 ppm) was related to that of the internal CH_2 groups of the dendritic PPI matrix (1.2–2.2 ppm), taking into account the different generations. Within the limits of this method, we found that 80 per cent (**8**), 86 per cent (**7**) and 94 per cent (**6**) of the NH_2 functionalities were converted with maltotriose (table 1). This means that a decreasing degree of maltotriose substitution of PPI dendrimers took place as the generation number increased. More detailed structural characterization of the

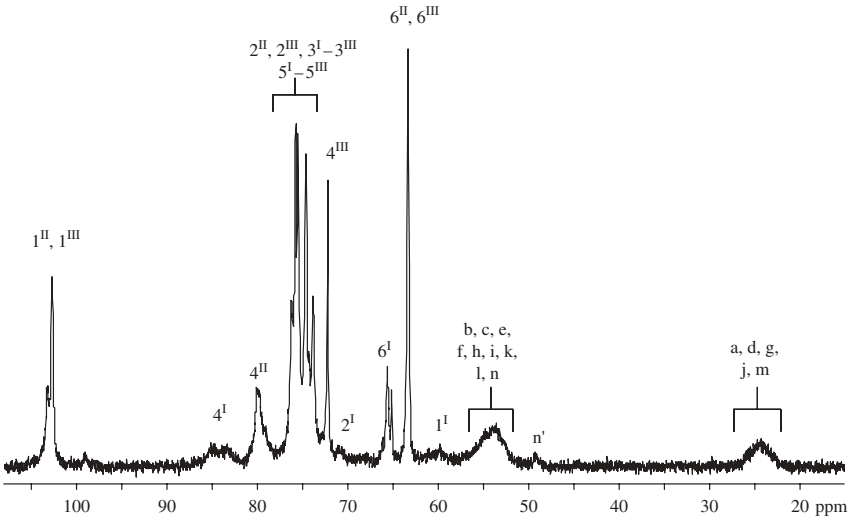

Figure 1. ^{13}C NMR spectrum of fourth-generation PPI **7** with maltotriose in D_2O (signal assignment is presented in scheme 1).

chemically coupled maltotriose units on the dendrimer surfaces was achieved using LILBID-MS and MALDI-TOF-MS. The mass spectrum of **7** obtained by LILBID-MS is presented in figure 2. The mass spectrometry results (table 1) confirmed the degree of substitution by maltotriose on the surfaces of PPI dendrimers **6**–**8**, which was determined by ^{1}H NMR. Only the mass spectrum of **8** (see electronic supplementary material) indicated a higher degree of substitution by maltotriose on the PPI surface when assayed by MALDI-TOF-MS compared with NMR.

We conclude that reductive amination is also applicable for the synthesis of maltotriose-modified PPI dendrimers of higher generations (third to fifth). This preferably leads to two bound maltotriose units per peripheral amino group. The mass spectrometry results (table 1 and figure 2; see figures in the electronic supplementary material) indicate a high degree of maltotriose substitution on the PPI dendrimer surface for which the fourth and fifth generations showed on average a lower degree of maltotriose substitution than theoretically predicted. Thus, reductive amination is highly efficient for converting higher generation PPI dendrimer surface with maltotriose units. Overall, reductive amination of parent PPI dendrimers has produced two complete series of glycodendrimers ranging up to the fifth generation (**1**–**8**), which have either dense maltose or maltotriose shells. Importantly, these are now synthetically available for further fundamental studies of their use in material and life sciences.

(*b*) *Metal ion complexation of the glycodendrimers observed by UV/Vis spectroscopy*

To gauge the complexation capacity of the glycodendrimers, a number of commercially available metal salts were used in a screening test. In addition to availability, the optical properties of UO_2(VI), Cu(II), Ni(II), VO(IV), Ag(I)

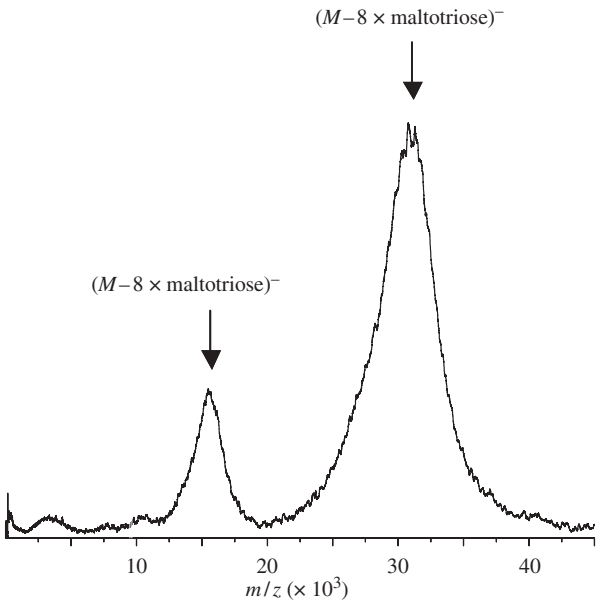

Figure 2. Mass spectrum of fourth-generation PPI **7** with maltotriose shell obtained from LILBID-MS (theoretical molar mass 34 773.8 g mol^{-1}; aqueous solution 5×10^{-6} M for **7**).

and Eu(III) were an important factor in their selection for this study. At this stage, we had no intention of focusing on the counter ion influence. However, we found that there is no dependence on counter ions detectable for $Cu(NO_3)_2$ and $CuSO_4$ (table 3; see electronic supplementary material). The metal ion complexation of the oligosaccharide-modified dendrimers **1**–**8** is mainly based on the presence of tertiary amino groups within the dendritic scaffold (table 1; table S1, electronic supplementary material). In other words, there are few secondary amino groups in the outer dendritic sphere that can also participate in metal ion complexation. These dense oligosaccharide-shelled dendrimers with low backfolding properties and preferred dendritic tertiary amino scaffold were selected for the metal complexation study in the aqueous phase using the metal ions Cu(II), Ni(II), VO(IV), Ag(I), Eu(III) and UO_2(VI) and observed by UV/Vis spectroscopy. The metal complexation study was divided into two parts: (i) a third-generation PPI dendrimer **2** with maltose shell was used to study general complexation behaviour towards various metal ions. This was done by determining and comparing the metal ion–dendrimer complex ratio (n_{MeD}) and (ii) PPI dendrimers **1**–**8** were used in a detailed investigation of Cu(II) complexation in order to elucidate the influence of molecular structure, generation number and oligosaccharide unit on complexation behaviour. The results of both investigations are summarized in tables 2 and 3. n_{MeD} was determined for Ni(II), Ag(I), Eu(III), VO(IV) and Cu(II) based on approaches described by Zhao *et al.* (1998) and Appelhans *et al.* (2007). Further details are given in the electronic supplementary material.

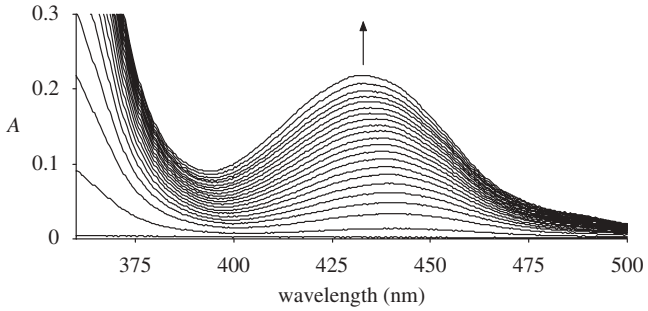

Figure 3. Absorbance spectra obtained by titration of **2** with UO_2(VI) in water ([**2**] = 0.0001 M, [UO_2(VI)] = 0. . .0.0019 M, d = 4 mm).

Table 2. Comparison of metal ion–third-generation dendrimer **2** ratios based on UV/Vis titration experiments.[a]

UO_2(VI)	Ni(II)	VO(IV)	Cu(II)	Ag(I)	Eu(III)
34[b]	16[c]	11[c]	9[b]	5[b]	2[c]

[a]30 N atoms are present in the dendritic scaffold of **2**.
[b][2] = 0.0001 M.
[c][2] = 0.001 M.

Table 3. Comparison of Cu(II)–dendrimer ratios calculated from UV/Vis titration study.

dendrimer		surface groups		
generation	N atoms	maltose	maltotriose	$-NH_2$[a]
second	14	3	3	4
third	30	9[b]	9	8
fourth	62	18[c]	15	16
fifth	126	34	25	32

[a]Literature data (Bosman *et al.* 1997) received in MeOH.
[b,c]Complexation experiments with $Cu(NO_3)_2$ gave the same n_{CuD}. For further information, see electronic supplementary material.

(*c*) *Approach to determine* n_{UO2D}

Figure 3 shows the absorbance spectra between 360 and 500 nm obtained by titrating **2** with UO_2(VI). Both UO_2(VI) and the complex absorb between 200 and 300 nm (shoulders; not shown in figure 3). Owing to this broad intersection region, use of an approach that considers the intersection of two extrapolated parts (Zhao

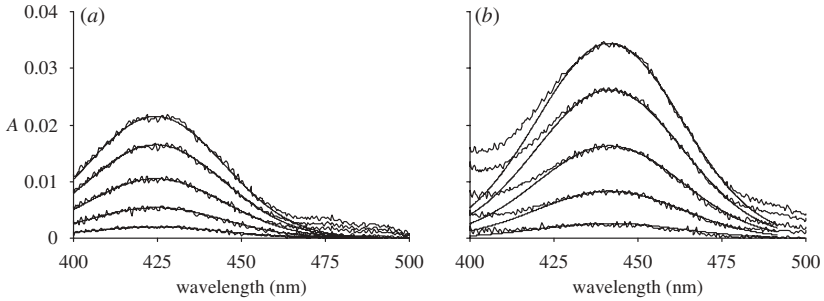

Figure 4. Absorbance spectra of UO_2(VI) (*a*) and the UO_2(VI)–**2** complex (*b*) in water additionally fitted with GAUSS curves ([**2**] = 0.001 M, [UO_2(VI)] in ascending order are 0.000134, 0.000324, 0.000562, 0.000836 and 0.00104 M, d = 4 mm).

et al. 1998) was inaccurate, but gave a rough estimation of between 30 and 40 for the maximum n_{UO2D} value. An additional absorption of both the complexed and free UO_2(VI) was observed between 380 and 500 nm (figure 3). Again, the extrapolation method was not applicable. Furthermore, it was observed that the maximum peak position is strongly dependent on the concentration ratio [UO_2(VI)]/[**2**] (figure 3). With increasing concentrations of UO_2(VI), a slight blue shift of this absorption was observed. Further analysis at a higher dendrimer concentration (0.001 M) demonstrated that, for [UO_2(VI)] $\leq$ 0.001 M, the peak maximum is at 441.5 nm, independent of [UO_2(VI)]. Furthermore, the absorption peak was approximated between 430 and 480 nm by means of a GAUSS function with the peak maximum at 441.5 nm and a width of 51 nm at half-height (figure 4*b*). Therefore, in this concentration range, nearly all ([UO_2(VI)] was complexed by **2**. Conversely, for pure UO_2(VI), the approximation of the absorption peak was also possible in the 400 and 450 nm range with a GAUSS curve possessing a peak maximum at 424.5 nm and a half-width of 48 nm (figure 4*a*). The absorbance versus [UO_2(VI)] relation is a linear one with correlation coefficients of 0.9975(**2** + UO_2(VI)) and 0.9977 ([UO_2(VI)]). As can be seen, the molar extinction coefficient of UO_2(VI) in the complex must be higher. Quantitative analysis yielded a factor of 1.6. Another conclusion can be drawn from the following fact: up to n_{UO2D} = 8, the molar extinction coefficient related to the uranyl ions is independent of the number of uranyl ions complexed in one dendrimer macromolecule. There is an overlapping region for the spectra modelling such that, between 430 and 450 nm, the spectra of both pure UO_2(VI) and its complex with **2** can be approximated by the corresponding GAUSS curves. For [**2**] = 0.0001 M and [UO_2(VI)] < 0.012 M, peak positions were observed between 430 and 441 nm and therefore exactly in this region. This enabled us to calculate a calibration curve to determine n_{UO2D} from the peak position by overlaying the corresponding GAUSS functions in dependence on the molar fractions of free UO_2(VI) and UO_2(VI)–**2** complex (figure S17*a*, electronic supplementary material). The experimentally observed values can be found in figure S17*b* in the electronic supplementary material. For 11 UO_2(VI) concentrations, the averaged values

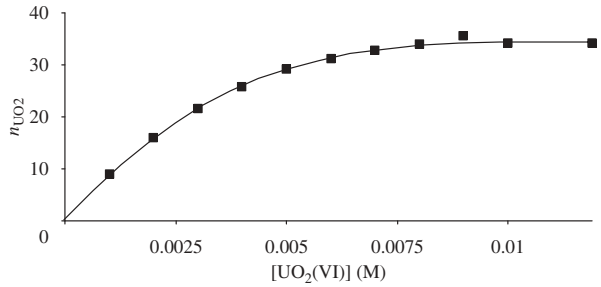

Figure 5. n_{UO2} as a function of UO_2(VI) concentration ([**2**] = 0.0001 M, water, room temperature).

of the peak positions were read from the line in figure S17*b* in the electronic supplementary material. Then, by means of the calibration curve in figure S17*a*, electronic supplementary material, the corresponding molar fraction of the UO_2(VI)–**2** complex was determined. From these data and the [**2**] and [UO_2(VI)] applied in this study, the n_{UO2D} values were calculated (figure 5) according to equation (3.1),

$$n_{UO2D} = x_{complex}{}^{*}\frac{[UO_2{}^{2+}]_0}{[\text{Dendrimer}]}. \tag{3.1}$$

The maximum UO_2(VI) to dendrimer ratio was calculated to be 34. This approach is based on the assumption that the molar extinction coefficient of the complexed uranyl ions is independent of n_{UO2D}. This point has been proven for an n_{UO2D} up to 8 (discussed earlier). The validity of this assumption is furthermore supported by the above-mentioned fact that the extrapolation method, which is inaccurate here owing to the broad transition region, led to a maximum n_{UO2D} value between 30 and 40.

(*d*) *Comparison of* n_{MeD} *for the third-generation glycodendrimer 2*

The complexation study of the third-generation dendrimer **2** with a maltose shell revealed the following decreasing n_{MeD} series: 34 for UO_2(VI) > 16 for Ni(II) > 11 for VO(IV) > 9 for Cu(II) > 5 for Ag(I) > 2 for Eu(III). In other words, **2** is suited to complex different heavy and noble metal ions, as well as the lanthanide Eu(III) and the actinide UO_2(VI) by the dendritic scaffold in the aqueous phase. In this context, the terms 'to complex' and 'complex' will be used generally to mean, for example, that metal ions can form strong complexes with the dendritic tertiary amino scaffold (Zhao & Crooks 1999; Diallo *et al.* 2008) or that physical encapsulation has occurred (Diallo *et al.* 2004).

In the following, we discuss the n_{MeD}, determined here along with results from the literature. To be comparable, previously reported data are considered only for samples obtained with no additional complexing ligands in the inner and outer spheres of the PPI dendrimers. One impressive finding was the large amount of UO_2(VI) complexed in **2**. This can only be explained by the strong interaction of actinide with the tertiary amino groups of the dendritic scaffold

in **2** (Diallo *et al.* 2008). For the UO_2(VI) complexation, only 30 tertiary amino groups were present in the dendritic scaffold of the third-generation dendrimer. The complexation ability of excess uranyl is a common behaviour of amino-terminated PPI and PAMAM dendrimers (Diallo *et al.* 2008). The unmodified fifth-generation PPI dendrimer could also complex about 140 UO_2(VI) in the aqueous phase, although only 126 N atoms were present in the dendritic scaffold. In other words, we find that **2** is able to complex one-quarter of uranyl ions in comparison with the parent fifth-generation PPI dendrimer. Thus, primary amino surface groups are not required in dendrimers for complexation of UO_2(VI) in a dendritic polyamino scaffold.

Complexation of Cu(II) and Ni(II) by the unmodified third-generation PPI dendrimer in MeOH previously revealed the complexation of eight cations in the outer sphere by the complexing unit of bis-(3-aminopropyl)amine (Bosman *et al.* 1997). We found that a similar amount of Cu(II) was complexed by **2** in the aqueous phase, which had no specific complexing units, and nearly double the amount of Ni(II) complexed in the glyco-shelled dendritic environment. One can assume that the more physical encapsulation of Ni(II) in **2** results from a weaker interaction with the dendritic polyamine scaffold compared with the strong binding of Cu(II) in the scaffold observed here and in the literature (Zhao & Crooks 1999).

The amount of VO(IV) complexed by **2** was slightly higher than that of Cu(II). The complex formation between VO(VI) and the dendritic polyamine scaffold in **2** was apparent by the appearance of a new absorption peak at 323 nm (figure S14, electronic supplementary material), which indicates another coordination sphere of VO(IV) in the dendritic PPI scaffold. Previous studies on vanadium–dendrimer complexes focused, for example, on the (hetero-)metal assembly in poly(phenylazomethin) dendrimers using VCl_3 (Imaoka *et al.* 2005; Takanashi *et al.* 2007) and molecular dynamics of vanadyl chelate complexes on PAMAM dendrimers (Wiener *et al.* 1996); thus, no direct comparison with our study can be made.

Ag(I) complexation by **2** had one of the lowest n_{MeD} values. This implies that the molecular structure of **2** is not suited to complex large amounts of Ag(I) as opposed to other metal ions. An analogous complexation study with PAMAM dendrimers showed that Cu(II) interacts more strongly with interior dendritic tertiary amino groups than Ag(I) (Zhao & Crooks 1999). Thus lower n_{AgD} values were determined compared with those using PAMAM dendrimers (Diallo *et al.* 2004; Banyai *et al.* 2005). A similar complexation behaviour towards Cu(II) and Ag(I) can be assumed for the glycodendrimer **2**. Furthermore, the UV/Vis spectra of Ag(I)–dendrimer complexes did not show any plasmon peaks ($\lambda = 400$–500 nm) for the undesired formation of Ag particles (Esumi *et al.* 2000; Ottaviani *et al.* 2002) under the given experimental conditions. Although the complexation behaviour of Ag(I) towards different PAMAM dendrimers is well studied (Ottaviani *et al.* 2002; Banyai *et al.* 2005), Ag(I) complexation for determining n_{AgD} of parent and surface-modified PPI dendrimers has not been reported in detail. Previous studies mainly focused on Ag(I) complexation and Ag particle formation by various PPI dendrimers (Esumi *et al.* 2000, 2005). The lowest value for n_{MeD} is given for the lanthanide Eu(III); thus, it possesses the lowest interaction properties with the dendritic PPI scaffold and only some physical encapsulation of Eu(III) in **2** occurs.

(*e*) *Cu(II) complexation of glycodendrimers with a dense maltose or maltotriose shell*

The successful complexation of various metal ions by **2** encouraged us to investigate Cu(II) complexation using higher dendrimer generations with variations in the oligosaccharide shell structure (table 3; figures S15 and S16, electronic supplementary material). From table 3, the following conclusions can be drawn.

(i) Both glycodendrimers series, **1**–**4** with a dense maltose shell and **5**–**8** with a maltotriose shell, show generation-dependent Cu(II) complexation.
(ii) In comparison with the n_{CuD} value for the parent PPI dendrimers in MeOH (Bosman *et al.* 1997), most glycodendrimers possess a similar Cu(II) complexation capacity. Thus, the n_{CuD} value of glycodendrimers **2**, **3**, **4**, **6** and **7** differs only in the range of 6–12% from those of the parent dendrimers. Both second-generation dendrimers **1** and **2** and the fifth-generation dendrimer **8** display a slightly stronger difference for the Cu(II) complexation capacity than the parent PPI dendrimers (25% for **1** and **2**, corresponding to 1 Cu(II) fewer; 22% for **8**, corresponding to 7 Cu(II) fewer; table 3). Thus, higher generation glycodendrimers, possessing only a dendritic tertiary amino scaffold and no complexing surface groups, are suited to complex surprisingly large amounts of Cu(II).
(iii) The nature of the attached oligosaccharide shells on the PPI dendrimer surface has no significant influence on Cu(II) complexation by the glycodendrimers. It is therefore possible that the dendritic PPI scaffold is mainly responsible for Cu(II) complexation.

The UV/Vis study did not indicate whether the coordination and location of the Cu(II) ions occurred at both the external and internal surfaces of the glycodendrimers. The only other experimental techniques available to provide such further detailed information are EPR and *e*xtended *X*-ray *a*bsorption *f*ine *s*tructure (EXAFS) (Ottaviani *et al.* 1994; Tran *et al.* 2004).

(*f*) *Cu(II) complexation of glycodendrimers observed by electron paramagnetic resonance technique*

Previous EPR studies on low-generation PPI dendrimers with aliphatic surface groups outlined different coordination spheres ($Cu{-}N_2O_2$ and $Cu{-}N_3O_2$ in different geometries), with increasing Cu(II) concentrations in organic solution (Domracheva *et al.* 2004). We found that Cu(II) is localized in different sites, internally and at the periphery (externally), of glycodendrimers in water solutions. Cu(II) coordination is affected by the nature of the functional groups in the periphery (NH_2 or tertiary amino groups bearing maltose or maltotriose units), the generation (generations 2–5, termed G2–G5) and the Cu(II)/dendrimer ratio. Different equilibration times (0–24 h) did not influence the results. The spectral features and magnetic parameters obtained from the simulation indicated two main geometries of the complexes: axial, characterized by $g_1 >> g_2 \geq g_3$, and rhombic, characterized by $g_1 > g_2 > g_3$.

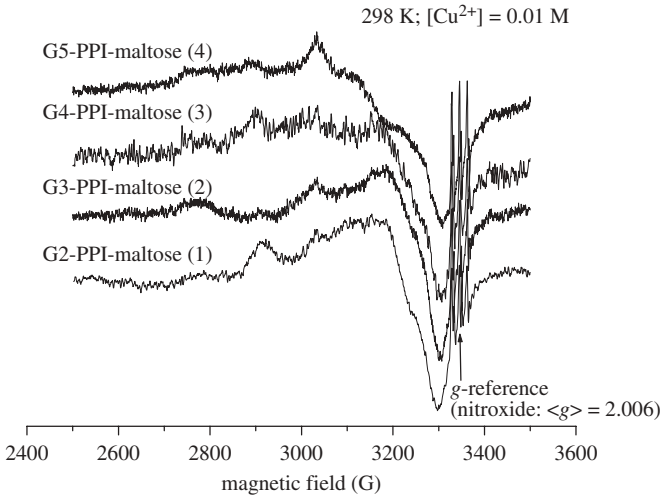

Figure 6. Experimental EPR spectra at 298 K of G*n*-PPI-maltose solutions containing Cu(II) at concentration 0.01 M.

In figure 6, the spectra of different dendrimer generations with a maltose shell (G*n*-maltose; $n = 2 - 5$) + Cu(II) at concentration 0.01 M and 298 K are shown as examples of measurements at room temperature. The three-line feature at high field arises from a nitroxide impurity used as g reference ($\langle g \rangle = 2.006$). In all cases, the room temperature spectra are characteristic of slow motion conditions of Cu(II), since the copper ions are trapped in the dendrimer structure. The anisotropic **g** and **A** components are already well resolved at room temperature and progressively change towards a rigid motion by decreasing the temperature; at temperatures below 250 K, the spectra do not change any more. An increase in temperature leads to a progressive and slow loss of the anisotropy, and the spectra at 318 K mostly become very complicated owing to different components in different motion regimes (from fast to slow: data not shown). The superposition of different components in different motion regimes already at room temperature renders the analysis unreliable since too many parameters are needed for the computation. Conversely, the low-temperature spectra need only g_i, A_i and line width values for the computation, and the analysis is reliable when the different components are extractable from the overall line shape.

At 150 K, the amino-terminated dendrimers, from **G2** to **G5**, show spectra that are similar to those previously reported for amino-terminated PAMAM dendrimers (Ottaviani *et al.* 1997, 2000, 2002). On the basis of the magnetic parameters obtained from the computation of the low-temperature spectra, almost square planar $Cu{-}N_4$ complexes with water molecules in the axial positions were formed in Cu(II) concentrations ranging from 0.01 to 0.1 M. An example of the experimental and computed patterns is shown in figure 7 for the G4-PPI-NH_2 dendrimer.

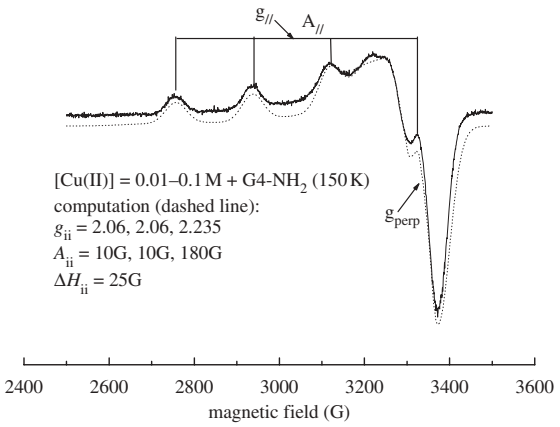

Figure 7. Experimental (solid line, 150 K) and computed (dashed line) EPR spectra of G4-PPI-NH_2 dendrimer (0.1 M in external sites) in solution with copper nitrate at concentrations in the range 0.01–0.1 M. The main parameters used for computation are also shown.

(*g*) *Influence of glycodendrimer generation on Cu(II) binding: electron paramagnetic resonance study*

When the amino groups are substituted by maltose or maltotriose units, the Cu(II) complex structure completely changes, depending on the experimental conditions (concentrations), generation number and the nature of the sugar moieties. EPR spectra in figure 8 show the *effects of generation* (*G2 to G5*) on Cu(II) binding by the maltose-functionalized PPI dendrimers, measured at 150 K, and with a Cu(II) concentration of 0.01 M. For glycodendrimer **1** ($G=2$) and **2** ($G=3$) (figure 8*a*,*b*), the spectra are characteristic for an almost *axial* coordination, but comparison with the parameters in the literature (Peisach & Blumberg 1974; Addison 1983; Solomon & Hanson 2006) indicates an equatorial distortion of a square bipyramidal structure; the spectrum is fitted by two components: (i) $g_{ii}=2.035$, 2.120, 2.277; $A_{ii}=5$G, 25, 145G+ and (ii) $g_{ii}=$ 2.050, 2.130, 2.295; $A_{ii}=5$G, 25G, 115G. Component (i) is 65 per cent for **1**. This component was attributed to a $Cu-N_2O_2$ or $Cu-NO_3$ coordination, corresponding to a square planar symmetry with a small but not negligible trigonal distortion. The less intense (35%) component (ii) was attributed to a $Cu-O_4$ coordination. The nitrogen-rich coordination increases its relative intensity for **2** (up to 80%) at the expense of the oxygen-rich coordination. This coordination indicates that Cu(II) ions are internalized within the dendrimer structure and that nitrogen coordination becomes more favoured when the dendrimer structure becomes more rigid with a larger number of nitrogen sites.

For glycodendrimers **3** ($G=4$) and **4** ($G=5$) (figure 8*c*,*d*), the spectra show two contributions from two geometries, indicated as *axial* and *rhombic*. The contributions were extracted by subtraction of the two experimental spectra. Dendrimer **4** showed a larger rhombic relative amount than **3**, with 80 per cent axial and 20 per cent rhombic for **G4** and 50 per cent axial and 50 per cent rhombic for **G5**. Computations of the axial and rhombic contributions are shown in

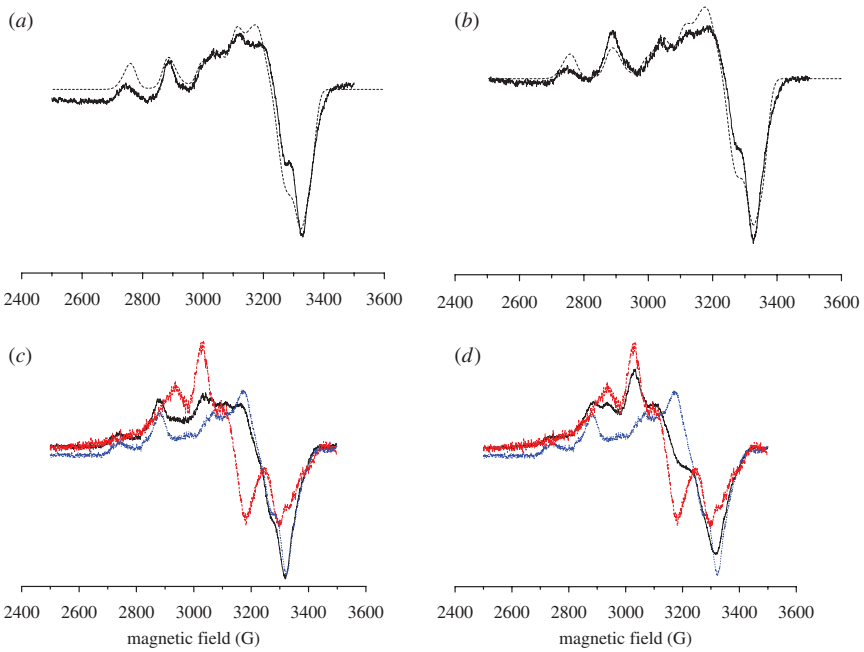

Figure 8. Experimental (solid line, 150 K) and computed (dashed line) EPR spectra of the **1** (*a*) and **2** (*b*) glycodendrimers (0.1 M in external sites) with a Cu(II) concentration of 0.01 M. (a) Solid line, G2-maltose (**1**); dotted line, 65%, $g_{ii} = 2.035$, 2.12, 2.277; $A_{ii} = 5$, 25, 145G and 35%, $g_{ii} = 2.05$, 2.13, 2.295; $A_{ii} = 5$, 25, 115G. (*b*) Solid line, G3-maltose (**2**); dotted line, 80%, $g_{ii} = 2.035$, 2.12, 2.277; $A_{ii} = 5$, 25, 145G and 20%, $g_{ii} = 2.05$, 2.13, 2.295; $A_{ii} = 5$, 25, 115G. Experimental EPR spectra (black line, 150 K) and subtracted axial (blue dotted line) and rhombic (red dotted line) components of the **3** (*c*: G4-maltose (80% axial + 20% rhombic)) and **4** (*d*: G5-maltose (50% axial + 50% rhombic)) glycodendrimers (0.1 M in external sites) with a Cu(II) concentration of 0.01 M.

figure 9*a*,*b*, respectively. It is interesting that, for the axial contribution attributed to the glycodendrimers **3** and **4**, the computation again needed the addition of two components: 60 per cent, $g_{ii} = 2.025$, 2.110, 2.260 and $A_{ii} = 5$G, 5G, 175G+ and 40 per cent, $g_{ii} = 2.035$, 2.120, 2.277 and $A_{ii} = 5$G, 25G, 145G. The 40 per cent component is the same as component (i) found for **G2** and **G3** and can be attributed to a Cu−N_2O_2 or Cu−NO_3 coordination. Conversely, the 60 per cent component may be attributed to a Cu−N_4 coordination, as it shows a further increase in A_{zz} and a correspondent decrease in g_{zz} with respect to the 40 per cent component. Thus by increasing generation, the axial component of copper decreases its relative intensity since a rhombic symmetry appears. But, this axial component modifies towards a nitrogen-rich coordination: essentially, this nitrogen complexation site for Cu(II) coordination may be identified in the less congested area within the dendrimer. The smaller the dendrimer, the more mobile the branches become and more Cu(II) ions retain an axial symmetry where the maltose unit and water molecules can also coordinate Cu(II). The bigger the dendrimer, the larger the amount of nitrogen sites available for the axial coordination.

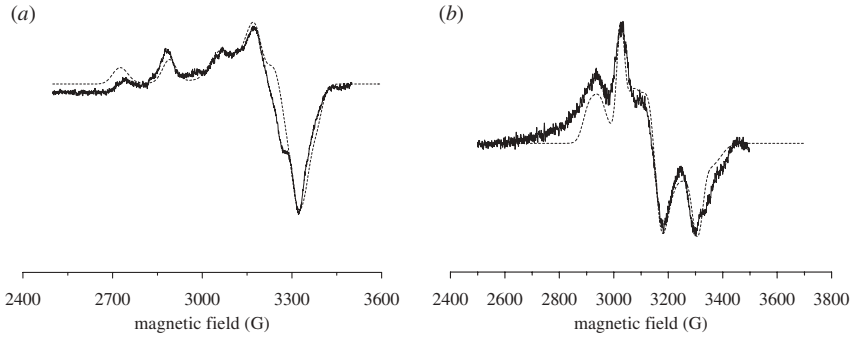

Figure 9. Axial (*a*) and rhombic (*b*) components (solid lines) for the **3** and **4** glycodendrimers and computed signals (dashed lines). (*a*) 60%, $g_{ii} = 2.025$, 2.11, 2.26; $A_{ii} = 5$, 5, 175G and 40%, $g_{ii} = 2.035$, 2.12, 2.277; $A_{ii} = 5$, 25, 145G. (*b*) 60%, $g_{ii} = 2.01$, 2.10, 2.19; $A_{ii} = 10$, 0, 7G and 40%, $g_{ii} = 2.005$, 2.135, 2.28; $A_{ii} = 35$, 25, 20G.

The rhombic component attributed to glycodendrimers **3** and **4** is also constituted by two contributions: 60 per cent, $g_{ii} = 2.010$, 2.100, 2.190 and $A_{ii} =$ 10G, 2G, 7G and 40 per cent, $g_{ii} = 2.005$, 2.135, 2.280 and $A_{ii} = 35$G, 25G, 20G. Such parameters correspond to a distorted trigonal bipyramidal structure with a mixed ligand coordination for oxygen and nitrogen (Hathaway & Tomlinson 1970; Saha *et al.* 2003; Koyama *et al.* 2008; Kurzac *et al.* 2008). $R = (g_2 - g_1)/(g_3 - g_2)$ (Cheruzel *et al.* 2006), describing that the ground state for Cu(II): $R > 1$, indicates a d_z2 ground state, whereas $R < 1$ indicates a $d_x2_{-y}2$ ground state. We found that the 60 per cent component has $R = 1$ and the 40 per cent component has $R = 0.9$. So, the **g** anisotropy is in line with a strong distortion of the square pyramidal geometry towards a trigonal bipyramidal geometry, which leads to a lowering of the $d_x2_{-y}2$ energy. This trigonal bipyramidal geometry is absent for the amino-terminated dendrimer and is attributed to coordination of Cu(II) with the maltose groups and congestion of the dendrimer periphery owing to the maltose groups themselves. Therefore, the increase in the relative intensity of this rhombic component by increasing the generation arises from the insertion of Cu(II) in the more congested external branches of the dendrimers. This also means that the participation of hydroxyl groups from maltose in the coordination of Cu(II) is more reliable.

(*h*) *Influence of oligosaccharide unit on Cu(II) binding: electron paramagnetic resonance study*

We next investigated the *effect of the oligosaccharide component* of the dendrimer on Cu(II) binding by substituting a maltotriose shell for the maltose one. The corresponding experimental EPR spectra (**G2**–**G5**) are shown in figure 10. Figure 10*a* shows the experimental spectra of **G3-, G4-** and **G5-maltotriose**, which consist of both an axial and a rhombic component. These were obtained by subtracting the experimental spectra from dendrimers of different generations. Dendrimers with a maltotriose shell show the contribution of a rhombic component already by generation 3 (glycodendrimer **6**),

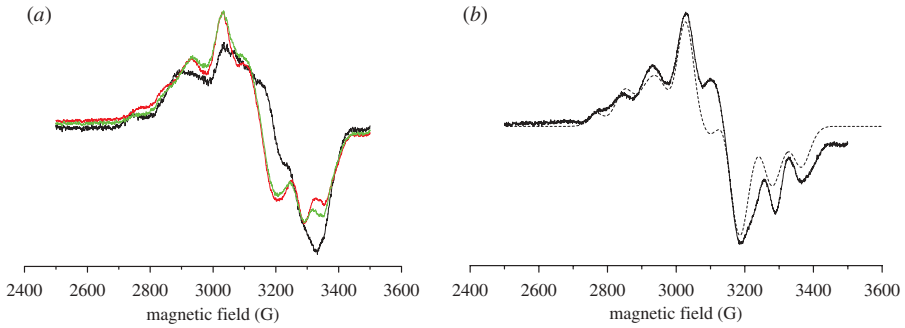

Figure 10. (*a*) Experimental EPR spectra of **6** (black line: G3-maltotriose (75% axial + 25% rhombic)), **7** (red line: G4-maltotriose (30% axial + 70% rhombic)) and **8** (green line: G5-maltotriose (40% axial + 60% rhombic)) glycodendrimers (0.1 M in surface sites, 150 K) containing Cu(II) at a concentration of 0.01 M. (*b*) Rhombic component (solid line) obtained from subtraction of the spectra of Gn-PPI-maltotriose (0.1 M in surface sites, 150 K) at different generations. Dotted line, 80%, $g_{ii} = 2.028$, 2.110, 2.200; $A_{ii} = 85$, 35, 85G and 20%, $g_{ii} = 2.06$, 2.163, 2.34; $A_{ii} = 80$, 103, 70G.

as the constraint exerted by the sugar functions in the periphery is stronger for maltotriose than for maltose. The experimental spectrum of **G2-maltotriose** (glycodendrimer **5**) almost corresponds to the sole axial component (figure S18, electronic supplementary material), which was the same observed for all glycodendrimers **5**–**8**, and was the same axial component described for **3** and **4** with a maltose shell. This means that, compared with maltose, the maltotriose units favour the copper coordination with four nitrogen sites even at the lowest generation. This is again due to the constraint induced by the maltotriose units and the larger size and rigidity of the dendrimer structure at the lower generations.

The extracted rhombic component for the dendrimer generations with maltotriose shells was computed (figure 10*b*) with different parameters from those used for the rhombic component of glycodendrimers with maltose shells: 80 per cent, $g_{ii} = 2.028$, 2.110, 2.200 and $A_{ii} = 85$G, 35G, 85G and 20 per cent, $g_{ii} = 2.060$, 2.163, 2.340 and $A_{ii} = 80$G, 103G, 70G. First, the A_{ii} values for the rhombic component of **6**–**8** are much greater than those of **3** and **4**. Similar sets of values for the $\boldsymbol{g}$ and $\boldsymbol{A}$ components were found in the literature for Cu(II) complexes with a structure changing from square bipyramidal to trigonal bipyramidal, with five nitrogen ligands (Ohtsu *et al.* 2001; Kurzac *et al.* 2008). Also with thiolate ligands, a similar distorted trigonal bipyramidal structure is formed (Brader *et al.* 1992). In these cases, as for the dendrimer generations with maltose shells, the ligand size and geometry forced the structure to geometrical distortions. However, the maltotriose functionalization of the PPI dendrimers further increases the A_i values owing to richer and/or stronger N-ligand coordination. The $R = (g_2 - g_1)/(g_3 - g_2)$ value for the 80 per cent species is 0.9, whereas for the 20 per cent species it is 0.58. In the first case, the ground state is shifting from the $d_x2_{-y}2$ to the d_z2 ground state, whereas in the second case, the $d_x2_{-y}2$ ground level is preferred, but the A_{ii} anisotropy indicates that a nitrogen ligand is approaching the copper nucleus in the Y-direction.

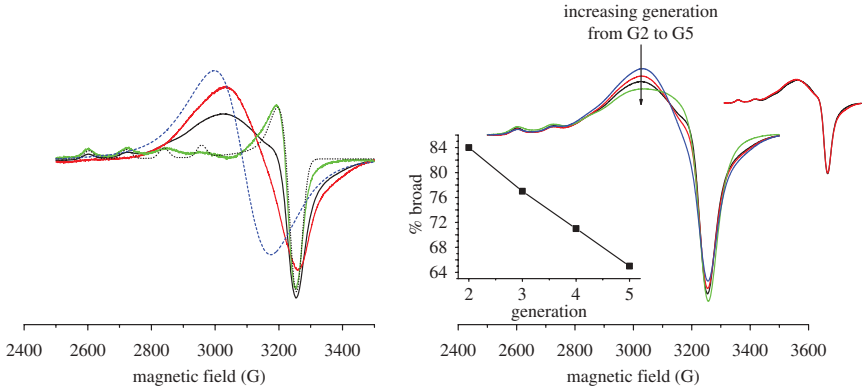

Figure 11. (*a*) Experimental EPR spectrum (black line, 150 K) of G4-PPI-maltose (**3**) (0.1 M in surface sites) solution containing Cu(II) at a concentration of 0.1 M; 'broad' (red line) and axial (green line) components obtained from subtraction of the spectra at different generations. The computation of the axial component is shown as the dashed line ($g_{ii} = 2.083$, 2.101, 2.438 + $A_{ii} = 5$, 5, 118G), whereas the blue-dashed line is the spectrum of the copper ion solution (150 K). (*b*) Experimental EPR spectra (150 K) obtained for G*n*-maltose (0.1 M in surface sites) with Cu(II) at a concentration of 0.1 M for the different generations (**1**, blue line; **2**, red line; **3**, black line; **4**, green line). Bottom-left inset: variation in the percentage of the broad signal as a function of generation. Top-right inset: comparison between the experimental spectra of G4-PPI-maltose (dashed line) and G4-PPI-maltotriose (solid line).

(*i*) *Influence of Cu(II) concentration on Cu(II) binding: electron paramagnetic resonance study*

Finally, we investigated the *effect of increasing Cu(II) concentration* on the EPR spectra. By increasing the concentration starting from 0.01 M, the spectra of the sugar functionalized dendrimers completely changed. We observed a progressive disappearance of the rhombic components and a progressive broadening of the axial components arising from nitrogen coordination. Figure 11*a* shows, as an example, the experimental spectrum recorded for **G4-maltose**, glycodendrimer **3**, with a 0.1 M concentration of Cu(II). The experimental spectrum is constituted by two components. These components were easily extracted by subtraction since they showed the same line shape but different relative intensities for different generations. The axial component shown in figure 11*a* was computed with the parameters $g_{ii} = 2.083$, 2.101, 2.428 and $A_{ii} = 5$G, 5G, 118G. These parameters are characteristic of a Cu−O_4 coordination because of Cu(II) coordinating oxygen ligands after saturation of the internal sites. The other component is a broad signal (red line, figure 11*a*) arising from an axial structure, but not showing any resolution of the ***g*** and ***A*** components. This signal arises from Cu(II) complexes at a high local concentration. We suggest that the Cu(II) ions concentrated internally within the dendrimer provide this broad signal (spin–spin interactions). The rhombic components are not visible anymore in this situation. It is interesting to note that the amino-functionalized dendrimers show a resolved Cu−N_4 coordination at this Cu(II) concentration, as previously found for the amino-functionalized PAMAM dendrimers (Ottaviani *et al.* 1997).

This means that the sugar units lead to a lower capacity of the dendrimers to internalize Cu(II) at the different nitrogen sites, like a structural barrier that partially impedes Cu(II) localization in the internal dendrimer generations.

By changing the generation, the relative intensity of the two components changes, as shown in figure 11*b*, which shows the spectra at 150 K obtained for the glycodendrimers **1**–**4** (G*n*-maltose) with a Cu(II) concentration of 0.1 M at different generations. Calculation of the relative intensities of the two components provided the variation of the percentage of the broad signal as a function of generation (left insert, figure 11*b*). The intensity of the broad component linearly decreases with the increase in generation. This is owing to the larger amount of Cu(II) involved in axial A_{ii}-resolved coordination since the available external surface sites increase by increasing the dendrimer size. Glycodendrimers **5**–**8** with a maltotriose shell show the same components and variation trend of relative intensity as the glycodendrimers with a maltose shell, but the broad component is slightly less broad for the fourth-generation glycodendrimer **7** with a maltotriose shell than the one with a maltose shell (**3**) (right inset in the top tight corner, figure 11*b*). This surely arises from a lower local concentration of Cu(II) inside the dendritic scaffold owing to the larger size of the maltotriose units. This last conclusion is supported by the experimental finding of lower n_{CuD} values for higher generations with maltotriose shells (table 3).

4. Conclusion

In summary, we find that reductive amination is a highly efficient tool for synthesizing third- to fifth-generation PPI dendrimers with densely organized maltotriose shells mostly having two maltotriose units per peripheral amino group. We used UV/Vis titration and EPR experiments to intensively study the Cu(II) complexation behaviour of a series of PPI dendrimers ranging up to the fifth generation that had either a dense maltose (Klajnert *et al.* 2008) or maltotriose shell (first and second generations in Appelhans *et al.* (2007). All glycodendrimers are characterized by an extended dendritic tertiary amino group scaffold surrounded by a dense oligosaccharide shell for metal ion complexation.

The dense-shell third-generation glycodendrimer **3** was used to study the different complexation capacities of these glycodendrimers towards various metal ions [Cu(II), Ag(I), VO(IV), Ni(II), Eu(III) and UO_2(VI)] in the aqueous phase and n_{MeD} was determined. We found that the binding capacity is very high towards UO_2(VI) and very low for Eu(III). The different complexation capacity is mainly governed by the structural features of the glycodendrimers, but also by the metal ion itself, which prefers different ligands for specific complex formation. Additionally, physical encapsulation during metal complexation can be considered as a possible driving force; for example, in the case of the high n_{MeD} for UO_2(VI).

The Cu(II) complexation of both series of dense-shell glycodendrimers showed generation-dependent complexation behaviour, which is similar to their parental counterparts in organic solution. The computer-aided analysis of EPR spectra recorded for copper nitrate solutions containing the glycodendrimers showed that both the Cu(II) coordination and symmetry of the generated complexes depend on the functionalization in the periphery (maltose or maltotriose), dendrimer

generation and the ratio of the copper and dendrimer concentrations. Both axial and rhombic symmetries were found. As generation increased, the maltose-functionalized dendrimer showed increased nitrogen coordination in the axial symmetry, which was expected given the increased number of nitrogen sites in the dendrimer interior. At higher generations, the structural distortion in the congested dendrimer periphery leads to the rhombic structure, in which maltose units are also able to coordinate the copper ions. In the case of maltotriose glycodendrimers, nitrogen coordination increased for both the axial and the rhombic geometries (figure S19, electronic supplementary material) owing to the large size of the maltotriose units relative to the maltose units and the fact that rhombic geometry is already favoured in low generations. Saturation of the external sites as copper concentration increases leads to copper coordination in the dendrimer periphery that also involves sugar and the water molecules.

Our findings can be further applied to aid development of targeted dendritic macromolecules that can substitute for protein function in metal ion transport (Kodama & Fujisawa 2008). In particular, the fourth- and fifth-generation glycodendrimers appear to be good candidates for Cu(II) carrier systems in a biological environment.

We thank the Saxonian Ministry of Science and Art and the German Ministry of Education and Science for financial support. We thank Dr N. Morgner for the assistance in the LILBID-MS investigations. This work was partly done under the COST Action TD0802 'Dendrimers in Biomedical Applications'.

References

Addison, A. W. 1983 Spectroscopic and redox trends from model copper complexes. In *Copper coordination chemistry: bio-chemical and inorganic perspectives* (eds K. D. Karlin & J. Zubieta), pp. 109–125. Guilderland, NY: Adenine Press.

Agarwal, A., Asthana, A., Gupta, U. & Jain, N. K. 2008 Tumour and dendrimers: a review on drug delivery aspects. *J. Pharm. Pharmacol.* **60**, 671–688. (doi:10.1211/jpp.60.6.0001)

Appelhans, D. *et al.* 2007 Oligosaccharide-modified poly(propylene imine) dendrimers: synthesis, structure determination, and Cu^{II} complexation. *Macromol. Biosci.* **7**, 373–383. (doi:10.1002/mabi.200600260)

Astruc, D., Ornelas, C. & Ruiz, J. 2008 Metallocenyl dendrimers and their applications in molecular electronics, sensing, and catalysis. *Acc. Chem. Res.* **41**, 841–856. (doi:10.1021/ar8000074)

Banyai, I., Orszagh, I., Berka, M. & Balogh, L. P. 2005 NMR studies of PAMAM dendrimers as intelligent delivery systems of drugs, cosmetics and personal care products. *Polym. Prepr.* **46**, 519–520.

Bennett, B., Antholine, W. E., D'souza, V. M., Chen, G. J., Ustinyuk, L. & Holz, R. C. 2002 Structurally distinct active sites in the copper(II)-substituted aminopeptidases from *Aeromonas proteolytica* and *Escherichia coli*. *J. Am. Chem. Soc.* **124**, 13 025–13 034. (doi:10.1021/ja026341p)

Boas, U. & Heegaard, P. M. H. 2004 Dendrimers in drug research. *Chem. Soc. Rev.* **33**, 43–63. (doi:10.1039/b309043b)

Bosman, A. W., Schenning, A. P. H. J., Janssen, R. A. J. & Meijer, E. W. 1997 Well-defined metallodendrimers by site-specific complexation. *Chem. Ber.* **130**, 725–728. (doi:10.1002/cber.19971300608)

Bosman, A. W., Janssen, H. M. & Meijer, E. W. 1999 About dendrimers: structure, physical properties, and applications. *Chem. Rev.* **99**, 1665–1688. (doi:10.1021/cr970069y)

Brader, M. L., Borchardt, D. & Dunn M. F. 1992 Ligand effects on the blue copper site. Spectroscopic studies of an insulin-stabilized copper(II) chromophore incorporating an exogenous thiolate ligand. *J. Am. Chem. Soc.* **114**, 4480–4486. (doi:10.1021/ja00038a006)

Cheruzel, L. E., Cecil, M. R., Edison, S. E., Mashuta, M. S., Baldwin, M. J. & Buchanan, R. M. 2006 Structural and spectroscopic characterization of copper(II) complexes of a new bisamide functionalized imidazole tripod and evidence for the formation of a mononuclear end-on Cu-OOH species. *Inorg. Chem.* **45**, 3191–3202. (doi:10.1021/ic051280s)

Crooks, R. M., Lemon III, B. I., Sun, L., Yeung, L. K. & Zhao, M. 2001*a* Dendrimers III. *Topics in current chemistry*, vol. 212 (ed. F. Vögtle), p. 82. Berlin, Germany: Springer.

Crooks, R. M., Zhao, M., Sun, L., Chechik, V. & Yeung, L. K. 2001*b* Dendrimer-encapsulated metal nanoparticles: synthesis, characterization and applications to catalysis. *Acc. Chem. Res.* **34**, 181–190. (doi:10.1021/ar000110a)

de Jesus, E. & Flores, J. C. 2008 Dendrimers: solutions for catalyst separation and recycling. *Indus. Eng. Chem. Res.* **47**, 7968–7981. (doi:10.1021/ie800381d)

Diallo, M. S., Christie, S., Swaminathan, P., Balogh, L., Shi, X., Um, W., Papelis, C., Goddard III, W. A. & Johnson Jr, J. H. 2004 Dendritic chelating agents. 1. Cu(II) binding to ethylene diamine core poly(amidoamine) dendrimers in aqueous solutions. *Langmuir* **20**, 2640–2651. (doi:10.1021/la036108k)

Diallo, M. S., Arasho, W., Johnson, J. H. & Goddard III, W. A. 2008 Dendritic chelating agents. 2. U(VI) binding to poly(amidoamine) and poly(propyleneimine) dendrimers in aqueous solutions. *Environ. Sci. Technol.* **42**, 1572–1579. (doi:10.1021/es0715905)

Domracheva, N., Mirea, A., Schwörer, M., Torre-Lorente, L. & Lattermann, G. 2004 EPR characterization of Cu-II complexes of poly(propylene imine) dendromesogenes: using the orienting effect of a magnetic field. *Chem. Phys. Chem.* **6**, 110–119. (doi:10.1002/cphc.200400328)

Esumi, K., Hosoya, T., Suzuki, A. & Torigoe, K. 2000 Formation of gold and silver nanoparticles in aqueous solution of sugar-persubstituted poly(amidoamine) dendrimers. *J. Colloid. Interf. Sci.* **226**, 346–352. (doi:10.1006/jcis.2000.6849)

Esumi, K., Matsumoto, T., Seto, Y. & Yoshimura, T. 2005 Preparation of gold-, gold/silver-dendrimer nanocomposites in the presence of benzoin in ethanol by UV irradiation. *J. Colloid. Interf. Sci.* **284**, 199–203. (doi:10.1016/j.jcis.2004.09.020)

Hathaway, B. J. & Tomlinson, A. A. G. 1970 Copper(II) ammonia complexes. *Coord. Chem. Rev.* **5**, 1–43. (doi:10.1016/S0010-8545(00)80073-9)

Hwang, S.-H., Moorefield, C. N. & Newkome, G. R. 2008 Dendritic macromolecules for organic light emitting diodes. *Chem. Soc. Rev.* **37**, 2543–2557. (doi:10.1039/b803932c)

Imaoka, T., Tanaka, R., Arimoto, S., Sakai, M., Fujii, M. & Yamamoto, K. 2005 Probing stepwise complexation in phenylazomethine dendrimers by a metallo-porphyrin core. *J. Am. Chem. Soc.* **127**, 13 896–13 905. (doi:10.1021/ja0524797)

Klajnert, B. *et al.* 2008 The influence of densely organized maltose shells on the biological properties of poly(propylene imine) dendrimers: new effects dependent on hydrogen bonding. *Chem. Eur. J.* **14**, 7030–7041. (doi:10.1002/chem.200800342)

Kodama, H. & Fujisawa, C. 2008 Copper metabolism and inherited copper transport disorders: molecular mechanism, screening, and treatment. *Metallomics* **1**, 42–52. (doi:10.1039/b816011m)

Koyama, N., Ishida, T., Nogami, T. & Kogane, T. 2008 A pyrazine-bridged linear penta-nuclear copper(II) complex and related tri- and dinuclear complexes showing various coordination structures and magnetic couplings. *Polyhedron* **27**, 2341–2348. (doi:10.1016/j.poly.2008.04.040)

Kurzac, B., Kamecka, A., Bogusz, K. & Jezierska, J. 2008 Stabilities and coordination modes of histidine in copper(II) mixed-ligand complexes with ethylenediamine, diethylenetriamine or N, N, N', N'', N''-pentamethyldiethylenetriamine in aqueous solution. *Polyhedron* **27**, 2952–2958. (doi:10.1016/j.poly.2008.05.029)

Lee, C. C., MacKay, J. A., Fréchet, J. M. & Szoka, F. C. 2005 Designing dendrimers for biological applications. *Nat. Biotechnol.* **23**, 1517–1526. (doi:10.1038/nbt1171)

Lesniak, W., Bielinska, A. U., Sun, K., Janczak, K. W., Shi, X., Baker Jr, J. R. & Balogh, L. P. 2005 Silver/dendrimer nanocomposites as biomarkers: fabrication, characterization, *in vitro* toxicity, and intracellular detection. *Nano Lett.* **5**, 2123–2130. (doi:10.1021/nl051077u)

Minchin, R. 2008 Sizing up targets with nanoparticles. *Nat. Nanotechnol.* **3**, 12–13. (doi:10.1038/nnano.2007.433)

Morgner, N., Barth, H.-D. & Brutschy, B. 2006 A new way to detect noncovalently bonded complexes of biomolecules from liquid micro-droplets by laser mass spectrometry. *Aust. J. Chem.* **59**, 109–114. (doi:10.1071/CH05285)

Ohtsu, H., Itoh, S., Nagatomo, S., Kitagawa, T., Ogo, S., Watanabe, Y. & Fukuzumi, S. 2001 Characterization of imidazolate-bridged dinuclear and mononuclear hydroperoxo complexes. *Inorg. Chem.* **40**, 3200–3207. (doi:10.1021/ic001036v)

Ottaviani, M. F., Bossmann, S., Turro, N. J. & Tomalia, D. A. 1994 Characterization of starbust dendrimers by the EPR technique. 1. Copper complexes in water solution. *J. Am. Chem. Soc.* **116**, 661–671. (doi:10.1021/ja00081a029)

Ottaviani, M. F., Montalti, F., Turro, N. J. & Tomalia, D. A. 1997 Characterization of starbust dendrimers by EPR technique. Copper(II) ions binding full-generation dendrimers. *J. Phys. Chem. B* **101**, 158–166. (doi:10.1021/jp962857h)

Ottaviani, M. F., Favuzza, P., Bigazzi, M., Turro, N. J., Jockusch, S. & Tomalia, D. A. 2000 A TEM and EPR investigation of the competitive binding of uranyl ions to starburst dendrimers and liposomes. Potential use of dendrimers as uranyl ion sponges. *Langmuir* **16**, 7368–7372. (doi:10.1021/la000355w)

Ottaviani, M. F., Valluzzi, R. & Balogh, L. 2002 Internal structure of silver-poly(amidoamine) dendrimer complexes and nanocomposites. *Macromolecules* **35**, 5105–5115. (doi:10.1021/ma010492f)

Peisach, J. & Blumberg, W. E. 1974 Structural implications derived from the analysis of electron paramagnetic resonance spectra of natural and artificial copper proteins. *Arch. Biochem. Biophys.* **165**, 691–708. (doi:10.1016/0003-9861(74)90298-7)

Reek, J. N. H., Arevalo, S., Van Heerbeek, R., Kamer, P. C. J. & Van Leeuwen, P. W. N. M. 2006 Dendrimers in catalysis. *Adv. Catal.* **49**, 71–151. (doi:10.1016/S0360-0564(05)49002-1)

Saha, M. K., Dey, D. K., Samanta, B., Edwards, A. J., Clegg, W. & Mitra, S. 2003 Synthesis, structure and magnetic properties of a mononuclear Cu(II) complex with a NNO donor Schiff base ligand and its oxalate- and oxamidato-bridged dinuclear complexes. *Dalton Trans.* 488–492. (doi:10.1039/b206076k)

Saudan, C., Balzani, V., Gorka, M., Lee, S.-K., van Heyst, J., Maestri, M., Ceroni, P., Vicinelli, V. & Vögtle, F. 2004 Dendrimers as ligands: an investigation into the stability and kinetics of Zn^{2+} complexation by dendrimers with 1,4,8,11-tetraazacyclotetradecane (cyclam) cores. *Chem. Eur. J.* **10**, 899–905. (doi:10.1002/chem.200305255)

Shi, X., Wang, S., Meshinchi, S., Van Antwerp, M. E., Bi, X., Lee, H. & Baker Jr, J. R. 2007 Dendrimer-entrapped gold nanoparticles as a platform for cancer-cell targeting and imaging. *Small* **3**, 1245–1252. (doi:10.1002/smll.200700054)

Solomon, E. I. & Hanson, M. A. 2006 Bioinorganic spectroscopy in inorganic electronic structure and spectroscopy. In *Applications and case studies* (eds E. I. Solomon & A. B. P. Lever), vol. II, pp. 1–130. New York, NY: John Wiley & Sons.

Takanashi, K., Fujii, A., Nakajima, R., Chiba, H., Higuchi, M., Einaga, Y. & Yamamoto, K. 2007 Heterometal assembly in dendritic polyphenylazomethines. *Bull. Chem. Soc. Jap.* **80**, 1563–1572. (doi:10.1246/bcsj.80.1563)

Tran, M. L., Gahan, L. R. & Gentle, I. R. 2004 Structural studies of copper(II)-amine terminated dendrimer complexes by EXAFS. *J. Phys. Chem. B* **108**, 20 130–20 136. (doi:10.1021/jp037569h)

Venditto, V. J., Regino, C. A. S. & Brechbiel, M. W. 2005 PAMAM dendrimer based macromolecules as improved contrast agents. *Mol. Pharm.* **2**, 302–311. (doi:10.1021/mp050019e)

Wiener, E. C., Auteri, F. P., Chen, J. W., Brechbiel, M. W., Gansow, O. A., Schneider, D. S., Belford, R. L., Clarkson, R. B. & Lauterbur, P. C. 1996 Molecular dynamics of ion-chelate complexes attached to starburst dendrimers. *J. Am. Chem. Soc.* **118**, 7774–7782. (doi:10.1021/ja9536126)

Zhao, M. & Crooks, R. M. 1999 Intradendrimer exchange of metal nanoparticles. *Chem. Mater.* **11**, 3379–3385. (doi:10.1021/cm990435p)

Zhao, M., Sun, L. & Crooks, R. M. 1998 Preparation of Cu nanoclusters within dendrimer templates. *J. Am. Chem. Soc.* **120**, 4877–4878. (doi:10.1021/ja980438n)

CHEMISTRY
AN ASIAN JOURNAL

FULL PAPERS

DOI: 10.1002/asia.200((will be filled in by the editorial staff))

Sugar-decorated dendritic nanocarriers: Encapsulation and release of the octahedral rhenium cluster complex $[Re_6S_8(OH)_6]^{4-}$

Manja Kuhlmann,[a] Holger Stephan,*[a] Hans-Jürgen Pietzsch,[a], Gerhard Geipel,[b] Dietmar Appelhans,[c] Brigitte Voit,[c] Jan Hoffmann,[d] Bernhard Brutschy,[d] Yuri V. Mironov,[e] Konstantin A. Brylev,[e] and Vladimir E. Fedorov[e]

Abstract: The encapsulation of a nanometer sized octahedral anionic rhenium cluster complex with six terminal hydroxo ligands $[Re_6S_8(OH)_6]^{4-}$ in maltose-decorated poly (propylene amine) dendrimers (POPAM, generation 4 and 5) has been investigated. Ultrafiltration experiments showed that maximal loading capacity of the dendrimers with the cluster complex is achieved after about ten hours in aqueous solution. To study the inclusion phenomena, three different methods have been applied: UV/vis, time-resolved laser-induced fluorescence spectroscopy (TRLFS) and laser induced liquid bead ion desorption mass spectrometry (LILBID-MS). From the results obtained, it could be concluded that: (i) the hydrolytic stability of the rhenium cluster complex is significantly enhanced in the presence of dendritic hosts; (ii) the cluster anions are preferentially bound inside the dendrimers; (iii) the number of cluster complexes encapsulated in the dendrimers increases with rising dendrimer generation. On average, 4 – 5 cluster anions can preferentially be captured in the interior of sugar-coated dendritic carriers. An asymptotical progression of the release of cluster complexes from the loaded dendrimers was observed under physiologically relevant conditions (isotonic sodium chloride solution: ~ 93% within 4 days for loaded POPAM-G4-maltose; ~ 86% within 4 days for loaded POPAM-G5-maltose). Those encapsulation and release properties of maltose-decorated nanocarriers imply the possibility for the development of the next generation of dendritic nanocarriers with specific targeting of destined tissue for therapeutic treatments.

Keywords: dendrimers • rhenium cluster • sugar • host-guest-chemistry • encapsulation

[a] M. Kuhlmann, Dr. H. Stephan, Dr. H.-J. Pietzsch
Forschungszentrum Dresden-Rossendorf, Institute of Radiopharmacy
PF 510119, 01314 Dresden (Germany)
Fax: (+49)351-260-3232
E-mail: h.stephan@fzd.de

[b] Dr. G. Geipel
Forschungszentrum Dresden-Rossendorf, Institute of Radiochemistry
PF 510119, 01314 Dresden (Germany)

[c] Dr. D. Appelhans, Prof. Dr. B. Voit
Leibniz Institute of Polymer Research Dresden, Hohe Strasse 6, 01069 Dresden (Germany)

[d] J. Hoffmann, Prof. Dr. B. Brutschy
Johann-Wolfgang-Goethe Universität, Institute for Physical and Theoretical Chemistry, Max-von-Laue-Strasse 7, 60438 Frankfurt/Main, (Germany)

[e] Dr. Y. V. Mironov, Dr. K. A. Brylev, Prof. Dr. V. E. Fedorov
Nikolaev Institute of Inorganic Chemistry, Siberian Branch of the Russia Academy of Sciences, 3 Acad. Lavrentiev prospect, 630090 Novosibirsk, (Russia)

Supporting information for this article is available on the WWW under http://dx.doi.org/10.1002/asia.200xxxxxx. Additional figures show mass spectra of pure dendrimers and some representative Re cluster/glycodendrimer associates. LILBID mass spectra of the pure glycodendrimers **1** and **2** (Figure 1-SI); LILBID mass spectra of Re cluster/glycodendrimer associates using a complexation ratio of 10 (cluster/dendrimer) as obtained after 5 weeks (Figure 2-SI); LILBID mass spectra of Re cluster/glycodendrimer associates using a complexation ratio of 20 (cluster/dendrimer) as obtained after 5 weeks (Figure 3-SI). Molar mass of dendrimer **1** and **2**, complexation ratio between the anionic cluster **3** and dendrimer, and molar mass of cluster-loaded glycodendrimer **1** and **2** are summarized in Table 1-SI.

Introduction

Due to their defined highly-branched symmetric architecture, dendrimers became of great interest for manifold applications in the last recent years.[1-7] The unique behavior of dendrimers is a reflection of their compact, tree-like molecular structure, providing an arrangement of inner and outer molecular functionalities. One promising application is highlighted in the use of them as receptor and carrier molecules at the nanometer level. The enormous versatility and variety of dendritic structures offer considerable opportunity particularly in medicine.[8-16] An intriguing application is the encapsulation of drug molecules for subsequent controlled release to certain organs and tissues. For the first time this principle was demonstrated by Meijer and co-workers using the so-called dendritic box which allows shape-selective liberation of encapsulated guests.[17, 18] Pegylation of dendrimer surface makes them more useful for pharmaceutical applications.[19-24] Recently, the development of dendritic sugar-containing biohybrids was reported which allow the encapsulation and controlled release of small drug molecules.[25-28] We have established glycodendrimers with dense maltose shell[29] which can be considered as amphiphilic macromolecules showing cationic core and neutral surface.[30] The neutral surface is provided by a dense sugar shell to give a high biocompatibility. It is worth highlighting that these dendrimers seem to be ideal hosts for nanometer sized guests. Gold nanoparticles (∅ ≤ 1 nm) can be produced and stabilized inside of a 5th generation POPAM-maltose dendrimer.[31] In a recent study the cellular uptake of green fluorescent nanodiamonds stabilized by different natural and artificial transport systems has been considered. Only in the case of maltotriose-decorated 4th generation POPAM dendrimer, aggregation of the nanodiamond in the cytoplasma does not occur, and the desired targeting of intracellular structures such as actin filament and mitochondria was thus possible.[32]

The exploration of biological activity of polynuclear cluster compounds revealed antiviral and antitumoral properties in cancer cells.[33] In this context we recently recognized polyoxometalates as a new class of potent enzyme inhibitors.[34-36] This holds true for octahedral rhenium cluster complexes with terminal hydroxo and carboxylate ligands.[37] However, many of such cluster compounds possess poor hydrolytic stability and show insufficient in vivo selectivity.[33] Encapsulation of clusters in dendrimers grafted with groups for biological targeting may help to overcome these drawbacks. The development of inorganic-organic hybrids consisting of polyoxometalates and dendritic structures has been reported for application in catalytic processes. That includes the covalent and non-covalent binding of cluster compounds onto the dendrimer surface.[38-42] Wrapping anionic clusters with dendrons containing ammonium groups at the focal point is often applied.[43-45] In contrast, assembling of cluster anions at positively charged branching units of dendrimers is quite scarce.[46, 47] Among the three basically different approaches to bind anionic cluster compounds non-covalently to a dendritic structure, ionic interaction at internal cavities seems to be the most appropriated strategy in view of medical applications. Thus, the dendritic surface may be used to influence the releasing properties of potential drug compounds. Moreover, bio-distribution and pharmacokinetics of loaded dendrimers can be tailor-made. In this perspective, cationic dendrimers with densely organized maltose shells are utilized to bind anionic cluster compounds by electrostatic interaction at the interior.

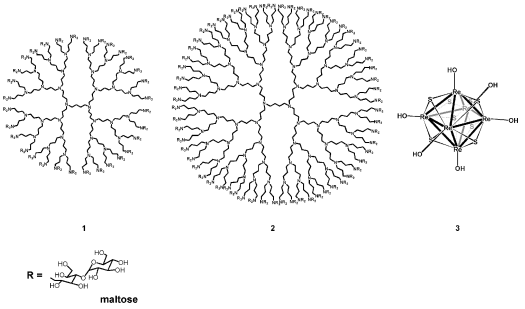

Scheme 1. General structure of maltose-modified POPAM dendrimers of 4th (**1**), 5th (**2**) generation and the anionic octahedral hexahydroxo rhenium sulfide cluster $[Re_6S_8(OH)_6]^{4-}$ (**3**).

The present work reports the inclusion properties of the hydroxo rhenium sulfur cluster anion $[Re_6S_8(OH)_6]^{4-}$ **3** into POPAM dendrimers **1** and **2** with dense maltose shell (Scheme 1). A range of techniques, including UV/vis and time-resolved laser fluorescence spectroscopy, inductively coupled plasma and laser-induced liquid bead ionization/desorption mass spectrometry, and ultrafiltration have been used to characterize the inclusion phenomena and releasing properties. Furthermore, in-situ encapsulation of anionic cluster was carried out in the presence of glycodendrimer synthesis to compare those uptake properties with the well-known uptake studies.

Results and Discussion

Before studying the uptake of the anionic cluster $[Re_6S_8(OH)_6]^{4-}$ by the glycodendrimers **1** and **2** in water, the stability of the anionic cluster $[Re_6S_8(OH)_6]^{4-}$ was checked. It is well-known that the cluster anion $[Re_6S_8(OH)_6]^{4-}$ is slowly converted into a neutral species $[Re_6S_8(H_2O)_4(OH)_2]$ in aqueous solution.[48] For that purpose, using diluted anionic cluster solution (c= 20µM), the charge transfer band[49] of $[Re_6S_8(OH)_6]^{4-}$ (bridging sulfur in Re-S-Re) at 220 nm (ε=41750 $M^{-1}\cdot cm^{-1}$) and its shoulder (λ=231 nm, ε=35000 $M^{-1}\cdot cm^{-1}$) was chosen to follow the conversion of the anionic cluster into a neutral cluster over two weeks. The neutral cluster is insoluble in

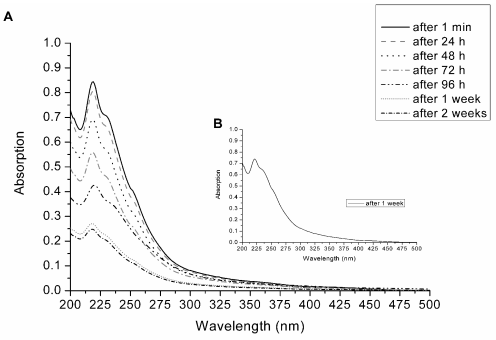

aqueous solution. As shown in Figure 1a, the charge transfer bands

Figure 1. (A) Absorption spectra of $[Re_6S_8(OH)_6]^{4-}$ (c_3=20µM in water) as function of time. (B) Absorption spectra of **1**+**3** (c_1= 2µM, c_3=20µM) after 1 week.

of $[Re_6S_8(OH)_6]^{4-}$ decrease as expected. Additional experiments showed us that after the addition of low amounts (2µM) of maltose dendrimers **1** (shown in Figure 1b) and **2** to a solution of **3**, the charge transfer bands of the cluster remained completely unchanged for at least one week proving that the cluster anion structure is unaffected.

To achieve complete uptake of the anionic cluster by the glycodendrimers **1** and **2**, the time dependence of the cluster uptake was investigated. Ultrafiltration technique was performed to determine the final cluster concentration in the filtrate by ICP-MS technique. The data given in Figure 2 show that less than 10% of the initial cluster concentration was found in the filtrate after 2.5 h for G4-dendrimer **1**. As expected, the attainment of the association equilibrium needs more time in the case of the G5-dendrimer **2** which has a more densely glyco shell. Overall, ultrafiltration gave evidence that almost all guest molecules are strongly bound by the dendrimers in about 10 h. All further samples were pre-equilibrated for 24 h in non-buffered aqueous solution before studied by different methods.

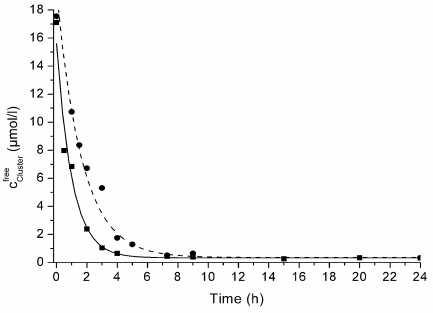

Figure 2. Cluster concentration in the filtrate after ultrafiltration as function of time (c_1, c_2=2µM, c_3=20µM) as determined by ICP-MS.

As recently examined, an aqueous solution containing the cluster anion $[Re_6S_8(OH)_6]^{4-}$ shows broad and structure-less emission in a wavelength region between 550 nm and 900 nm with maximum wavelengths varying with pH from ~655 nm in an alkaline solution and to ~685 nm in an acid solution.[48] Time-resolved laser fluorescence spectroscopy was applied to investigate in detail the association process of the cluster anion **3** with maltose dendrimers **1** and **2**. Under the experimentally chosen conditions, the maltose dendrimers do not show any fluorescence. Interestingly, both fluorescence intensity and lifetime of the cluster compounds are significantly increased after addition of the dendrimers (Figure 3). In the concentration range investigated, the influence of pH change is negligible. There is only an increase of pH from 7.5 to 7.8 if the dendrimer concentration rises from 2 to 40 µM. Therefore, the boost of both parameters should be caused by an additional process. After addition of the dendrimers, the fluorescence lifetime increases from 1.1 µs to 2.6 µs for both systems and shows a single monoexponential decay. We assume that hydrate molecules of the cluster complexes cause a quenching effect and propose that the encapsulation process is accompanied by the delivery of the outer sphere water molecules of the cluster complexes. It is known that water molecules determine a dynamic quenching effect [50, 51] and the fluorescence intensities and lifetimes undergo a deactivation

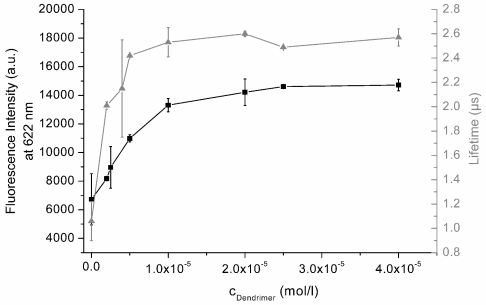

Figure 3: Fluorescence intensity (black line) and lifetime (gray line) of **3** (20µM) as function of dendrimer **1** concentration (0…40µM) in water.

process. Thus, the dehydration process manifests in increasing fluorescence lifetimes. More than 40 years ago *Kropp* and *Horrocks*[50, 51] have established that the high-frequency OH stretch vibrations play an important role in the radiation-less de-excitation path. The energy transfer from excited state back to the ground state takes place in an energy gap. The lower the number of vibrational quanta given in energy gap, the higher the value of oscillators overlaps integral. This theory implies that the number of oscillator quanta significantly affects the rate of radiation-less de-excitation. Due to the isotope effect of D_2O (2500 cm^{-1}) the frequency vibration is much lower than for H_2O (3600 cm^{-1}) which causes an increase in number of vibrational quanta and consequently, the quenching is reduced. Therefore, radiation-less de-excitation path depends on the number of OH oscillator in the first coordination sphere, only.[50] This evidence emphasizes the encapsulation of clusters in the sugar-coated dendrimers. In order to confirm this, we exchanged H_2O for sample **3** against D_2O because heavy water decreases the effect of quenching. The octahedral hexahydroxo rhenium cluster complex in H_2O solution has an emission lifetime of 1.1 µs while it was found to be nine times longer in D_2O solution (Table 1). Thus, water quenches the fluorescence of the cluster and supports the former given theory. Furthermore, both fluorescence intensity and fluorescence lifetime showed similar behavior.

Table 1. Fluorescence intensities (I) at 622 nm and lifetimes (τ) of cluster (20µM) in water and heavy water

Cluster/solvent	I (a.u.)	τ (µs)
H_2O	6752	1.1
D_2O	10414	10.1

In order to determine the number of cluster molecules bound by the dendrimers, we applied an approach by using the Scatchard method.[29, 52] On the basis of the fluorescence spectra **1**+**3** (Figure 4) depending on different dendrimer concentrations, $1/c_{free}$ is applied versus $c_{dendrimer}/c_{cluster,bound}$ (Figure 5). However, the application is considered only for the dynamic range where the cluster exists in

excess. From the slope of the linear regression, the association constant (K_{ass}) and from the intersection with the ordinate, the number of cluster molecules encapsulated per dendrimer (n) can be

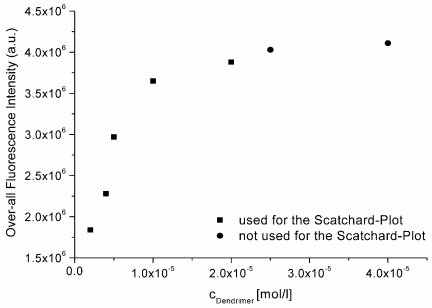

Figure 4. Over-all fluorescence intensities of sample **1**+**3** depending on the dendrimer concentration. Only (■) were used to determine the number of hosted cluster by Scatchard-Plot.

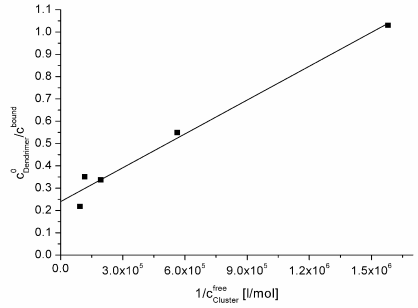

Figure 5. Scatchard-Plot of the values (■) which are shown in Figure 4. The intersection with the ordinate gives the inverse value of hosted cluster.

calculated (Table 2). Derived from the experimental results of fluorescence measurements, a mean value of 4 and 5 cluster molecules bound by dendrimers **1** and **2** can be calculated. This finding is in good agreement with results obtained from experiments with a fifth generation dendritic box and alkyl amide G5-dendrimers using Bengal Rose as guest which showed that 4 to 7 dye molecules can be captured.[18, 53] Deduced from the molecular structure of the rhenium cluster complex **3** [47], a comparable size to the Bengal Rose molecule can be supposed. Molecular dynamics simulations in dichloromethane indicate that 4 Bengal Rose molecules are encapsulated within the internal cavities. [54] Very recently, it was proven by molecular dynamics calculations in trichloromethane that also cluster anions as α-Keggin ions can be efficiently bound by a dendritic skeleton.[55] The association constants of maltose dendrimers **1** and **2** with **3** are in the same range as found for pegylated dendrimers and Bengal Rose[19], and POPAM dendrimers containing terminal amino groups and 1-anilinonaphthalene-8-sulfonic acid (ANS), respectively.[29] The maltose-decorated dendrimers **1** and **2** form weaker complexes with ANS (K_{ass} ~ $2.5 \cdot 10^4$ M^{-1} [29]) than obtained for the rhenium cluster **3**. That seems to be plausible because of the higher charge density of the tetravalent cluster **3** comparing to the monovalent ANS anion.

Table 2. Association constant (K_{ass}) and number of encapsulated cluster complexes per dendrimer (n)

Host-guest system	K_{ass} [M^{-1}]	n
1 + **3**	4.8 x 10^5	4-5
2 + **3**	5.5 x 10^5	4-5

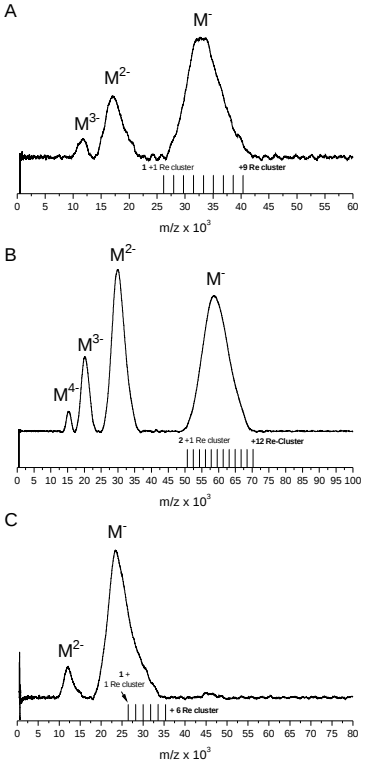

Figure 6. LILBID mass spectra of Re cluster/glycodendrimer associates determined by LILBID MS experiments. (A) Re cluster/1 associates obtained from ultrafiltration (c_1=40µM, c_3=400µM): M^- for **1** with 4-5 Re cluster; (B) Re cluster/2 associates obtained from ultrafiltration (c_2=25µM, c_3=250µM): M^- for **2** with 5-6 Re cluster; (C) Re cluster-loaded **1** as obtained by in-situ preparation during the synthesis of glycodendrimer **1**: M^- without Re cluster and highest uptake of **1** with 3 Re cluster. Solid lines indicate the cluster/glycodendrimer associates with corresponding experimental masses. LILBID mass spectra of pure glycodendrimers 1 (A) and 2 (B) are shown in Supporting Data (Figure 1-SI).

To enhance the loading capacity of dendrimers, the concentration of the cluster complex was distinctly increased. In a typical experiment, an aqueous solution of 1 mg/mL dendrimer **1** and **2** was treated with a 10-fold excess of $[Re_6S_8(OH)_6]^{4-}$ for 24 hours. Afterwards, the solution was ultrafiltrated and the retentate was analyzed by LILBID-MS after 1 week of their preparation

(Figure 6). As can be seen from Figure 6, the peak maxima correspond to following cluster/glycodendrimer associates: (A) 4-5 cluster are loaded by **1** and (B) 5-6 cluster are loaded by **2**. The possible mass peaks and peak maxima of several cluster/glycodendrimer associates, determined by LILBID-MS, are summarized in Table 1-SI (Supporting Information). For long-term stability, cluster/glycodendrimer associates were investigated by LILBID-MS after 5 weeks of their preparation. Similar cluster/glycodendrimer associates were determined (Supporting Information Figure 2-SI). This result confirms significantly the high loading capacity of the glycodendrimers with the anionic cluster over a longer period. The mass spectrometry results, obtained after 1 week and 5 weeks of their preparation, indicate also the formation of higher loaded species if a 20-fold excess of cluster complex is used (up to 12 cluster for **1** and up to 14 cluster for **2**, Supporting Information Figure 3-SI).

Furthermore, the in-situ preparation of cluster/glycodendrimer associates was investigated. Thus, during the attachment of the maltose shell to the G4-dendrimer **1**, cluster anions were added whereby the same reaction conditions were used as recently described.[29] Surprisingly, results of LILBID-MS (Figure 6c) confirmed a lower binding capacity (only 1-3 anionic clusters) as obtained for the inclusion experiments. Additionally, the peak maximum found for the in-situ preparation was assigned for the unloaded dendrimer **1**. Most likely, this can be explained by the fact that the reaction was performed in the presence of borate buffer (0.1 M), and consequently the huge excess of the competing borate anion hinders the encapsulation of many cluster anions. Overall, the loading of glycodendrimers with cluster complexes in deionized water is superior over the in-situ preparation.

The dendrimer-rhenium cluster associates are quite stable in non-buffered aqueous solution. After ultrafiltration or dialysis, no rhenium could be detected by ICP-MS in the filtrate at least out to 1 week. To investigate the ability to liberate the cluster molecules encapsulated, aqueous solutions of dendrimers **1** and **2** (15µM) and cluster **3** (150µM) were mixed and stored for 24 h. The loaded dendrimers (retentate) were separated from the excess of cluster (filtrate) by ultrafiltration. The concentration of encapsulated cluster was found as 54 µM for **1** and 68 µM for **2** which corresponds to 3-4 $[Re_6S_8(OH)_6]^{4-}$ anions per POPAM-G4-maltose and 4-5 $[Re_6S_8(OH)_6]^{4-}$ anions per POPAM-G5-maltose molecule. Under the experimentally chosen conditions, the cluster molecules remain inside of the dendrimers for at least 7 days. After addition of isotonic sodium chloride solution (huge excess of competing chloride anions) to the loaded dendrimers, an asymptotical progression of the release of rhenium cluster was observed (Figure 7). While the main part of cluster complexes is released after one day, the residual is rather slowly delivered. Under these physiologically relevant conditions, 93% of the cluster complex was liberated from POPAM-G4-maltose dendrimer **1** within 4 days. In the case of G5-dendrimer **2**, the amount of released guest molecules was 86% after 4 days.

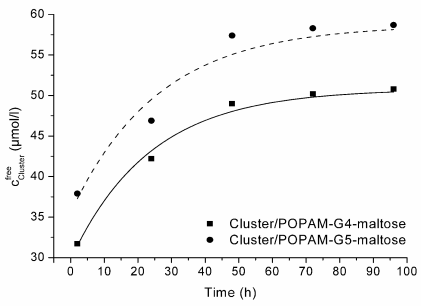

Figure 7. Release profile of $[Re_6S_8(OH)_6]^{4-}$ from loaded dendrimer **1** (■) and 2 (●).

Additionally, dynamic light scattering experiments (DLS) were carried out to clarify the point whether isolated Re cluster/glycodendrimer associates or tendentiously aggregated Re cluster/glycodendrimer associates are responsible for the slow release properties of the anionic Re cluster from the amphiphilic macromolecules **1** and **2** [30]. For that purpose, Re cluster/glycodendrimer **2** associates were investigated using the same experimental condition as mentioned before [1 mg of **2** in 1 ml water with an excess of Re cluster (5, 10 or 20 equivalents)]. The DLS results (Scheme 2) show the presence of Re cluster/glycodendrimer **2** associates with size dimensions of about 6 nm for 5 and 10 equivalents of Re cluster and Re cluster/glycodendrimer **2** associates with size dimensions of about 20 nm for 20 equivalents after 24 h. Therefore, only a large excess of cluster anions favors the formation of higher aggregates. It can be deduced for the relevant uptake studies with a Re cluster/glycodendrimer **2** complexation ratio of 10 that no aggregated cluster/glycodendrimer associates are present in the solution. The cluster/glycodendrimer associates formed possess the same size dimension as the pure glycodendrimer **2** (∅ 6 nm). Thus, one can assume a preferred location of cluster complexes within the dendritic scaffold of **2**. This gives good correlation to results found for Rose Bengale/POPAM dendrimer associates [17-19]. The final study carried out by DLS experiments exhibit the certainty that isolated Re cluster/glycodendrimer associates are responsible for the slow release of Re cluster under physiologically relevant conditions.

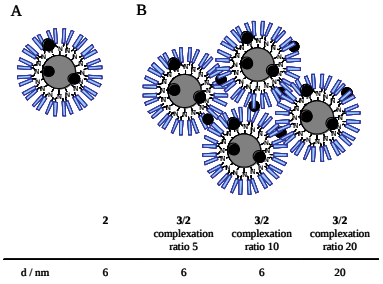

Scheme 2. Sketch for isolated (A) and aggregated (B) Re cluster/glycodendrimer associates observed for various **3**/**2** complexation ratios and average dimension sizes for **3**/**2** associates determined by DLS measurements. Black spots present the Re cluster complexes. A belongs to a complexation ratio 5 and 10. B belongs to a complexation ratio 20.

Conclusion

In summary, we have shown that sugar-capped POPAM dendrimers are well-suited to encapsulate and slowly release nanosized guest molecules, such as anionic hexanuclear rhenium cluster complexes. Results obtained from time-resolved laser fluorescence spectroscopy indicate that guest molecules are partially de-solvated during the process of inclusion. Ultrafiltration and LILBID-MS experiments provide strong evidence that the guest molecules are preferentially bound in the interior of the dendritic skeleton. Electrostatic

interaction of anionic cluster complexes with the ammonium groups of the dendrimers is quite strong (Kass: 4.8 x 10^5 M^{-1} for fourth generation dendrimer **1**; 5.5 x 10^5 M^{-1} for fifth generation dendrimer **2**). Furthermore, the hydrolytic stability of the rhenium cluster complex is significantly enhanced in the presence of the dendrimers. These features may be utilized for the development of novel drug delivery systems. The synthetic pathway conveniently allows the modification of dendrimer surface with additional biologically active molecules, hence offering great potential for using such dendritic nano-container for in vivo targeting.

Experimental Section

Materials: Maltose-modified POPAM dendrimers of fourth **1** (M = 24.5 kDa) and fifth **2** (M = 47.9 kDa) generation were prepared by reductive amination. Detailed studies about the preparation and characterization were described elsewhere.[29] The cluster compound $K_4[Re_6S_8(OH)_6]\cdot 8H_2O$ (M_r = 1776,3 g/mol; $[Re_6S_8(OH)_6]^{4-}$: M_r = 1475.8 g/mol) was synthesized as previously reported by the reaction of cluster polymer $Re_6S_8Br_2$ with molten KOH.[56] All other reagents were commercially available products of reagent grade and used as purchased. The in-situ uptake study of the anionic cluster complex **3** was carried out with the 4th generation dendrimer **1** according the synthetic procedure described in the literature.[29] The molar ratio applied was 10/1 (cluster/dendrimer).

Instrumentation: UV/vis spectra were recorded on a Specord 210 spectrophotometer (Analytik Jena, Germany) in a 1 cm quartz cuvette (Helma, Germany). Fluorescence spectra were performed by time-resolved laser-induced fluorescence spectroscopy (TRLFS). The aqueous solutions of **1**, **2**, **3**, **1**+**3** and **2**+**3** were measured in a 1 cm fluorescence quartz cuvette (Helma, Germany). Each spectrum was measured 2 times. A Nd:YAG laser system (Miniligtht, Continuum Corp., USA) was used. The samples were excited with a laser pulse at a wavelength of 266 nm. The measurements of the spectra were performed by an intensified CCD camera system (Horiba Jobin Yvon). The settings are as follows: gate width (200 nm), accumulation on CCD (100), time resolution (200 ns for sample **3**, 500 ns for sample **1**+**3** and **2**+**3**) and delay range (40-10040 ns for sample 3 and 40-25040 ns for sample **1**+**3** and **2**+**3**). Ultrafiltration experiments of loaded dendrimers were performed with a Labofuge 400R (Heraus). Vivaspin 2 (cellulose) and 4 (polyethersulfone) membranes (Sartorius Stedim Biotech) with a cut-off of 10 kDa were used. The solutions were centrifuged with 4000 g for 20 min. The recovery of the retentate was achieved by centrifugation with 3000 g for 3 min, and was than transferred in a defined volume of deionized water. The rhenium content was determined by ICP-MS (Perkin Elmer, Elan 9000, Quadrupol technique) in both filtrate and retentate. Each sample was measured 2 times. Membrane tubes (ZelluTransRoth VSerie with 2000 MWCO, Carl Roth GmbH&Co, Karlsruhe/Germany) for dialysis of Re cluster 3/glycodendrimer 1 associates for three days in deionized water were used after washing with deionized water. LILBID-MS analyses were used to determine the molar mass of dendrimers **1** and **2**, and their corresponding cluster associates; the method is described elsewhere.[57-60] The dendrimer samples were prepared in aqueous solution with concentrations between 1 x 10^{-6} – 5 x 10^{-6} M for **1** and **2**. All measurements were performed in anionic mode. The instrument was calibrated with bovine serum albumin. Dynamic light scattering measurements were carried out by using Zetasizer Nano S (ZEN 1600) of Malvern Instruments, UK. The instrument was equipped with a monochromatic coherent 4 mW Helium Neon laser (l = 633 nm) as light source and the so-called NIBS$^{\circ}$-technology (Non-Invasive Back-Scattering; patent from ALV GmbH, Germany). The light scattered by particles is recorded at an angle of 173°, so the effects of multiple scattering and possible contaminants are greatly reduced. As a result of the very sensitive detector (Avalanche Photodiode), the embedded moveable lens and the automatic laser attenuation (transmission of 100% to 0.0003%) we are able to determine particle size in a wide size range (0.6 nm to 6 µm) and in very expanded concentration range. Complexation solutions were filtered by PTFE-filters with pore size of about 0.45 µm.

Acknowledgements

The authors would like to thank Stephan Weiß for excellent technical assistance. Ursula Schäfer is acknowledged for ICP-MS and Franka Ennen for DLS measurements. This research was supported by the Bundesministerium für Bildung und Forschung (WTZ-Projekt RUS 07/005).

[1] G. R. Newkome, C. N. Moorefield, F. Vögtle, *Dendrimers and Dendrons*, Wiley-VCH, Weinheim, **2001**.

[2] J. M. J. Fréchet, D. A. Tomalia (Eds.), *Dendrimers and Other Dendritic Polymers*, Wiley, Chichester, **2001**.

[3] C. A. Schalley, F. Vögtle (Eds.), *Dendrimers V*, *Top. Curr. Chem.* **2003**, *228*, and previous volumes I-IV.

[4] A. W. Bosman, H. W. Janssen, E. W. Meijer, *Chem. Rev.* **1999**, *99*, 1665-1688.

[5] D. Astruc, *C. R. Chimie*, **2003**, *6*, 709-1212.

[6] J. P. Majoral, *New J. Chem.* **2007**, *31*, 1025-1380.

[7] F. Vögtle, G. Richardt, N. Werner, *Dendrimer Chemistry: Concepts*, *Syntheses*, *Properties*, *Applications*, Wiley-VCH,Weinheim, **2009**.

[8] F. Vögtle, S. Gestermann, R. Hesse, H. Schwierz, B. Windisch, *Prog. Polym. Sci.* **2000**, *25*, 987-1041.

[9] O. M. Koo, I. Rubinstein, H. Onyuksel, *Nanomedicine: Nanotechnology, Biology, and Medicine* **2005**, *1*, 193-212.

[10] S. D. Caruthers, S. A. Wickline, G. M. Lanza, *Curr. Opin. Biotechnol.* **2007**, *18*, 26-30.

[11] I. J. Majoros, C. R. Williams, J. R. Baker, *Curr. Top. Med. Chem.* **2008**, *8*, 1165-1179.

[12] Y. Y. Cheng, J. R. Wang, T. L. Rao, X. X. He, T. W. Xu, *Front. Biosci.* **2008**, *13*, 1447-1471.

[13] R. K. Tekade, P. V. Kumar, N. K. Jain, *Chem. Rev.* **2009**, *109*, 49-87.

[14] S. E. Stiriba, H. Frey, R. Haag, *Angew. Chem. Int. Ed.* **2002**, *41*, 1329-1334.

[15] R. Haag, F. Kratz, *Angew. Chem. Int. Ed.* **2006**, *45*, 1198-1215.

[16] V. Gajbhiye, V. K. Palanirajan, R. K. Tekade, N. K. Jain, *J. Pharm. Pharmacol.* **2009**, *61*, 989-1003.

[17] J. F. G. A. Jansen, E. M. M. de Brabander-van den Berg, E. W. Meijer, *Science* **1994**, *266*, 1226-1229.

[18] J. F. G. A. Jansen, E. W. Meijer, E. M. M. de Brabander-van den Berg, The dendritic box: Shape-selective liberation of encapsulated guests, J. Am. Chem. Soc. 117 (1995) 4417-4418.

[19] M. W. P. L. Baars, R. Kleppinger, M. H. J. Koch, S. L.Yeu, E. W. Meijer, *Angew. Chem. Int. Ed.* **2000**, *39*, 1285-1288.

[20] M. Liu, K. Kono, J. M. J. Fréchet, *J. Control. Release* **2000**, *65*, 121-131.

[21] H. Stephan, G. Geipel, G. Bernhard, D. Appelhans, D. Tabuani, H. Komber, B. Voit, *Tetrahedron Lett.* **2005**, *46*, 3209-3212.

[22] N.A. Stasko, C.B. Johnson, M.H. Schoenfisch, T.A. Johnson, E.L. Holmuhamedov, *Biomacromolecules* **2007**, *8*, 3853-3859.

[23] R. K. Kainthan, D. E.Brooks, *Bioconjugate Chem.* **2008**, *19*, 2231-2238.

[24] V. Gajbhiye, P.V. Kumar, R. K. Tekade, N. K. Jain, *Eur. J. Med. Chem.* **2009**, *44*, 1155-1166.

[25] T. Dutta, N. K. Jain, *Biochim. Biophys. Acta* **2007**, *1770*, 681-686

[26] P. Agrawal, U. Gupta, N. K. Jain, *Biomaterials* **2007**, *28*, 3349-3359.

[27] D. Bhadra, A. K. Yadav, S. Bhadra, N. K. Jain, *Int. J. Pharm.* **2005**, *295*, 221-233.

[28] X.-H. Dai, H.-D. Zhang, C.-M. Dong, *Polymer* **2009**, *50*, 4626-4634.

[29] B. Klajnert, D. Appelhans, H. Komber, N. Morgner, S. Schwarz, S. Richter, B. Brutschy, M. Ionov, A. K. Tonkikh, M. Bryszewska, B. Voit, *Chem. Eur. J.* **2008**, *14*, 7030-7041.

[30] M. Fischer, D. Appelhans, S. Schwarz, B. Klajnert, M. Bryszewska, B. Voit, M. Rogers, *Biomacromolecules* **2010**, *11*, accepted.

[31] T. Pietsch, D. Appelhans, N. Gindy, B. Voit, A. Fahmi, *Colloids Surf., A* **2009**, *341*, 93-102.

[32] M. Mkandawire, A. Pohl, T. Gubarevich, V. Lapina, D. Appelhans, G. Rödel, W. Pompe, J. Schreiber, J. Opitz, *J. Biophoton.* **2009**, *2*, 596-606.

[33] J. T. Rhule, C. L. Hill, D. A. Judd, R. F. Schinazi, *Chem. Rev.* **1998**, *98*, 327-357.

[34] C. E. Müller, J. Iqbal, Y. Baqi, H. Zimmermann, A. Röllich, H. Stephan, *Bioorg. Med. Chem. Lett.* **2006**, *16*, 5943-5947.

[35] E. Coppi, A. M. Pugliese, H. Stephan, C. E. Müller, F. Pedata, *Purinergic Signalling* **2007**, *3*, 203-219.

[36] F. M. Sansom, P. Riedmaier, H. J. Newton, M. A. Dunstone, C. E. Müller, H. Stephan, E. Byres, T. Beddoe, J. Rossjohn, P. J. Cowan, A. J. F. d'Apice, S. C. Robson, E. L. Hartland, *J. Biol. Chem.* **2008**, *283*, 12909-12918.

[37] C. E. Müller, H. Stephan, V. E. Fedorov, work in progress.

[38] H. D. Zeng, G. R. Newkome, C. L. Hill, *Angew. Chem. Int. Ed.* **2000**, *39*, 1771-1774.

[39] J. R. Morgan, M. J. Cloninger, *J. Polym. Sci., Part A: Polym. Chem.* **2005**, *43*, 3059-3066.

[40] L. Plault, A. Hauseler, S. Nlate, D. Astruc, J. Ruiz, S. Gatard, R. Neumann, *Angew. Chem. Int. Ed.* **2004**, *43*, 2924-2928.

[41] M. V. Vasylyev, S. Gatard, I. Bar-Nahum, L. Konstantinovski, E.J. Wachtel, R. Neumann, *J. Cluster Sci.* **2006**, *17*, 235-243.

[42] S. Nlate, L. Plault, D. Astruc, *New J. Chem.* **2007**, *31*, 1264-1274.

[43] D. Volkmer, B. Bredenkotter, J. Tellenbroker, P. Kogerler, D.G. Kurth, P. Lehmann, H. Schnablegger, D. Schwahn, M. Piepenbrink, B. Krebs, *J. Am. Chem. Soc.* **2002**, *124*, 10489-10496.

[44] S. Nlate, D. Astruc, D. Neumann, *Adv. Synth. Catal.* **2004**, *346*, 1445-1448.

[45] S. Nlate, L. Plault, D. Astruc, *Chem. Eur. J.* **2006**, *12*, 903-914.

[46] C. Jahier, L. Plault, S. Nlate, *Isr. J. Chem.* **2009**, *49*, 109-118.

[47] S. Lin, X. F. Zhang, M. H. Luo, *J. Solid State Electrochem.* **2009**, *13*, 1585-1589.

[48] K. A. Brylev, Y. V. Mironov, S. S. Yarovoi, N. G. Naumov, V. E. Federov, S.-J. Kim, N. Kitamura, Y. Kuwahara, K. Yamada, S. Ishizaka, Y. Sasaki, *Inorg. Chem.* **2007**, *46*, 7414-7422.

[49] T. G. Gray, C. M. Rudzinski, E. E. Meyer, R. H. Holm, D. G. Nocera, *J. Am. Chem. Soc.* **2003**, *125*, 4755-4770.

[50] W. D. Horrocks, D. R. Sudnick, *J. Am. Chem. Soc.* **1979**, *101*, 334-340.

[51] J. L. Kropp, M. W. Windsor, *J. Chem. Phys.* **1965**, *42*, 1599-1608.

[52] D. Shacharbin, B. Klajnert, V. Mazhul, M. Bryszewska, *J. Fluoresc.* **2005**, *15*, 21-28.

[53] S. Stevelmans, J. C. M. van Hest, J. F. G. A. Jansen, D. A. F. J. van Boxtel, E. M. M. de Brabander-van den Berg, E. W. Meijer, *J. Am. Chem. Soc.* **1996**, *118*, 7398-7399.

[54] P. Miklis, T. Cagin, W. A. Goddard III, *J. Am. Chem. Soc.* **1997**, *119*, 7458-7462.

[55] R. Brodbeck, T. Tonsing, D. Andrae, D. Volkmer, *J. Phys. Chem. B* **2008**, *112*, 5153-5162.

[56] S. S. Yarovoi, Y. V. Mironov, D. Y. Naumov, Y. V. Gatilov, S. G. Kozlova, S.-J. Kim, V. E. Federov, *Eur. J. Inorg. Chem.* **2005**, 3945-3949.

[57] N. Morgner, H.-D. Barth, B. Brutschy, *Aust. J. Chem.* **2006**, *59*, 109-114.

[58] N. Morgner, T. Kleinschroth, H.-D. Barth, B. Ludwig, B. Brutschy, *J. Am. Soc. Mass Spectrom.* **2007**, *18*, 1429-1438.

[59] J. Hoffmann, Th. L. Schmidt, A. Heckel, B. Brutschy, *Rapid Comm. Mass Spectrom.* **2009**, *14*, 2176-2180.

[60] J. Hoffmann, L. Aslimovska, C. Bamann, C. Glaubitz, E. Bamberg, B. Brutschy, *Phys. Chem. Chem. Phys.* **2010**, *12*, 3480-3485.

Received: ((will be filled in by the editorial staff))
Revised: ((will be filled in by the editorial staff))
Published online: ((will be filled in by the editorial staff))

Entry for the Table of Contents

Layout 1:

Catch Phrase

M. Kuhlmann, H. Stephan, H.-J. Pietzsch, G. Geipel, D. Appelhans, B. Voit, J. Hoffmann, B. Brutschy, Y. V. Mironov, K. A. Brylev, V. E. Fedorov* ……..…… Page – Page

Sugar-decorated dendritic nanocarriers: Encapsulation and release of the octahedral rhenium cluster complex $[Re_6S_8(OH)_6]^{4-}$

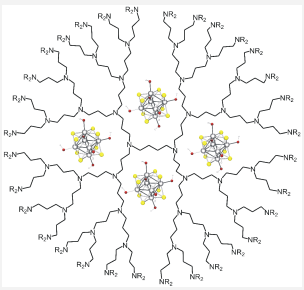

Dendrimer-encapsulated rhenium cluster complexes.
The encapsulation and release of nanometer sized anionic rhenium cluster complexes in biocompatible maltose-decorated dendrimers have been studied in detail applying different physico-chemical methods.

RAPID COMMUNICATIONS IN MASS SPECTROMETRY
Rapid Commun. Mass Spectrom. 2009; **23**: 2176–2180
Published online in Wiley InterScience (www.interscience.wiley.com) DOI: 10.1002/rcm.4129

RCM

Probing the limits of liquid droplet laser desorption mass spectrometry in the analysis of oligonucleotides and nucleic acids

Jan Hoffmann[1], Thorsten. L. Schmidt[2], Alexander Heckel[2] and Bernd Brutschy[1]*

[1]Institute for Physical and Theoretical Chemistry, Goethe University Frankfurt, Max-von-Laue-Str. 7, 60438 Frankfurt/M, Germany
[2]Cluster of Excellence Macromolecular Complexes, Goethe University Frankfurt, Max-von-Laue-Str. 9, 60438 Frankfurt/M Germany

Received 1 April 2009; Revised 14 May 2009; Accepted 19 May 2009

In the present work we demonstrate the advantages of LILBID mass spectrometry (laser-induced liquid bead ion desorption) in the analysis of nucleic acids and large oligonucleotides. For established methods like matrix-assisted laser desorption/ionization (MALDI) and electrospray ionization (ESI), the mass analysis of oligonucleotides or of noncovalent oligonucleotide-protein complexes, in particular of very large ones, still represents a considerable challenge either due to the lack of native solutions or nonspecific adduct formation or due to a reduced salt tolerance or a high charge state of the ions. With LILBID, oligonucleotides, solvated in micro-droplets of aqueous buffer at certain pH and ion strength, are brought into the gas phase by laser ablation. We show that our method is able to detect single- and double-stranded oligonucleotides with high softness, demonstrated by the buffer dependence of the melting of a duplex. The absolute sensitivity is in the attomole range concomitant with a total analyte consumption in the femtomole region. The upper mass limit of oligonucleotides still detected with good signal-to-noise ratio with LILBID is the 1.66 MDa plasmid pUC19. With DNA ladders from short duplexes with sticky ends, we show that LILBID correctly reflects the relative thermodynamic stabilities of the ladders. Moreover, as an example for a specific DNA–protein complex we show that a NF-κB p50 homodimer binds sequence specifically to its match DNA. In summary we demonstrate that LILBID, although presently performed only with low mass resolution, due to these advantages, is an alternative mass spectrometric method for the analysis of oligonucleotides in general and of specific noncovalent nucleic acid–protein complexes in particular. Copyright © 2009 John Wiley & Sons, Ltd.

Nucleic acids have long represented a considerable challenge for analysis by mass spectrometric methods owing to their polarity and thermal lability.[1] This situation has changed dramatically with the advent of both electrospray ionization mass spectrometry (ESI-MS) and matrix-assisted laser desorption/ionization mass spectrometry (MALDI-MS). In ESI ions of nucleic acids are produced from solutions by a complex charge-assisted desolvation process – in MALDI. analytes, embedded in special matrices, are desorbed by UV lasers.[2] Despite the great success of these methods they also have certain drawbacks or encounter problems with special analytes. In ESI the ionization yield is very sensitive to salt contaminations, and the ions are mainly formed in high and often broad charge states, which may make the mass assignment of large ions difficult or even impossible. MALDI suffers from the loss of sensitivity for detecting large oligomers and often has problems to detect specific intermolecular complexes.[2] Therefore, new MS methods, avoiding these problems, are of interest.

**Correspondence to*: B. Brutschy, Institute for Physical and Theoretical Chemistry, Goethe University Frankfurt, Max-von-Laue-Str. 7, 60438 Frankfurt/M, Germany.
E-mail: brutschy@chemie.uni-frankfurt.de
Contract/grant sponsor: DFG; contract/grant number: SFB 579, SFB 624 and EXC 115.

EXPERIMENTAL

Chemicals

All oligonucleotides for the study were purchased with HPLC purification from Metabion.[3] pUC19 was purchased from NEB (Catalog# N3041L) and ethanol precipitated from NH_4OAc. NF-κB (p50) was purchased from Promega (Catalog# E3770, human, recombinant, storage buffer: 50 mM NaCl, 5 mM DTT, 0.5 mM PMSF, 20 mM HEPES pH 7.9, 10 μM $Zn(OAc)_2$, 0.1% NP40, 10% glycerol). The binding capability to the match binding site was confirmed using fluorescence-correlation spectroscopy (FCS). For the competition experiment (Fig. 5(b)) the stock of p50 was diluted with water and the oligonucleotides (dissolved in water) were added to yield the final concentrations given in the legend of Fig. 5.

Sequence of the oligonucleotide O from which the spectra in Fig. 2 were obtained
5′-TTCCGCAGTCCGTGTAATCGATCTGTAATCGACAT-CAGTTGGAGCTCTGACGACAGTCAG-3′
Sequences of the oligonucleotides used for Fig. 3(a)
5′-GATTACAGATCGATTACACGGACTGCGGAACTGAC-TGTCGTCAGAGCTCCAACTGATGTC-3′

Table 1. Masses of all oligonucleotides used sorted according to their occurrence

	Masses of the single strands [Da]	Masses of the corresponding double strand [Da]
Fig. 2	18466.0	
Fig. 3(a)	18466.0	36950
	18484.0	
Fig. 3(b)	18484.0	36950
	18466.0	
Fig. 4	4949.4	9754.6
	4805.2	
Fig. 6(b), match	5115.6 (5′-Cy5)	9676.6
	4561.0	
Fig. 6(b), control	14766.6	29533.2
	14766.6	

5′-TTCCGCAGTCCGTGTAATCGATCTGTAATCGACAT-CAGTTGGAGCTCTGACGACAGTCAG-3′

Sequences of the oligonucleotides used for Fig. 3(b)

5′-GATTACAGATCGATTACACGGACTGCGGAACTGAC-TGTCGTCAGAGCTCCAACTGATGTC-3′

5′-CGTGTAATCGATCTGTAATCGACATCAGTTGGAGC-TCTGACGACAGTCAGTTCCGCAGTC-3′

Sequences of the oligonucleotides used for Fig. 4

5′-AAAAAAAAAAAAAAAA-3′

5′-TTTTTTTTTTTTTTT-3′

Sequence of the constituting oligonucleotides of the DNA M containing the match binding site (shown in bold)

5′-Cy5-ATG**GGGACTTTCC**TA-3′

5′- TA**GGAAAGTCCC**CAT-3′

Sequence of the constituting oligonucleotides of the DNA C

5′-GATTACATCAGTTGGAGCTCTCTAGACAGTCAGTT-GGCCAGTCAATAC-3′

5′-GTATTGACTGGCCAACTGACTGTCTAGAGAGCTCC-AACTGATGTAATC-3′

Mass spectrometry

We recently introduced a new mass spectrometry method which uses liquid micro-droplets (diameter 50 μm) as carrier for the analyte and a pulsed IR laser for ion desorption/ablation.[4] The principle of this method termed LILBID (laser-induced liquid bead ion desorption) is schematically depicted in Fig. 1. Droplets from a commercial droplet generator are transferred into vacuum, where they are irradiated one by one by focused mid-IR laser pulses. The droplets explode at power densities of several MW/cm^2. Due to an incomplete charge neutralization in the desolvation process of the explosion preformed solvated ions are ejected into vacuum. There they may be analyzed by mass spectrometry. The advantages of LILBID are first that the analyte is studied in a more or less native environment (buffer, pH, detergents etc.) and second that only a few microliters of a micromolar solution are enough for an analysis. The ions in general appear only in low charge states ($n < 12$). Its present main problem is a modest mass resolution mainly caused by noncompensated initial energies of the ions and by an incomplete desolvation. The mass analysis is presently performed by a home-built time-of-flight setup (TOFMS) with a high mass detector, extending the upper mass limit to $m/z \sim 10^6$. At low laser intensity LILBID works in ultrasoft mode which allows the sampling of weakly bound noncovalent complexes such as large solubilized membrane molecules. At higher laser power these complexes can be dissociated into their covalent subunits.[5,6]

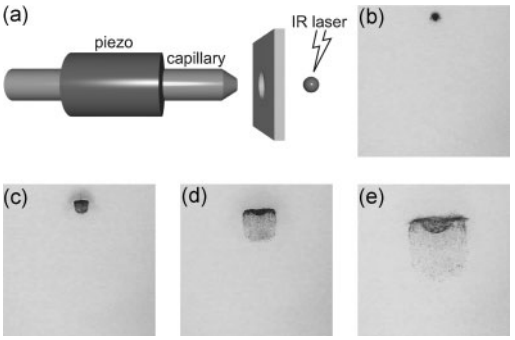

Figure 1. (a) In a LILBID source pulsed droplets (diameter: ca. 50 μm, volume: ca. 65 pL) are generated and irradiated in vacuum with an IR laser (3 μm) one by one. (b–e) Series of photographs (Δt ~1 μs) showing the explosion of a droplet after laser irradiation.

Here we investigate in a few benchmark measurements the advantages and eventual drawbacks of LILBID-MS in the analysis of small and very large oligonucleotides and oligonucleotide–protein complexes.

RESULTS AND DISCUSSION

As the first step we addressed the issue of detection sensitivity of LILBID-MS for single-stranded DNA. For this reason we analyzed a 60-mer oligonucleotide O (the masses of this oligonucleotide and the following ones discussed are listed in Table 1) as purchased without further treatment in a 9 nM aqueous solution with 3 mM NH_4OAc buffer. Figure 2 shows the mass spectra obtained in the anion mode. For the spectrum in Fig. 2(a) the signals of 200 droplets were averaged which corresponds to a total of 117 amol of sample. The spectrum only shows singly and doubly charged species of the single strand. In the cation mode the signals were negligible. Thus, the polarity of the oligonucleotides in solution is conserved in LILBID-MS but in general the number of charges is strongly reduced. The observed charge states are in general much lower than in ESI-MS but larger than in MALDI-MS.[2] Testing the limits of sensitivity, surprisingly only three droplets are still sufficient to obtain a signal with reasonable signal-to-noise ratio (Fig. 2(b)). They correspond to 1.8 amol of sample or to approximately one million molecules. For this experiment we required typically a total volume of solution of 2 μL (18 fmol).

We further examined if double-stranded DNA can be detected unfragmented with LILBID-MS. Therefore, we used a mixture of two complementary oligonucleotides (60 bp)

DOI: 10.1002/rcm

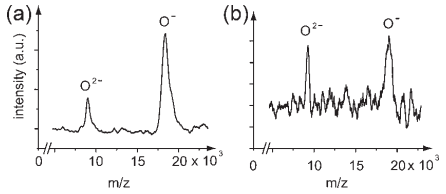

Figure 2. A typical LILBID anion spectrum of an oligonucleotide (60-mer, 18.5 kDa) obtained from (a) 117 amol or (b) 1.8 amol sample (9 nM in aqueous NH_4OAc, 3 mM, pH 7.4, 1 mM $MgCl_2$).

forming duplexes with sticky ends of different length (see cartoon representation in Fig. 3). These were able to self-assemble thereby forming long DNA ladders: As illustrated in Fig. 3 in one set the complementary regions were of the same size (30 bp/30 bp) while in the other one complementary region was longer than the other (40 bp/20 bp). Upon self-assembly the two sets result in DNA ladders of different thermodynamic stabilities determined by the shortest binding region. For the sample preparation the oligonucleotides were again used as purchased and only dissolved in aqueous buffer. Figure 3 depicts the obtained LILBID anion spectra. The intensities of the respective peaks corresponding to ladders of various length decrease for the symmetric strands exponentially with their length whereas those of the

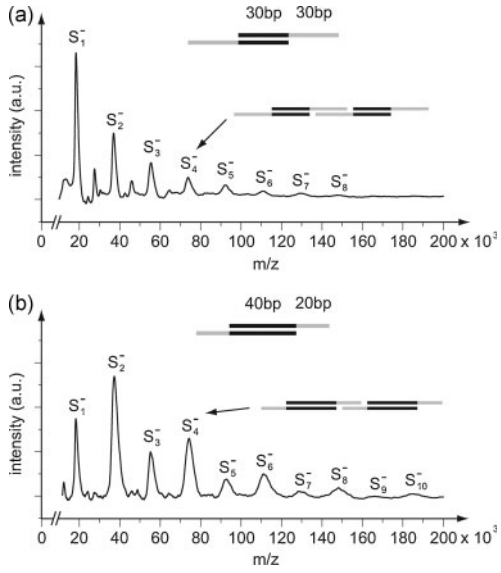

Figure 3. LILBID anion spectra of a mixture of two complementary oligonucleotides with different lengths of the designed sticky ends (see cartoon representation): (a) 30 bp/30 bp and (b) 40 bp/20 bp. The stability of a duplex chain is determined by the shortest base-pairing length. Both spectra were recorded under the same conditions (12.5 μM sample, aqueous solution, NH_4OAc buffer, 3 mM, pH 7.4, 1 mM $MgCl_2$). Subscripts according to the number of single strands.

asymmetric strands show an alternating intensity pattern, with the series of even-numbered ladders being more intense than odd-numbered ones. For the asymmetric pair the probability to encounter polymer fragments with an even number of duplexes is higher due to the higher binding enthalpy of a 40 bp region as compared to a 20 bp region existing in an uneven-numbered ladder. For the symmetric DNA pair the probability for odd and even multiples of duplexes can be expected to be the same. The corresponding predicted melting temperatures for the 20 bp, 30 bp and the 40 bp regions are 60°C, 73°C and 79°C, respectively.[7] Figure 3 shows that these thermodynamic considerations are correctly reflected in the LILBID mass spectrum. The longest detected ladder in the present experiments had a mass of around 185 kDa corresponding to 300 base pairs (bp). With MALDI-MS for comparison, the detection of such large oligonucleotides is often a problem and heavily depends on the matrix. In addition, in MALDI, DNA is often detected both as cations and anions.

A large amount of experimental evidence is available for the effects of magnesium ions on the structure and the stability of the DNA double helix. Magnesium ions interact as counter ions with the phosphate groups, thus neutralizing the negative charges on the DNA backbone.[8] This is reflected in the findings of an early investigation, which established that the melting temperature of the DNA increases with increasing Mg^{2+} concentration.[9] This effect of divalent as compared to alkaline ions on the melting temperature of the duplex was studied with LILBID using a double-stranded 16-mer at 4.5 μM concentration in 5 mM NH_4OAc buffer at pH 7.5. The intensity of the single strand relative to the duplex both depend on the temperature of the droplet, i.e. the equilibrium in the condensed phase, and on the energy input by the laser, which may eventually destroy it by fragmentation. The resulting spectra shown in Fig. 4 were except for different salt concentrations recorded under the same conditions including laser intensity. As can be clearly seen, in aqueous buffer the ratio of double to single strands (D/S) is 0.04. For comparison the calculated[10–12] melting temperature is below 11°C. It is considerably below the ambient temperature of the droplet of 23°C. Thus duplexes are nearly quantitatively dissociated already in solution. Adding 10 mM NaCl increases this ratio to 0.23 and is also responsible for the significant peak broadening and mass shift due to salt adducts. In this case the calculated melting point is 19.2°C. Thus at ambient temperature a certain percentage of duplexes should survive. Exchanging the 10 mM Na^+ ions for only 1 mM Mg^{2+} ions increases the stability of the double strands further as expected.[13] Now the ratio S/D is 1. The calculated melting temperature is 45.6°C. Since the S/D ratio at the melting point is 1 and since this temperature is not that of the droplet before the laser ablation it must be induced by the laser. So the energy input by the laser corresponds to a thermolysis equivalent to a temperature of roughly 45°C. Thus the duplex represents a thermometer to measure via its melting point the laser-induced heating of the ablated species, which of course also depends on the laser intensity. These observations give evidence of the softness of the ion formation process in LILBID. It should be pointed out that with other ionization techniques for oligonucleotides – especially ESI – salts

DOI: 10.1002/rcm

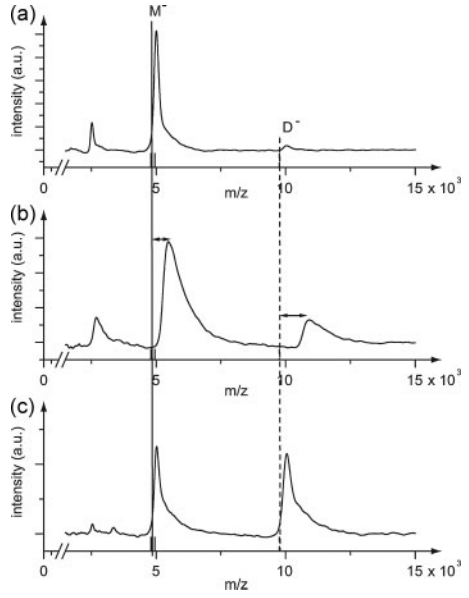

Figure 4. LILBID anion spectra of a 16-mer using NH_4OAc buffer containing (a) no salt, (b) 10 mM NaCl (ionic strength $I_{NaCl} = 10$ mM) or (c) 1 mM $MgCl_2$ (ionic strength $I_{MgCl2} = 3$ mM). Signals of the single strands are denoted with M^-, those of the double strand with D^-. Solid marks: theoretical mass of the two single strands; dashed line: theoretical mass of the dimer.

usually must be rigorously excluded,[14] although recent developments have improved this situation,[15,16] especially in the analysis of proteins.[17] In contrast, LILBID readily tolerates for example a 10 mM concentration of Na^+ in the analysis of oligonucleotides and in fact addition of Mg^{2+} at lower millimolar concentrations increases the stability of duplexes just as shown.

Encouraged by these results we addressed the question whether with LILBID we can even detect a plasmid with a mass in the MDa range. Ionization and detection of oligonucleotides by ESI-MS is widely applied. The multiple charging of the ESI process brings ions into the mass spectral region, where high resolution can readily be obtained. However, each species present produces many different charge states that can significantly complicate the spectra. Since a single large species can give rise to a broad distribution of peaks, eventually complicated by fragmentation either in the source or in a tandem mass spectrometer, these spectra may be difficult to interpret.[2] Thus the detection of plasmids was reported in earlier studies,[18] but no confirmation was possible due to the inability of resolving distinct charge states as needed for molecular weight determination. Cheng *et al*. reported the ionization and molecular weight determination of a 1.95 ± 0.07 MDa plasmid DNA by ESI with Fourier transform ion cyclotron resonance (FTICR).[19] The problem of many overlapping charge states was solved by employing charge reduction techniques using gas-phase reactions with acetic acid on individual highly charged ions of plasmid DNA trapped in an FTICR cell. The same group

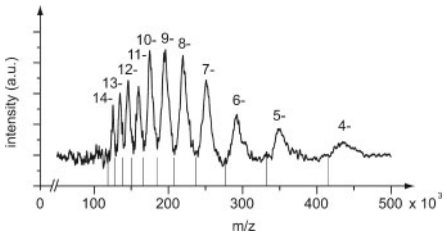

Figure 5. LILBID anion spectrum of the plasmid pUC19 (2686 bp, 1.66 MDa, 80 nM in aqueous NH_4OAc buffer (2.5 mM, pH 7.4)) plus 1.5 mM $MgCl_2$, averaged over 200 droplets. The charge states are indicated and a charge state ruler corresponding to the expected mass of 1.66 MDa is shown.

also detected DNA with a molecular weight of even 91 ± 9 MDa.[20] Thus mass determination was possible due to the feature of ESI to generate highly charged species. On the other hand this does not allow the accurate determination of the charge state and mass without applying laborious methods together with an FTICR mass spectrometer.

Here the challenge was to see if LILBID – due to its lower charge states – is able to detect and identify also plasmids out of solution without additional treatment of the ions. For our investigation we chose the plasmid pUC19 with 2686 bp and a calculated mass of 1.66 MDa (calculated with H^+ as counter ions). To obtain the spectrum shown in Fig. 5 we used pUC19 in aqueous buffer. In the anion LILBID spectrum one clearly sees a distribution of ions with different m/z starting with 4 charges and going up to 14 charges all corresponding to the same mass of 1.66 ± 0.01 MDa. The peaks are relatively broad which is not surprising since water, buffer and divalent ions are supposed to increase the mass of the plasmid ions observed in the gas phase. However, the left edge of each peak corresponds to the theoretical parent mass. Several facts are important: firstly all concentrations in the nanomolar range still afford good spectra, secondly no fragmentation of the plasmid was observed in any of the spectra and, most importantly, the mass spectrum was readily obtained without having to resort to elaborate sample preparation or ion population trimming techniques. This is in contrast to all other reports on the mass spectrometry of large complexes in which other ionization techniques were used.[2] Again no rigorous exclusion of salts is necessary. Thus LILBID allows the easy detection of plasmids even with an amount of about 100 fmol; however, admittedly, the mass resolution is presently still quite modest.

Finally, a crucial test of the softness and specificity of a mass spectrometric method is its ability to detect specific complexes from solution also in the gas phase. Thus, apart from isolated oligonucleotides and nucleic acids alone, a subject of intensive current research in mass spectrometry is the investigation of selective protein–nucleic acid complexes – which according to Robinson is ''still in its infancy''.[21] To start probing the scope of LILBID in this area we chose the p50 subunit of the transcription factor NF-κB which can bind as a homodimer to dsDNA containing the binding site.[22] For these studies we purchased p50 and the constituting

DOI: 10.1002/rcm

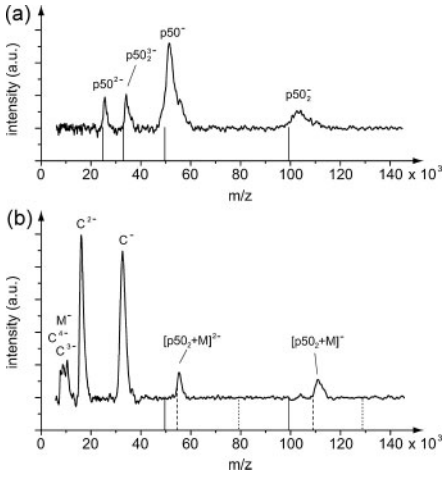

Figure 6. LILBID anion spectra of (a) the p50 subunit of NF-κB and (b) p50 in the presence of double-stranded match DNA M and mismatch DNA C. The charge state rulers correspond to p50 (solid), or the complex of p50 and M (dashed) or C (dotted) (concentrations: p50 460 nM, M 1 μM, C 1 μM).

oligonucleotides for a double-stranded match DNA M (15 bp, 9.9 kDa) and a control DNA C (48 bp, 29.9 kDa) which was about three times longer and did not contain the binding site. All binding partners were again used without further treatment. Figure 6(a) shows the LILBID anion spectrum of p50 alone and Fig. 6(b) shows the spectrum of a competitive experiment in which p50 and the two dsDNAs M and C were present in the same sample solution. Figure 6(b) clearly shows the signals of the complex of the p50 homodimer with the match DNA M whereas no signal at all can be detected of a complex containing the longer mismatch DNA C. This nicely demonstrates that LILBID can even be used to study selective protein nucleic acid interactions of modest strength and that nonspecific adduct formation at these concentrations may be neglected.

CONCLUSIONS

We have shown that in the context of the mass analysis of oligonucleotides the sensitivity and softness of LILBID together with the reduced native charge state of the ions and the specificity of the observed noncovalent oligonucleotide-protein complexes is remarkable. Admittedly, the mass resolution is not yet state of the art. This is attributed to the initial energy of the desorbed ions together with an incomplete desolvation of the ions. We presently adapt LILBID to a QTOF in which the initial energy of the ions is reduced by collisional cooling probably resulting in a greatly improved mass resolution.

Most notably with LILBID very sensitive analyses can be performed with solutions that are as native as possible, with salts being tolerated to a considerable extent.

Acknowledgements

AH and BB are very grateful for the financial support by the DFG (SFB 579, SFB 624 and EXC 115). We are grateful to Dr. C. K. Nandi for FCS measurements and Dr. H.-D. Barth for his technical assistance

REFERENCES

1. Cole RB. *Electrospray Ionization Mass Spectrometry. Fundamentals, Instrumentations and Applications*. John Wiley: New York, 1997.
2. Kaltashov IA, Eyles SJ. *Mass Spectrometry in Biophysics. Conformation and Dynamics of Biomolecules*. Wiley Interscience: Hoboken, 2005.
3. www.metabion.de.
4. Morgner N, Barth HD, Brutschy B. *Austr. J. Chem*. 2006; **59**: 109.
5. Morgner N, Kleinschroth T, Barth HD, Ludwig B, Brutschy B. *J. Am. Soc. Mass Spectrom*. 2007; **18**: 1429.
6. Morgner N, Zickermann V, Kerscher S, Wittig I, Abdrakhmanova A, Barth HD, Brutschy B, Brandt U. *BBA-Bioenergetics* 2008; **1777**: 1384.
7. Markham NR, Zuker M. *Nucleic Acids Res*. 2005; **33**: W577–W581.
8. Manning GS. *Q. Rev. Biophys*. 1978; **11**: 179.
9. Every AE, Russu IM. *J. Phys. Chem. B* 2008; **112**: 7689.
10. Allawi HT, Peyret N, Seneviratne PA, SantaLucia J. *Abstr. Papers Am. Chem. Soc*. 1997; **213**: 270.
11. Owczarzy R, You Y, Moreira BG, Manthey JA, Huang LY, Behlke MA, Walder JA. *Biochemistry*. 2004; **43**: 3537.
12. Owczarzy R, Moreira BG, You Y, Behlke MA, Walder JA. *Biochemistry* 2008; **47**: 5336.
13. Luan B, Aksimentiev A. *J. Am. Chem. Soc*. 2008; **130**: 15754.
14. Beck JL, Colgrave ML, Ralph SF, Sheil MM. *Mass Spectrom. Rev*. 2001; **20**: 61.
15. Gupta R, Kapur A, Beck JL, Sheil MM. *Rapid Commun. Mass Spectrom*. 2001; **15**: 2472.
16. Sudhir PR, Wu HF, Zhou ZC. *Rapid Commun. Mass Spectrom*. 2005; **19**: 1517.
17. Chang DY, Lee CC, Shiea J. *Anal. Chem*. 2002; **74**: 2465.
18. Nohmi T, Fenn JB. *J. Am. Chem. Soc*. 1992; **114**: 3241.
19. Cheng XH, Camp DG, Wu QY, Bakhtiar R, Springer DL, Morris BJ, Bruce JE, Anderson GA, Edmonds CG, Smith RD. *Nucleic Acids Res*. 1996; **24**: 2183.
20. Chen RD, Cheng XH, Mitchell DW, Hofstadler SA, Wu QY, Rockwood AL, Sherman MG, Smith RD. *Anal. Chem*. 1995; **67**: 1159.
21. McCammon MG, Robinson CV. *Curr. Opin. Chem. Biol*. 2004; **8**: 60.
22. Kunsch C, Ruben SM, Rosen CA. *Mol. Cell. Biol*. 1992; **12**: 4412.

Rapid Reports

Multiple Targets for Suppression of RNA Interference by Tomato Aspermy Virus Protein 2B[†]

Umar Jan Rashid,[‡] Jan Hoffmann,[§] Bernhard Brutschy,[§] Jacob Piehler,[||] and Julian C.-H. Chen*[,‡]

Institute of Biophysical Chemistry, Institute of Physical and Theoretical Chemistry, and Institute of Biochemistry, Goethe University Frankfurt, Max-von-Laue-Strasse 9, 60438 Frankfurt, Germany

Received July 9, 2008; Revised Manuscript Received September 30, 2008

ABSTRACT: Viral suppressors of RNA interference (RNAi) appear to have evolved as a response to this innate genomic defense. We report the nucleic acid binding properties of the *Cucumovirus* RNAi suppressor tomato aspermy virus protein 2B (TAV 2B). Using total internal reflection fluorescence spectroscopy (TIRFS), we show that TAV 2B binds double-stranded RNA corresponding to siRNAs and miRNAs, as well as single-stranded RNA oligonucleotides. A number of positively charged residues between amino acids 20 and 30 are critical for RNA binding. Binding to RNA oligomerizes and induces a conformational change in TAV 2B, causing it to form a primarily helical structure and a 4:2 protein−RNA complex.

RNA interference (RNAi), an ancient mechanism for gene silencing triggered by recognition of dsRNA, is thought to have emerged as a way of safeguarding the genome against mobile genetic elements and the infection of viruses, and thus is a way of maintaining genomic integrity (*1*−*5*). Therefore, it is not surprising that viruses have evolved different strategies for suppressing the host RNAi response in the form of viral suppressor protein. These viral suppressors are widespread, having been identified in a number of different viral families. Not surprisingly, they generally share little sequence homology with one another, although they appear to exist as oligomers built upon an ∼100−200-amino acid protomer.

Tomato aspermy virus, a member of the Cucumoviruses, encodes protein 2B (TAV 2B, 95 amino acids, ∼11.3 kDa) that acts as an RNAi suppressor. Intriguingly, a similar genomic arrangement is seen in RNAi suppressors in the Nodaviruses, a family of viruses that can infect both plants and animals, such as Flock house virus b2 (FHV b2). The 2B and b2 proteins are both derived from a frame-shifted open reading frame (ORF) within the RNA polymerase gene (*6*). In spite of this genomic similarity, the 2B and b2 proteins share little sequence identity, and it is not well understood how the *Cucumovirus* 2B proteins suppress RNAi. To address this question, we report the characterization and oligonucleotide binding properties of TAV 2B and discuss possible modes of suppression of RNAi by this protein.

Full-length TAV 2B expressed poorly and was marginally soluble. On the basis of a sequence alignment with other 2B suppressors of the Cucumoviruses, and previous domain swapping experiments, a truncated construct consisting of amino acids 1−71 (TAV71) was expressed and purified (*7, 8*). Affinity-purified TAV71 migrates as a monomeric species on a Superdex 200 gel filtration column, at a physiological salt (150 mM) concentration (data not shown).

The high percentage of basic residues in the primary sequence suggested that it may bind nucleic acids. To investigate the potential oligonucleotide binding properties of TAV71, total internal reflection fluorescence spectroscopy (TIRFS) was used to probe the binding of fluorescently labeled oligonucleotide substrates to TAV71 in real time. For this purpose, TAV71 is immobilized onto a sensor chip through its His tag (*9, 10*). The fluorescently labeled oligonucleotide is excited by the evanescent wave emanating from the surface. Thus, a signal is recorded only when the labeled molecule is bound to protein immobilized on the surface (Figure 1 of the Supporting Information).

Suppression of RNAi may occur through a direct interaction with siRNAs. Plants have a distribution of different siRNA lengths; shorter species (21−23 nucleotides) are involved in the RNAi response, while longer siRNAs (25−27 nucleotides) are associated with transcriptional silencing and the spread of silencing. To determine if TAV71 binds siRNAs, and if so, whether there was a length preference for this recognition, fluorescently labeled siRNAs of 21, 25, and 27 nucleotides were probed for binding to TAV71 immobilized on a Ni-NTA chip. At a given protein concentration on the surface, the observed fluorescence amplitude is ∼3-fold higher for the 21-nucleotide siRNA (400 mV) than for 25- and 27-nucleotide siRNAs (110 and 130 mV, respectively). As a control, no appreciable fluorescence signal is observed in the absence of immobilized protein (Figure 2 of the Supporting Information). Thus, TAV71 recognizes siRNAs and preferentially binds 21-nucleotide siRNA compared to 25- and 27-nucleotide siRNAs (Figure 1a). The

[†] This work was funded by DFG SFB 579 and the Hessian Ministry for Science and Culture.

* To whom correspondence should be addressed. Phone: +49 (0) 69 798 29641. Fax: +49 (0) 69 798 29632. E-mail: chen@chemie.uni-frankfurt.de.

[‡] Institute of Biophysical Chemistry.

[§] Institute of Physical and Theoretical Chemistry.

[||] Institute of Biochemistry.

10.1021/bi801281h CCC: $40.75
Published on Web 11/06/2008

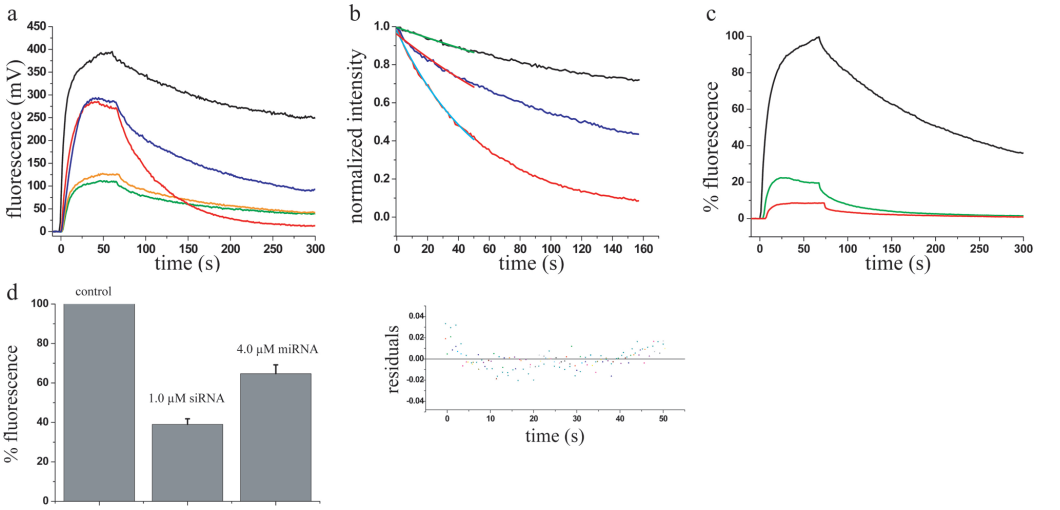

FIGURE 1: Interaction of different RNAs with TAV71 as probed by TIRFS. (a) Sensorgram of kinetics of binding of 21-nucleotide (black), 25-nucleotide (orange), and 27-nucleotide (green) siRNAs and 21-nucleotide (red) and 30-nucleotide (blue) ssRNAs to TAV71, plotted as a function of fluorescence (millivolts) vs time (seconds). (b) Single-exponential fit of the early phase of dissociation, for 21-nucleotide siRNA (black), 30-nucleotide ssRNA (blue), and 21-nucleotide ssRNA (red). (c) Binding of RAKA (green) and KAKA (red) mutants to 21-nucleotide siRNA, normalized to the wild type (black). (d) Competition with unlabeled siRNA, showing the specificity of binding. The maximum fluorescence in the wild type is normalized to 100% in the histogram (left), with 1.0 μM unlabeled siRNA (center) and 4.0 μM unlabeled miRNA (right).

length preference is similar to that of P19, which recognizes 21-nucleotide siRNAs (*11*).

We next tested the ability of TAV71 to bind single-stranded nucleic acids, as these may represent mimics of mRNA. Both 30-nucleotide ssRNA and 21-nucleotide ssRNA are bound by immobilized TAV71, albeit with different kinetic profiles (Figure 1a). A fit of the curves shows markedly faster dissociation in the case of the shorter ssRNA (0.018 s^{-1} for the 21-mer vs 0.0068 s^{-1} for the 30-mer), compared with 0.0029 s^{-1} in the case of the double-stranded 21-mer siRNA (Figure 1b). Thus, TAV71 is able to bind ssRNA, although with a preference for longer species. Notably, TAV71 binds to its ligands only when a certain critical concentration of the protein ($\sim$2−3 ng/mm^2) is present on the chip. Any concentration of the protein below that critical level shows no binding to the oligonucleotides (Figure 3 of the Supporting Information). This implies that oligomerization of TAV71 is required for binding to these oligonucleotides. Due to the relatively high concentration of protein on the chip, interpretation of the kinetics is complicated by the high probability for rebinding of the ligands to the protein at such high surface concentrations. To minimize this possibility, fitting of the dissociation curves was done in the early phase of dissociation, where rebinding of the ligands to the protein is minimized.

The *Cucumovirus* 2B proteins contain a particularly rich stretch of highly conserved, basic residues between amino acids 20 and 30. To further examine the roles of specific residues that may be involved in siRNA binding, two sets of double mutants of TAV71, K21A/K22A (KAKA) and R26A/K27A (RAKA), were assayed for their ability to bind 21-mer siRNA. The level of binding to siRNA was significantly reduced in both mutants, compared to that of wild-type TAV71 under similar conditions on the chip (Figure 1c). In the case of the two double mutants, equilibrium is reached quickly, and the amplitude of fluorescence is reduced, indicative of a weaker binding affinity. These residues are therefore important for the recognition of RNA.

To check the specificity of binding, immobilized TAV71 was injected with unlabeled siRNA mixed with 200 nM labeled siRNA with an identical sequence. At 1.0 μM unlabeled siRNA, the level of binding to labeled siRNA is significantly reduced (Figure 1d). Thus, the interaction of siRNA with TAV71 is specific and unaffected by the presence of the label.

Having established the specificity of the TAV71−siRNA interaction, we next examined whether miRNA can also bind to TAV71. Immobilized TAV71 was injected with 4.0 μM unlabeled miRNA (*Arabidopsis* miR-171b), mixed with 200 nM labeled siRNA. There was a significant decrease in the level of binding of labeled siRNA (Figure 1d). This shows that in addition to siRNAs, miRNAs are also able to bind to TAV71 (Figure 1d).

To investigate the oligomeric properties of TAV71 in the presence of siRNA, 4.0 μM unlabeled 21-mer siRNA was incubated with 40 μM TAV71, and the mixture was applied to an analytical Superdex-200 gel filtration column. Compared to protein alone and siRNA alone, a new peak appears at $\sim$67 kDa, and the magnitude of the siRNA peak is diminished, indicative of siRNA binding and an oligomeric TAV71−siRNA complex (Figure 4 of the Supporting Information).

LILBID mass spectrometry (*12*) was used to determine the molecular mass of the complex. This method is useful for resolving the masses of noncovalent protein and nucleic acid complexes. For the TAV71−siRNA complex, the major peak runs as a molecular mass of 68900 $\pm$ 700 Da, which corresponds to a 4:2 protein−RNA complex [calculated mass

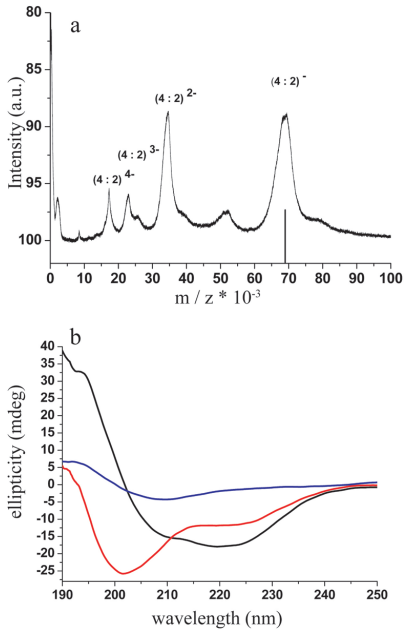

FIGURE 2: Oligomerization and secondary structure of the TAV71−siRNA complex. (a) LILBID mass spectrometry of the TAV71−siRNA complex, showing a mass of 68.9 kDa with up to four net charges corresponding to a 4:2 stoichiometry. (b) CD spectra of TAV71 (6 μM) in the absence (black) and presence of 3 μM siRNA (maroon). The spectrum for siRNA alone (3 μM) is blue.

of 69.6 kDa (Figure 2a)]. This mass is in good agreement with the gel filtration data and the recently published structure (Figures 4 and 5 of the Supporting Information) (*13*). The stoichiometry of the complex was independently determined by analytical gel filtration with UV−vis spectroscopic detection using fluorescently labeled siRNA, showing a 2:1 molar stoichiometry (Figure 6 of the Supporting Information).

Conformational changes in TAV71 that occur upon binding of RNA were probed using circular dichroism (CD). A CD spectrum of TAV71 alone (6 μM) shows a high percentage of random coil structure. Upon incubation at a 2:1 ratio with siRNA, the protein assumes a primarily helical secondary structure, with an approximate secondary structure content of 60% α-helix, 7% β-strand, and 33% random coil (Figure 2b). Upon incubation with 30-mer ssRNA, TAV71 forms a similarly ordered secondary structure (Figure 7 of the Supporting Information). Thus, on the basis of mass spectrometry and CD data, we conclude that binding to RNA orders and oligomerizes TAV71. It is worth noting, however, that the presence of the C-terminal residues may influence this oligomerization behavior.

The data presented here demonstrate that TAV 2B is able to bind a variety of different RNA species, such as siRNAs, miRNAs, and ssRNA. These results suggest that suppression of RNAi by TAV 2B may occur via targeting of different stages of the RNAi pathway. TAV 2B falls under the category of more general RNAi suppressors, with potentially multiple targets for suppression, similar to P21 (*14*). Although only a limited number of suppressors have been biochemically characterized, they can be divided into ones that are specific, such as P19, and more generalized suppressors, as described in this study (*11*).

A comparison of TAV 2B and FHV b2 shows some remarkable similarities. Both proteins have a two-domain structure, with an N-terminal region involved in RNA binding, and are primarily helical in secondary structure content (*6*). Thus, it is notable that these two proteins, in spite of having little sequence similarity, have arrived at similar solutions for suppressing RNAi.

Of particular interest are viral suppressors that also bind miRNAs. We also showed that miRNAs are bound by TAV 2B, a property that has been characterized in the NS3 suppressor from rice hoja blanca virus, as well as CMV 2B. Binding of miRNAs by viral suppressors is potentially detrimental to the host (*15*). The suppression effect of TAV 2B, and perhaps in the case of other suppressors, is likely to be fine-tuned for the balance between viral reproduction and host survival. Further studies of this and other suppressors, in their native context, will be necessary for improving our understanding of these proteins and the complex interplay between virus and host.

ACKNOWLEDGMENT

We thank Volker Dötsch, Ajazul Hamid, Changjiang You, and Maniraj Bhagawati for helpful discussions.

SUPPORTING INFORMATION AVAILABLE

Detailed experimental procedures and Figures 1−7. This material is available free of charge via the Internet at http://pubs.acs.org.

REFERENCES

1. Hock, J., and Meister, G. (2008) *Genome Biol. 9*, 210.
2. Lecellier, C. H., and Voinnet, O. (2004) *Immunol. Rev. 198*, 285–303.
3. Rashid, U. J., Paterok, D., Koglin, A., Gohlke, H., Piehler, J., and Chen, J. C. (2007) *J. Biol. Chem. 282*, 13824–13832.
4. Song, J. J., Smith, S. K., Hannon, G. J., and Joshua-Tor, L. (2004) *Science 305*, 1434–1437.
5. Vastenhouw, N. L., and Plasterk, R. H. (2004) *Trends Genet. 20*, 314–319.
6. Chao, J. A., Lee, J. H., Chapados, B. R., Debler, E. W., Schneemann, A., and Williamson, J. R. (2005) *Nat. Struct. Mol. Biol. 12*, 952–957.
7. Li, H. W., Lucy, A. P., Guo, H. S., Li, W. X., Ji, L. H., Wong, S. M., and Ding, S. W. (1999) *EMBO J. 18*, 2683–2691.
8. Palukaitis, P., and Garcia-Arenal, F. (2003) *Adv. Virus Res. 62*, 241–323.
9. Gavutis, M., Lata, S., Lamken, P., Muller, P., and Piehler, J. (2005) *Biophys. J. 88*, 4289–4302.
10. Lata, S., and Piehler, J. (2005) *Anal. Chem. 77*, 1096–1105.
11. Ye, K., Malinina, L., and Patel, D. J. (2003) *Nature 426*, 874–878.
12. Morgner, N.; Barth, H. D.; Brutschy, B.; Scheffer, U.; Breitung, S.; Gobel, M. 2008, *J. Am. Soc. Mass Spectrom.* [Online early access]. DOI: 10.1016/j.jasms.2008.7.001
13. Chen, H. Y., Yang, J., Lin, C., and Yuan, Y. A. (2008) *EMBO Rep. 9*, 754–760.
14. Ye, K., and Patel, D. J. (2005) *Structure 13*, 1375–1384.
15. Hemmes, H., Lakatos, L., Goldbach, R., Burgyan, J., and Prins, M. (2007) *RNA 13*, 1079–1089.

BI801281H

Studying the stoichiometries of membrane proteins by mass spectrometry: microbial rhodopsins and a potassium ion channel

Jan Hoffmann,[a] Lubica Aslimovska,[b] Christian Bamann,[c] Clemens Glaubitz,[b] Ernst Bamberg[c] and Bernd Brutschy*[a]

Received 23rd November 2009, Accepted 1st February 2010
First published as an Advance Article on the web 24th February 2010
DOI: 10.1039/b924630d

In the present work we demonstrate the advantages of LILBID mass spectrometry in the mass analysis of membrane proteins with emphasis on ion-pumps and channels. Due to their hydrophobic nature, membrane proteins have to be solubilized by detergents. However, these molecules tend to complicate the analysis by mass spectrometry. In LILBID, detergent molecules are readily tolerated which allows for the study of solution phase quaternary structures of membrane proteins. This is shown for the proton-pump bacteriorhodospin and the potassium channel KcsA where in both cases the stoichiometries found by LILBID reflect the known structures from 2D or 3D crystals. With proteorhodopsin we demonstrate a preliminary detergent screening showing different structures in different detergents and the implications for the functionality of this protein. We show that Triton-X 100 prevents the formation of the pentamer of proteorhodopsin. Furthermore, the quaternary structures of proteorhodopsin cloned without the signal peptide and of the cation channel channelrhodopsin-2 were studied. The intrinsic properties of channelrhodopsin-2 allow for mass spectrometric analysis in very high salt concentrations up to 100 mM of NaCl. In summary we demonstrate that LILBID is an alternative mass spectrometric method for the analysis of membrane proteins from solution phase.

1. Introduction

Mass spectrometry (MS) has revolutionized the analysis of proteins. MS-Methods like matrix assisted laser desorption ionization (MALDI)[1] and electrospray ionization (ESI)[2] are widely used both to determine a protein's primary structure, its post translational modifications and possibly its quaternary structure. Recent achievements[3] include the detection of large complexes of both solvable[4] and membrane proteins.[5] However these methods often require elaborate sample protocols in which the ions no longer exist under ''native'' conditions. Our group has developed an alternative approach termed laser induced liquid bead ion desorption (LILBID).[6] There, the analyte is laser-desorbed from droplets of solution containing the analyte in a more or less native environment. Thus, the method is tolerant to the use of various buffers, salts and detergents. These conditions are in general crucial to mimic a more or less native complexation behavior. LILBID MS is a top-down method allowing study of both the intact non-covalent complexes and their subunit compositions.[7] The analysis of membrane proteins is a real challenge for mass spectrometry due to their hydrophobicity. Solubilization in an adequate detergent is quite common to make them suitable for analysis and often evidence was given for the structural and functional integrity of the complexes under this treatment.[28] In this article we investigate the influence of different buffer conditions on the stoichiometry of membrane proteins of moderate size. We focused the investigation on two light-driven proton pumps, a light-gated ion channel and a K^+ channel.

First we studied two exemplary light-driven proton pumps, bacteriorhodopsin[8] (bR), photoactive in haloarchea, and proteorhodopsin[9] (PR) found in marine bacterioplanktons. The first example, bR, converts the energy of light into a proton gradient across the membrane. It is the main constituent of a two-dimensional hexagonal crystal lattice; the purple membrane (PM), naturally present as part of the plasmic membrane of the bacterium. PM films maintain structural and functional integrity under wide environmental conditions. It is a well characterized and well understood membrane protein and thus serves as a model system for many retinal proteins.[10] The investigation on PR, on the other hand, is of particular interest as bR and PR share a high sequence- and structure-homology. Here, the effect of different detergents on the quaternary structure of PR is studied and compared to the structure of PR without an N-terminal signal sequence.

Yet another, only recently detected and analyzed retinal protein, is the light-gated ion channel channelrhodopsin-2[11]

[a] *Institut für Physikalische und Theoretische Chemie, Cluster of Excellence Frankfurt ''Macromolecular Complexes'', Centre for Membrane Proteomics Goethe-Universität, Max-von-Laue Str. 7, 60438 Frankfurt am Main, Germany*
[b] *Institut für Biophysikalische Chemie, Cluster of Excellence Frankfurt Macromolecular Complexes, Centre for Membrane Proteomics Goethe-Universität, Max-von-Laue Str. 9, 60438 Frankfurt am Main, Germany. E-mail: brutschy@chemie.uni-frankfurt.de*
[c] *Max-Planck-Institut für Biophysik, Cluster of Excellence Frankfurt ''Macromolecular Complexes, Centre for Membrane Proteomics Goethe-Universität, Max-von-Laue Str. 3, 60438 Frankfurt am Main, Germany*

(ChR2) which is found in the green algae *Chlamydomonas reinhardtii*. It shares homology with sensory rhodopsin or bacteriorhodopsin. Not much is known up to now about its quarternary structure and its functional relations. Here we demonstrate a possible approach to analyze its stoichiometry in the solution phase using different buffer conditions.

For comparison we present results of the stoichiometry of the well studied potassium channel KcsA[12] of *Streptomyces lividans* which has a sequence similarity to known potassium channels. We give evidence that the liquid phase structure is similar to that found in 3D crystals.

To our knowledge it this the first time that complete solution phase quaternary structures of bR, PR, ChR2 and KcsA have been studied by mass spectrometry. For ChR2, one possible approach is demonstrated but too little is known until now to draw any conclusions from these findings.

2. Experimental

2.1 Sample preparation

Bacteriorhodopsin (bR) was prepared as described elsewhere.[13] For the measurements shown in Fig. 1 solubilized bR was desalted and transferred into 10 mM ammonium acetate (NH_4OAc) buffer containing 0.05% dodecylmaltoside (DDM).

Green proteorhodopsin (PR) was expressed in *Escherichia coli* and purified according to the literature,[14] resulting in a protein concentration of 0.5 mg ml^{-1}. The final sample buffer contained 50 m MES of pH 7.0, 20 mM NaCl and either of the following detergents: 0.2% Triton-X 100; 1% DDM; 0.5% DDM; or 0.05% DDM. The buffer containing 0.05% DDM was adjusted to pH 6.0. For comparison a small aliquot of the Triton-X solubilized PR was buffer-exchanged with 10 mM Tris–HCl adjusted to pH 7.5, 0.08% DDM.

PR lacking the N-terminal signal peptide was created by restriction digesting the PR gene without the signal sequence from the pIVEX 2.3d (Roche) cell free expression vector, a kind gift from Professor Dötsch (Frankfurt) and inserting it at the NdeI/XhoI cloning site of pET27b+ (Novagen).

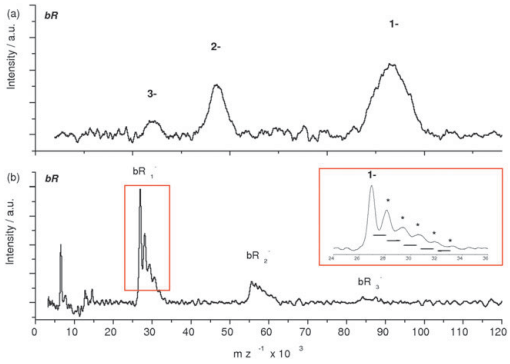

Fig. 1 LILBID anion spectra of bR: (a) recorded under soft conditions (depicted are the charge states of the trimer); (b) recorded under harsh conditions. Oligomeric states are labeled respectively. The inset shows the monomer with the lipid attachments.

The protein was expressed and purified using the same conditions as for the PR with the N-terminal signal sequence.[14]

Channelrhodopsin-2 (ChR2) was prepared in yeast (*Pichia pastoris*) as reported previously,[15] yielding a protein concentration of 2 mg ml^{-1}. The sample buffer contained 20 mM HEPES adjusted to pH 7.4, 100 mM NaCl and 0.2% decylmaltoside (DM). Additional buffers were a low-salt form of the sample buffer and a buffer composed of 10 mM Tris–HCl of pH 7.5, 0.08% DDM.

KcsA was prepared as described in the literature.[16] Since the protein was modified for PELDOR experiments,[17] the sample was a mutation (R84SL) incorporating the spin label. In addition to the initial preparation,[16] further purification steps were applied.[17] For the mass spectrometric measurements the sample was diluted to 10% in a 10 mM Tris–HCl buffer of pH 7.5 and 0.08% DDM resulting in a protein concentration of 5 μM.

In all cases buffer exchange was performed using Zeba™ Micro Desalt Spin Columns (Pierce) following a standard procedure. The proteins were kept either on ice or at 4 °C during storage and preparation.

2.2 Mass spectrometry

The LILBID method was described previously.[6] Briefly its source consists of a commercial droplet dispenser (Microdrop) which injects on demand tiny micro droplets ($Ø \sim 50$ μm; $V \sim 65$ pL) from 300 Torr *via* pressure reduction apertures into high vacuum. There they are irradiated one-by-one by high intensity mid-IR laser pulses ($\lambda \sim 3$ μm) from a home-built Nd:Yag pumped $LiNbO_3$ optical parametric oscillator (OPO), whereupon they explode, ejecting analyte ions. The method functions at low laser intensity in an "ultra soft" mode, which allows the study of noncovalent integral membrane complexes.

At elevated laser intensity *i.e.* at "harsh desorption conditions" less stable complexes are thermolyzed into their subunits in a top-down fashion. The mass analysis is currently performed by a home-built time of flight (TOF) mass spectrometer with a simple Wiley–McLaren-type acceleration region and an ion reflector (reflectron). For detecting ions of large m/z we utilize a home-built Daly-type high mass detector, with the conversion electrode being a multichannel plate, extending the detectable m/z range to about 10^6. Non-compensated initial energies of the ions, together with an incomplete ion desolvation are currently the main reasons for a rather moderate mass resolution. If not stated otherwise only 200 droplets were sampled for each mass spectrum. Normally less than 10 μl of solution with an analyte concentration in the μM range are required for an analysis, resulting in an analyte consumption typically in the pmol range.

3. Results and discussion

3.1 Bacteriorhodopsin

As visualized in 2D and 3D crystals bR adopts a trimeric state, where interdispersed endogenous lipids mediate inter-trimer contacts.[18,19] The trimers partition the lipid bilayer into two discontinuous compartments: a central one cylindrically

enclosed by the bR trimer with space for 6 lipids and an outer continuous bulk phase with space for 24 lipids per trimer. Although the monomer is the active unit,[20] the trimer is crucial for *in vivo* physiology.[18] The LILBID mass spectrum of bR, recorded under soft conditions is depicted in Fig. 1(a)). It shows only contributions of a trimer $(bR)_3$, however the mass peaks are unusually broad. Under harsh conditions (high laser energy) the bR trimer dissociates almost completely showing mainly the monomer (Fig. 1(b)) with a measured mass of about 26.9 kDa (calculated mass: 27 050 Da[21]). Magnification of the monomer peak (Fig. 1(b), inset) reveals the reason for the low resolution of the trimer: a series of small adducts with a mass difference of about 1.2 kDa each appear, with steadily decreasing intensity to higher mass. These adducts may be assigned to lipid molecules attached to the monomer. The most likely candidate for these ligands is the sulfated triglycoside lipid S-TGA-1 with a mass of 1217.9 Da. Such lipids have also been identified in lipid extracts from the purple membrane (PM) by ESI-MS.[18] The X-ray structure shows ten lipid molecules bound in the bR trimer.[18] Thus, lipid-mediated stabilization is crucial for the structure of the bR trimer. Neutron diffraction data also indicate the presence of three S-TGA-1 molecules in the central compartment.[18] The additional number of lipid molecules found in the adduct distribution of the LILBID mass spectrum are accounted for by lipids attached to the hydrophilic outer surface of the trimer, as S-TGA-1 is known to be crucial for the native structure of bR.[18] Thus, the LILBID mass spectra readily depict the native quaternary structure including the crucial attachment of lipid molecules visible in case of its fragmentation. In addition, from these results we may conclude that the trimeric structure is conserved in the solubilization.

3.2 Proteorhodopsin

The LILBID mass spectrum of a PR preparation in 0.2% Triton-X 100 shows an oligomeric distribution ranging from the monomer up to the hexamer (Fig. 2(a)). Independent of the laser energy, the most dominant signals are from the monomer and the dimer respectively. Purifying PR using DDM instead of Triton-X 100 surprisingly reveals a different stoichiometry of the solubilized protein. Depending on the DDM concentration either only the pentamer with low charge states is observed (Fig. 2(b)) or the charge distribution of the pentamer is the most abundant signal (Fig. 2(c)). In the latter case smaller oligomers also appear with lower signal intensity. In a buffer like the one used for recording the spectrum in Fig. 2(c), lowering the laser energy enhanced the fraction of the pentamer. However it was not possible to obtain by 100% the pentameric signals (data not shown; for further buffer conditions refer to Table 1). The mass peak of the monomer is split into a signal of about 28.7 kDa (calculated mass of the monomer: 28 823 Da[22]) and of about 30.7 kDa (Fig. 2(c) inset).

A cleavable signal sequence MGKLL-LILGSVIALPTFA of PR is located at the N-terminal of the protein, which is required for correct insertion into the membrane. It is known that when PR is expressed in *E. coli* with the signal sequence, it is not completely cleaved off.[23] Thus, the double peak is

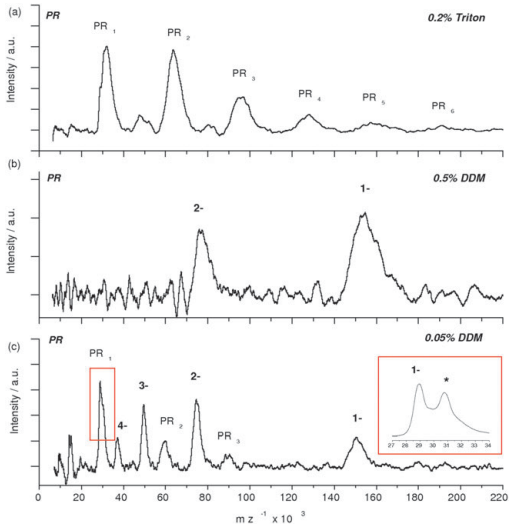

Fig. 2 LILBID anion spectra of proteorhodopsin using different detergents: (a) PR in 0.2% Triton-X 100 showing an oligomeric distribution; (b) PR in 0.5% DDM. The charge states of the pentamer are labeled. (c) PR in 0.05% DDM. The charge states of the pentamer are labeled. The inset shows the signal of the single charged monomers: the one including the signal peptide is indicated by an asterisk.

consistent with the assumption of two different monomers:[22] one without the signal peptide and one still including it (calculated mass: 30 662 Da[22]). The effect of the signal peptide on the oligomeric state is not known. From the LILBID mass spectra we conclude that cloning PR without the signal peptide has no effect on the oligomeric states under different buffer conditions (Fig. 3).

In 2D crystals PR forms mostly donut-shaped hexamers with about 10% pentamers,[19] whereas in the dense-packed non crystalline case mostly pentamers were found.[19] The LILBID mass spectra of solubilized PR in DDM are consistent with the structure of PR reconstituted in lipids. Interestingly the buffer used for crystallizing the protein contained Triton-X 100 as detergent. The preferred stoichiometry of a pentamer disagrees with findings from size exclusion chromatography[24] which show a trimer for PR solubilized in DDM. An overview of all the tested combinations of buffer, pH, detergent and salt, listed in Table 1, clearly suggests that the effect of preferential formation of a pentamer in the case of solubilized PR is due to the chosen detergent, in this case DDM. Since the initial solubilization was done in DDM[14] the quaternary structure of PR apparently is disrupted by Triton-X 100. Changes in pH or the type of buffering agents did not show any significant influence on the formation of the pentamer. Furthermore the concentration of DDM has a strong influence on the protein's stability, which can be seen in the respective mass spectra (Fig. 2(b) and (c)). In 0.5% DDM the only observable stoichiometry is the pentamer even at very high laser energies. These findings nicely demonstrate that the formation of the pentamer is not

Table 1 Most significant oligomeric states of PR for different buffer combinations

Buffer	Detergent	Complex
50 mM MES, pH 7, 20 mM NaCl	0.2% Triton-X 100	Monomer and dimer
50 mM MES, pH 6, 20 mM NaCl	1% DDM	Pentamer
50 mM MES, pH 7, 20 mM NaCl	1% DDM	Pentamer
50 mM MES, pH 7, 20 mM NaCl	0.5% DDM	Pentamer
50 mM MES, pH 6, 20 mM NaCl	0.05% DDM	Pentamer
10 mM Tris–HCl, pH 7.5	0.08% DDM	Pentamer

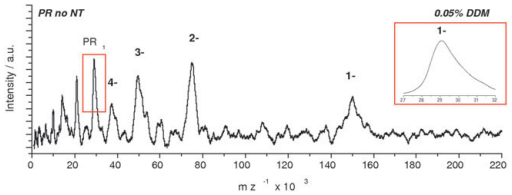

Fig. 3 PR without N-terminal signal sequence is exemplarily shown by means of PR in 0.05% DDM. The charge states of the pentamer are labeled. Inset: magnification of the monomer signal shows no evidence of the signal peptide.

constrained to *in vivo* environments; instead it is also observed *in vitro*.

Finally the photocycles of solubilized PR in Triton-X 100 and of 2D crystals were found to be almost identical.[25] Our results from the mass spectrum in Fig. 2(a) together with the visual data of the 2D crystals suggest that the photocycle seems to be independent of the oligomeric state. A comparison of the photocycles of PR solubilized using different detergents is the only way to solve this question. Furthermore this would suggest that the monomer is the active unit. This would be an analogy to bR and further stimulate a discussion about the actual reason for the high stoichiometry found by independent methods in the solubilized or crystallized form of PR.

3.3 Channelrhodopsin 2

The purification in an essentially salt free HEPES buffer including 0.2% DM lead to the LILBID mass spectrum of ChR2 depicted in Fig. 4(a). Only the dimer with a mass of about 72 kDa (calculated mass: 36 135 Da for the monomer) with up to 4 charge states is observed. Using the sample buffer with 100 mM of NaCl added leads to massively broadened peaks of the same dimer-spectrum (Fig. 4(b)). It is known that ChR2 contains an unusually high amount of polar residues[26] compared to other rhodopsins. This most likely accounts for the fact that ion signals with a reasonable signal-to-noise ratio could be detected at all in such high salt concentrations. In calibrated size exclusion chromatography, ChR2 runs as a major peak of about 170 kDa. As the exact amount of detergent in the mixed protein–detergent micelle is not known it is difficult to compare these results. ChR2, expressed in yeast, shows up as a dimer and in fact this the only stoichiometry observed under all conditions. Therefore it is possible that ChR2, in analogy to other rhodopsins, can exist in higher oligomeric states in the native membrane and should form at least a dimer. As a side note, this dimer must be really

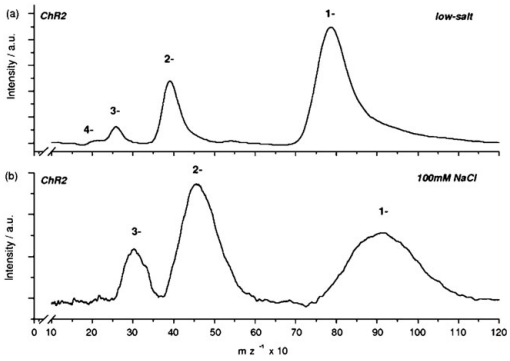

Fig. 4 LILBID anion spectra of ChR2: (a) in a low-salt form of the sample buffer; and (b) in sample buffer containing 100 mM NaCl. In each case the charge distribution of the dimer is labeled.

stable—it could not be dissociated neither in the harsh mode of LILBID at higher laser intensities nor by an SDS gel.

3.4 KcsA

In the mass spectrum of the K^+-channel recorded in soft mode (Fig. 5(a)) mostly the tetramer with a mass of about 54 kDa and a low intensity peak of the KcsA monomer are observed. The spectrum recorded under harsh conditions (Fig. 5(b)) shows, on the other hand, mostly monomeric species.

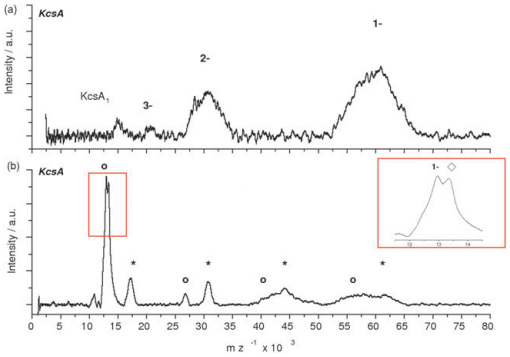

Fig. 5 LILBID anion spectra of KcsA: (a) recorded under soft conditions (the charge states of the tetramer are labeled); (b) recorded under harsh conditions. The peak series labeled with an asterisk or a circle denote two distinct distributions of fragments. The inset shows the two masses observed for the monomer (the heavier one being indicated by the square).

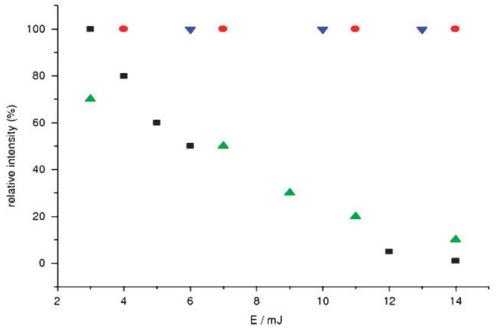

Fig. 6 Relative signal abundances of the intact structures depending on the lasers pulse energy: ChR2 dimer (red circles); bR trimer (black squares); PR pentamer in 0.5% DDM (blue triangles); and PR pentamer in 0.05% DDM (green triangels).

In addition higher oligomeric states appear at low signal intensity. The inset in Fig. 5(b) shows a splitting of the monomer peak with a mass difference of almost 400 Da. This shift in mass was already observed by ESI-MS and interpreted as possible post-translational modifications.[27] Furthermore, two distinct stoichiometric distributions are visible which differ in a mass of about 4 kDa (indicated by circles and asterisks in Fig. 5(b)). As this protein preparation involved chymotryptic cleavage of the C-terminal sequence of 33 amino acids and the His-tag,[17] the observed mass shift currently is accounted for by an incomplete cleavage.

3.5 Laser intensity

For each of the studied rhodopsins, the relative signal intensities of the observed complexes for varying laser energies is shown in Fig. 6. For the given buffer conditions the most stable complex is the dimer of ChR2 coincidental with the pentamer of PR in 0.5% DDM, while the most unstable is the trimer of bR. In case of PR the pentamer shows a varying abundance depending on the type and concentration of the detergent used. Purifying PR in Triton-X 100 provides mainly signals from the mono- and dimer and also higher oligomers with no clear preference for the pentamer.

Using DDM in low concentrations the main species is the pentamer accompanied by a small amount of fragments due to solution phase dissociation. By increasing the laser energy more-and-more fragment products appear. Purifying PR in DDM at high concentration changed this situation completely: Then the pentamer is the only oligomeric state observed and no laser induced thermolysis could be detected.

4. Conclusions

In the context of the analysis of membrane proteins we have shown that LILBID-MS is capable of analyzing their native quaternary structures after solubilization. The observed softness of this method is also remarkable. By mass spectrometry we could show that the preservation of native structures of membrane proteins in solution mainly depends on buffer conditions. The mass resolution is not yet state-of-the-art and work is in progress to improve on this matter.

Complementing other MS methods like MALDI and ESI LILBID clearly is an alternative mass spectrometric method, tolerant to a large extend to buffering agents, detergents and salts.

List of abbreviations

LILBID	Laser induced liquid bead ion desorption
ESI	Electrospray ionization
MALDI	Matrix assisted laser desorption/ionization
DDM	*N*-Dodecyl-β-D-maltoside
DM	Decylmaltoside
HEPES	4-(2-hydroxyethyl)-1-piperazine-ethane sulfonic acid
MES	2-(*N*-Morpholino)ethanesulfonic acid
Tris	Tris(hydroxymethyl)aminomethane
Triton X-100	Polyoxyethyleneoctylphenyl ether

Acknowledgements

We thank Prof. J. Wachtveitl for providing us with the solubilized bR sample as well as Prof. T. Prisner and Prof. R. MacKinnon for the KcsA sample. We are grateful to Cornelia Münke (group of Prof. H. Michel) for performing the calibrated size exclusion chromatography. We are very much obliged to Dr H.-D. Barth for his technical assistance and to L. Sokolova for helpful discussions.

This research was carried out with the financial support of the Deutsche Forschungsgemeinschaft (DFG) (SFB 579; The Cluster of Excellence Frankfurt (CEF) "Macromolecular Complexes") and of the Centre for Membrane Proteomics.

References

1 M. Karas and F. Hillenkamp, *Anal. Chem.*, 1988, **60**, 2299.
2 C. M. Whitehouse, R. M. Dreyer, M. Yamashita and J. B. Fenn, *Anal. Chem.*, 1985, **57**, 675; J. B. Fenn, M. Mann, C. K. Meng, S. F. Wong and C. M. Whitehouse, *Science*, 1989, **246**, 64–71.
3 C. Bich and R. Zenobi, *Curr. Opin. Struct. Biol.*, 2009, **19**, 632–639.
4 H. Hernández and C. V. Robinson, *Nat. Protoc.*, 2007, **2**, 715–726; K. Lorenzen, C. Versluis, E. van Dujin, R. H. H. van den Heuvel and A. R. J. Heck, *Int. J. Mass Spectrom.*, 2007, **268**, 198–206.
5 N. P. Barrera, S. C. Isaacson, M. Zhou, V. N. Bavro, A. Welch, T. A. Schaedler, M. A. Seeger, R. N. Miguel, V. M. Korkhov, H. W. Van Veen, H. Venter, A. R. Walmsley, C. G. Tate and C. V. Robinson, *Nat. Methods*, 2009, **6**, 585–U90.
6 N. Morgner, H.-D. Barth and B. Brutschy, *Aust. J. Chem.*, 2006, **59**, 109–114.
7 N. Morgner, T. Kleinschroth, H.-D. Barth, B. Ludwig and B. Brutschy, *J. Am. Soc. Mass Spectrom.*, 2007, **18**, 1429–1438; T. Meier, N. Morgner, D. Matthies, D. Pogoryelov, S. Keis, G. M. Cook, P. Dimroth and B. Brutschy, *Mol. Microbiol.*, 2007, **65**, 1181–1192.
8 D. Oesterhelt and W. Stoecken, *Proc. Natl. Acad. Sci. U. S. A.*, 1973, **70**, 2853–2857.
9 O. Beja, L. Aravind, E. V. Koonin, M. T. Suzuki, A. Hadd, L. P. Nguyen, S. Jovanovich, C. M. Gates, R. A. Feldmann, J. L. Spudich, E. N. Spudich and E. F. DeLong, *Science*, 2000, **289**, 1902–1906.
10 U. Haupts, J. Tittor and D. Oesterhelt, *Annu. Rev. Biophys. Biomol. Struct.*, 1999, **28**, 367–399.
11 G. Nagel, T. Szellas, W. Huhn, S. Kateriya, N. Adeishvili, P. Berthold, D. Ollig, P. Hegemann and E. Bamberg, *Proc. Natl. Acad. Sci. U. S. A.*, 2003, **100**, 13940–13945.
12 H. Schrempf, O. Schmidt, R. Kümmerlen, S. Hinnah, D. Müller, M. Betzler, T. Steinkampf and R. Wagner, *EMBO J.*, 1995, **14**, 5170–5178.

13 H. Patzelt, A. S. Ulrich, H. Egbringhoff, P. Düx, J. Ashurst, B. Simon, H. Oschkinat and D. Oesterhelt, *J. Biomol. Nucl. Magn. Reson.*, 1997, **10**, 95–106.
14 S. Shastri, J. Vonck, W. Haase, N. Pfleger, W. Kuehlbrandt and C. Glaubitz, *Biochim. Biophys. Acta, Biomembr.*, 2007, **1768**, 3012–3019; N. Pfleger, M. Lorch, A. Wörner, S. Shastri and C. Glaubitz, *J. Biomol. Nucl. Magn. Reson.*, 2008, **40**, 15–21.
15 I. Radu, C. Bamann, M. Nack, G. Nagel, E. Bamberg and J. Heberle, *J. Am. Chem. Soc.*, 2009, **131**, 7313–7319.
16 D. A. Doyle, J. M. Cabral, R. A. Pfuetzner, A. Kuo, J. M. Gulbis, S. L. Cohen, B. T. Chait and R. MacKinnon, *Science*, 1998, **280**, 69.
17 B. Endeward, J. A. Butterwick, R. MacKinnon and T. Prisner, *J. Am. Chem. Soc.*, 2009, **131**, 15246–15250.
18 L.-O. Essen, R. Siegert, W. D. Lehmann and D. Oesterheldt, *Proc. Natl. Acad. Sci. U. S. A.*, 1998, **95**, 11673–11678.
19 A. L. Klyszejko, S. Shastri, S. A. Mari, H. Grubmüller, D. J. Muller and C. Glaubitz, *J. Mol. Biol.*, 2008, **376**, 35–41.
20 N. A. Dencher, K. D. Kohl and M. P. Heyn, *Biochemistry*, 1983, **22**, 1323–1334.
21 D. R. Barnidge, E. A. Dratz, A. J. Jesaitis and J. Sunner, *Anal. Biochem.*, 1999, **269**, 1–9.
22 T. Friedrich, S. Geibel, R. Kalmbach, I. Chizhov, K. Ataka, J. Heberle, M. Engelhard and E. Bamberg, *J. Mol. Biol.*, 2002, **321**, 821–838.
23 N. Pfleger, A. C. Wörner, J. Yang, S. Shastri, U. A. Hellmich, L. Aslimovska, M. S. M. Maier and C. Glaubitz, *Biochim. Biophys. Acta, Bioenerg.*, 2009, **1787**, 697–705.
24 H. Liang, G. Whited, C. Nguyen and G. D. Stucky, *Proc. Natl. Acad. Sci. U. S. A.*, 2007, **104**, 8212–8217.
25 G. Schäfer, S. Shastri, M.-K. Verhoefen, V. Vogel, C. Glaubitz, J. Wachtveitl and W. Mäntele, *Photochem. Photobiol.*, 2009, **85**, 529–534.
26 P. Hegemann, *Annu. Rev. Plant Biol.*, 2008, **59**, 167–89.
27 J. A. A. Demmers, A. v. Dalen, B. d. Kruijff, A. J. R. Heck and J. A. Killian, *FEBS Lett.*, 2003, **541**, 28–32.
28 K. Nakamura and S. Mizushima, *J. Biochem.*, 1976, **80**, 1411–1422.

PCCP

Physical Chemistry Chemical Physics

www.rsc.org/pccp Volume 12 | Number 41 | 7 November 2010 | Pages 13345–13852

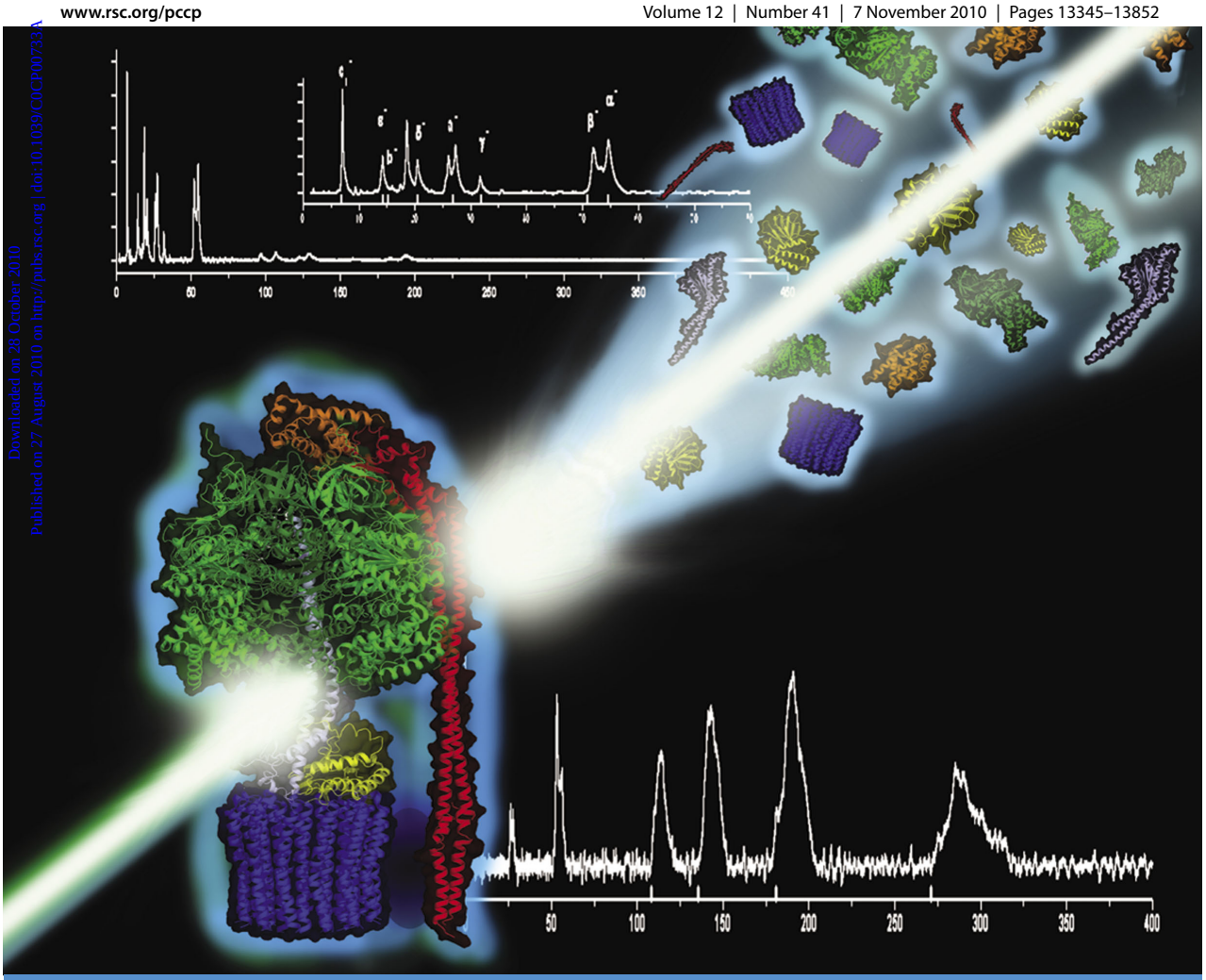

Includes a collection of articles on the theme of advances in mass spectrometry for biological science

ISSN 1463-9076

1463-9076(2010)12:41;1-X

ATP synthases: cellular nanomotors characterized by LILBID mass spectrometry

Jan Hoffmann,[a] Lucie Sokolova,[a] Laura Preiss,[b] David B. Hicks,[c] Terry A. Krulwich,[c] Nina Morgner,[d] Ilka Wittig,[e] Hermann Schägger,[e] Thomas Meier*[b] and Bernd Brutschy*[a]

Received 28th May 2010, Accepted 28th July 2010
DOI: 10.1039/c0cp00733a

Mass spectrometry of membrane protein complexes is still a methodological challenge due to hydrophobic and hydrophilic parts of the species and the fact that all subunits are bound non-covalently together. The present study with the novel laser induced liquid bead ion desorption mass spectrometry (LILBID-MS) reports on the determination of the subunit composition of the F_1F_o-ATP synthase from *Bacillus pseudofirmus* OF4, that of both bovine heart and, for the first time, of human heart mitochondrial F_1F_o-ATP synthases. Under selected buffer conditions the mass of the intact F_1F_o-ATP synthase of *B. pseudofirmus* OF4 could be measured, allowing the analysis of complex subunit stoichiometry. The agreement with theoretical masses derived from sequence databases is very good. A comparison of the ATP synthase subunit composition of 5 different ATPases reveals differences in the complexity of eukaryotic and bacterial ATP synthases. However, whereas the overall construction of eukaryotic enzymes is more complex than the bacterial ones, functionally important subunits are conserved among all ATPases.

1. Introduction

F-type ATP synthases are essential enzymes ubiquitously found in bacteria, mitochondria and chloroplasts. They are ion-driven nanomotors which have two working directions. They synthesize adenosine triphosphate (ATP) from adenosine diphosphate (ADP) and a free phosphate (P_i) and therewith provide the organism with the "energy currency" of cells. The energy for this process is provided by an electrochemical gradient of protons (or less commonly Na^+), which are pumped across the membrane by primary pumps such as those found in the respiratory chain. In the other direction, ATP is hydrolyzed by the ATPase, which is used then as a pump for cell pH homeostasis or to acidify intracellular compartments.[1,2]

The simplest form of F_1F_o ATP synthases can be found in bacteria, schematically shown in Fig. 1. The F_1 complex (subunits $\alpha_3\beta_3\gamma\delta\varepsilon$) is the water soluble domain of the enzyme and protrudes into the cytoplasmic reservoir of the cell. F_1[3] is connected with the F_o complex by peripheral (subunits $b_2\delta$) and central stalks (subunits $\gamma\varepsilon$). The F_o complex, the "turbine-motor", is highly hydrophobic and consists of the subunits ab_2c_{10-15}. It is responsible for ion translocation across the membrane.[4] A more complex composition can be found in mitochondria. Beside the same core subunits as in the bacterial ATP synthase (a, b and c), the additional subunits d, e, f, g, 8, F_6 and OSCP are associated with the mitochondrial enzyme.[5] From a functional point of view, the subunits of an ATP synthase can be

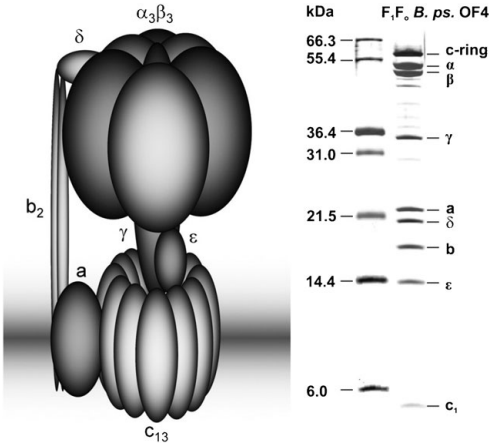

Fig. 1 Cartoon representation of the subunit composition of a bacterial F_1F_o-ATP synthase (left) and for comparison results from a 15% SDS polyacrylamide gel electrophoresis[35] of 10 µg purified *B. pseudofirmus* OF4 ATP synthase (right). A marker lane and the indicated masses in kDa are given on the left. The gel was stained with silver.[36]

[a] *Institute for Physical and Theoretical Chemistry, Cluster of Excellence Frankfurt "Macromolecular Complexes", Centre for Membrane Proteomics, Goethe-Universität, Max-von-Laue Str. 7, 60438 Frankfurt am Main, Germany. E-mail: brutschy@chemie.uni-frankfurt.de*
[b] *Department of Structural Biology, Max-Planck Institute of Biophysics, Max-von-Laue-Str. 3, 60438 Frankfurt am Main, Germany. E-mail: thomas.meier@biophys.mpg.de*
[c] *Department of Pharmacology and Systems Therapeutics, Mount Sinai School of Medicine, 1 Gustave L. Levy Place, New York 10029, USA*
[d] *Department of Chemistry, Physical and Theoretical Chemistry Laboratory, South Parks Road, Oxford OX1 3QZ, UK*
[e] *Molecular Bioenergetics, Medical School, Goethe-Universität Frankfurt, Theodor-Stern-Kai 7, Haus 26, D-60590 Frankfurt am Main, Germany*

divided into two parts, a rotor (subunits $\gamma\varepsilon c_{10-15}$) and a stator (subunits $\alpha_3\beta_3\delta ab_2$).[6] The rotor is driven by the ions, which are translocated through the F_o motor, and acts as a rotating camshaft within the F_1 headpiece. By rotation it causes conformational changes within the three catalytic centers in each of the β-subunits,[7] which finally converts ADP and P_i into ATP. The overall molecular mass of the holo-F_1F_o ATP synthase complex is approx. 540 kDa[8] in bacteria and 570–585 kDa in mitochondria.[9] Information about the mass of the functional holo complex (F_1F_o) is of interest since it allows the confirmation of the correct assembly[8] and, in some cases,[10] the determination of subunit stoichiometries.

The different biochemical conditions, needed for complex stability of the soluble and the membrane-embedded part of ATP synthases, make the investigation of the intact enzyme very difficult for traditional mass spectrometric biology approaches. Non-covalent mass spectrometries such as electrospray ionization mass spectrometry (ESI-MS) and laser induced liquid bead ion desorption mass spectrometry (LILBID-MS) are well established for the investigation of soluble complexes, while membrane protein complexes remained an invincible challenge for a long time. The first intact membrane protein complexes in the gas phase were observed with LILBID[11] and nano ESI (nESI)[12] recently.

The particular challenge in the investigation of ATP synthases compared to smaller membrane protein complexes with smaller soluble parts is the spatial separation of the membrane part and the soluble head that are connected by non covalently bound subunits. In the case of ESI, detergent micelles are used to protect the complex while it is transferred from solution to gas phase. These protein-containing detergent aggregates are then activated by collisions in the gas phase to release the complex from the vast detergent aggregates. The two part structure of the ATP synthase is therefore particularly challenging, since the soluble part is prone to dissociate under conditions that are needed to release the membrane-embedded region from the detergent aggregates. ATP synthases have been studied intact by nESI[12,39] and LILBID.[8,13]

LILBID-MS has turned out to be a particularly suitable alternative to ESI for the analysis of non-covalently bound membrane protein complexes solubilized by detergents. Here, solvated biomolecules are transferred from aqueous micro droplets into vacuum by means of infrared laser pulses, the wavelength of which is tuned to the strongest absorption band of water (3 μm), to achieve an effective energy transfer into the liquid matrix rather than into the biological sample. The method has proven to be soft and sensitive, allowing the investigation of detergent-solubilized samples at typically micromolar concentrations and at a desired buffer and pH.

The goal of this work was to determine and compare the masses and subunit composition of three exemplary ATP synthases; from the bacterium *Bacillus pseudofirmus* OF4 and from bovine and human heart mitochondria by LILBID mass spectrometry. Furthermore, we compare the masses of these subunits with those determined for the ATP synthases from the yeast *Yarrowia lipolytica*[14] and from *Bacillus* sp. strain TA2.A1,[8] which both have been previously measured by LILBID-MS.

2. Materials and methods

2.1 Sample preparation

***Bacillus pseudofirmus* OF4 F_1F_o-ATP synthase.** The ATP synthase was purified from *Bacillus pseudofirmus* OF4 cells[15] in which a hexa-histidine tag was inserted after the N-terminal methionine in the chromosomal gene encoding the β-subunit of the ATP synthase. The complex was extracted from everted vesicles with 1% dodecyl maltoside (DDM) in the presence of 3 mg ml^{-1} soybean asolectin and purified by affinity chromatography on Ni-NTA agarose. The sample with a final concentration of 1 mg ml^{-1} was dialized for 24 h against 10 mM ammonium acetate buffer (NH_4OAc) at pH 7.5 and 0.05% (w/v) dodecyl maltoside.

Bovine heart mitochondrial F_1F_o-ATP synthase. Isolation of mitochondria from *Bos taurus*, solubilization of mitochondrial membranes by DDM, blue native electrophoresis (BN-PAGE) and electroelution were performed as described by Wittig *et al.*[16] Briefly, sedimented mitochondria (4 mg protein) were solubilized by DDM setting a detergent/protein ratio of 2.5 g g^{-1}. Following 15 min of centrifugation at 100 000 × *g*, the supernatant was recovered, supplemented with Coomassie blue G-250, and applied to a 3–13% acrylamide gradient gel for BN-PAGE. Following BN-PAGE the visible blue band of ATP synthase was cut out and the protein was electroeluted. Glycerol was added to 10% and the sample was shock frozen and stored at −80 °C.

Human heart mitochondrial F_1F_o-ATP synthase. Human (*Homo sapiens*) ATP synthase[17] was prepared from post mortem heart tissue, essentially as described by Wittig *et al.*[16] Briefly, frozen heart tissue (105 mg; wet weight) was thawed, frayed out using tweezers, and homogenized in 1 ml of solution (250 mM sucrose, 20 mM Na-phosphate, pH 7.0) using a tightly fitting glass/Teflon homogenizer. The total volume was apportioned into aliquots corresponding to 5 mg and 2 × 50 mg of cells, sedimented by 10 min centrifugation at 20 000*g*, and frozen after removal of the supernatants or used immediately. One sediment from 50 mg heart tissue containing nuclei, larger cell fragments, and mitochondria was suspended with 450 μl of buffer (50 mM NaCl, 2 mM 6-aminohexanoic acid, 1 mM EDTA, 50 mM imidazole/HCl, pH 7.0) and solubilized by adding 40 μl DDM (10%). Following 15 min of centrifugation at 100 000*g*, the supernatant was recovered, supplemented with 10 μl of 5% Coomassie blue G-250, and the total volume of 500 μl was applied to a 3–13% acrylamide gradient gel for blue native electrophoresis. The band of ATP synthase was cut out and the protein was electroeluted. 10% of glycerol was added and aliquots corresponding to 16 mg heart were shock frozen and stored at −80 °C. An aliquot corresponding to 16 mg heart was used for the preparation of a single sample for LILBID measurement.

In all cases proteins were kept either on ice or at 4 °C during storage and preparation. Where necessary buffer exchange/desalting was performed using Zeba(™) Micro Desalt Spin Columns (Pierce) following standard procedures.

2.2 Mass spectrometry

LILBID-MS was described in detail previously.[18] Briefly, the ion source contains a commercial droplet dispenser (Microdrop) which injects on demand tiny micro droplets ($\varnothing \approx 50$ μm; $V \approx 65$ pL) from 300 Torr through pressure reduction apertures into high vacuum (10^{-6} Torr). There they are irradiated one by one by high intensity mid-IR laser pulses ($\lambda \approx 3$ μm) generated by a home-built Nd:Yag pumped $LiNbO_3$ optical parametric oscillator (OPO). Due to the absorption of the laser light by the solvent, beyond a certain intensity threshold the droplets are disrupted, ejecting preformed analyte ions into vacuum. At low laser intensity this method functions in an "ultra soft" mode, which allows studying noncovalent solubilized integral membrane complexes. At increased laser intensity *i.e.* at "harsh desorption conditions" less stable complexes are thermolyzed into their subunits in a top-down fashion. The mass analysis is currently realised using a home-built time of flight (TOF) mass spectrometer of the Wiley–McLaren-type including an ion reflector (reflectron). For detecting ions of large m/z we utilize a home-built Daly-type high mass detector, with the conversion electrode being a multichannel plate, extending the detectable m/z range to about 10^6. The main reason for a rather moderate mass resolution is the non-compensated isotropic initial energy of the ions together with an incomplete ion desolvation. Unless otherwise stated only 200 droplets were sampled for each mass spectrum. Typically less than 10 μl of solution with an analyte concentration in the micromolar range are required for an analysis, resulting in an analyte consumption in the pmol range.

3. Results and discussion

We first studied the F_1F_o-ATP synthase from *Bacillus pseudofirmus* OF4, a facultative alkaliphilic strain, which grows at a pH up to 11.2 but still uses an exclusively proton-coupled ATP synthase.[15] It was prepared as described in Materials and methods. Theoretically it consists of 8 different proteins (Table 1) in a stoichiometry of $\alpha_3\beta_3\gamma\delta\varepsilon ab_2c_{13}$ making a total of 25 proteins for one F_1F_o complex (chemical composition: $C_{24\,213}H_{39\,209}N_{6435}O_{7171}S_{146}$; with a total number of atoms of 77 174 and with 4999 amino acids as calculated with: www.expasy.org/cgi-bin/protparam). The overall theoretical calculated mass of the holo enzyme is 540290.53 Da. The schematically drawn common structure of a bacterial F_1F_o-ATP synthase is illustrated together with its subunit composition on an SDS polyacrylamide gel in Fig. 1. Our aim was to determine the total mass of the complex (F_1F_o), the mass of its subcomplexes (F_1 and F_o) and of the single subunits by LILBID mass spectrometry. The mass spectrum (Fig. 2(a)) recorded under soft conditions, *i.e.* low laser intensity, shows two distinct charge distributions (n = 1–6) of anions, which can be very likely assigned to the water soluble F_1 subcomplex and the F_1 subcomplex, lacking the δ-subunit (for a comparison of measured and expected masses see Table 1). Additionally, signals of the highly hydrophobic F_o subcomplex are visible. Thus in the low m/z range charge distributions of the α- and β-subunits can be observed. These findings suggest that dissociation already took place in solution phase. At high laser energy (Fig. 2(b)) almost all the signals of the subcomplexes are strongly diminished, while signals for the single subunits appear. As shown in the enlarged inset of Fig. 2(b), all 8 expected subunits (α, β, γ, δ, ε, a, b and c) were present in the enzyme preparation (Fig. 1)and can also be seen in the LILBID anion spectrum (Fig. 2(a) and (b)). The observed masses of the subunits are in good agreement with the calculated values from a sequence database (Table 1). Thus, the LILBID spectra do not only reflect the exact single subunit masses but also the composition of the enzyme's subcomplexes. The dissociation observed under the buffer conditions used for recording these spectra was surprising. It resulted in the loss of the intact F_1F_o complex. For this reason we also measured this sample in Tris/HCl buffer containing 1 mM of $MgCl_2$.

Fig. 3(a) shows the LILBID mass spectrum measured under the same soft desorption conditions as for the spectrum in Fig. 2(a). Here the main peaks correspond to a mass of approximately 542 kDa, visible in various charged states (N = 2–8) matching the theoretically calculated mass of the intact F_1F_o complex (with the mass of the complex corresponding to the onset of the peak). The peak broadening is due to nonspecific association of Tris buffer, lipids and detergent molecules. Furthermore, the increased stability of the intact

Table 1 Calculated and experimental masses of *Bacillus* OF4 F_1F_o-ATP synthase (as determined from GenBank Locus AF330160.1)

Subunit/subcomplex	Uniprot	Calc. mass[a]/Da	LILBID mass/kDa
a	AAG48358.1	26863.77	
b	AAG48359.1	18510.16	18.6 (±0.2)
c	AAC08039.1	6956.06	7.0 (±0.1)
α	AAG48361.1	54674.48	54.1 (±0.5)
β[b]	AAG48363.1	51752.14	51.3 (±0.5)
γ	AAG48362.1	31835.49	31.5 (±0.5)
δ	AAG48360.1	20534.63	20.3 (±0.2)
ε	AAG48364.1	14327.68	14.4 (±0.2)
F_1 ($\alpha_3\beta_3\gamma\delta\varepsilon$)		385977.66	384.0 (±3)
F_1-δ ($\alpha_3\beta_3\gamma\varepsilon$)		365443.03	363.0 (±3)
F_o (ab_2c_{13})[c]		154312.87	154.0 (±2)
F_1F_o ($\alpha_3\beta_3\gamma\delta\varepsilon ab_2c_{13}$)[c]		540290.53	542.0 (±5)

[a] Calculations were performed with BioEdit (www.mbio.ncsu.edu/BioEdit/bioedit.html). [b] All β-subunits contain a hexa-histidine tag at the N-terminus (840.86 Da), which is included in the calculation, see Materials and methods for details. [c] The tridecameric rotor ring stoichiometry of *Bacillus pseudofirmus* OF4 was determined in Preiss *et al.*[38]

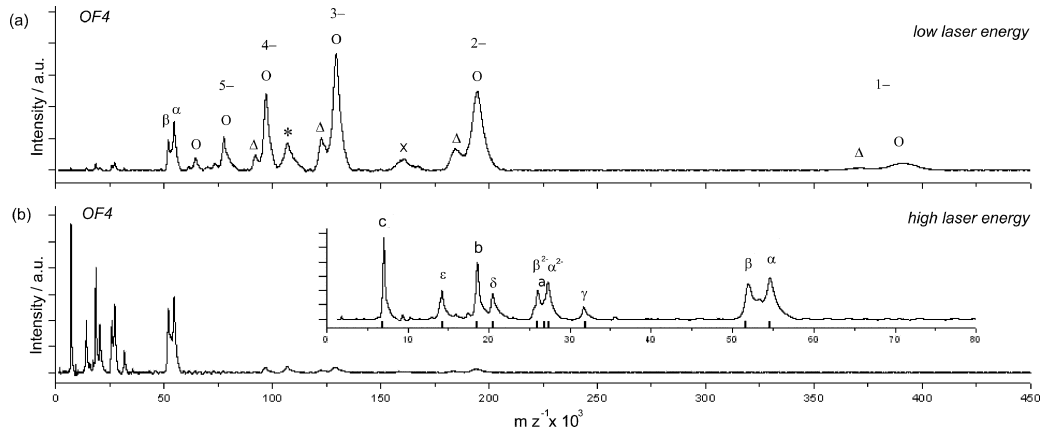

Fig. 2 LILBID anion spectra of *B. pseudofirmus* OF4 F_1F_o-ATP synthase after dialysis in a 10 mM ammonium acetate buffer. (a) Recorded under soft conditions. Shown are the charge distributions of F_1 (circles), F_1 without δ subunit (triangles) and F_o (cross) and presumably α + β (asterisk). (b) Recorded under harsh conditions, with a magnification given in the inset. The subunits are labelled with the black bars indicating the respective calculated masses.

complex due to the addition of Mg^{2+} reflects the relative solution phase stability in the mass spectra as has already been shown for nucleic acids.[19] Moreover an additional charge distribution of the highly charged[3] α- and β-subunits is observed, which indicates that dissociation still takes place to some minor extent. To investigate whether the Tris buffer or the Mg^{2+} ions are responsible for the increased stability of the whole complex, we transferred the sample into an ammonium acetate (NH_4OAc) buffer containing 1 mM of $MgCl_2$. Fig. 3(b) shows the corresponding LILBID mass spectrum recorded using the same conditions as for the sample in Tris/HCl buffer. The signal-to-noise ratio considerably increased as compared with the spectrum in Fig. 3(a) while the resolution under soft desorption conditions hardly changed. The charge distribution of the anions is now shifted to lower charged states compared to the spectrum in Fig. 3(a). This difference in the charge distribution of the complex is attributed to the protonating effect of the NH_4^+ ions. Moreover it was not possible to obtain signals of the intact complex when transferring the sample into a NH_4OAc buffer without $MgCl_2$. This further demonstrates that Mg^{2+} ions are crucial for complex stability and function, a fact, which was investigated very early in ATP synthase research[20] and confirmed many times since. Our results demonstrate that LILBID-MS is able to analyse the mass of an intact ATP synthase.

Human and bovine F_1F_o

Bovine and human samples from Blue Native Electrophoresis (BNE) were transferred into 30 mM NH_4HCO_3, 0.05% DDM

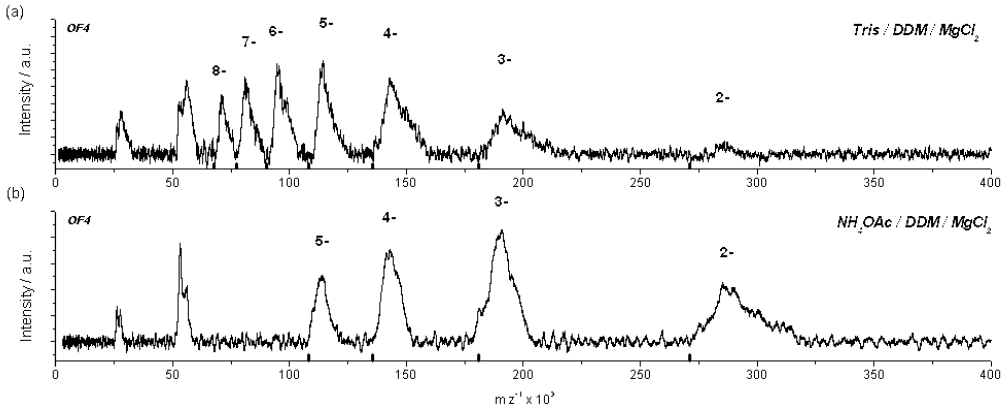

Fig. 3 LILBID anion spectrum of *B. pseudofirmus* OF4 F_1F_o-ATP synthase recorded under soft conditions. (a) Sample buffer was 10 mM Tris/HCl of pH 7.5, 0.08% DDM and 1 mM of $MgCl_2$. (b) Sample buffer was 10 mM NH_4OAc of pH 7.5, 0.08% DDM and 1 mM of $MgCl_2$. Depicted are the charge states of the bacterial F_1F_o complex.

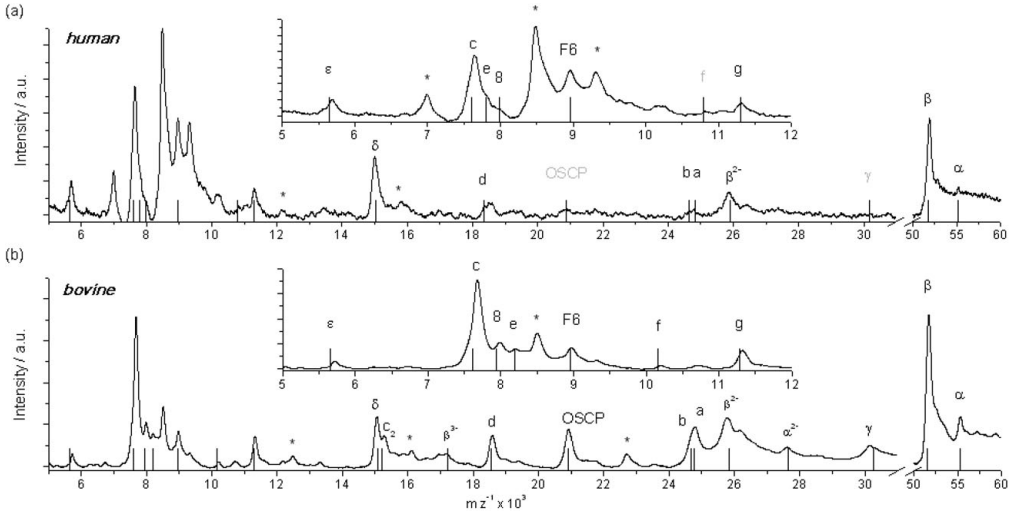

Fig. 4 LILBID anion spectrum of human (a) and bovine (b) F_1F_o-ATP synthases recorded at harsh conditions using 1000 and 900 droplets respectively. The insets show a magnification of the lower mass range. The black bars represent calculated masses of the subunits as stated in Table 2. Missing peaks of subunits are marked gray. An asterisk marks a contamination.

and measured in a harsh desorption mode. Final concentrations of the bovine and human samples were approximately in the sub-micromolar range in both cases. While the mass spectrum of bovine ATPase was recently reported by Carroll *et al.*[21] the mass spectrum of human ATP synthase presented in this work is the first mass spectrum of human ATP synthase reported so far. Both spectra (Fig. 4) show great similarity especially regarding the most intense peaks of the β-, δ- and c subunits, however subtle differences are expected and also observed for other subunits (see Table 2). The peaks labelled with an asterisk appeared repeatedly for both samples from different preparations of bovine ATP synthase and also for that of human ATP synthase. Most likely these peaks originate from foreign proteins, since the preparative conditions used for both samples are not sufficient to completely remove contaminations. When the spectrum of bovine ATP synthase is compared to a previously reported MS analysis,[21] the masses agree within ±150 Da with the masses reported before and with the theoretical masses. All subunits except for the AGP and MLQ proteins (named after amino-terminal sequencing) are

Table 2 Calculated and experimental masses of bovine and human mitochondrial ATP synthase

	Bovine				Human		
Subunit	Uniprot	Calc. mass[a]/Da	ESI mass/Da[20]	LILBID mass/kDa	Uniprot	Calc. mass[a]/Da	LILBID mass/kDa
α	P19483	55263.39	55244.6	55.3 (±0.2)	P25705	55209.32	55.2 (±0.21)
β	P00829	51562.97	51709.1	51.7 (±0.3)	P06576	51769.25	51.9 (±0.3)
γ	P05631	30255.71	30141.7	30.2 (±0.1)	P36542	30165.73	Not detected
δ	P05630	15064.93	15066.1	15.1 (±0.1)	P30049	15019.93	15 (±0.1)
ε	P05632	5651.67	5651.8	5.7 (±0.05)	P56381	5648.57	5.7 (±0.05)
b	P13619	24668.72	24670.7	24.7 (±0.3)[b]	P24539	24625.61	24.5 (±0.3)[b]
OSCP	P13621	20929.75	20931.6	20.9 (±0.1)	P48047	20875.49	Not detected
a	P00847	24787.91	24817.6	24.7 (±0.2)	P00846	24817.21	24.8 (±0.3)[b]
	Q8SFX8						
d	P13620	18561.28	18604.6	18.6 (±0.1)	O75947	18360.02	18.5 (±0.2)
e	Q00361	8189.47	8189.8	8.2 (±0.05)	P56385	7802.02	7.8 (±0.3)[b]
f	Q28851	10165.99	10208.6	10.2 (±0.1)	P56134	10786.67	Not detected
g	Q28852	11286.26	11327.6	11.3 (±0.1)	O75964	11428.48	11.3 (±0.05)
					Q8N5M1	11036.99	
						11386.44	
8	P03929	7936.56	7964.4	8 (±0.05)	P03928	7991.65	8 (±0.3)[b]
c	P32876	7608.01	7650.0	7.7 (±0.1)	P05496	7608.01	7.6 (±0.1)
	P07926				Q06055		
	Q3ZC75				P48201		
F6	P02721	8958.09	8959.0	9 (±0.05)	P18859	8960.15	8.9 (±0.1)

[a] As published in Meyer *et al.*[22] [b] These signals occur in a shoulder only and hence the error range is untypically large.

detected. These proteins are missing, since DDM, a detergent that is known to strip both proteins from the complex,[22] was used for solubilisation and also for a buffer exchange in this work.

The spectrum of human ATP synthase measured at an even lower protein concentration than that of the bovine ATP synthase is characterized by a reduced overall signal intensity compared to the bovine system. However, 8 subunits from the 15 expected ones can be clearly assigned. Only the subunits f and γ presumably disappeared in the noise of the spectrum. They are also of low intensity in the spectrum of the bovine ATPase, recorded at a slightly higher concentration. Another 5 peaks appear as shoulders of intense peaks.

The absence of the OSCP peak, which is intense in the bovine ATPase spectrum, is surprising. In addition it was not possible to record spectra of the intact complexes which most likely is a result of the rather low concentration of these samples. The unusual high amount of droplets needed to obtain the signals of the subunits (1000 for human and 900 for bovine ATP synthase) is a further indication of an insufficient sample concentration. In general respiratory complexes can be recovered in native state from BN gels as shown for bovine complex I[23] and for the ATP synthase from yeast.[24] Furthermore the detection of intact complexes with LILBID-MS after electro-elution from BN gels was already demonstrated for complex I from *Yarrowia lipolytica*.[33] Nevertheless we think that the lack of detectable native ATP synthase complexes is mainly a result of our sample preparation protocol applied for LILBID analysis using detergent to remove Coomassie-dye from the protein which is delipidating and denaturing especially when handling very low protein amounts.

4. Comparison

A comparison of the ATP synthase subunit compositions in Table 3 reveals differences in the complexity of eukaryotic and bacterial ATP synthases.[22] However, whereas the overall construction of eukaryotic enzymes is more complex than the bacterial ones, selected but functionally important subunits remain conserved among all ATP synthases. This includes, for example, the catalytically active β-subunits; these are known to show subtle but nevertheless important differences in structure:[3] These subunits maintain different conformational states and nucleotide affinities for ADP + P_i to ATP conversion, as proposed for the enzyme's binding change mechanism.[7] A high conservation can also be found in the subunits α and γ of the F_1 subcomplex, a fact which is also reflected by the masses obtained in LILBID-MS. In the F_o motor, the most highly conserved subunit is the subunit c, which is known to form the rotor ring in all ATP synthases. High-resolution structures of several rotor rings are available.[26–29,38] From these structures it has become clear that the overall construction of rotor rings is highly conserved, whereas subtle variations within the rotor ring shape and construction of their ion binding sites are responsible for the specificity of the coupling ions (H^+ or Na^+),[28,30,38] which drive the F_o motor. In the context of this study of the ATP synthase rotor rings, LILBID-MS proved to be a novel tool for the determination of rotor ring stoichiometries (c_n), of which *n* represents the number of subunits necessary to form one c-ring.[10] Interestingly, the number of c-subunits in principle equals the number of ions (*n*) transported across the membrane[26,29] for every 360° rotation of the rotor[1,3,25,31] in which three ATP molecules are synthesized in the three β-subunits of the F_1 complex. Hence the ion-to-ATP ratio of the ATP synthase can be expressed by *n*/3. LILBID-MS has been proven to be applicable for the assignment of rotor ring stoichiometries[10] and hence also represents a relatively easy-and-fast but nevertheless accurate method for the determination of ion-to-ATP ratios in ATP synthases,[32] which represents an important parameter in cell bioenergetics. In addition it should be pointed out that the relative signal intensities of the single charged α and β subunits may be different for various ATP synthases. In bacterial F_1F_o-ATP synthases the intensities of these two subunits usually are approximately equal as can be seen for OF4 (Fig. 2(b)) and as observed for TA2.[8] This is not surprising when comparing the theoretical isoelectric points (pI): in OF4 the pI for α is 5.11 and that for β is 5.01 (calculated with "compute pI/Mw tool" at http://www.expasy.ch/tools/pi_tool.html for all values). In the mammalian F_1F_o-ATP synthases presented in this work the β subunits occur with a relative high signal intensity whereas the α subunits are hardly visible. For the human complex the pIs for α and β subunits are 8.28 and 5.0 while for the bovine complex the pIs are 8.27 and 5.0, respectively. Thus at the given buffer conditions the α subunits carry less negative charges than β and hence are only weakly detected in anion mode. In F_1F_o-ATP synthases from *Yarrowia lipolytica*[14] the α subunit (pI 6.6) occurs at about half the intensity of the β subunit (pI 4.81).[14] Though calculated pIs may not reflect the accurate charge state in the functioning proteins, the LILBID spectra correctly reflect the relative charge states in solution for the presented complexes.

Table 3 Comparison of subunit masses (given in kDa) of F_1F_o ATP-synthases measured by LILBID

Subunit	*Bacillus pseudofirmus* OF4	*Bacillus* sp. strain TA2.A1[8,36,37]	*Yarrowia lipolytica*[14]	*Bos taurus* F_1F_o (excerpt of Table 2)	*Homo sapiens* F_1F_o (excerpt of Table 2)
a		26.6		24.7	27.8
b	15.8	19.6	22.4	24.7	24.6
c	7.0	7.1	7.7	7.7	7.6
α	54.1	55.0	55.6	55.3	55.3
β	51.3	51.2	51.1	51.7	51.7
γ	31.5	31.9	30.1	30.2	30.2
δ	20.3	20.3	6.7	15.1	15.1
ε	14.4	14.9	14.7	5.7	5.7

5. Conclusions

We determined the molecular masses of the subunits of three different F-type ATP synthases, *i.e.* a bacterial complex from *Bacillus pseudofirmus* OF4 and an eukaryotic ATP synthase from *Bos taurus* (bovine) and, for the first time, of human (*Homo sapiens*) heart mitochondria, by laser induced liquid bead ion desorption-mass spectrometry (LILBID-MS). This novel method allows the mass determination of non-covalently assembled membrane protein complexes up to the MDa-range with high accuracy. Low amounts of protein complexes (micrograms or less) can be dissolved in detergent solution at easily manageable concentrations. The method can be applied in several modes, from soft laser desorption, giving the intact macromolecular complexes to medium to harsh laser intensity, which disassembles the protein complexes partially into subcomplexes. At even higher laser intensities, the subcomplexes become disassembled and the single subunit composition can be determined. By combining these top-down mass data for those cases where all subunits and the mass of the integral complex are identified, the determination of the stoichiometry of the fully assembled complexes is possible.

Comparing LILBID with nESI

LILBID and nESI, which may be considered as native mass spectrometries, can be used on biological samples with similar sensitivity. Nevertheless they are complementary in respects, so it is quite likely that LILBID will continue to contribute value to the investigation of noncovalent complexes and especially membrane complexes. For example, while detergents are needed for solubilisation of hydrophobic complexes and remain a challenge for ESI, they seem to have a less critical impact for LILBID. LILBID is also more tolerant to addition of salt or various buffers other than ammonium acetate. Therefore non-covalent membrane complexes, or complexes that contain soluble and hydrophobic parts can reliably be detected without dissociation with LILBID, while the ESI results mirror the stability of a membrane complex, giving the method a strong bias towards soluble complexes. The softness of LILBID results in ions, which are still protected by a shell of buffer/detergent molecules, which may even be an entire micelle surrounding the protein. This leads to a noticeable broadening of the peaks towards higher masses and hence hampers the determination of the exact mass of the complex, more than for a well-resolved ESI spectrum. This drawback of LILBID-MS is evident when comparing the results presented in the present work with the analysis of a V-type ATP synthase by ESI-MS.[39] On the other hand the assignment challenges for the highly charged ESI ions rather lie in determination of the right charge states as well as overlapping peak series, which may cause congestion of the spectra. Ions in LILBID generally carry much less charges than in ESI and show an enhanced propensity for the detection of negative ions. This may be an advantage in fragmentation studies due to a reduced coulombic repulsion.

Both methods offer soft and harsh mode for measurements in a top-down fashion. While CID (collision induced dissociation) for nESI leads to the dissociation of usually one or two proteins in peripheral position, harsh laser conditions of LILBID will result in a complete disassembly of all subunits by thermolysis. Their charge states will mirror their net charge in solution, while in ESI the charging is mainly caused by the ammonium acetate buffer. Medium laser conditions in LILBID can allow the survival of strongly interacting subcomplexes. So the different fragmentation pathways of both methods can deliver truly complementary results. The mass resolution of LILBID is presently not yet satisfactory, but the next generation of a LILBID mass spectrometer with improved mass resolution is currently under development.

Outlook

LILBID-MS offers a novel way to determine masses of hydrophobic membrane protein complexes at low concentrations and in detergent solution. The applicability of the method encompasses not only selected mid-sized membrane complexes such as ATP synthases (Complex V) reported here, but also other even larger membrane complexes such as Complex I from the mitochondrial respiratory chain with 41 subunits and a total mass of 960 kDa.[33] Furthermore, the stoichiometry in the quaternary structure of rhodopsins and a potassium channel have been recently analyzed by this method.[34]

Acknowledgements

This work was supported in part by the research grant GM28454 from the National Institute of General Medical Sciences (to TAK), the Cluster of Excellence "Macromolecular Complexes" at the Goethe University Frankfurt (DFG Project EXC 115) (to BB and TM) and the DFG Collaborative Research Center (SFB) 807 (to TM). IW was supported by the Deutsche Forschungsgemeinschaft, Sonderforschungsbereich 815, Project Z1 (Redox-Proteomics).

References

1 P. D. Boyer, *Annu. Rev. Biochem.*, 1997, **66**, 717–749.
2 W. Junge, H. Sielaff and S. Engelbrecht, *Nature*, 2009, **459**, 364–370.
3 J. P. Abrahams, A. G. W. Leslie, R. Lutter and J. E. Walker, *Nature*, 1994, **370**, 621–628.
4 P. Dimroth, C. v. Ballmoos and T. Meier, *EMBO Rep.*, 2006, **7**, 276–282.
5 I. R. Collinson, J. M. Skehel, I. M. Fearnley, M. J. Runswick and J. E. Walker, *Biochemistry*, 1996, **35**, 12640–12646.
6 R. A. Capaldi and R. Aggeler, *Trends Biochem. Sci.*, 2002, **27**, 154–160.
7 P. D. Boyer, *Biochim. Biophys. Acta, Bioenerg.*, 1993, **1140**, 215–250.
8 N. Morgner, J. Hoffmann, H.-D. Barth, T. Meier and B. Brutschy, *Int. J. Mass Spectrom.*, 2008, **277**, 309–313.
9 I. Wittig and H. Schägger, *Biochim. Biophys. Acta, Bioenerg.*, 2008, **1777**, 592–598.
10 T. Meier, N. Morgner, D. Matthies, D. Pogoryelov, S. Keis, G. M. Cook, P. Dimroth and B. Brutschy, *Mol. Microbiol.*, 2007, **65**, 1181–1192.
11 N. Morgner, T. Kleinschroth, H.-D. Barth, B. Ludwig and B. Brutschy, *J. Am. Soc. Mass Spectrom.*, 2007, **18**, 1429–1438.
12 N. P. Barrera, N. Di Bartolo and C. V. Robinson, *Science*, 2008, **321**, 243–246.
13 J. Vonck, K. Y. Pisa, N. Morgner, B. Brutschy and V. Müller, *J. Biol. Chem.*, 2009, **284**, 10110–10119.
14 L. Sokolova, I. Wittig, H.-D. Barth, H. Schägger, B. Brutschy and U. Brandt, *Proteomics*, 2010, **10**, 1401–1407.

15 D. B. Hicks and T. A. Krulwich, *J. Biol. Chem.*, 1990, **265**, 20547–20554.
16 I. Wittig, H.-P. Braun and H. Schägger, *Nat. Protoc.*, 2006, **1**, 418–428.
17 R. Aggeler, J. Coons, S. W. Taylor, S. S. Gosh, J. C. Garcia, R. A. Capaldi and M. F. Marusich, *J. Biol. Chem.*, 2002, **277**, 33906–33912.
18 N. Morgner, H.-D. Barth and B. Brutschy, *Aust. J. Chem.*, 2006, **59**, 109–114.
19 J. Hoffmann, T. L. Schmidt, A. Heckel and B. Brutschy, *Rapid Commun. Mass Spectrom.*, 2009, **23**, 2176–2180.
20 M. E. Pullman, H. S. Penefsky, A. Datta and E. Racker, *J. Biol. Chem.*, 1960, **235**, 3322–3329.
21 J. Carroll, I. M. Fearnley, Q. Wang and J. E. Walker, *Anal. Biochem.*, 2009, **395**, 249–255.
22 B. Meyer, I. Wittig, E. Trifilieff, M. Karas and H. Schägger, *Mol. Cell. Proteomics*, 2007, **6**, 1215–1225.
23 T. Clason, T. Ruiz, H. Schägger, G. Peng, V. Zickermann, U. Brandt, H. Michel and M. Radermacher, *J. Struct. Biol.*, 2010, **169**, 81–88.
24 I. Wittig, R. A. Stuart, J. Velours and H. Schägger, *Mol. Cell. Proteomics*, 2008, **7**, 995–1004.
25 R. K. Nakamoto, J. A. Baylis Scanlon and M. K. Al-Shawi, *Arch. Biochem. Biophys.*, 2008, **476**, 43–50.
26 T. Meier, P. Polzer, K. Diederichs, W. Welte and P. Dimroth, *Science*, 2005, **308**, 659–662.
27 T. Murata, I. Yamato, Y. Kakinuma, A. G. Leslie and J. E. Walker, *Science*, 2005, **308**, 654–659.
28 T. Meier, A. Krah, P. J. Bond, D. Pogoryelov, K. Diederichs and J. D. Faraldo-Gómez, *J. Mol. Biol.*, 2009, **391**, 498–507.
29 D. Pogoryelov, Ö. Yildiz, J. D. Faraldo-Gómez and T. Meier, *Nat. Struct. Mol. Biol.*, 2009, **16**, 1068–1073.
30 A. Krah, D. Pogoryelov, J. D. Langer, P. J. Bond, T. Meier and J. D. Faraldo-Gómez, *Biochim. Biophys. Acta, Bioenerg.*, 2010, **1797**, 763–772.
31 H. Noji, R. Yasuda, M. Yoshida and K. Kinosita, Jr, *Nature*, 1997, **386**, 299–302.
32 S. J. Ferguson, *Curr. Biol.*, 2000, **10**, R804–R808.
33 N. Morgner, V. Zickermann, S. Kerscher, I. Wittig, A. Abdrakhmanova, H.-D. Barth, B. Brutschy and U. Brandt, *Biochim. Biophys. Acta, Bioenerg.*, 2008, **1777**, 1384–1391.
34 J. Hoffmann, L. Aslimovska, C. Bamann, C. Glaubitz, E. Bamberg and B. Brutschy, *Phys. Chem. Chem. Phys.*, 2010, **12**, 3480–3485.
35 H. Schägger and G. von Jagow, *Anal. Biochem.*, 1987, **166**, 368–379.
36 M. V. Nesterenko, M. Tilley and S. J. Upton, *J. Biochem. Biophys. Methods*, 1994, **28**, 239–242.
37 D. Matthies, L. Preiss, A. L. Klyszejko, D. J. Müller, G. M. Cook, J. Vonck and T. Meier, *J. Mol. Biol.*, 2009, **388**, 611–618.
38 L. Preiss, Ö. Yildiz, D. B. Hicks, T. A. Krulwich and T. Meier, *PLoS Biol.*, 2010, **8**, e1000443.
39 Z. Y. Zhang, Y. Zheng, H. Mazon, E. Milgrom, N. Kitagawa, E. Kish-Trier, A. J. R. Heck, P. M. Kane and S. Wilkens, *J. Biol. Chem.*, 2008, **283**, 35983–35995.

